Numerical investigation of restricted curved waterways on ship hydrodynamics for maneuverability considerations

Bo Yang

Par **Bo YANG**

Numerical investigation of restricted curved waterways on ship hydrodynamics for maneuverability considerations

Thèse présentée
pour l'obtention du grade
de Docteur de l'UTC

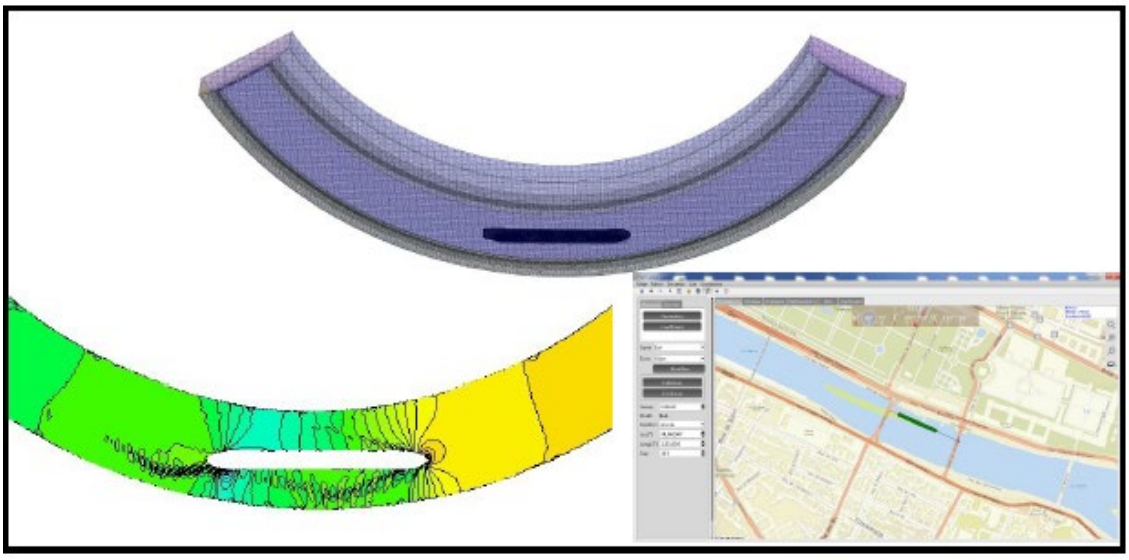

Soutenue le 12 avril 2023
Spécialité : Mécanique Numérique : Unité de recherche en Mécanique - Laboratoire Roberval (FRE UTC - CNRS 2012)
D2735

Numerical investigation of restricted curved waterways on ship hydrodynamics for maneuverability considerations

Thesis submitted for the degree of Doctor

by **Bo YANG**

Université de Technologie de Compiègne, Laboratoire Roberval

Defended on April 12, 2023

Devant le jury composé de :

M. P. VILLON (Président)

M. S. KAIDI (Directeur de thèse)

M. E. LEFRANÇOIS (Directeur de thèse)

Mme F. LARRARTE (Rapporteur)

M. Y-M. SCOLAN (Rapporteur)

M. D. CALLUAUD

Étude numérique des efforts hydrodynamiques impactant la manœuvrabilité des navires en canaux confinés incurvés

Thèse présentée pour l'obtention du grade de Docteur

Par Bo YANG

Université de Technologie de Compiègne, Laboratoire Roberval

12 avril 2023

Acknowledgements

First and foremost, I'd like to sincerely express my deepest and strongest gratitude to both of my supervisors, Pro. Emmanuel Lefrançois, and Senior researcher Dr. Sami Kaidi. I really feel it great fortune and honor for me to get the chance of working with them during the three years and a half. They are always so patient, motivated, enthusiastic and full of knowledge. They have a lot of skills and techniques, and I honestly thank them a lot for their instructing me so carefully. They instructed me in STARCCM+, helped me correct my publications little by little, and gave me much advice and help in my difficulties. I still and will forever remember the daily meetings with them, the detailed advice from them, the constructive analysis and discussion together with them.

They were always so patient with me, and tried to encourage me to be confident. Even for my minor progress, they were never stingy with compliments. Without their great help, I couldn't finish my Ph.d work fluently. I appreciate all their contributions of patience, time, ideas and energy that were poured into me and I'm thankful for the resources they created for me. I learned a lot from them within these years. It is them who help me gradually grow into a real researcher.

I would like to thank CEREMA for the precious resources they provided, such as the computers with high performance, and the cost of international conference, etc. Even though I worked in UTC at ordinary times, many resources were offered by CEREMA. However, the only regret for me is that I didn't get to know the other staff in CEREMA.

I have to also show my profound appreciation to my family. Since I arrived in France in 2019, I never returned to China for vacation due to the sudden outbreak of

Covid-19. Within these years, it was their encouragement that kept me going. They are the strongest support behind me.

Finally, thank you to everyone who ever helped me during my time in Compiegne. It's really a good time in my life.

Abstract

Inland waterway transport is now playing a significant role thanks to its various advantages over the other transportation modes, for example, low cost, low environmental pollution, and large capacity, etc. However, inland waterways are not only naturally curved but also narrow and shallow, which causes complex flow environments and navigational conditions. Inland ships are consequently susceptible to accidents in restricted curved waterways. Especially during these years, this mode of transport has seen significant progress by the arrival of the new generation of ships (larger size and more powerful), and this makes ships' maneuverability in such sensitive waters severer.

To conduct this investigation, the CFD model based on an unsteady Navier-Stokes solver in STARCCM+ is used. The verification and validation of this model are realized by respecting the ITTC recommendations. The latter is then used to perform a series of simulations by testing the following key parameters: a series of navigational environmental parameters, including channel angle, channel bottom width, channel slope angle; a set of parameters related to ship behaviors and geometry, containing water depth to draft ratio, ship speed, drift angle and ship type (ship length) on ship hydrodynamics in restricted curved fairways. Relative frame motions are applied to the computational domains to produce centrifugal force in bending fairways.

The aim of the present thesis is firstly to characterize the variables connected to a circular channel's topology that have a substantial impact on a ship's maneuverability. Second, it helps to well understand the flow behaviors that occur around a ship in bending zones. Thirdly, the fluctuations in hydrodynamic force (bank cushion and suction phenomena) and the sensitivity of a number of variables in bending zones are investigated. Finally, the inland ship simulator is improved by adding the bending zone

effect for pilots, so that the behaviors of ships in the sensitive regions can thus be corrected.

Key words: CFD simulations; bending effect; inland navigation; restricted waterways; ship hydrodynamics; inland ship simulator

Résumé

Le transport par voies navigables joue aujourd'hui un rôle important grâce aux divers avantages qu'il présente par rapport aux autres modes de transport, par exemple son faible coût, sa faible pollution environnementale et sa grande capacité, etc. Cependant, les voies navigables intérieures ne sont pas seulement naturellement courbées, mais aussi étroites et peu profondes, ce qui entraîne des environnements d'écoulement et des conditions de navigation complexes. Les bateaux de navigation intérieure sont donc susceptibles d'avoir des accidents dans les voies d'eau à courbure limitée. Ces dernières années, ce mode de transport a connu des progrès significatifs avec l'arrivée de la nouvelle génération de navires (plus grands et plus puissants), ce qui rend la manœuvrabilité des navires plus difficile dans ces eaux sensibles.

Pour réaliser cette étude, le modèle CFD basé sur un solveur Navier-Stokes instationnaire dans STARCCM+ est utilisé. La vérification et la validation de ce modèle sont réalisées en respectant les recommandations du CTI. Ce dernier est ensuite utilisé pour effectuer une série de simulations en testant les paramètres clés suivants : une série de paramètres environnementaux de navigation, comprenant l'angle du chenal, la largeur du fond du chenal, l'angle de pente du chenal ; une série de paramètres liés au comportement et à la géométrie du navire, contenant le rapport entre la profondeur d'eau et le tirant d'eau, la vitesse du navire, l'angle de dérive et le type de navire (longueur du navire) sur l'hydrodynamique du navire dans les chenaux courbes restreints. Les mouvements du cadre relatif sont appliqués aux domaines de calcul pour produire la force centrifuge dans les chenaux courbés.

L'objectif de la présente thèse est d'abord de caractériser les variables liées à la topologie d'un canal circulaire qui ont un impact substantiel sur la manœuvrabilité d'un navire. Deuxièmement, elle permet de bien comprendre les comportements d'écoulement qui se produisent autour d'un navire dans les zones de flexion.

Troisièmement, les fluctuations de la force hydrodynamique (phénomènes de coussin de berge et de succion) et la sensibilité d'un certain nombre de variables dans les zones de flexion sont étudiées. Enfin, le simulateur de navire intérieur est amélioré en ajoutant l'effet de zone de flexion pour les pilotes, de sorte que les comportements des navires dans les régions sensibles peuvent ainsi être corrigés.

Mots clés : Simulations CFD ; effet de flexion ; navigation intérieure ; voies navigables restreintes ; hydrodynamique des navires ; simulateur de navire intérieur

Contents

List of Figures

List of Tables

Chapter 1

1.Introduction

1.1 Background and state of the art review

The inland waterway transport has a range of advantages over rail and road transport, including large capacity, low cost, and low energy consumption, etc [1]. However, there are various forms in inland rivers or canals, such as bending, straight and bifurcated sectors, among which the bending sectors are the most common and dangerous zones (see Fig 1. 1). On one hand, inland curved waterways are both very narrow and shallow, making them become restricted waters. On the other hand, special and complex flows will be induced due to the centrifugal force in curved fairways. Many scholars were devoted to figuring out the flow characteristics in bending zones[2-7], and the general flow characteristics of the water in the bend have been understood. The current will move in a curve when it flows through the bending zones due to the centrifugal force, causing unequal water levels between both banks[4, 8, 9]. The water surface is not perpendicular to the gravity direction of the ship, which affects the stability of the ship during cornering. The surface current tends to own higher velocity and centrifugal force, flowing towards the concave bank, while the opposite is true for the bottom current, it flows to the convex bank due to the low velocity and centrifugal force. Eventually, a closed loop flow is formed coupled with the gravitational force and frictional resistance of the flow[5, 10, 11].

Fig 1. 1 Inland curved fairways

(a) Source： Peakpx
(b) Source：Don River, Russia, by HARRY VALENTINE

In this way, the submerged part of the ship is subjected to a longitudinal spiral current. Due to the presence of loop current, the currents in curved channels will generate lateral flow velocities which are the main cause of ship yaw. Besides, the free surface on both banks is divided into high and low levels owing to the bending of the main flow line, and it's often accompanied by abnormal water flows such as sweeping water, oblique flow and backflow, etc [12, 13]. And what's more, this further causes uneven distribution of water depths between both banks. Commonly, the water depth on the concave bank side is larger, while the water depth on the convex bank side is smaller. The convex shore is often silted up to form a side beach with the sand mouth, sand feet and other silt, some of which lurk underwater and extend far into rivers [14, 15]. So upstream ships are liable to run aground when sailing along convex banks. Because of the uneven distribution of water depth in the curved channel, the ship is more prone to shore suction and shore cushion[16-18].

The complex flow characteristics is the root cause for the high accidental rate for ships' passing the bending zones, due to which the motion state of ships will be consequently changed, bringing enormous difficulty in ships' maneuvering. Especially this is currently coupled with an increasingly larger size of vessels in inland waterways, and inland ships are always with more complex setups than seagoing ships. However, given the existing infrastructure (harbors, locks, inland waterways, ...) that have become restricted waters, this new generation of ships has severe maneuverability issues. The flow pattern around the ship hull will surely change under such situations owing to boundary constraints such as fairway bulkheads or quay bulkheads, and the associated ship hydrodynamics will likewise change dramatically[19, 20]. As a result, the state of motion of ships will vary, making ship maneuverability extremely difficult. All of these above increase the risk of accidents for ships' navigating.

Till now, research on bending scales is insufficient, and there is no unified conclusion about how to set the bending scales safely and effectively. Importantly, when ships sail in shallow bending zones, the flow characteristics in such regions will also change accordingly [21, 22], which makes it different from what it would be without ships navigating. Even so, many researchers have attempted research work in this area[11, 13, 15, 16, 23-30]. Some research and analysis have been done on the water flow characteristics and sediment transport characteristics of curved rivers [9, 31]. The mechanism and characteristics of water movement in curved rivers have been basically known [7, 9]. Later, a nonlinear closure submodel for predicting flow characteristics that overcomes the feedback of the commonly used linear closure submodels was studied by Koen Blanckaert and Huib J. de Vriend [2] so that the performance of depth-integrated models accounting for the secondary circulation in curved channels was improved. Nevertheless, most researchers are numerically concerned with the water flows in the bends without ships sailing. Few numerical investigations have looked at the details of the flow field in curves with ships sailing so far.

In recent years, combining experiments, Maslikova et al. [32] proposed a model to describe the joint effect of a flow on curved banks, including in the process of rock thawing, and the impact of ship waves. Vujičić et al. [33] gave a practical and theoretical approach to assessing safe navigating in waterways based on expertise and experience, the aim of which is to propose a way of control for seamen working at sea. Ai and Gan [34] proposed some factors influencing the occurrence of accidents in curved channels and brought forward a formula to calculate the safe navigation probability when ships pass curved fairways. Then through theoretical analysis, Ai and Zhu [26] put forward a measurement equation for calculating drift angle by including a set of parameters like channel radius and water depth, etc. Li et al. [35] compared and analyzed the flow characteristics of currents in curved rivers with 3 different channel angles employing the CFD tool Fluent. Aseperi [10] investigated the

impact of curvature radius and inertial forces on the flow characteristics of an idealistic river bend with the CFD method. Lee et al. [36-38] explored the ship's maneuvering motion centered on the hydrodynamic interaction effects of two large vessels traveling through a curved narrow channel with numerical calculations based on the PALMI island canal in Korea. Via this research, the influence of the speed ratio and the separation of two vessels were summarized and analyzed. Wang and Cheng [39] performed a series of experiments under different conditions of bend flow and width of the curved fairway, through which the link between channel width and flow was outlined while a ship sails in bend scope. The results showed that the navigation breadth around the bend upwards is much narrower than down, and it becomes broader with velocity or flow angle increasing. Also, they gave advice on ship turning operations and peer safety management. However, there is no study of the effect of bending channels on ships' navigation, and whether ships' navigation has an effect on the flow behaviors around the ship in the bends. Except that Yang et al. [40-42] studied the influence brought by a series of key parameters in confined curved fairways on ship hydrodynamics via CFD technique, which helps understand the flow behavior around an inland ship in such sensitive waters.

The bank effect can be defined, when a ship is sailing along the bank (close to the bank wall)[43-46], the hydrodynamic forces on port and starboard sides of the ship will be different, because the asymmetric flow around a ship induced by the vicinity of banks causes pressure differences between port and starboard sides. Many researchers have ever focused on this orientation [47]. H. Yasukawa [48] utilized a basic analytical approach to study the course stability of a ship sailing close to a bank and obtained the hydrodynamic derivatives by captive model tests. Using a scale model of the KRISO very large crude carrier (KVLCC2), Liu et al. [49] carried out planar motion mechanism (PMM) tests in various water depths to evaluate the impact of ship-bank interaction on ship maneuvering motion. Șerban and Panaitescu [50] gave a case study of ship-to-shore contact while a bulk carrier navigates a constrained

channel in the Suez Canal at a variety of speeds. Sano et al. [51] investigated the impact of shallow water and bank effects on hydrodynamic force characteristics by captive model tests. Based on CFD analysis, Sian et al. [52, 53] examines ship-bank interaction effects of a LNG tanker in shallow water by analyzing the hull hydrodynamic forces/moments and ship-bank interaction forces/moments. A mathematical model for bank effects was proposed in [43, 54], which considers a longitudinal force and two sway forces at each perpendicular. However, the work above mainly focused on ships navigating in straight channels, and no research has ever investigated the bank effect of a ship navigating in curved fairways with considering various configurations. In curved fairways, a ship normally has to navigate close to the concave bank because of the larger water depth on this side. Although the bending effect is similar to the bank effect in some ways, the flow in curves is greatly different. While the bending effect concerned in this work is induced by the special flow conditions in curves (caused by centrifugal force) that can greatly influence and change ship motion and hydrodynamic forces on ship. This is also the motivation of the current thesis.

Nowadays, the CFD technique has witnessed great progress and it has been adopted as a greatly effective tool to conduct explorations by researchers in both deep waters and confined shallow waters [55-63], because experiments not only are costly but also will omit the details of the flow field [64-66], while numerical research with CFD both costs less and contributes to 3D analyzing of the flow mechanisms[67-69]. Seemontini Roy Choudhury et al. [70] researched steady motions of drift and yaw based on a specific crude ship with the CFD solver SHIPFLOW both in deep and shallow waters, and the simulation results were in agreement with those from experiments. Ivan Shevchuk and Nikolai Kornev [71] assessed the effect of shallow water conditions on ship hull vibration hydrodynamic exciters with the CFD tool OpenFOAM, through which it is found that the ship's stern may be affected by intermittent pressures and moments due to the depth limit.

Lu Zou et al. [72] utilized CFD methods to study the bank effects on a tanker hull by considering varying water depths, ship-to-bank distances and bank geometries, and conducted verification and validation by a grid convergence survey for assessing the accuracy in numerical calculations. Momchil Terziev combined the CFD method with Slender-Body theory and empirical methods to research the behavior and performance of the DTC container ship passing through shallow restricted waters, and found good agreement among different methods when the ship navigates at low speed [73]. Besides, Du et al. investigated the resistance, ship-generated waves [74] and ship maneuverability [75] of inland ships in confined straight waterways based on numerical simulations. Tezdogan et al. [60] utilized the CFD tool STARCCM+ to predict the squat and resistance of a model container ship under different ship drafts and ship speeds. Their numerical results were highly consistent with experimental ones. After this, they conducted a computational analysis of ship movements in shallow water to model the ship's heave and pitch reactions to head waves [62]. Subsequently, a parametric comparison of the behavior and efficiency prediction techniques in shallow waters was carried out by [73], the key goal of which is to determine how a change in channel topography affects ship sinkage, trim, and resistance.

With the CFD method, Kaidi et al. numerically investigated the effect of the bank-propeller-hull relationship on ship maneuvering [76]. After that, they studied the impact of confined waters on force interaction between hull, propeller, and rudders of an inland container ship [77, 78]. Also, Razgallah et al. looked at how free surface simulation affected ship hydrodynamic forces in inland channels, taking into account varying water depths, ship speeds, and even drift angle [79, 80]. More recently, they checked the capacity of the CFD method for modeling and measuring the impact of mud on the hydrodynamic loads exerted on the vessel [81]. Compared with the results from experiments, their results showed good agreement, which proves the ability of the CFD system to replicate difficult-to-achieve configurations in a towing tank. Also,

Bechthold and Kastens[82] simulated the sinkage and trim of 3 postpanamax of neopanamax container ships in confined shallow waters by virtue of STARCCM+. Their results displayed reliable uniformity when compared with model test data. To evaluate the relative effects of canal depth and/or width constraints on the overall ship sailing performance, Khaled Elsherbiny et al. analyzed hydrodynamic phenomena of ships sailing through the Suez Canal in the permitted speed range utilizing STARCCM+ [83, 84]. Finally, a clear correlation between the canal's cross-section and all the parameters studied was revealed.

1.2 Motivation and research objectives

The chief objective of this thesis is to improve the inland ship navigator. In order to achieve this, a numerical investigation about the hydrodynamic forces and moment acting on ship in restricted curved waterways is carried out. A range of key parameters (introduced in the next paragraph) that may seriously impact the ship controllability in restricted bending channels are taken into consideration. The CFD method based on an unsteady Navier-Stokes solver in STARCCM+ is used to conduct this study. An inland container ship is selected for this investigation. The flow behaviours around the ship in restricted curved fairways are analysed in detail.

This thesis firstly aims at the verification and validation of the CFD model based on ITTC recommendations. The optimum mesh settings are set up and numerical results are compared to those from experiments in towing tanks for validation. Secondly, a set of important parameters concerned navigational environment and ship behaviors and geometry in restricted curved channels are investigated with the validated CFD model. Thirdly, the factors related to the topology of a circular channel and ship particulars are characterized, which can significantly influence the maneuverability of the ship. Secondly, it helps us understand the flow behaviors around the ship in the bending sections of waterways. Fourthly, the hydrodynamic force variations and sensitivity of several parameters in bending zones are studied.

The navigational environment parameters considered are channel angles(α), channel bottom width(W) and channel slope angle (γ); parameters of ship behaviors and geometry are water depth to draft ratio(h/T), ship speed(Vs), ship's drift angle(β), and ship type. Then the force and moment variations are fitted and analyzed to check whether they can be expressded by simplified formulas. Finally, the inland ship simulator developed in CEREMA can be improved by adding the bending zone effect for pilots so that the behaviors of ships in the sensitive regions can thus be corrected.

The proposed approach is based on a sensitivity analysis (conducted by CFD calculations) of these factors on the hydrodynamic forces undergone by ships. However, we will limit ourselves to the case of a circular channel with no current flow and traveled by a ship.

1.3 Methodology

This thesis highlights the factors that can influence the ship navigability in restricted channels. Here the circular canal cases are clearly pointed out that are potentially more dangerous on the aspects of controllability of the ship due to restricting geometry dimensions.

The equilibrium of a ship is governed by the fundamental principle of dynamics and can be expressed through the following two mathematical relations in equation (1.1):

$$m\frac{d^2u}{dt^2} = F_{pilot} + F_{hydro}\ ,\ \text{ב}|_G\frac{d^2\emptyset}{dt^2} = M_{pilot}(G) + M_{hydro}(G) \qquad (1.1)$$

We respectively denote by m and $\text{ב}|_G$ the mass and the inertia of the ship taken at its center of mass G. The forces F and resulting moments M are here decomposed in two major contributions. We distinguish the forces and torques controlled by the pilot through the controls of the rudder and propeller (see equation 1.2):

$$F_{pilot} = F_{propeller} + F_{rudder},\ M_{pilot}(G) = M_{propeller}(G) + M_{rudder}(G) \qquad (1.2)$$

The hydrodynamic-related external contributions resulting from the vessel's interaction with the surrounding fluid flow [85-89], which is expressed in equation (1.3):

$$F_{hydro} = F_{buoyancy} + F_{resistance} + F_{sway}, M_{hydro}(G) = M_{yaw}(G) + M_{pitch}(G) + M_{roll}(G) \quad (1.3)$$

The forces and moments are illustrated in Fig 1. 2.

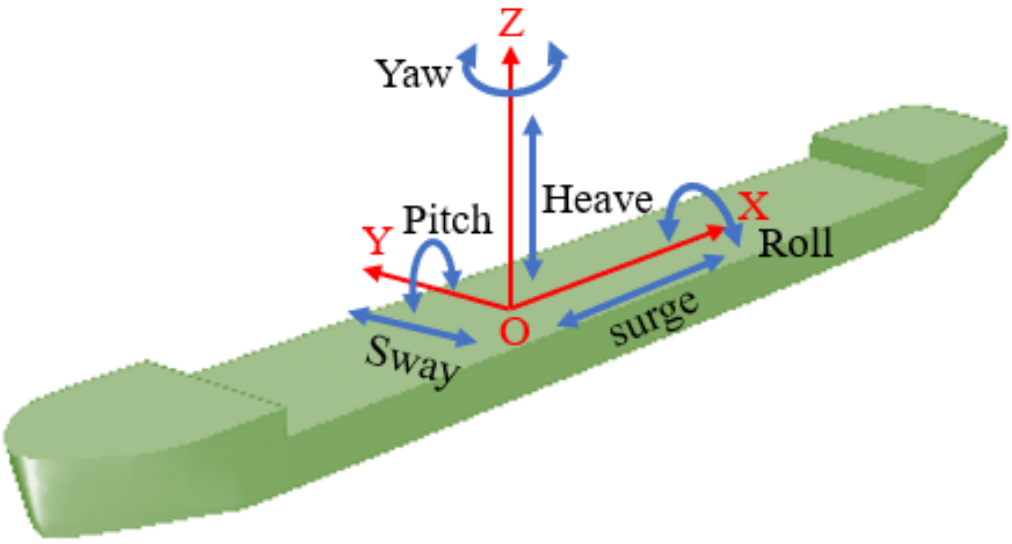

Fig 1. 2 Motion and force illustrations of the ship model in this work

Each component of force and moment is generally associated with a dimensionless cœfficient which allows, among other things, to facilitate the comparison between different geometries and between theory and measurements [90-92]. The main coefficients are generally linked to the buoyancy C_z, to the resistance C_x and to the yaw moment C_m.

The equilibrium equations (1.1) and (1.2) reflect a subtle balance between hydrodynamic forces and pilot actions. The controllability of the ship requires that the manœuvering margin available to the pilot through the rudder and the propeller (engine speed) is such that it makes it possible to counter any hydrodynamic contribution that would make dangerously deviate the ship from its path [93, 94]. For

example, an increase in resistance can have an impact on the ability to pull up a local current effect and also on fuel consumption (environmental impact), a reduction in buoyancy may be at the origin of an over-sinking of the ship with the risk of hitting the bottom (squat effect). At least a significant variation in the hydrodynamic yaw moment can cause a ship to yaw put across the channel, for example, a recent accident has happened to the Evergreen ship in Suez Canal, which blocked traffic [232-234]. Another important parameter is related to the inertia effects that characterize the reaction time of a pilot action (typically propeller thrust) but this study is not considered here in this article.

The proposed approach is based on a sensitivity analysis (conducted by CFD calculations) of these factors on the hydrodynamic forces undergone by ships. However, this thesis will limit itself to the case of a circular channel with no current flow and traveled by a ship. This thesis doesn't focus on the transient response, but concentrates on the drag convergence because of a series of fixed values of h/T ratios.

1.3.1 Decomposition of hydrodynamic forces and moment

Hydrodynamic forces and moment acting on a ship navigating through water can be normally divided into two components, that is, pressure component and frictional component [95, 96].

The cause of frictional component is the friction between the fluid and the surfaces over which it is flowing. This friction scales with Reynolds number and is related to the development of boundary layers [97-99]. While the pressure component is motivated by the eddying movements that are set up in the fluid by the passage of the ship hull. It is often less sensitive to Reynolds number than the frictional drag and is connected to the development of a wake, which can be easily observed behind a passing ship (see Fig 1. 3)[63, 100].

The difference between the two different kinds of force components is quite useful, because the two types are due to different flow phenomena [71, 101-103]. For

attached flows (where there is no separation), the frictional component is significant and is correlated with the surface area exposed to the flow. For separated flows, the pressure component is crucial, because it is correlated with the cross-sectional area of the body [12, 75, 104].

Fig 1. 3 Ship generated waves and wake.

Source: [105]

1.4 Outline of this thesis

This thesis is organized as follows:

—Chapter 2 describes the mathematical and numerical methods utilized in this thesis. The fundamental equations adopted are illustrated; numerical methods including finite volume method, algebraic multigrid method and boundary conditions are explained; then turbulence models used are illustrated and compared to choose the most proper one for this work; after that, the VOF method used to simulate free surface is presented, and overset mesh approach is narrated via a real simulation done in this thesis.

—Chapter 3 concentrates on the verification and validation of the CFD model. In this chapter, numerical settings of the simulations in this thesis are first introduced; then mesh generation process for the CFD model is specified to select the optimum mesh settings, and y^+ is also verified; finally, validation of the current numerical model is executed. Experiments conducted in the towing tank of Liege university and the same simulations done with the numerical model are described respectively. The comparison between simulation and experimental results is able to prove the reliability of the current CFD model. Besides, the initial conditions and solver settings for simulations in this thesis are presented.

—Chapter 4 firstly introduces some key parameters that are only related to navigational environment, that is, channel angle (α), channel bottom width (W), and channel slope angle (β). Then simulation case settings based on these parameters are set up. Finally, the effects brought by these parameters on ship hydrodynamics are investigated and analyzed in detail.

—Chapter 5 depicts some key parameters that are relevant with ship behaviors and geometry, that is, h/T ratio, ship speed (V_s), drift angle (β), ship type. Then the simulation case settings concerned with these parameters are arranged. Finally, the effect induced by these parameters on ship hydrodynamics are researched and tested explicitly. Then propellers and rudders are considered to investigate the equilibrium of moment by the two devices under different ship drift angles.

—Chapter 6 first introduces the developing course of ship bridge simulators; then Abkowitz model and MMG model are presented in detail; next, the simulation results obtained in previous sections have been fitted as fitting surfaces and will be integrated into the programming codes of the inland ship simulator of CEREMA.

—Chapter 7 draws conclusions of this thesis and also proposes some advice for future work.

1.5 Nomenclature

$\boldsymbol{V}$ Velocity [m s^{-1}]

V_s Ship speed [m s^{-1}]

p Pressure [Pa]

ρ Fluid density [Pa s]

η Kinematic viscosity [N s m^{-1}]

α Channel angle [°]

h/T Water depth to draft ratio [-]

W Channel bottom width [m]

β Drift angle [°]

L_{pp} Length between perpendiculars [m]

B Beam [m]

H Height [m]

C_b Block coefficient [-]

W_s Wetted surface area of ship [m^2]

C_s Cross area of ship [m^2]

X Resistance force [N]

Y Sway force [N]

N Yaw moment [N]

X' Non-dimensional resistance force [-]

Y' Non-dimensional sway force [-]

N' Non-dimensional yaw moment [-]

R_i Convergence ratio [-]

C_i Correction factor [-]

δ_i Numerical error [-]

P_i Order of accuracy [-]

U_i Uncertainty [-]

E Errors [%]

ω Angular velocity [rad/s]

R Channel radius [m]

M Moment [N/m]

m mass of ship [kg]

F_r Froude number

R_e Reynolds number

Chapter 2

2. Mathematical models and numerical methods

2.1 Governing equations

Fluid flow is governed by the law of conservation of mass, the law of conservation of momentum and the law of conservation of energy, which are the mathematical description of these conservation laws, called the governing equations. Governing equations are the foundations of solving for fluid motion. The flow field of the ship's maneuvering motion can be considered as incompressible flow, where the heat exchange is so small that it can be ignored, and the law of conservation of energy is not considered.

2.1.1 General form of conservation law

Fluid flow is governed by the laws of physical conservation, and the basic conservation laws include: the law of conservation of mass, the law of conservation of momentum and the law of conservation of energy. The general law of conservation for $\mathcal{X}$ is shown in equation (2.1). If $\mathcal{X}$ change with the density ρ, then the mass conservation equation will be got; if $\mathcal{X}$ equals momentum, then Navier-Stokes equation will be acquired; if $\mathcal{X}$ is the energy, then the first thermal dynamic principle will be gained.

$$\frac{d}{dt}\iiint_{\mathcal{V}_m(t)} \mathcal{X}d\mathcal{V} = \begin{cases} 0 & \leftarrow \text{if } \mathcal{X} \equiv \rho \quad \leftarrow \text{Mass} \\ \sum \mathcal{F}_{\text{ext}} & \leftarrow \text{if } \mathcal{X} \equiv \rho \text{V} \quad \leftarrow \text{QDM} \\ d\mathcal{W}/dt + d\mathcal{Q}/dt & \leftarrow \text{if } \mathcal{X} \equiv \rho \text{E} \quad \leftarrow Energy \end{cases} \tag{2.1}$$

For ship maneuvering, the entire flow field is a three-dimensional, viscous, incompressible fluid flow. Therefore, only the laws of conservation of mass and momentum need to be considered. These conservation laws can be described by a set of hydrodynamic partial differential equations, called the governing equations [106].

2.1.1.1 Conservation equations with mesh motion

In both solid mechanics and fluid mechanics, mesh motion has several meanings. In solid mechanics, a Lagrangian formulation is used to represent a component of the solid body inside the computational domain. As a result, the solid mesh's motion is the same as the solid body's motion. By using an Eulerian description, fluid mechanics makes use of a section of the computational domain to describe a region of space where material moves. In this situation, the fluid mesh can be adjusted to consider changes in the shape and location of the boundaries, such as those caused by the movement of nearby bodies.

The conservation equations are changed by mesh motion by including an extra flux in the convective terms. Additionally, the momentum equation considers the fictitious forces resulting from the non-inertial reference frame, if motion is defined with regards to a moving reference frame.

Considering the most common case, where the mesh motion is defined with regards to a reference frame that is moving relative to the laboratory reference frame. The conservation equations can be written in terms of the fluid velocity in the laboratory frame (absolute velocity) (Source: STARCCM+ user's guidelines):

$$\frac{\partial}{\partial t}\int_V \rho dV + \oint_A \rho(\mathbf{v}_r - \mathbf{v}_g)\cdot d\mathbf{a} = \int_V S_u dV \tag{2.2}$$

$$\frac{\partial}{\partial t}\int_V \rho\mathbf{v}dV + \oint_A \rho\mathbf{v}\otimes(\mathbf{v}_r - \mathbf{v}_g)\cdot d\mathbf{a} = \oint_A \boldsymbol{\sigma}\cdot d\mathbf{a} + \int_V \mathbf{f}_b dV - \int_V \rho\boldsymbol{\omega}\times\mathbf{v}dV \tag{2.3}$$

$$\frac{\partial}{\partial t}\int_V \rho E dV + \oint_A \rho E(\mathbf{v}_r - \mathbf{v}_g)\cdot d\mathbf{a} = -\oint_A \mathbf{q}\cdot d\mathbf{a} + \oint_A (\mathbf{v}\cdot\boldsymbol{\sigma})\cdot d\mathbf{a} + \int_V \mathbf{f}_b\cdot\mathbf{v}dV + \int_V S_E dV \quad (2.4)$$

Where $\mathbf{v}_g$ is the grid velocity in the laboratory reference frame, and $\mathbf{v}_r$ is the relative velocity. $\int_V \rho\boldsymbol{\omega}\times\mathbf{v}dV$ is the fictitious force introduced by the non-inertial moving reference frame, and the fictitious force is made up of Coriolis force and centrifugal force. If the reference frame is stationary, this fictitious force disappears and $\mathbf{v}_r$=$\mathbf{v}$.

2.1.2 Continuity equation

According to the definition of the law of conservation of mass, the mass per unit time that flows out of a fluid micro-element is equal to the reduction of the mass in that fluid micro-element during the same time. The conservation of mass equation is often referred to as the continuity equation. Considering incompressible fluid with a constant density, the following mass conservation equation can be obtained [107-109]:

$$\frac{\partial\rho}{\partial t} + \frac{\partial(\rho u)}{\partial x} + \frac{\partial(\rho v)}{\partial y} + \frac{\partial(\rho w)}{\partial z} = 0 \quad (2.5)$$

Where, ρ is density of fluid; u, v and w are spatial velocity components in x, y and z directions respectively.

2.1.3 Navier-Stokes equation

Navier-Stokes equation is also called the conservation of momentum equation. According to the definition of the law of conservation of momentum: the resultant force of the external forces acting on a fluid micro-element is equal to the changing rate of the momentum of the fluid micro-element with respect to time. On condition that the mass force is apart from consideration, the following equation can be obtained [110, 111]:

$$\begin{cases} \rho\left(\frac{\partial(u)}{\partial t}+\frac{\partial(uu)}{\partial x}+\frac{\partial(uv)}{\partial y}+\frac{\partial(uw)}{\partial z}\right)=-\frac{\partial p}{\partial x}+\mu\left(\frac{\partial^2 u}{\partial x^2}+\frac{\partial^2 u}{\partial y^2}+\frac{\partial^2 u}{\partial z^2}\right)+S_u \\ \rho\left(\frac{\partial(v)}{\partial t}+\frac{\partial(uv)}{\partial x}+\frac{\partial(vv)}{\partial y}+\frac{\partial(vw)}{\partial z}\right)=-\frac{\partial p}{\partial y}+\mu\left(\frac{\partial^2 v}{\partial x^2}+\frac{\partial^2 v}{\partial y^2}+\frac{\partial^2 v}{\partial z^2}\right)+S_v \\ \rho\left(\frac{\partial(w)}{\partial t}+\frac{\partial(uw)}{\partial x}+\frac{\partial(vw)}{\partial y}+\frac{\partial(ww)}{\partial z}\right)=-\frac{\partial p}{\partial z}+\mu\left(\frac{\partial^2 u}{\partial x^2}+\frac{\partial^2 u}{\partial y^2}+\frac{\partial^2 u}{\partial z^2}\right)+S_w \end{cases} \tag{2.6}$$

Where, ρ is density of fluid; u, v and w are spatial velocity components in x, y and z directions respectively; t is time; p is pressure acting on micro-element of fluid; μ is the dynamic coefficient of viscosity; S_u, S_v and S_w are sources term of the momentum equation.

2.2 Numerical methods for CFD

2.2.1 Generalities on CFD

Computational fluid dynamics (CFD) is a popular discipline in recent years, having first emerged in the USA in the 1970s. It is a new and independent discipline based on classical fluid dynamics and numerical calculation methods, which is closely related to the development of computer technology. After decades of development, positive progress has been made in several areas such as potential flow wave resistance research, viscous flow around the hull, propeller performance calculation, ship wave resistance and ship maneuverability, etc [17, 72, 112-114].

The basic idea of CFD that comes from fluid mechanics theory, is to replace a field of physical quantities that are continuous in the time and space domains by a collection of variable values at a finite number of discrete points, and an algebraic system of equations for the relationship between the field variables at the relevant discrete points can be established by means of certain principles and methods. The algebraic equations are then solved to obtain the approximate values of the field variables. So the method makes it possible to simulate various complex flow fields including the flow fields around ships. Concretely, based on the physical problems described, the mathematical model of the ship's bypass field in navigation is reasonably constructed under certain assumptions. The controlling equations of the

fluid motion around the ship are solved using relevant numerical calculation methods to obtain the ship's bypass field, and the hydrodynamic forces acting on the ship's hull are calculated [115, 116].

Compared with model tests, CFD methods are more informative, less costly, shorter, easier to parallelize, and can achieve faster response time [117, 118]. It has become an increasingly important auxiliary tool in ship design because of its characteristics and advantages such as rapid response. The application will be of great importance for optimizing ship-related design and shortening performance forecasting cycles. Specifically, the flow of both the whole space and local areas can be displayed and examined, and a lot of information including pressure, velocity and streamlines around the ship can be revealed.

Secondly, mechanistic exploratory studies are more feasible. CFD technology has clear advantages in terms of microscopic, mechanistic investigation. Researchers using CFD tools will have a positive effect on improving designs by understanding the mechanisms by which new technological measures can improve performance.

Last but not the least, analytical calculations can be performed for solid dimensions. Due to the difference in scale between models and the entities, the scale effects exist, so model-entity correlation analysis must be performed in order to have model test results to predict the performances of entities. While the CFD technique allows the prediction of performance at the entity scale, making the prediction of entity performance more reasonable. The application of CFD technology allows for the prediction of performance at the solid scale, making the prediction of solid performance more reasonable.

With the development of computer technology and the innovation of theoretical and numerical calculation methods, CFD is gradually replacing some of the classical fluid mechanics approximate calculation methods and graphical methods. Due to the possibility of varying of ship types and conditions, the method allows a series of

calculations to be easily and efficiently performed to investigate the effects of specific conditions on the ship's hydrodynamic effects of specific conditions, so it is currently widely used in the field of hydraulic engineering (ship hydrodynamics), marine structural engineering, etc. This also provides a way to carry out research on ship hydrodynamics in restricted inland waterways.

CFD solution process is divided into three parts: pre-processing, iterative solver and post-processing, which correspond to three program modules: pre-processor, solver and post-processor[119]. The pre-processing is the creation of the computational domain mesh, including both geometric modelling and partitioning of the mesh, and it is also used for defining boundary conditions and for numerical data input. Iterative solution is to discretize the control equations using effective discretization methods, and then calculate the partial differential equations after discretization. There are three main types of discretization methods: the finite difference method, the finite element method and the finite volume method, which will be described in a later section. The post-processing mainly helps engineers carry out subsequent data processing, which not only improves the efficiency of data processing in simulations, but also enables engineers to visualize and analyze the calculation results. The specific CFD computation procedures are illustrated in Fig 2. 1.

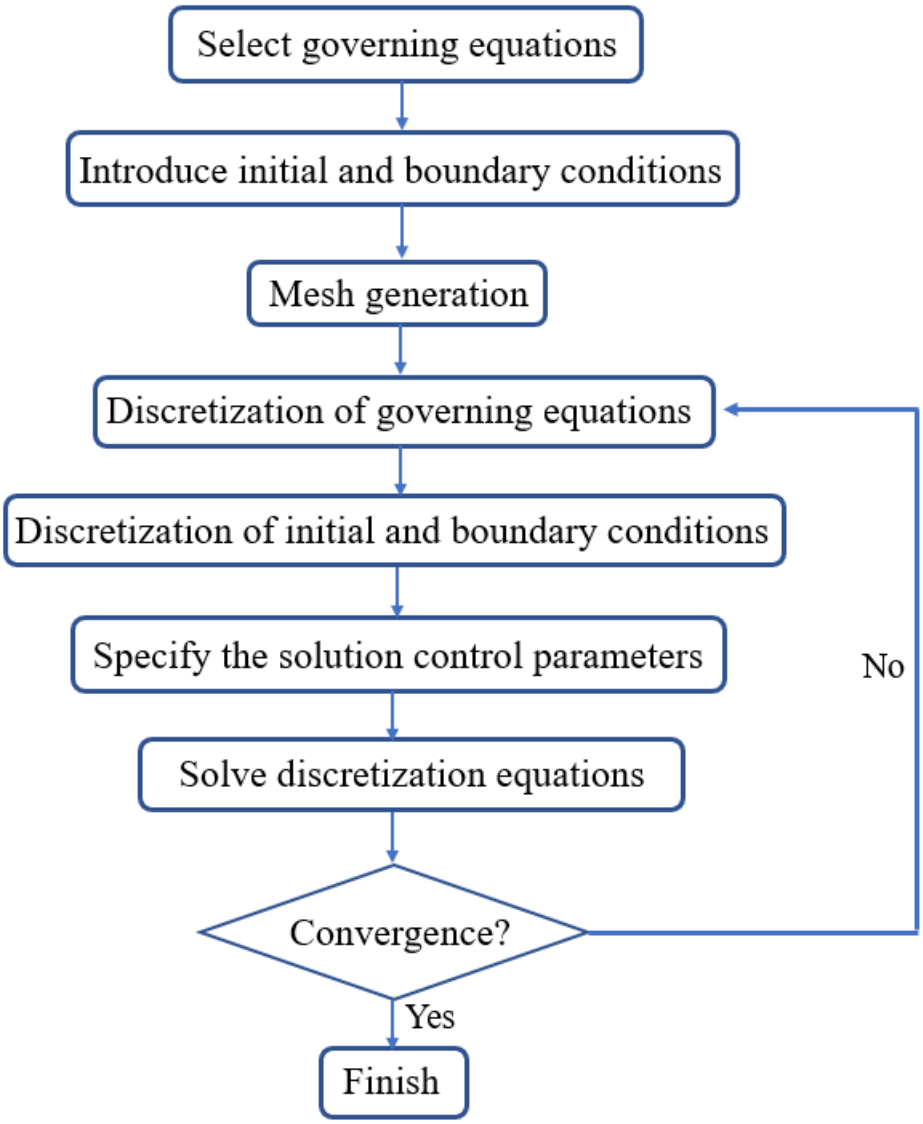

Fig 2. 1 Flow chart of CFD solution process

2.2.2 Brief overview of finite volume method

The finite volume method, which is used widely in CFD, was proposed by Maccormack [120] in the year 1972.

The basic idea of the finite volume method is that the computational domain space is divided into a finite number of grids, and each grid is a control body, so that each grid point is surrounded by a control body that does not duplicate each other[121, 122]. The partial differential equations to be solved (the governing equations) are integrated for each control body, and the Gaussian divergence theorem is applied to

obtain a set of discretization equations expressed in integral forms, with the variables on the grid nodes being the unknown quantities to be solved. For the finite volume method, the grid node is taken to be the volume center of the mesh cell.

An elementary cell (denoted by *e*) that is in polygon type with n facets (segments) on its contour is isolated from the computational domain, and then the conservation laws are applied to the individual cell.

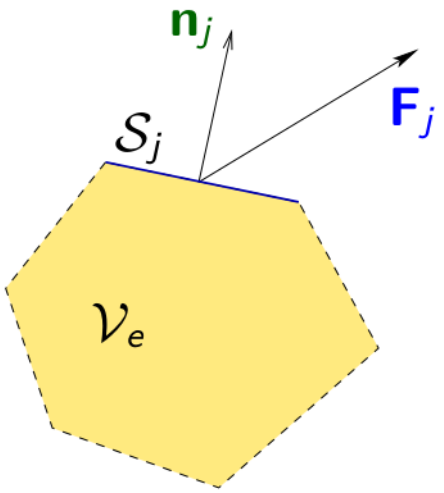

Fig 2. 2 Illustration for one side of a certain cell

Each time, we have to solve equation (2.7):

$$\frac{\partial}{\partial t}\iint_{\mathcal{V}_e} \phi d\mathcal{V} = -\oint_{\mathcal{S}_e} \mathbf{F}\cdot\mathbf{n}d\mathcal{S} + \iint_{\mathcal{V}_e} S_\phi d\mathcal{V} \tag{2.7}$$

Where **F** is the flux that goes through each frontier; S_ϕ is volume force.

According to average-size approach, there is (see Fig 2. 2) :

$$\phi_e = \frac{1}{\mathcal{V}_e}\iint_{\mathcal{V}_e} \phi d\mathcal{V} \tag{2.8}$$

$$\mathbf{F}_j = \frac{1}{\mathcal{S}_j}\int_{\mathcal{S}_j} \mathbf{F} d\mathcal{S} \tag{2.9}$$

Based on Finite Volume Method, there is (see Fig 2. 3):

$$\frac{\partial \phi_e}{\partial t} = -\frac{1}{\mathcal{V}_e}\sum_{j}^{n}\left(\mathbf{F}_j \cdot \mathbf{n}_j \mathcal{S}_j\right)_e + \frac{1}{\mathcal{V}_e}\left(S_\phi\right)_e \tag{2.10}$$

$$\frac{\partial \phi_e}{\partial t}\mathcal{V}_e = -(\mathbf{F}_1 \cdot \mathbf{n}_1 \mathcal{S}_1 + \mathbf{F}_2 \cdot \mathbf{n}_2 \mathcal{S}_2 + \cdots + \mathbf{F}_6 \cdot \mathbf{n}_6 \mathcal{S}_6) + S_\phi \tag{2.11}$$

The equation (2.10) will be calculated from cell to cell as a loop. Then a set of linear algebraic equations will be acquired, where the total number of unknowns in every equation system correspond to the number of cells. Finally, the resulting linear equations are solved with an algebraic multigrid solver.

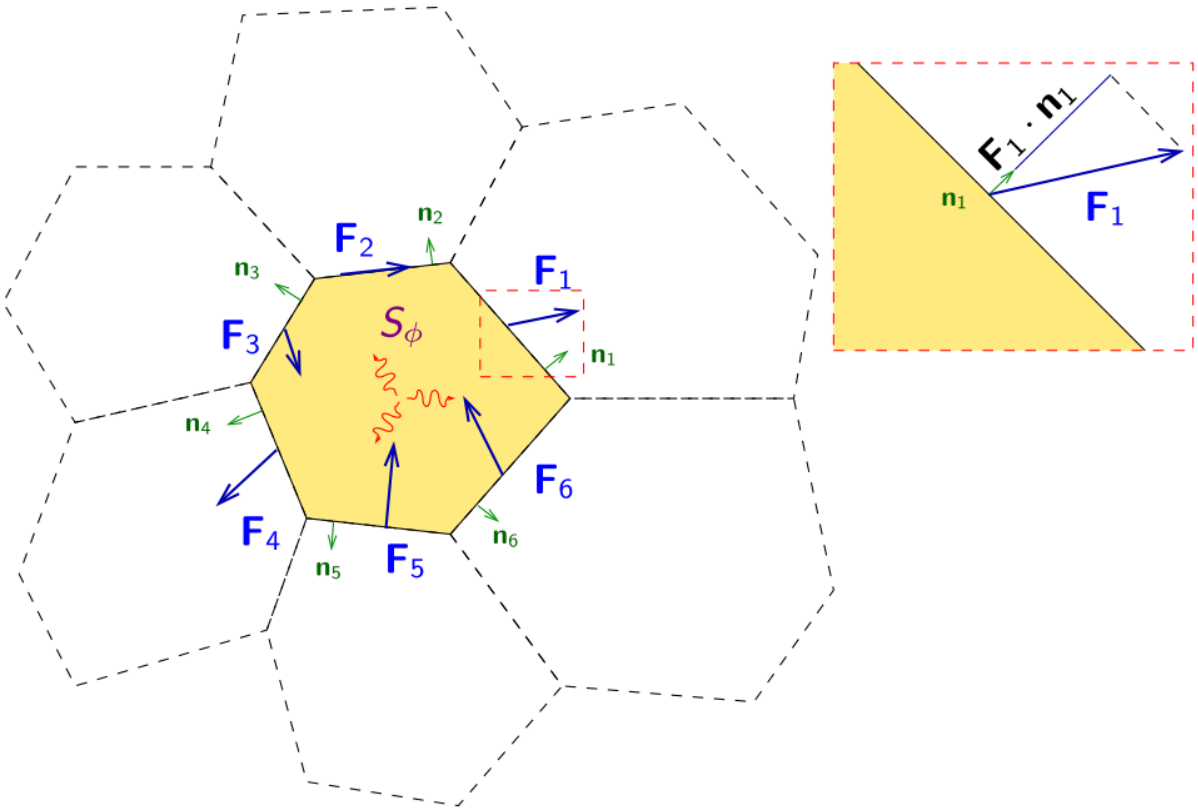

Fig 2. 3 Illustration for all the faces of a certain cell

2.2.3 Boundary conditions

The control equations normally allow for an infinite number of possible solutions. A complete mathematical description for CFD problems must therefore include both

the controlling equations and the corresponding boundary conditions, so that the solution of fluid field is unique.

STARCCM+ provides a variety of boundary conditions that cover many practical situations for Newtonian flow. Boundary conditions enable the flow to enter or to leave the domain. Each boundary has its own properties, for example, the flow can be confined or blocked by a wall [123]. By using symmetry or periodic boundary conditions, the geometry can be simplified and the runtime of the simulation can be reduced. Fig 2. 4 shows a simple region where the lines surrounding the region denote the boundaries. It should be noted that boundaries can never be shared between regions, and a specific boundary belongs to only one region. Fig 2. 5 illustrates three adjacent individual regions, where the dotted lines show the boundaries that isolate each region. The boundaries at the interface of one region and its neighbor are coincident in space.

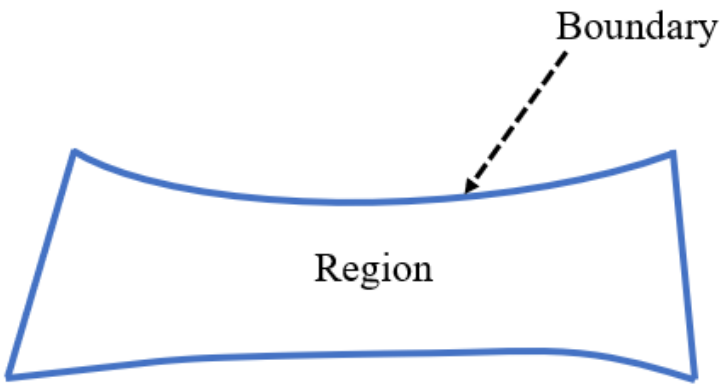

Fig 2. 4 A simple region surrounded by boundaries

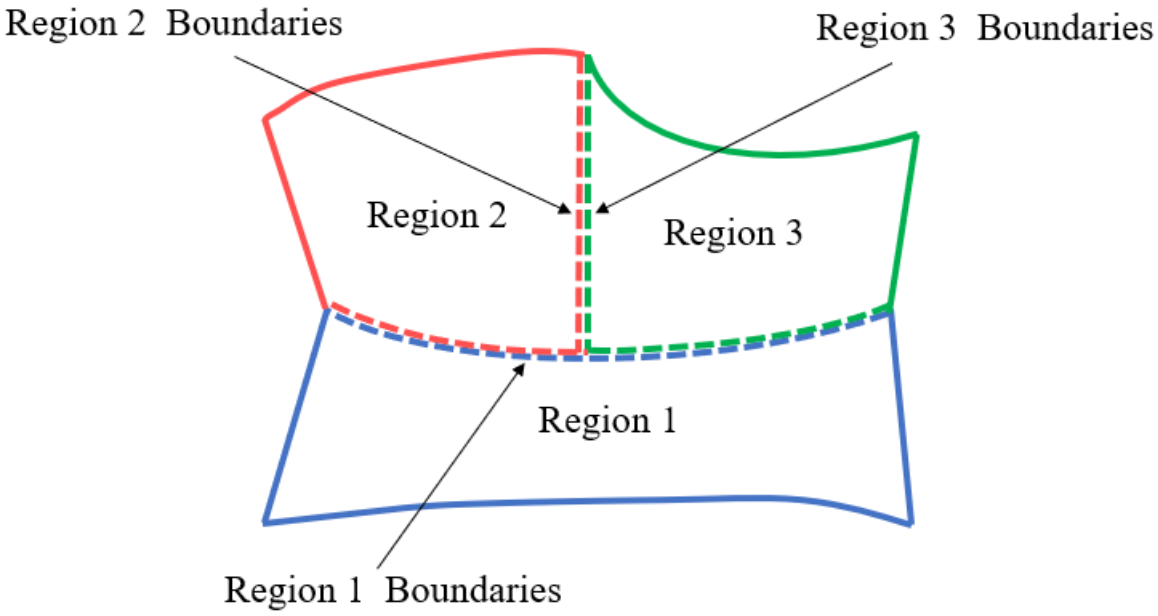

Fig 2. 5 Three separate regions surrounded by respective boundaries

The specific boundary conditions used in this thesis are summarized as follows (Source: STARCCM+ user's guidelines):

1) Velocity inlet

The velocity inlet boundary is usually used as an inflow condition, where the distributions of velocity and fluid properties are known. At this inflow boundary, the conditions are prescribed and used to calculate the inlet volume flux as well as the fluxes of momentum and energy.

For any velocity inlet boundary, the variables: velocity (with respect to a reference frame), inflow direction, and static temperature should be specified. Because it's valid for both incompressible and compressible flows, the following values will be imposed or computed at the boundary depending on the flow situation: Velocity, static pressure, static temperature.

2) Pressure outlet

The pressure outlet boundary is an outflow condition which imposes the working pressure. This boundary pressure can be considered as the static pressure of the

environment into which the fluid enters. In normal outflow conditions, the boundary face values of all other variables such as velocity or temperature are extrapolated from the interior of the solution domain.

3) Symmetry plane

A symmetry plane boundary represents an imaginary plane of symmetry in the simulation. Normally, it's used to reduce the extent of the computational domain in locations where the geometry and the flow are symmetric. Besides, it can also be used as a planar "slip wall" with the shear stress being zero.

4) Wall

A wall boundary represents an impermeable surface that confines fluid or solid regions. Generally, it's used to model different types of walls. For viscous flows, the no-slip condition is applied by default. The no-slip conditions means that the fluid sticks to the wall and moves with the same velocity as the wall. Thus, for a stationary wall, the fluid has zero velocity at the wall. While modelling the motion of a wall can be achieved by specifying a tangential velocity component. Depending on the geometry, it's possible to model a translational or rotational motion of the wall in the plane of the boundary.

For the no-slip condition, this means that the fluid moves at the same velocity as the specified tangential velocity component. Alternatively, the wall can be modelled as a slip wall representing an impenetrable but traction-free surface.

2.3 Turbulence modelling

Turbulence is extremely common in engineering practice, which is caused by the viscosity of fluid. In turbulent flow, fluid particles all move in a disorderly manner, and the physical quantities such as velocity and pressure change randomly with time and space. Therefore, turbulence is a highly non-linear and complex flow, and it involves the movement of fluids on many spatial and temporal scales, from the

microscopic to the macroscopic, and its structure and mechanisms of generation are still unclear. The understanding of people on it is still in the process of deepening.

In CFD simulations, if no turbulence model is activated, then the exact turbulence equation will be solved, and in turn non-stationary turbulence results will be obtained. To get time-averaged results, turbulence models need to be applied, because turbulence model is able to cancel the non-stationary response. For DNS, there is no turbulence model used, and all the turbulence scales which are non-stationary can be observed, so it can be really expensive. For LES, only large turbulence scales are got. For RANS, there is no turbulence observed (See Fig 2. 6).

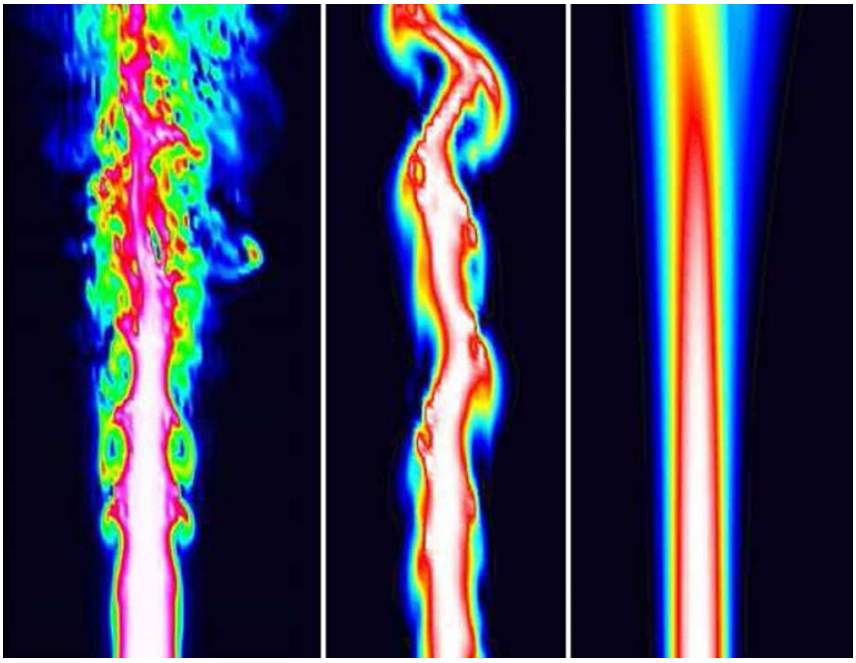

Fig 2. 6 Comparison among DNS, LES, RANS

(Source: A. Maries, University of Pittsburgh)

Various numerical simulation methods have been developed to simulate turbulence. At present, numerical simulation methods for turbulence can be divided into two main categories, direct numerical simulation methods and non-direct numerical simulation methods [124, 125], which are depicted in Fig 2. 7. Direct numerical simulation means the direct use of instantaneous equations to solve for

turbulence. Although relatively accurate calculation results can be obtained theoretically, this method requires high computer hardware and is not currently available for engineering calculations. While non-direct numerical simulation doesn't require calculating the pulsation characteristics of turbulence directly, but seeks for an approximation or simplification of turbulence to a certain extent, after which the approximate mathematical expression of the control equations is calculated numerically [126, 127]. Therefore, it is not possible to take into account all the factors affecting the structure and mechanism of turbulence, and their scope of application is narrow and is lacking in universality, which makes it very important to choose a suitable turbulence model according to the characteristics of the actual flow.

In non-direct numerical simulation method, the large eddy simulation (LES) [128] and RANS are the most widely used [129, 130]. The large eddy simulation method (LES) uses direct numerical simulations to calculate the motion of turbulent eddies larger than the grid scale, and simulates the effect of small-scale turbulent vortex motion on large-scale turbulent vortices based on an approximate model. This method requires less computer memory and computational speed than the DNS method [131]. The requirement for computer memory and computational speed of this method is lower than the DNS method, but is actually still very high. While Reynolds-Averaging Navier-Stokes (RANS) method focuses only on the changes in the mean characteristics of the flow field due to turbulence, but ignores the details of turbulent pulsations [132]. The Reynolds-averaged N-S (RANS) equations are obtained by time-averaging the transient values of the physical quantities in the N-S equation, which is then solved numerically. However, among these approximation methods, the RANS method can greatly reduce the computational cost and improve the computational efficiency, while ensuring a certain degree of computational accuracy [133]. It is currently the mainstream method for calculating the 3D viscous flow fields of ships. Considering a balance between the advantages and disadvantages, RANS method is adopted in this work.

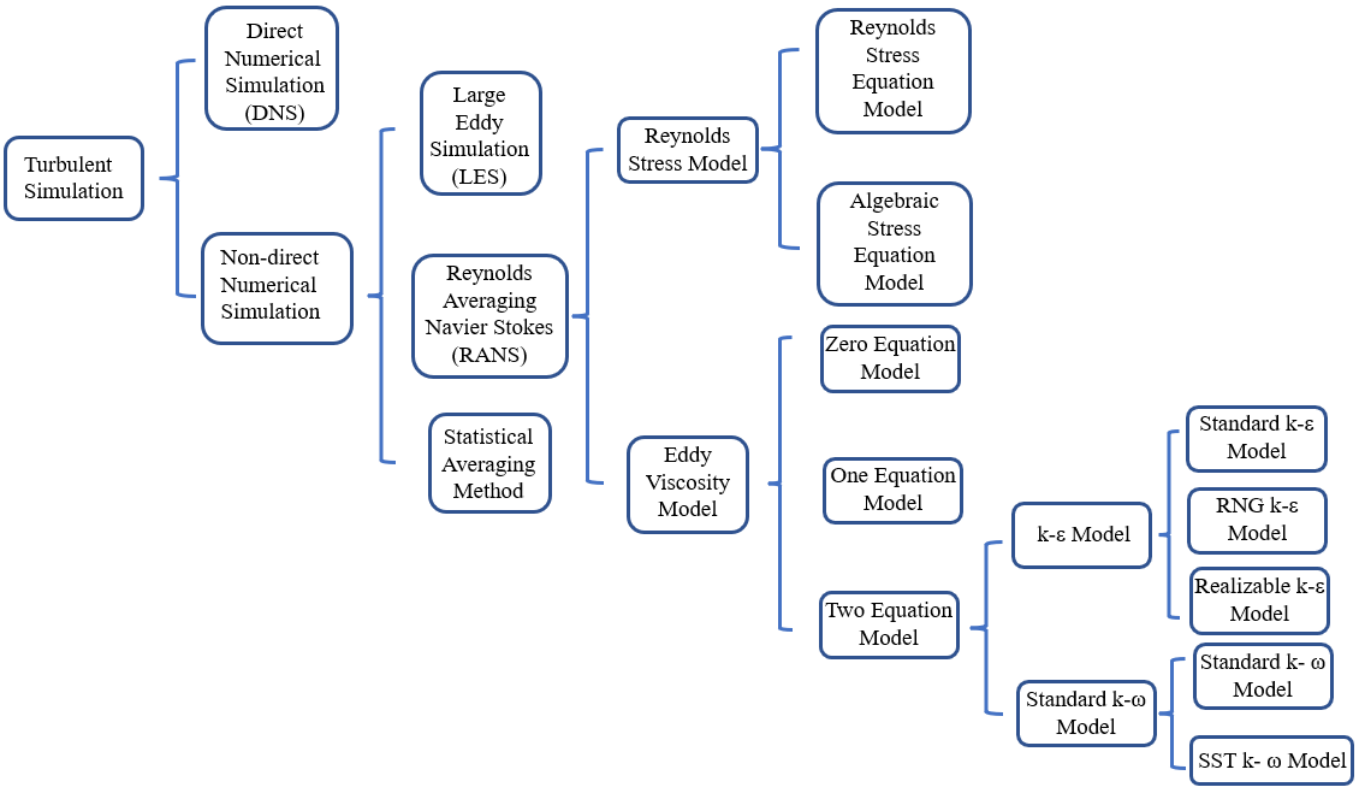

Fig 2. 7 Numerical simulation for turbulence

2.3.1 Reynolds-Averaged Navier-Stokes equation

Due to the fact that the complexity of turbulence makes it exceptionally difficult to solve Navier-Stokes equation directly, hence, Reynolds-Averaged method that is firstly proposed by Reynolds is taken widely to solve this problem. The basic idea of this method is to regard turbulence flow as superimposed by two kinds of flow, one is time-averaged flow and the other is instantaneous pulsation flow. Reynolds-Averaged Navier-Stokes (RANS) equation for incompressible fluid can be consequently obtained as follows [69, 112, 134]:

$$\begin{cases} \rho\left(\frac{\partial(u)}{\partial t}+\frac{\partial(uu)}{\partial x}+\frac{\partial(uv)}{\partial y}+\frac{\partial(uw)}{\partial z}\right)= \\ -\frac{\partial p}{\partial x}+\mu\left(\frac{\partial^2 u}{\partial x^2}+\frac{\partial^2 u}{\partial y^2}+\frac{\partial^2 u}{\partial z^2}\right)+\left[\frac{\partial(-\rho\overline{u'u'})}{\partial x}+\frac{\partial(-\rho\overline{u'v'})}{\partial y}+\frac{\partial(-\rho\overline{u'w'})}{\partial z}\right] \\ \rho\left(\frac{\partial(v)}{\partial t}+\frac{\partial(vu)}{\partial x}+\frac{\partial(vv)}{\partial y}+\frac{\partial(vw)}{\partial z}\right)= \\ -\frac{\partial p}{\partial y}+\mu\left(\frac{\partial^2 v}{\partial x^2}+\frac{\partial^2 v}{\partial y^2}+\frac{\partial^2 v}{\partial z^2}\right)+\left[\frac{\partial(-\rho\overline{u'v'})}{\partial x}+\frac{\partial(-\rho\overline{v'v'})}{\partial y}+\frac{\partial(-\rho\overline{v'w'})}{\partial z}\right] \\ \rho\left(\frac{\partial(w)}{\partial t}+\frac{\partial(wu)}{\partial x}+\frac{\partial(wv)}{\partial y}+\frac{\partial(ww)}{\partial z}\right)= \\ -\frac{\partial p}{\partial z}+\mu\left(\frac{\partial^2 w}{\partial x^2}+\frac{\partial^2 w}{\partial y^2}+\frac{\partial^2 w}{\partial z^2}\right)+\left[\frac{\partial(-\rho\overline{u'w'})}{\partial x}+\frac{\partial(-\rho\overline{v'w'})}{\partial y}+\frac{\partial(-\rho\overline{w'w'})}{\partial z}\right] \end{cases} \tag{2.12}$$

Where, $-\rho\overline{u'u'}$, $-\rho\overline{u'v'}$, $-\rho\overline{u'w'}$ are Reynolds stress terms.

Compared with N-S equation, the turbulent stress in RANS equation includes not only the stress caused by viscosity, but also Reynold stress due to turbulent pulsating motion. So the equation system is not closed. Depending on the assumptions made or the treatment of stress, there are two main types of turbulence models in common use today, which are called Reynolds stress model and vortex viscosity model. The concept of turbulent viscosity coefficient was introduced based on Boussinesq's vortex viscosity assumption, and the Reynolds stress can be expressed as a function of the turbulent viscosity coefficient, as is illustrated by equation (2.13):

$$-\rho\overline{u_i'u_j'}=\tau_{ij}=\mu_t\left(\frac{\partial u_i}{\partial x_j}+\frac{\partial u_j}{\partial x_i}\right)-\frac{2}{3}\left(\rho k+\mu_t\frac{\partial u_k}{\partial x_k}\right)\delta_{ij},(i,j=1,2,3) \tag{2.13}$$

For incompressible fluid, equation (2.4) can be simplified as equation (2.14):

$$-\rho\overline{u_i'u_j'}=\tau_{ij}=\mu_t\left(\frac{\partial u_i}{\partial x_j}+\frac{\partial u_j}{\partial x_i}\right)-\frac{2}{3}\rho k\delta_{ij},(i,j=1,2,3) \tag{2.14}$$

Where, μ_t is turbulent dynamic viscosity coefficient; k is turbulent kinetic energy, which can be defined as:

$$k=\frac{1}{2}\overline{u_i'u_i'}=\frac{1}{2}\left(\overline{u_1'^2}+\overline{u_2'^2}+\overline{u_3'^2}\right) \tag{2.15}$$

Turbulent viscosity coefficient μ_t is a function of spatial coordinates and are parameters of the fluid flow state rather than physical properties of the fluid parameter. As long as μ_t can be determined, and the value is then put together with RANS equation so that the equation set can be closed. Depending on the number of differential equations determined, vortex viscosity model can be classified as zero-equation model, one-equation model and two-equation model, among which the two-equation model treats Reynolds stresses better and is the most widely used in engineering calculations [135]. The two-equation model is used in this work.

2.3.2 Turbulence models

Turbulence model is based on the Reynolds mean equation of motion and the pulsating equation of motion. It is a closed set of equations describing the mean Reynolds flow based on a combination of theoretical and empirical assumptions [136].

In two-equation model, k-ε model and k- ω model are dominated. The k-ε model calculates the turbulent viscosity coefficient by solving the transport equation for the turbulent kinetic energy k and the turbulent dissipation rate ε, which is the most widely used model in engineering applications. The k-ε model mainly incorporates Standard k-ε model, RNG k-ε model [137, 138] and Realizable k-ε model [139-142]. The k-ω model is based on solving for the transport equation of the turbulent kinetic energy k and the turbulent specific dissipation rate ω (dissipation rate per unit of turbulent kinetic energy ε/k) to calculate the turbulent viscosity coefficient. The k-ε model mainly includes Standard k-ω Model and SST k-ω Model [143, 144].

2.3.2.1 Standard k-ε Model

To closed RANS equation, $k-\varepsilon$ turbulence model is applied due to the fact that the two-equation turbulence model is one of the most widely utilized in numerical calculations of viscous hydrodynamics of ships (k is turbulent kinetic energy, and ε is turbulent kinetic dissipation rate). For incompressible fluid, standard $k-\varepsilon$ turbulence model can be expressed [145, 146]:

$$\frac{\partial(\rho k)}{\partial t}+\frac{\partial(\rho k u_i)}{\partial x_i}=\frac{\partial}{\partial x_j}\left[\left(\mu+\frac{\mu_t}{\sigma_k}\right)\frac{\partial k}{\partial x_j}\right]+G_k-\rho\varepsilon \tag{2.16}$$

$$\frac{\partial(\rho \varepsilon)}{\partial t}+\frac{\partial(\rho \varepsilon u_i)}{\partial x_i}=\frac{\partial}{\partial x_j}\left[\left(\mu+\frac{\mu_t}{\sigma_\varepsilon}\right)\frac{\partial \varepsilon}{\partial x_j}\right]+\frac{C_{1\varepsilon}\varepsilon}{k}G_k-C_{2\varepsilon}\rho\frac{\varepsilon^2}{k} \tag{2.17}$$

Where, G_k is the average velocity gradient term induced by turbulent kinetic energy k; σ_k, σ_ε are Prandt number corresponding to turbulent kinetic energy k and dissipation rate ε; $C_{1\varepsilon}$ and $C_{2\varepsilon}$ are empirical constants.

According to the recommended values from Launder et al. and later experimental verification, it is defined that $C_{1\varepsilon}$=1.44, $C_{2\varepsilon}$=1.92, σ_ε=1.3, σ_k=1.0.
Besides, the model above is established as for the turbulence with high Reynolds number, therefore, realizable $k-\varepsilon$ two-layer is adopted for a special treatment in situations with low Reynolds number like near-wall flow.

2.3.2.2 Standard k-ω Model

In the Standard k-ω model, low Reynolds number and compressible flow are considered, and at the same time, the sensitivity to adverse pressure gradients is improved. Hence, better results can be obtained when solving problems of boundary layer under pressure gradients. Besides, there is no need to determine the object surface normal to the near-wall flow problem, overcoming the shortcomings of the Standard k-ε Model for near-wall flow [147, 148].

$$\frac{\partial}{\partial t}(\rho k)+\frac{\partial}{\partial x_j}(\rho k\bar{u}_j)=\frac{\partial}{\partial x_j}\left[\left(\mu+\frac{\mu_t}{\sigma_k}\right)\frac{\partial k}{\partial x_j}\right]+G_k-\rho\beta^* k\omega \tag{2.18}$$

$$\frac{\partial}{\partial t}(\rho \omega)+\frac{\partial}{\partial x_j}(\rho \omega\bar{u}_j)=\frac{\partial}{\partial x_j}\left[\left(\mu+\frac{\mu_t}{\sigma_\omega}\right)\frac{\partial \omega}{\partial x_j}\right]+\alpha\frac{\omega}{k}G_k-\rho\beta\omega^2 \tag{2.19}$$

Thereinto,

$$G_k = -\rho\overline{u_i'u_j'}\frac{\partial \bar{u}_i}{\partial x_j} \tag{2.20}$$

$$\mu_t = \rho\frac{k}{\omega} \tag{2.21}$$

According to the assumption by Boussinesq, the equation (2.18) and (2.19) can be transformed into:

$$\begin{gathered} G_k = \mu_t S^2 \\ S = \sqrt{2S_{ij}S_{ij}} \\ S_{ij} = \frac{1}{2}\left(\frac{\partial \bar{u}_i}{\partial x_j} + \frac{\partial \bar{u}_j}{\partial x_i}\right) \end{gathered} \tag{2.22}$$

Where $\sigma_k = 2.0, \sigma_\omega = 2.0, \alpha = 5/9, \beta^* = 0.09, \beta = 0.075$

However, Standard k-ω model also has certain drawbacks, such as its dependence on the free incoming flow and the dependence of the numerical results on the dissipation rate ω given by the flow inlet boundary.

To sum up, the most significant advantage of k-ω Model is that it can be applied throughout the boundary layer (including the viscous sublayer) without further modification, but its disadvantage is that it is very sensitive to the value of ω in the free flow and to the inlet boundary conditions, whereas the k-ε Model does not have this problem.

In this work, after a series of tests, SST k-ω Model didn't produce good wave patterns, while in contrast, k-ε Model produced wave patterns well and always converged faster, so k-ε turbulence model was adopted after weighing the pros and cons.

2.3.3 y^+ in simulations

The behavior of the flow near walls is a complex phenomenon, and the idea of a wall has been developed to help differentiate the various areas near walls. y^+ is called

the dimensionless wall distance, which is a dimensionless quantity and is measured in terms of viscous lengths from the wall [149-152].

In CFD calculations, y^+ is mainly used to calculate the height of the first layer of grid nodes in the process of grid division. The calculation process is as follows [153-156]:

$$\begin{aligned} U^+ &= \frac{U}{u_\tau} \\ y^+ &= \frac{y u_\tau}{\nu} \\ u_\tau &= \sqrt{\tau_w/\rho} \end{aligned} \tag{2.23}$$

τ_w is frictional force; y is the distance from the wall; u_τ is the shear velocity of fluid near the wall; ν is kinematic viscosity

At different Reynolds numbers, the dimensionless y^+ can divide the region near the wall into several parts (see Fig 2. 8). When y^+ is very small, the fluid is close to the wall, and the fluid pulsation velocity on the wall is zero. At this point, the Reynolds stress is small, while the viscous stress is dominant. That is to say, the inertia force is smaller than the viscous force when y+ is small, so the viscous effect accounts for a significant proportion [69, 157]. Specially:

$0<y^+<5$ viscous sublayer

$5<y^+<30$ buffer layer

$30<y^+$ log-law layer

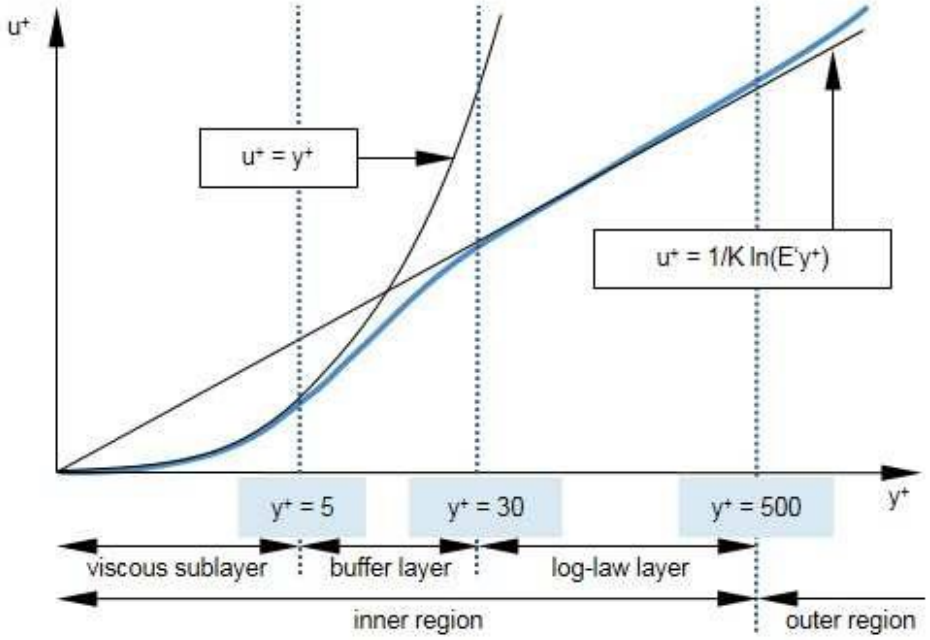

Fig 2. 8 Lindgren boundary layer profiles

(Source: StevePortal)

By checking the distance of the first cell near the wall, the following conclusions can be derived: If y+ is lower than 5, then the simulations belong to low-Reynold turbulent simulations; for y+ >30, the simulations can be high-Reynold turbulent simulations. However, for 5<y+<30, the simulation can be proved to be incorrect.

2.4 Free surface simulation

Fluid mechanics problems involving two phases, liquid and air, are commonplace. The interface is defined as the boundary between the two phases. Fig 2. 9 gives an illustration of the real interface between air and water for flow around a hydrofoil. Fig 2. 10 depicts an example to show the interface in a CFD simulation concerning a tank discharge flow, where the red part refers to liquid and the blue part corresponds to gas.

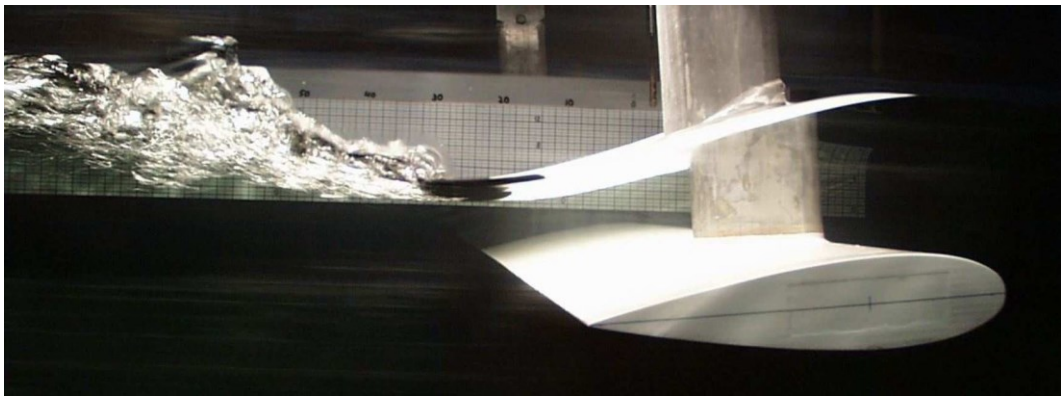

Fig 2. 9 Flow around a hydrofoil

(Source: CD-Adapco)

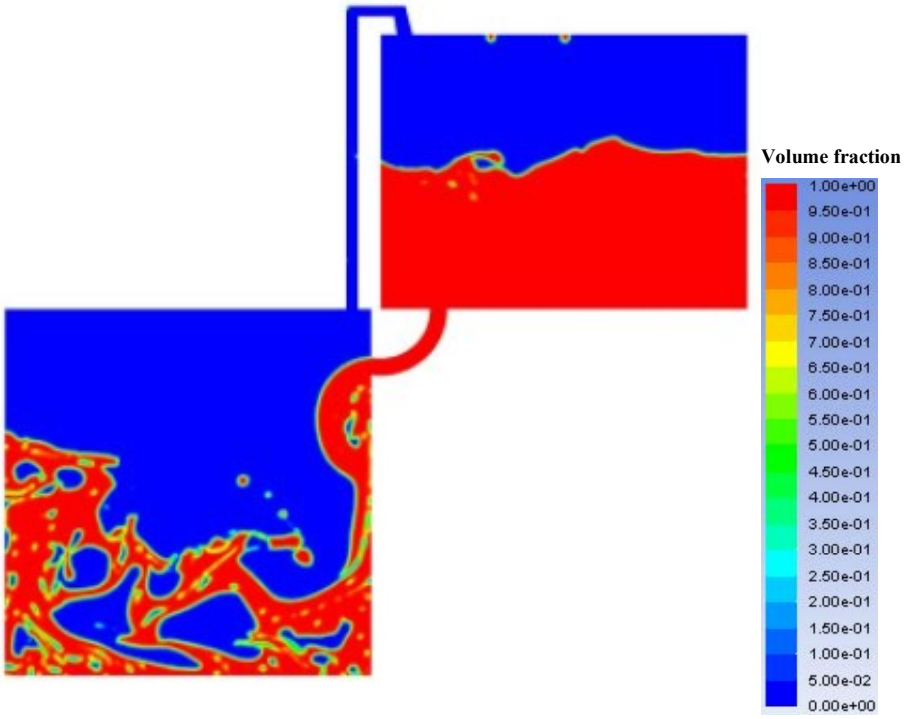

Fig 2. 10 A tank discharge flow in CFD simulation

(Source: Advanced Engineering Tutorial)

When ships navigate in water, the water surface will contact air whose density is very small. Therefore, fluid can't be rigidly constrained like solid boundaries. The free surface in simulations is just the interface between water and air, and this belongs to a two-phase flow problem of mutual impermeability. The formation of free surface is

complicated, and the whole interface position is in the continuous changing process, which consequently increases the difficulty of calculations about free surface.

The problem of free surface simulation plays a very important role in the study of CFD. The correct simulation of free surface will directly affect the reliability and accuracy of calculation results. At present, there are mainly three possible approaches dealing with interface monitoring issues, namely Front Tracking, Level-Set, and Volume of fluid(VOF) [158], among which volume of fluid (VOF) is the most commonly used.

VOF method is proposed by Hirt and Nichols [159] which can be used to deal with arbitrary free surfaces. The interface capture is achieved chiefly by two specific algorithms called SLIC (simple line interface calculation) and PLIC (piecewise-linear interface calculation), which will be introduced below. The method assumes that all immiscible fluids present in the control volume share temperature, pressure, and velocity. The principle of it is to solve the indissoluble fluids with the same momentum equations in the whole control domain, and track the volume fractions of each kind of fluid [159-164]. The VOF model is virtually an Eulerian model for processing a continuous medium containing multiple fluids, and it's better at investigating multiphase flow simulations where two phases are interfaced but don't mix with each other. Also, the multiphase segregated flow model based on an Eulerian-Eulerian formulation where each separate phase has its own set of conservation equations is employed.

In view of its characteristics, VOF is often utilized to deal with liquid flows by gravity effects. The areas of application commonly include:

- interaction between one or more liquids and a gas;
- flow of liquids under gravity effects;
- consideration of surface tension effects;

In STARCCM+, the two phases (liquid and gas) are normally defined water and air, the densities and dynamic viscosities of whom are considered constant. For water, the density is 997.561kg/ m^3, and dynamic viscosity is $8.8871 * 10^{-4}$ Pa·s; for air, the density is 1.18415 kg/ m^3, and dynamic viscosity is $1.85508 * 10^{-5}$ Pa·s.

Some specific examples are given in Fig 2. 11 to showcase the applications. Fig 2. 11(a) shows the interaction between two different liquids with the change in time; Fig 2. 11(b) displays a CFD simulation of a river flowing under gravity; Fig 2. 11(c) describe the liquid in a fuel tank when there is a sudden brake.

(a)

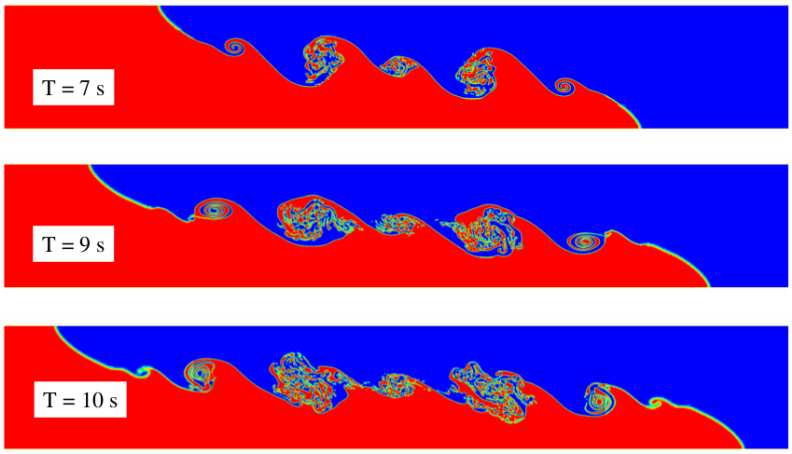

(b)

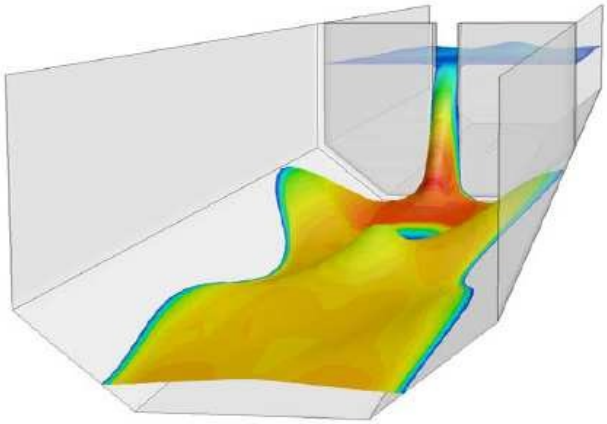

(c)

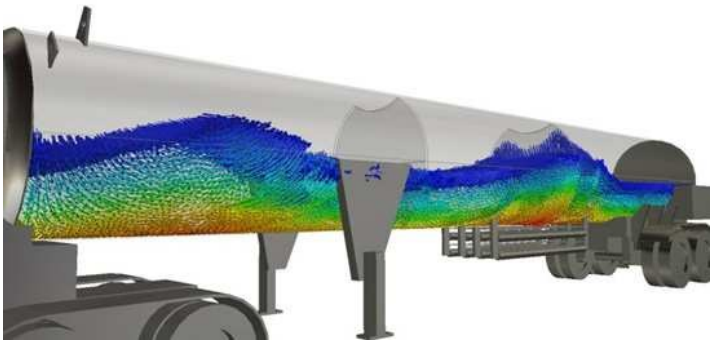

Fig 2. 11 Applicable cases of VOF method

(a) Interaction between two liquids (Source: Courses A. Bakker)

(b) Fluid flow under gravity (Source: LEAP CFD Team))

(c) Liquid flow in a fuel tank (Source: Autodesk)

In the VOF model, the volume fraction of phase *n* in the cells is defined as a_n, then [165, 166]

For a_n=0, that is, there is no phase fluid *n* in the cells.

For a_n=1, that is, the cells are full of the phase fluid *n*.

For 0<a_n<1, that is, there is both phase fluid n and other fluid in the cells (there exists an interface).

In naval engineering, there are normally two phases (liquid and gas), and then the volume fraction a_2 can be defined:

$$a_2 = \frac{V_{liquid}}{V_2}\begin{cases} 0 & air \\ 0.5 & interface \\ 1 & liquid \end{cases} \tag{2.24}$$

Where V_{liquid} is the volume of phase liquid in the cell, and V_2 is the volume of the cell.

Fig 2. 12 shows different volume fractions with corresponding phases in a cell clearly, where the blank region is air, while the blue region is liquid. Fig 2. 13 depicts the volume fraction of air in an actual CFD simulation, in which a_2=0.5 corresponds to the interface. While for a_2 >0.5, the region is full of air, and for a_2<0.5, the region is filled with water.

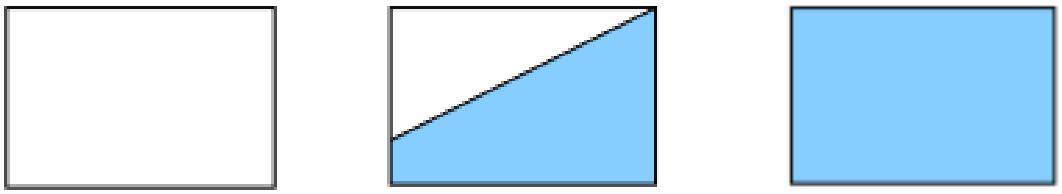

Fig 2. 12 Definition of the volume fraction in a cell

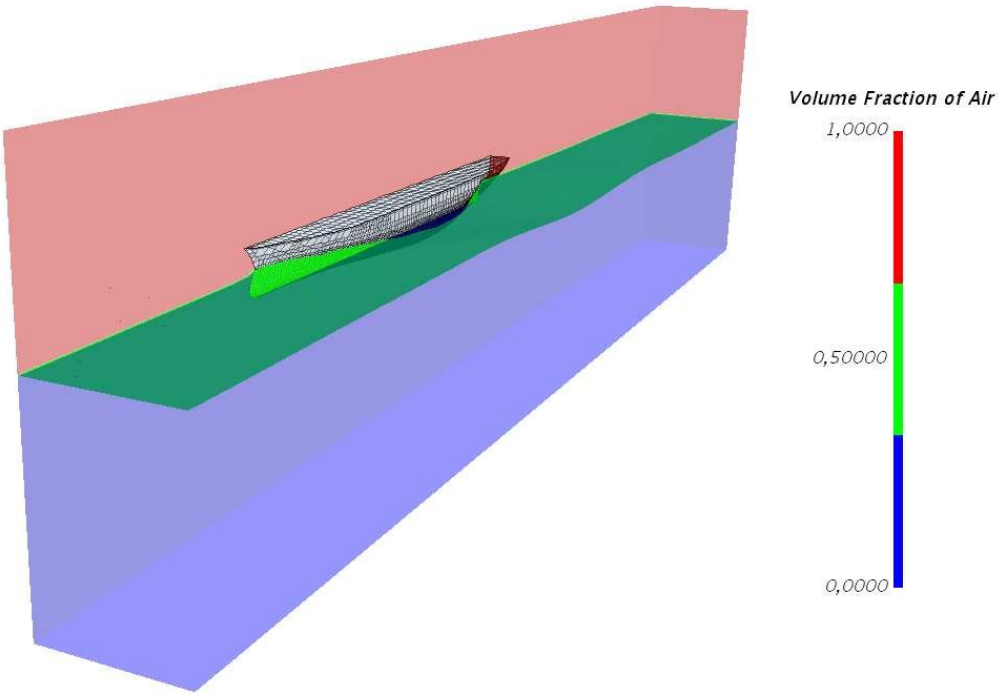

Fig 2. 13 Definition of the volume fraction in a CFD simulation

(Source: KCS container carrier (scale model))

For every interface, the fundamental equations for VOF model is to solve the physical properties of the equivalent fluid as a function of the physical properties of its constituent phase and its volume fraction, which are expressed as [167, 168]:

$$\frac{1}{\rho_n}\left[\frac{\partial}{\partial_t}(a_n\rho_n) + \nabla\cdot(a_n\rho_n v_n)\right] = S_{a_n} + \sum_{n=1}^{n}(m_{mn} - m_{nm}) \qquad (2.25)$$

Where, m_{nm} is the mass transfer of the n fraction relative to the m phase; m_{mn} is the mass transfer of the m fraction relative to the n phase; S_{a_n} is the source item.

The calculation of the main phase volume ratio has the following constraints

$$\sum_{n=1}^{n} a_n = 1$$

If air and water are expressed by subscript 1 and 2 respectively, then the density and dynamic viscosity of each unit are given by the equation:

$$\rho = a_2\rho_2 + (1 - a_2)\rho_1 \tag{2.26}$$
$$\mu = a_2\mu_2 + (1 - a_2)\mu_1$$

Likewise, the velocity and pressure of each unit can be expressed:

$$\mathbf{u} = a_2\rho\mathbf{u}_2 + (1 - a_2)\mathbf{u}_1 \tag{2.27}$$

$$p = a_2 p_2 + (1 - a_2)p_1$$

Then based on the equations above, the Correction of averaged Navier-Stokes equations can be derived:

$$\rho\frac{\partial \mathbf{u}}{\partial t} + \nabla \cdot (\rho\mathbf{u}\mathbf{u}) = -\nabla p + \rho\mathbf{g} + \nabla \cdot \left(\mu(\nabla\mathbf{u} + \nabla\mathbf{u}^{\mathrm{T}})\right) + \mathbf{F_c} \tag{2.28}$$

$$\nabla \cdot \mathbf{u} = 0$$

Addition of a transport equation for a_2,

$$\frac{\partial a_2}{\partial t} + \mathbf{u} \cdot \nabla a_2 = 0$$

Interface is "geo-located" by locating the cells for which $0 < n < 1$. Fig 2. 14 (a) describes the position of the interface; Fig 2. 14 (b) shows the interface captured by simple line interface calculation donor-acceptor (SLIC); Fig 2. 14 (c) exhibits the interface captured by piecewise line interface calculation (PLIC).

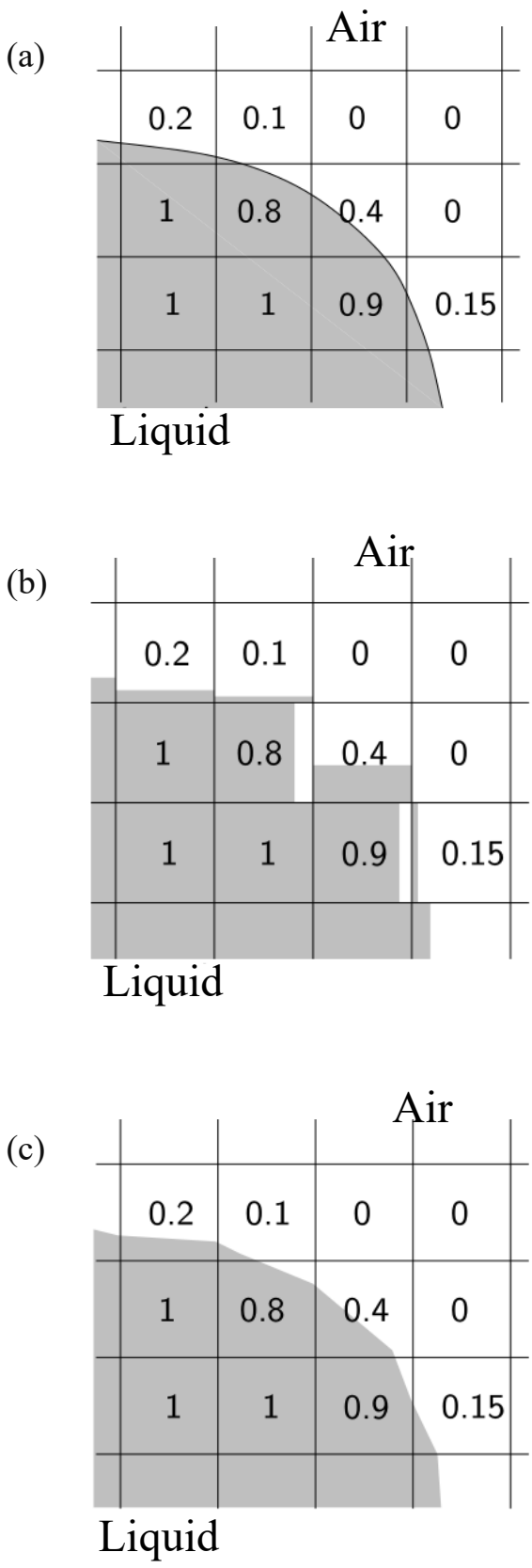

Fig 2. 14 Reconstruction techniques for the interface

(Source: (Vimal, 2016))

Fig 2. 15 demonstrates the interface in an actual CFD simulation conducted by Simcenter STARCCM+ that simulates the flow around a KCS container. The 'Flat Wave' model in Simcenter STARCCM+ is used to produce a flat wave representing a calm plane of water. Fig 2. 15 (a) shows the mesh view of the interface between air and water regions. To generate proper meshes in the interface, the following considerations needs to be taken:

- locally refine the mesh to properly capture the moving interface;
- favor cell geometries aligned with the interface;
- adapt the size of the mesh to the constraints of the turbulence model.

Fig 2. 15 (b) and (c) depict the interface with wave patterns.

(a)

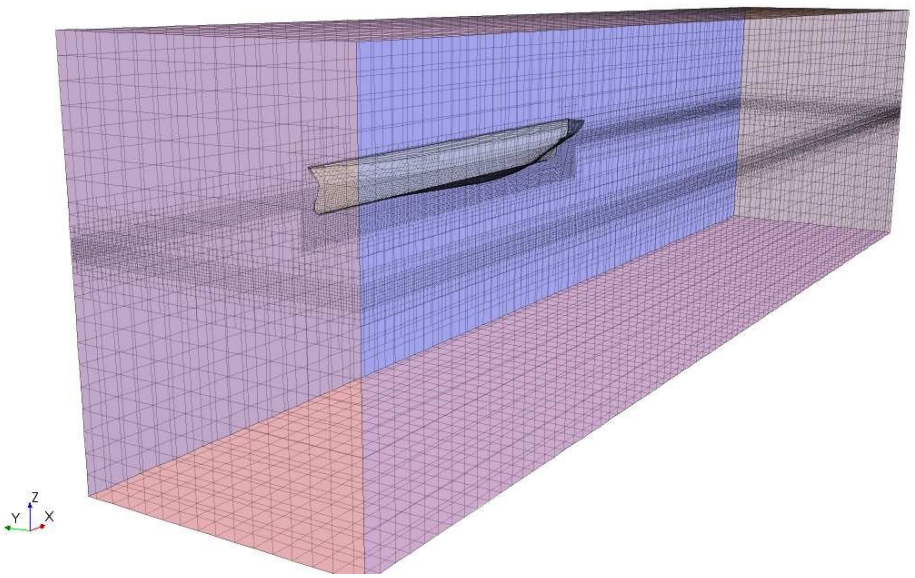

(b)

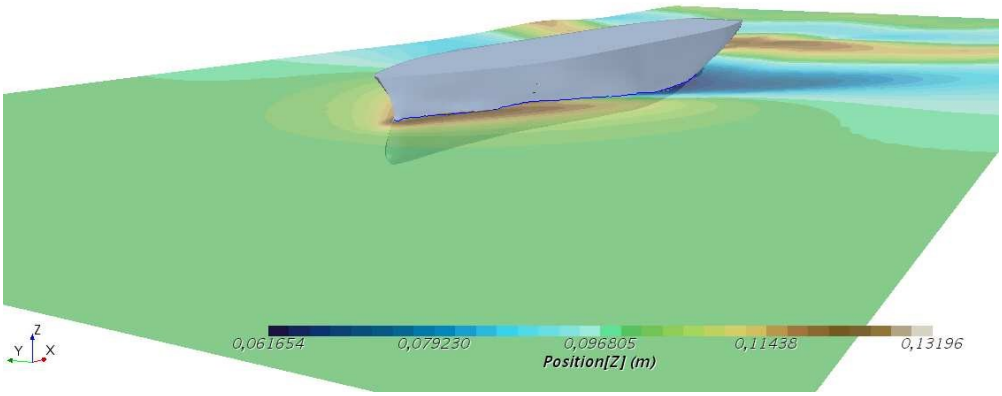

(c)

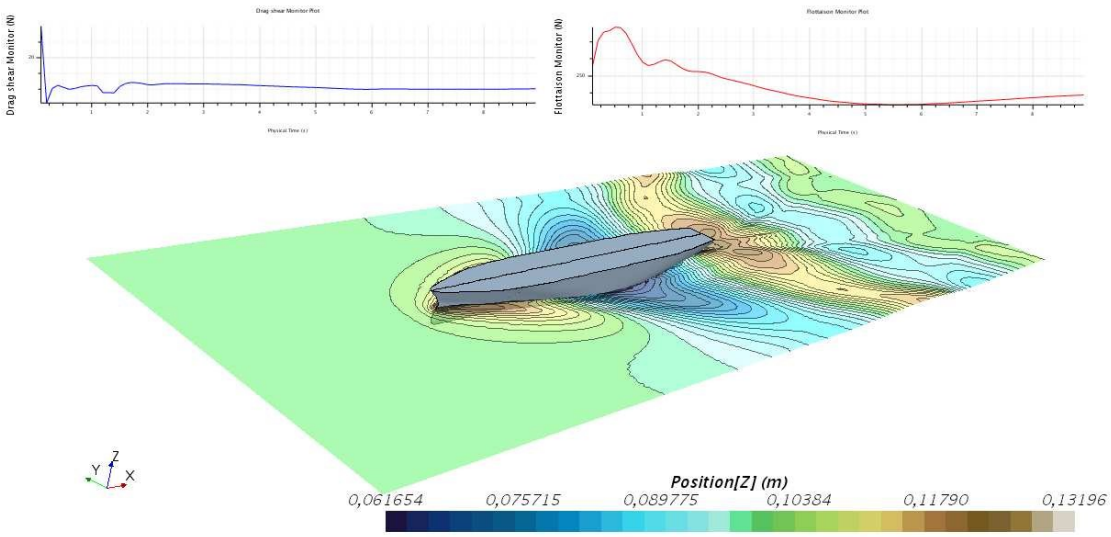

Fig 2. 15 Flow around a KCS container hull (scale model)

Fig 2. 16 shows the mesh refined process around the interface, and the three columns respectively represent the square, triangle and polygon meshes in three different resolutions (The red line is the exact interface; the blue line is for volume fraction=0.5). It's necessary to increase the density of the meshes to capture the interface.

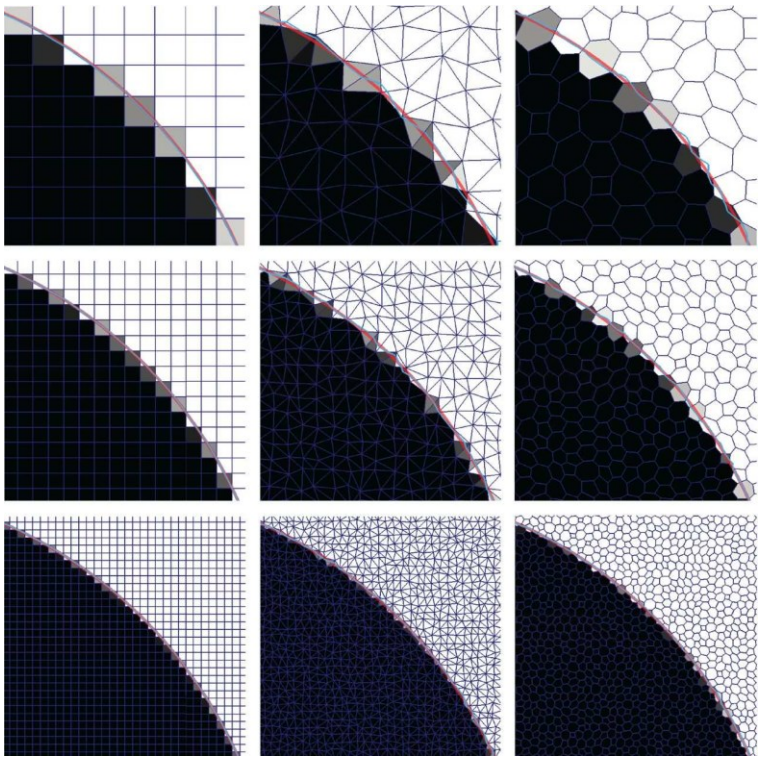

Fig 2. 16 Refinement of meshes at the interface

(Source: [169])

2.5 Numerical settings

2.5.1 Discretization method

As is shown above, the governing equations of fluid flow problem are a set of continuous nonlinear partial differential equations, so generally it's very difficult to obtain an analytic solution directly. After finishing mathematical modeling for a specific issue, it's necessary to conduct discretization on computational domain and the mathematical model. For steady issues, discretization mainly focuses on spatial domain, while time domain should also be included for unsteady issues. Spatial domain discretization includes discretization in computing domain and governing equations. Computing domain discretization refers to dividing computing domain into a finite number of small sub-regions and determining sub-region nodes to generate meshes; The discretization of the governing equations refers to the discretization of

the governing equations based on these mesh nodes, and the algebraic equations on each node are consequently obtained. Then these algebraic equations are solved simultaneously, so as to obtain the values of unknown quantities on each node. These values are approximate solutions of the flow field. Then the values between mesh nodes can be obtained by interpolating, and thus the approximate solution of the whole flow field is derived.

At present, discretization methods mainly include finite difference method, finite volume method, finite element method, boundary element method, and spectral method and so on. Among those methods, finite volume method is used widely, since it absorbs the reasonable kernel of finite difference method, and at the same time draws lessons from the principle of subfield method, so that it has its own obvious characteristics

The solver included in STARCCM+ utilizes a finite volume method to simulate fluid flow, which employs the integral form of the conservation equations and splits the theoretical domain into a finite number of adjacent control volumes.

2.5.2 Discretization scheme

Discretization scheme is actually a kind of spatial interpolation, the purpose of which is to find the physical quantities and their derivative nodes in the control equations by interpolation to create a discrete set of equations.

In this work, 2nd-order upwind scheme is selected as the discretization scheme for all simulations [134], because using this scheme can gives better accuracy.

For a second-order upwind (SOU) scheme, the convective flux is computed as [170]:

$$(\dot{m}\phi)_f = \begin{cases} \dot{m}_f \phi_{f,0} & \text{for } \dot{m}_f \geq 0 \\ \dot{m}_f \phi_{f,1} & \text{for } \dot{m}_f < 0 \end{cases} \tag{2.29}$$

Where the face values $\phi_{f,0}$ and $\dot{m}_f\phi_{f,1}$ are linearly interpolated from the cell center values on either side of the face:

$$\phi_{f,0}\& = \phi_0 + \mathbf{s}_0 \cdot (\nabla\phi)_{r,0}$$
$$\phi_{f,1}\& = \phi_1 + \mathbf{s}_1 \cdot (\nabla\phi)_{r,1} \quad (2.30)$$

Where:

$$\mathbf{s}_0 = \mathbf{x}_f - \mathbf{x}_0$$
$$\mathbf{s}_1\& = \mathbf{x}_f - \mathbf{x}_1$$

2.5.3 Algebraic Multigrid (AMG) Method

With increasing mesh sizes, conventional iterative solution algorithms such as Jacobi, Gauss-Seidel, Conjugate gradient method and Successive over-relaxation converge greatly slower (see Fig 2. 17). This sluggish convergence causes a quadratic rise in calculation time as a result.

If the meshes are not fine, then convergence will be fast; if the meshes are fine enough, then slow convergence will be observed. A fine-mesh simulation in STARCCM+ are normally conducted as this format: coarse-mesh setting is firstly used until the simulation converges, then the results obtained will be projected into a finer mesh setting; finally, it will be projected into the finest mesh setting.

Actually, the AMG linear solver used in segregated VOF is not a solver, but a technique to speed up convergence, which degrades convergence for fine meshes. The foundation of multigrid approaches is the effective reduction of numerical error components whose wave lengths correspond to the size of the cell (high-frequency errors) using an iterative solution algorithm. However, with such a strategy, the long-wavelength (low-frequency) errors are decreased rather slowly.

Through an iterative procedure on a hierarchy of gradually coarsened linear systems, multigrid approaches minimize the low-frequency errors. Without taking into account the underlying grid geometry, algebraic multigrid creates a coarse level

system. The fine-grid coefficients are combined in arithmetic operations to create the coarse-grid equations. A multigrid algorithm moves the calculation from a narrow linear system to a coarse linear system after a number of iterations. Because the error function is thus smooth, that is, devoid of high-frequency components of the error, these iterations are also known as smoothing iterations. Since the solution process was moved to a coarser linear system, the mistakes are now more frequent relative to the cell size and may be effectively minimized. A defect equation is created to lower the inaccuracy of the fine linear system solution on a coarser linear system.

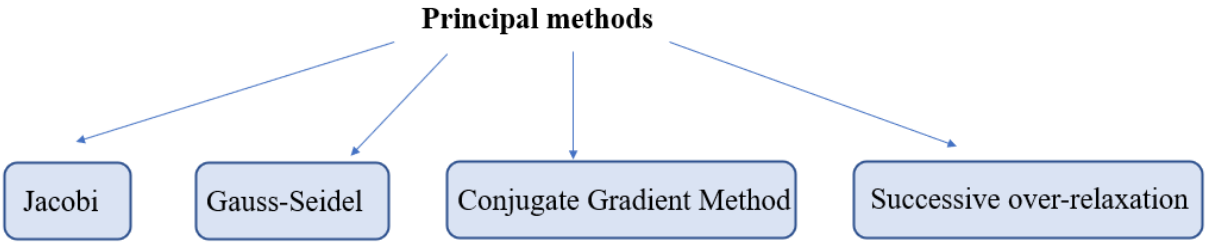

Fig 2. 17 Flow / Iterative resolution algorithms

With AMG, STARCCM+ will start a simulation by a coarse mesh setting, and converge will be attained fast. Then the results will be projected to a finer mesh setting…In such a way, STARCCM+ will finally project the results to the target mesh setting.

2.6 Overset mesh approach

The basic principle of overset mesh technique is to divide the computational domain into several regions with overlapping parts when generating meshes on a complex shape, and to generate meshes on each region individually. When conducting calculations in the fluid field, interpolation is carried out between the meshes in the overlapping area, and the flow field information can be transferred between the two sets of meshes by establishing the interpolation relationship. Specifically, it connects

regions by exchanging data between acceptor meshes in one region and donor meshes (active meshes with unique markings) in another [171].

A typical overset simulation is normally composed of one or more overset regions that overlap the background region. While if necessary, multiple overlapping overset regions without a background region can also be established. The first step to create an overset simulation is to determine a proper arrangement of regions, that is, where the overset mesh boundaries should be assigned and the regions are coupled together utilizing overset interfaces. A background region encircles the whole solution domain in a typical overset simulation, while one overset region surrounds a body like a boat hull or an airfoil. The outer surface of the overset region is defined as an overset boundary. If the overset region slides on the boundary of the background region, then the portion of the overset region boundary that slides on the background region boundary must have the same boundary type as the boundary on which it slides.

Fig 2. 18 is the real simulation done in this thesis, which shows the composition of the computational domain, where the domain ahead of the ship model has been extended so that the ship has a longer way to navigate. The outer sides of the overset region were set overset mesh boundary, but the bottom was set wall boundary, which was applied the same boundary condition as the bottom of the background region.

There are two types of overset interfaces, namely, overset mesh interface and overset mesh zerogap interface, and the former is used and introduced in this thesis. Overset mesh interface is the normal type of overset interface. While utilizing an regular overset mesh interface, 4 to 5 mesh layers are always present in the overlapping zone between the overset region and the background region.

In order to ensure the accuracy of the interpolation and the quality of the mesh, the mesh size should be as consistent as possible in the overlapping mesh area. If the difference in mesh size between overset region and background region is too large,

the interpolation may not be possible. This is also one of the most challenging tasks in overset simulations.

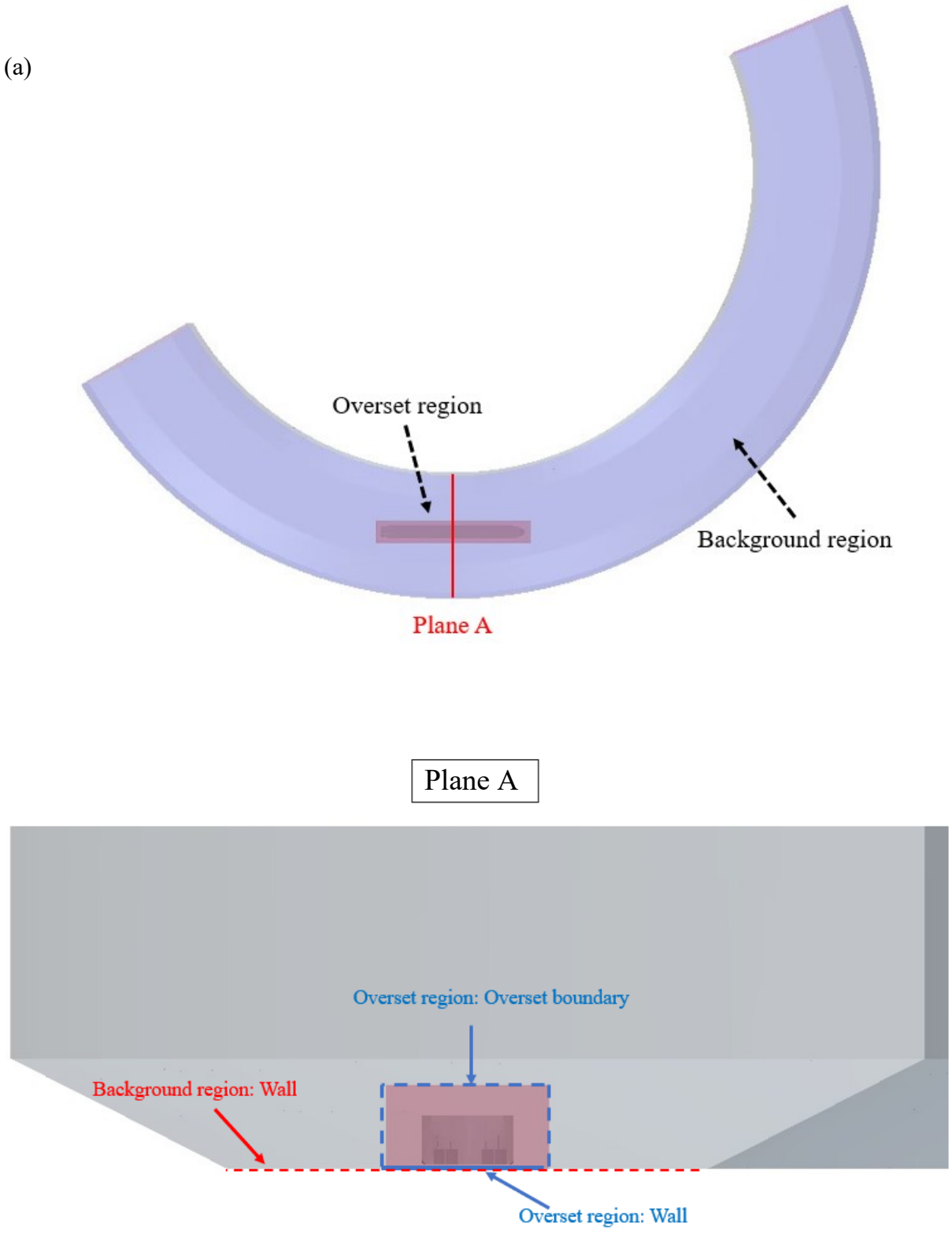

Fig 2. 18 3D view of the computational domain for overset simulation with a cross section shown (cross section: Plane A)

(a) 3D view of the computational domain for overset simulation

(b) Cross section view of Plane A

The meshes are implicitly coupled, so the solution is computed for all active meshes in all regions at the same time. Within the discretized system of equations, when a reference is made to the variable value in an acceptor mesh of one region, a blend of variable values at donor meshes from another region is used to supply the value. This value is reflected directly in the coefficient matrix of the algebraic equation system. The overset and background regions are tightly coupled, allowing for a solution with an arbitrarily low degree of iteration mistakes. As a result, the iterative solution method's rate of convergence is comparable to that of a single mesh of the same resolution.

Overset meshes are mainly used in the following situations: Parametric studies, such as when similar bodies are oriented at various relative locations or when separate bodies are immersed in the same environment. Fewer meshes are created for these scenarios when employing overset meshes. Complicated body motions, such as those involving bodies that are close together, have crossing paths, or have large motions.

The overset hole-cutting procedure is similar to mesh marking. The hole in one region, largely in the background region is imaginary because no meshes are really removed. They are inactive and don’t contribute to the solution process. After the hole-cutting operation, meshes are categorized into the following mesh types:

Active meshes: discrete governing equations are solved inside active meshes.

Inactive meshes: no equations are solved in inactive meshes. However, if the overset region shifts, these meshes may become active.

Acceptor meshes: the acceptor meshes between active and inactive meshes define the boundary of the overset interface for an overset region or background region.

2.6.1 Hole-cutting approach

Two methods for hole-cutting approaches are offered in STARCCM+. According to STARCCM+ user's guidelines, layered approach and alternate hole cutting approach work as follows:

Layered approach: This is by default. It marks the mesh types in the overset region firstly, and then in the background region. For the first step, a single layer of meshes next to the overset boundaries is designated as acceptor meshes in the overset region, whereas the other meshes are designated as active meshes. A layer of meshes is identified as possible donor meshes (a kind of active meshes) of the overset region from the active meshes, close to the acceptor meshes. For the second step, a single layer of meshes in the background region becomes the acceptor meshes when they are in close proximity to the prospective donor meshes in the overset region. This single layer is around four mesh layers distant from the overset region's interface. In the background region, the four intermediate mesh layers between the acceptor meshes and the overset boundaries are labeled as donor meshes. Background meshes within the overset interface hole are inactive and do not participate in the solution process.

Alternate hole cutting approach: For instances with small gaps, this method is more reliable. The method checks whether the mesh centroid of each mesh in the background region is outside or inside the overset region for each mesh. A background region mesh that has its mesh centroid inside the overset region becomes inactive.

With the method described above, the generated overset meshes of the real simulation done in this thesis were shown in Fig 2. 19.

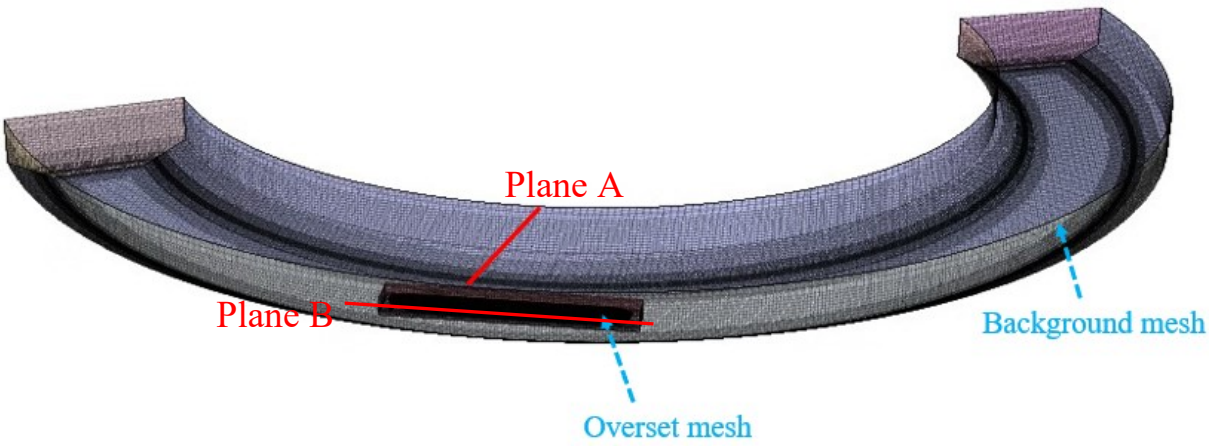

Plane A

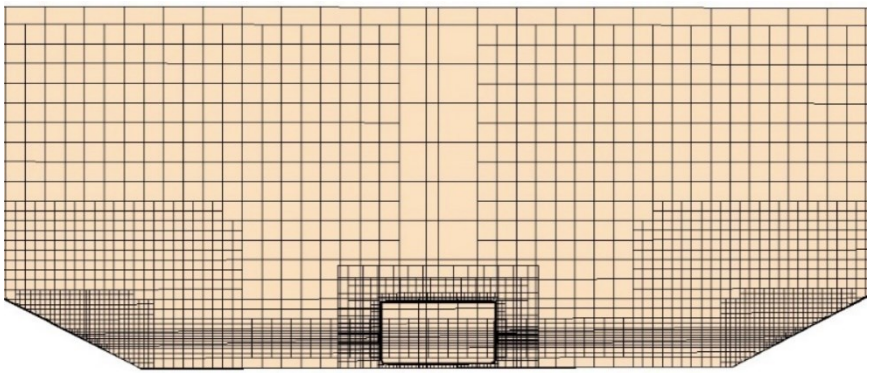

Before initializing

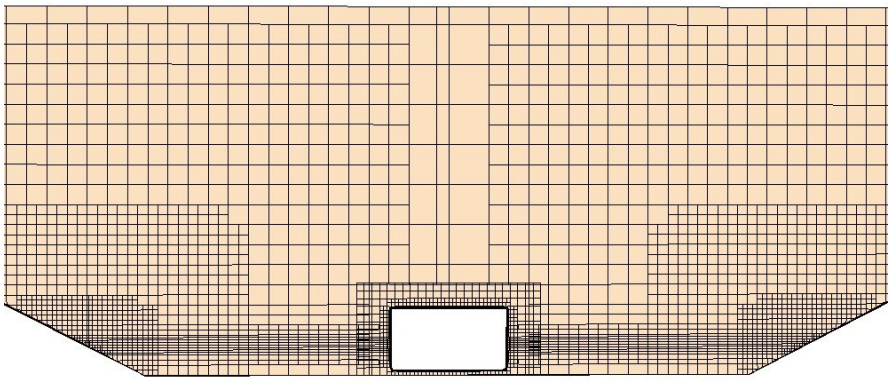

After initializing

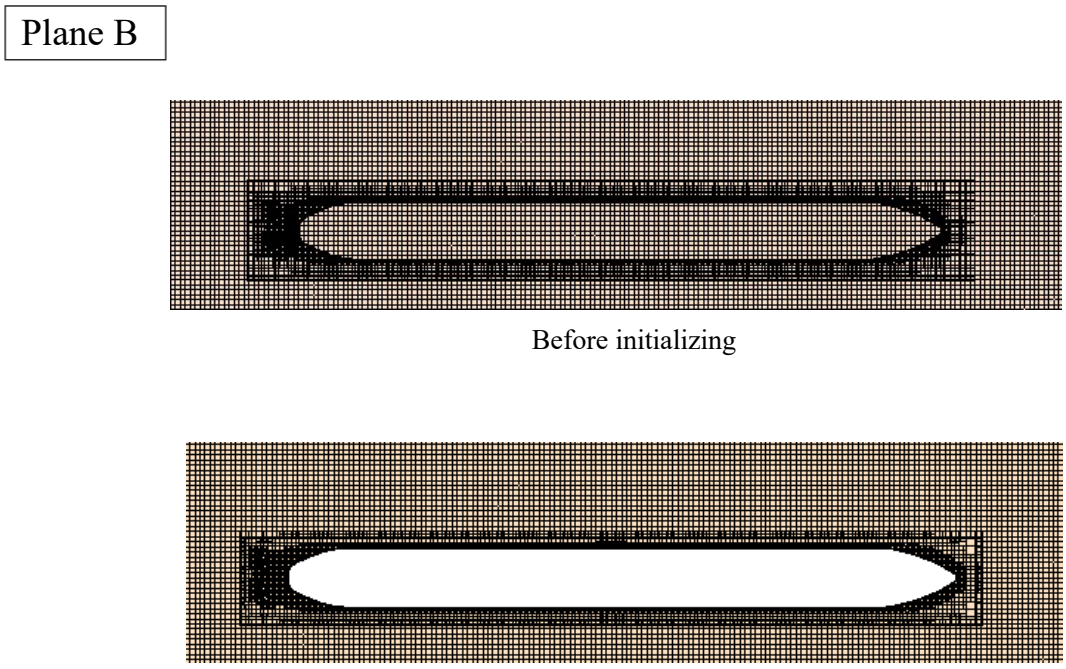

Fig 2. 19 Overset mesh scene of the computational domain, the overset region and the background region

2.7 Conclusion remarks

In this chapter, the details of the numerical solver and mathematical models for the simulations in this thesis were presented and summarized.

The CFD calculation process with its characteristics were introduced. The fundamental equations including continuity equation, Navier-Stokes equation were illustrated respectively. Then a variety of turbulent models with appropriate expressions were shown in detail. After weighing the pros and cons, as well as the wave profiles presented by testing different turbulent models, realizable $k-\varepsilon$ model was finally selected.

The VOF multiphase model used to simulate free surface was presented, and finite volume method that was adopted as the discretization method was introduced. All kinds of boundary conditions used for the computational domains in this thesis were recommended. For verifying the reliability of the simulation results obtained in

this thesis, overset mesh approach was utilized, and the principle of this method was depicted. The actual overset mesh simulations done in this thesis were shown as an illustration to introduce the process of overset mesh generation.

Chapter 3

3.CFD Setup for hydrodynamics around ship

In this chapter, the process of CFD simulation setup is introduced. Specifically, the setup of the computational domain with boundary conditions are explained in detail; the simulations are based on rendering the rotational motion to the meshes in the domain, while the ship is fixed in the domain; the mesh generation method is concluded and mesh sensitivity analysis is carried out; the validation of the CFD model is conducted; the initial conditions and solver settings for the simulations in curved channels are summarized and displayed.

3.1 Ship geometry model

The actual ship model was firstly constructed by a CAD software dedicated to the ship design. Then it was imported into STARCCM+ in the numerical simulations, and scaled with isotropic scale factor of 1/25. The main characteristics of full scale for the real ship and model scale for the model ship are depicted in Table 3. 1. The lines plan and 3D CFD model are shown in Fig 3. 1 and Fig 3. 2 respectively. After transforming the real ship, the mass center of the model ship is situated at (2.7, 0, 0.096879).

Table 3. 1 Characteristics of the ship model

	Length between perpendiculars, L_{pp}/m	Beam, B/m	Moulded depth, H/m	Draft, T/m	Block coefficient, C_b	Wetted surface, $\frac{W_s}{m^2}$	Cross area of ship, $\frac{C_s}{m^2}$
Full scale	134.58	11.4	6	2.5	0.899	2104.8	34.114
Model scale	5.4	0.45	0.24	0.1	0.899	3.367	0.045

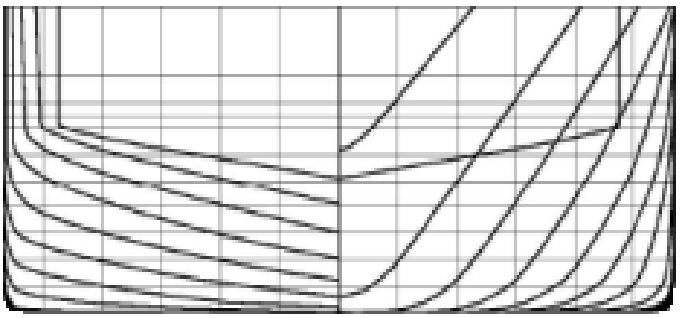

Fig 3. 1 Lines plan of the self-propelled ship

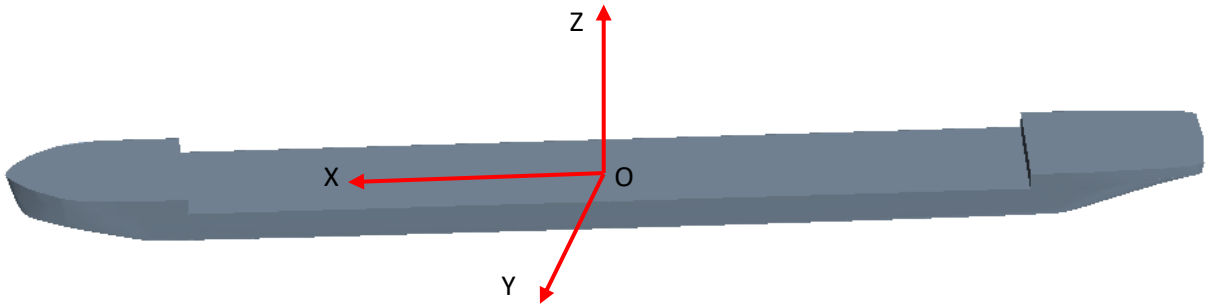

Fig 3. 2 Full CFD model of the studied ship

3.2 Simulation setup

Inland canals are mainly composed of narrow bending sectors, and sometimes, there will be even two or more ships passing through the bending zones at the same time (See Fig 3. 3). In France, there are many significant rivers that play the key role of transportation, for example, the transportation lines in Fig 3. 4. Transportation by inland rivers has been one of the most significant transporting modes now. Therefore, it's significantly meaningful to conduct research on ship hydrodynamics and maneuverability in such sensitive waters.

Fig 3. 3 Canal Seine-Nord Europe vue 3D

(Source: TERRES et Territoires)

Fig 3. 4 Narrow bending canals in France

(a) Narrow bending canals in Northern France (Source: France vélo TOURISME)

(b) Seine river (Source: Winnipeg Trails Association)

3.2.1 Illustration of rotational motion in curved fairways

Bending sections in nature rivers are normally not in regular circles, combined with the effect of wind which further complicates the issue. To establish a mathematical model and investigate the problem better, two assumptions are made: firstly, the curved channels in this work are assumed to be extracted from part of circles; secondly, winds are omitted. Because we are mainly interested in the effect of hydrodynamic forces.

The ship model is initialized in the middle of curved fairways (see Fig 3. 5), and the curved domain is ideally regarded as part of a circle and rotates at a speed of ω (which corresponds to the linear ship speed) around the channel center (Point O). The drift is supposed to be 0. The rotational rate is given to the meshes of the whole domain, inside which the ship is fixed. So there is no absolute velocity imposed at the inlet, but a relative velocity resulting from the rotating meshes.

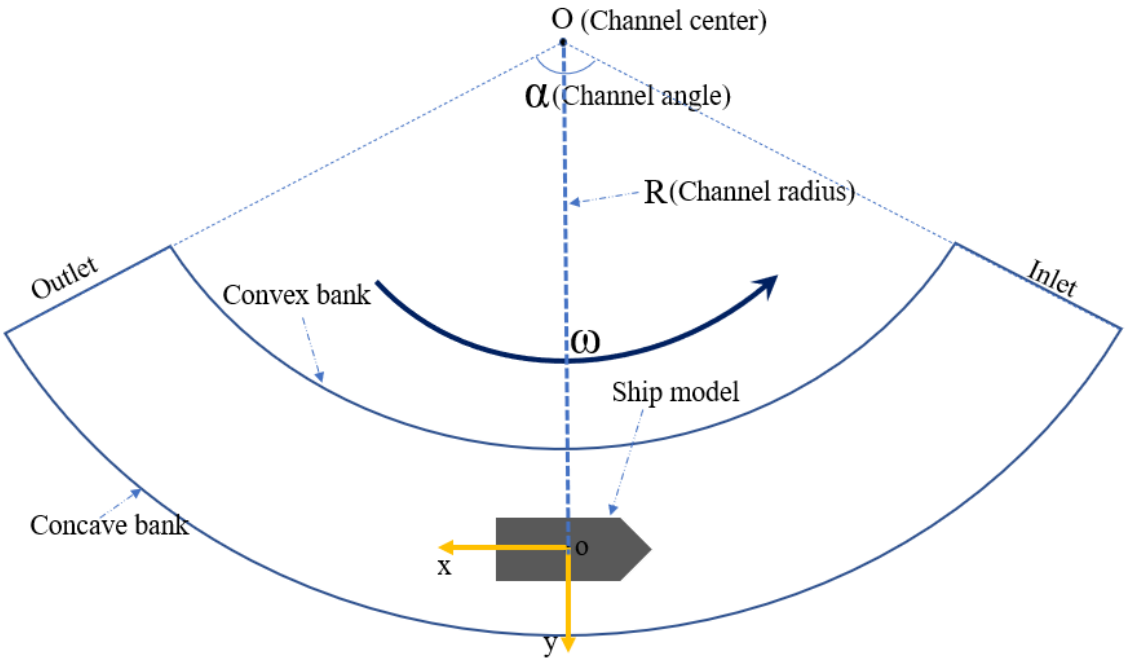

Fig 3. 5 2D-view of the computational domain

3.2.2 Computational domain and boundary conditions

The computational domain with channel angle 120° can be seen in Fig 3. 6, where boundary conditions and coordinate system are shown as well. The positive directions of x and y axes in the coordinate system are assumed to point towards the ship stern and concave bank respectively, and the positive direction of z axis is perpendicular to the horizontal plane pointing upwards. The total length of the domain is set $5 \times L_{pp}$, in which the gravity of the ship model is situated in the middle. The distances between inlet and ship bow, outlet and stern are $2 \times L_{pp}$ respectively according to the ITTC recommendations. On one hand, this setting will be able to eliminate the influence of any reflected waves at the outlet. On the other hand, after trying adjusting the distances from the ship for the inlet and outlet respectively, no significant difference in results can be observed.

Besides, the boundary conditions for inlet and outlet are velocity inlet and pressure outlet respectively; channel bottom, concave side and convex side are all

moving walls, which are assigned a velocity the same as the ship model. The top is chosen as a symmetry boundary condition so that the normal component velocity is explicitly set to zero and the prism layer on them can be eliminated. It's worth mentioning that throughout all the cases, to prevent wave reflection from the walls, the VOF wave damping capability of the software is applied to the solution domain with a damping length equal to 5m. Also, a fixed time step that equals 0.05s is selected for all the simulations.

The relationship among channel angle, channel radius and the length of domain is determined by equation (3.1).

$$5L_{pp} = \frac{\alpha * \pi * R}{180} \tag{3.1}$$

The cross-section view of the domain are shown in Fig 3. 7 as an example. The slope angle of both bank sides is 27°, and the height of the domain is 5 times ship moulded depth.

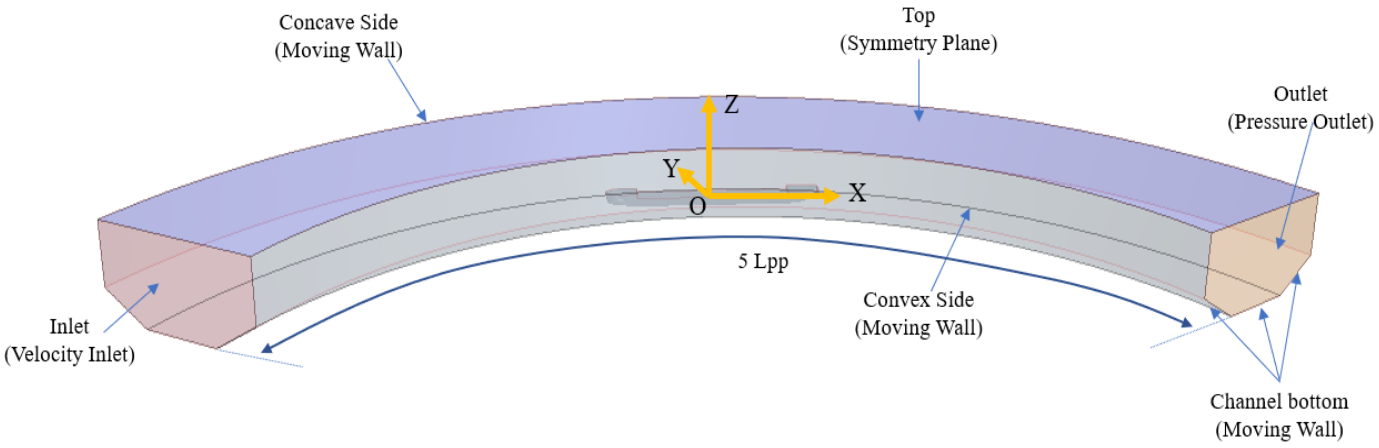

Fig 3. 6 3D-view of the Computational domain(α=120°) with boundary conditions

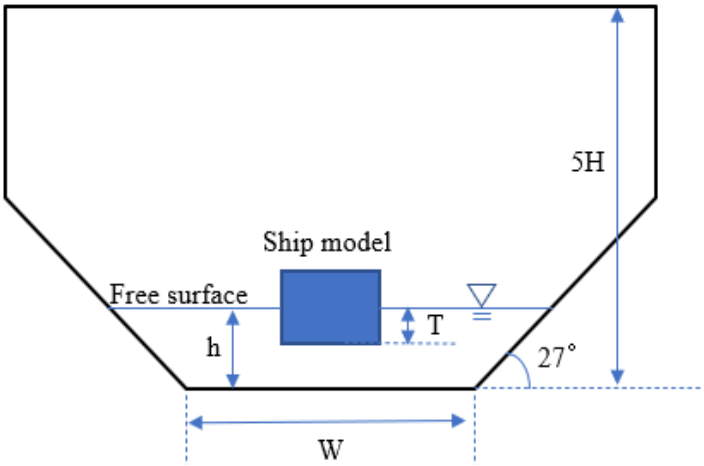

Fig 3. 7 Cross-section view of fluid domains

3.3 State of art for hydrodynamic calculations

3.3.1 Mesh generation and sensitivity analysis test

Mesh generation is carried out with the automated meshing technique in STARCCM+. Trimmed meshes are used to create a high-quality grid for complicated geometric profiles. The trimmed cell mesher in STARCCM+ provides a reliable and effective way to generate a high qualitied meshes for both easy and complicated mesh production issues. In a single meshing technique, it combines a variety of very desirable meshing features, including:

- mostly hexahedral mesh with little cell skewness;
- refinement based on surface mesh size and other user-defined refinement controls;
- independence of surface quality;
- alignment with a coordinate system that the user has chosen.

Fig 3. 8 described the process of generation for a trimmed mesh for an input surface. The template is firstly generated from hexahedral cells using the target size; then the core mesh is trimmed using the input surface; the resulting mesh consists predominantly of hexahedral cells with trimmed cells next to the surface. Trimmed cells are polyhedral cells but can normally be regarded as hexahedral cells with one or

more corners and/or borders that are cut off. Fig 3. 9 gives an example to illustrate the 3D view of trimmed cell core meshes.

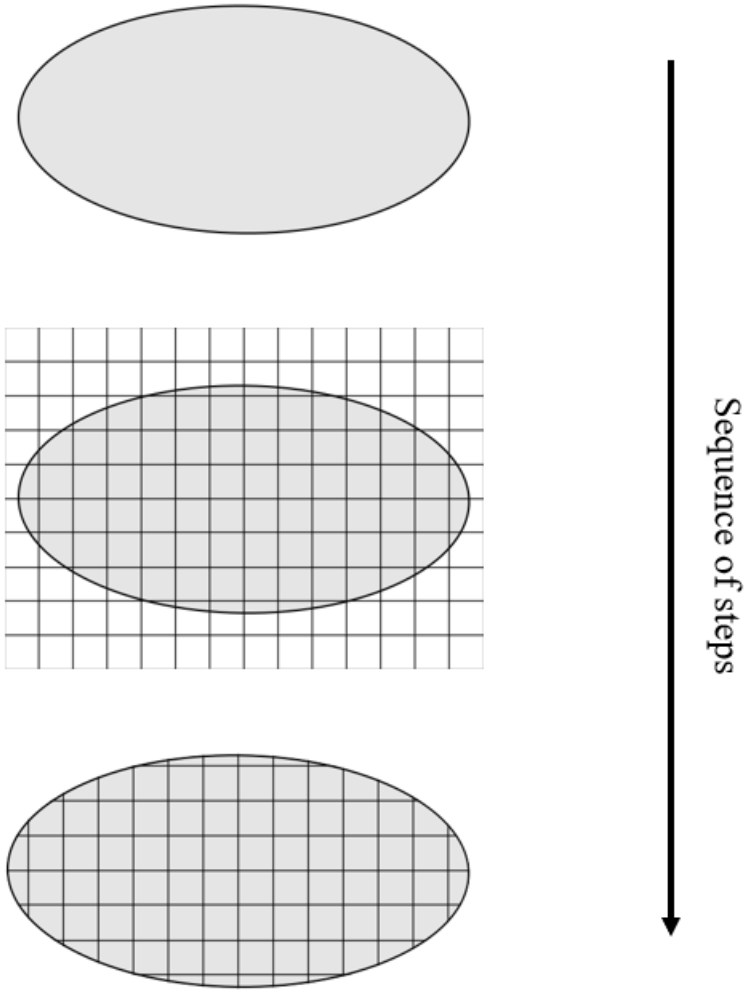

Fig 3. 8 The process for generation of a trimmed mesh

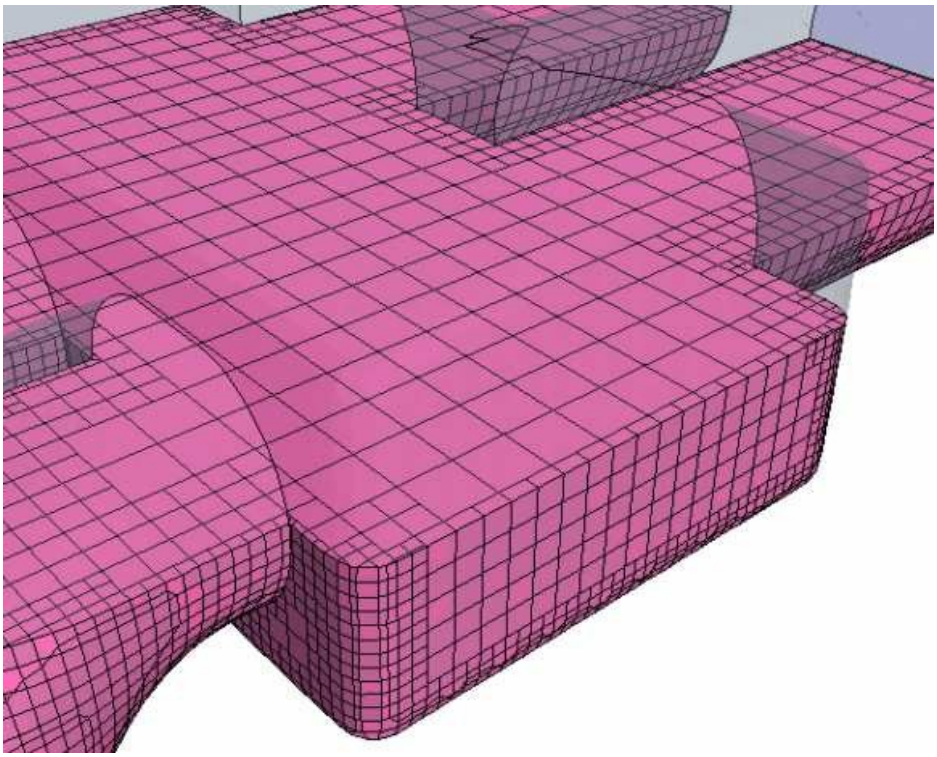

Fig 3. 9 3D illustration of trimmed meshes

(Source: STARCCM+ user's guidelines)

On the other hand, in viscous fluid, there exists a boundary layer on the body owing to the no-slip boundary condition. This boundary layer ought to be meshed more precisely to capture the near-wall flow accurately, which is critical in measuring forces and flow characteristics. Thus, prismatic meshes incorporating 6 prism layers with a growth factor of 1.5 are generated on the surface of ship hull in order to correctly capture the boundary layer and ensure a higher degree of accuracy for the flow solution. Especially, a mesh refinement using volumetric control is applied on the free surface to achieve a proper wave propagation in the domain. While the grids far from the ship hull, including the top, the inlet and outlet boundaries are coarsened by way of surface controls. In this study, to avoid unexpected mesh transitions between the refinements, a slow growth rate is utilized so as to allow the mesher to use several cell layers per transition to facilitate a gradual mesh transition.

A mesh sensitivity analysis test is then conducted to verify the dependency of the solution to the mesh and to select the most appropriate mesh quality in curvature-effect calculations. In this test, the parameter refinement ratio between two adjacent sizes is $\sqrt{2}$ according to ITTC [56, 72, 172-175]. The lowest depth to draft ratio (i.e., h/T=1.2), the largest channel angle (i.e., α=120 degrees) and a relatively high ship speed (i.e., Vs=0.6173m/s), channel bottom width W=2.36m and drift angle β=0° in this work are chosen as the simulation conditions. Based on this, the predicted hydrodynamic force and moment including resistance force, sway force, and yaw moment are denoted by X, Y, N. The numerical results are then transformed into non-dimensional longitudinal resistance X', sway force Y', and yaw moment N', which are normalized according to:

$$X' = \frac{X}{\frac{1}{2}\rho V_s^2 L_{pp} T}, Y' = \frac{Y}{\frac{1}{2}\rho V_s^2 L_{pp} T}, N' = \frac{N}{\frac{1}{2}\rho V_s^2 L_{pp}{}^2 T} \tag{3.2}$$

To analyze the results, the recommended procedures for the numerical uncertainty estimation proposed by ITTC are adopted [172]. Firstly, the convergence ratio R_i is defined using the changes between medium-fine ε_{21} and coarse-medium ε_{32} solutions, that is [176]

$$R_i = \frac{\varepsilon_{21}}{\varepsilon_{32}} \tag{3.3}$$

The convergence conditions are judged:

(a) $0 < R_i < 1$ refers to monotonic convergence

(b) $R_i < 0$ refers to oscillatory convergence

(c) $R_i > 1$ refers to divergence

Secondly, the numerical error δ_i and order of accuracy P_i are estimated by Equation (3.4) and (3.5):

$$\delta_i = \frac{\varepsilon_{21}}{r_i{}^{P_i} - 1} \tag{3.4}$$

$$P_i = \frac{\ln(\varepsilon_{32}/\varepsilon_{21})}{\ln(r_i)} \tag{3.5}$$

Where r_i is refinement ratio of grid.

Then if the convergence condition is monotonic convergence, uncertainty is evaluated according to Equation (3.6) and (3.7):

$$U_i = \begin{cases} [9.6(1-C_i)^2 + 1.1]|\delta_i|, & |1-C_i| < 0.125 \\ [2|1-C_i| + 1]|\delta_i|, & |1-C_i| \geq 0.125 \end{cases} \tag{3.6}$$

$$C_i = \frac{{r_i}^{P_i} - 1}{{r_i}^{P_{iest}} - 1} \tag{3.7}$$

Where P_{iest} is an approximated value for the limiting order of precision of the first term as spacing size goes to zero, and here it's set 2.

If the convergence condition is oscillatory convergence, uncertainty is determined based on oscillation maximums S_U and minimums S_L by $U_i = 0.5(S_U - S_L)$.

The mesh scenes for coarse, medium and fine grid settings are illustrated in Fig 3. 10. The mesh verification results are shown in Table 3. 2 and Fig 3. 12, where all the results are expressed in non-dimensional forms according to equation (3.2). It can be seen that X' and Y' are both monotonic convergences, whereas N' is oscillatory convergence with a very small convergence ratio (absolute value below 0.3%). The mesh uncertainty of X', Y' and N' for all three grid settings are below 1%, which implies that the present simulations can predict results to a satisfying degree. Besides, according to the wave elevation contours of different grid settings in Fig 3. 11, the coarse grid setting produces poor resolution, while the medium grid setting and the fine grid setting show very similar and good results. In view of the computational efficiency, the medium grid setting is a reasonable balance between estimation time

and solution precision. Therefore, the medium grid setting is chosen to be applied to the following simulations. The mesh scene of the computational domain (α=120°, h/T=1.2, V_s=0.6173m/s, W=2.36m, and β=0°) is showed in Fig 3. 13.

Coarse grid

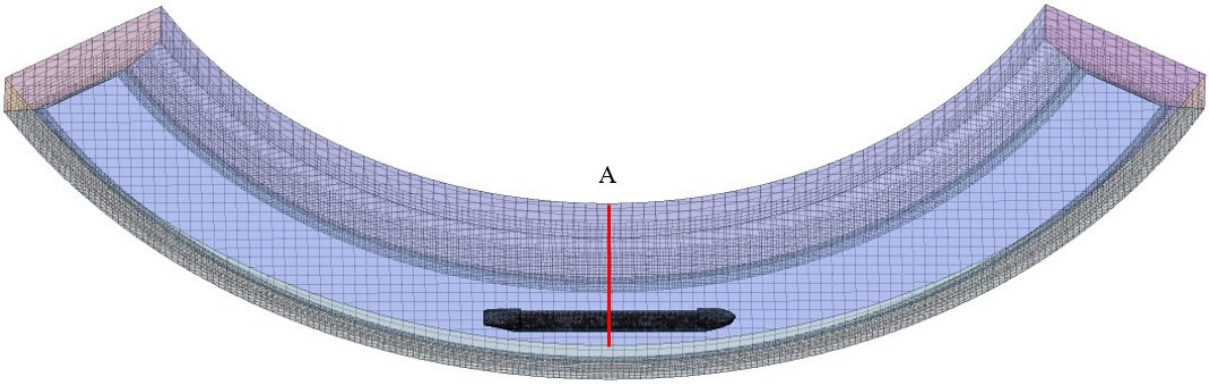

Cross section A

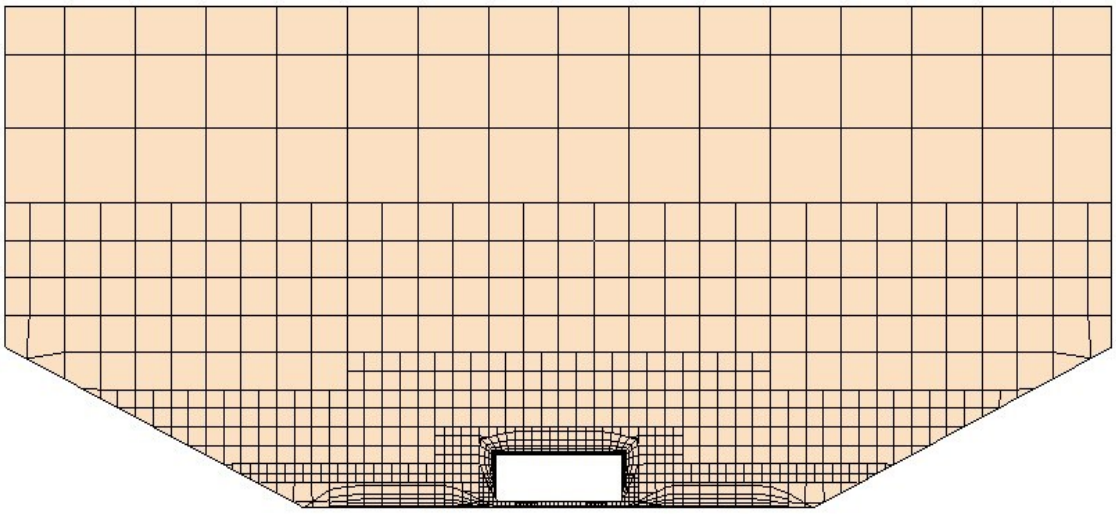

Medium grid

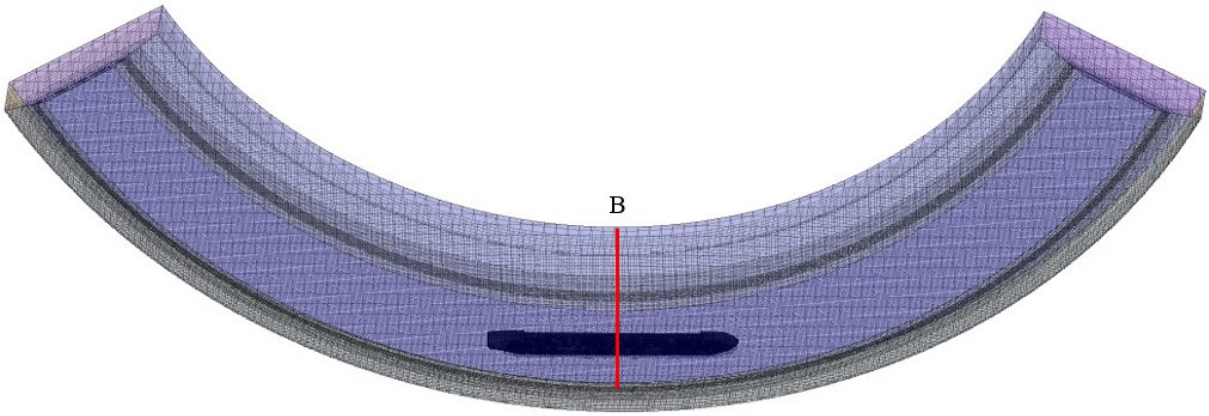

Cross section B

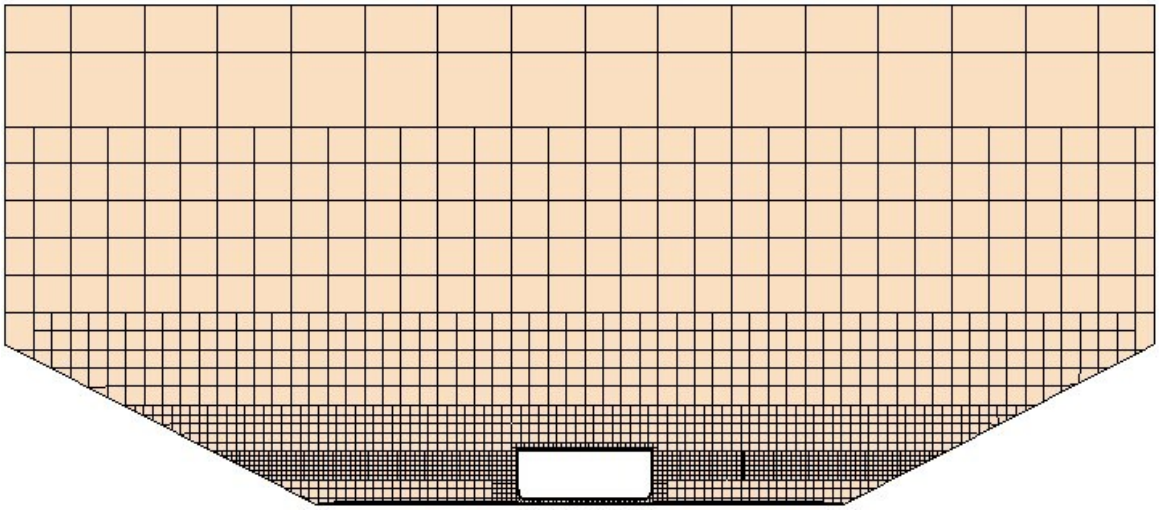

Fine grid

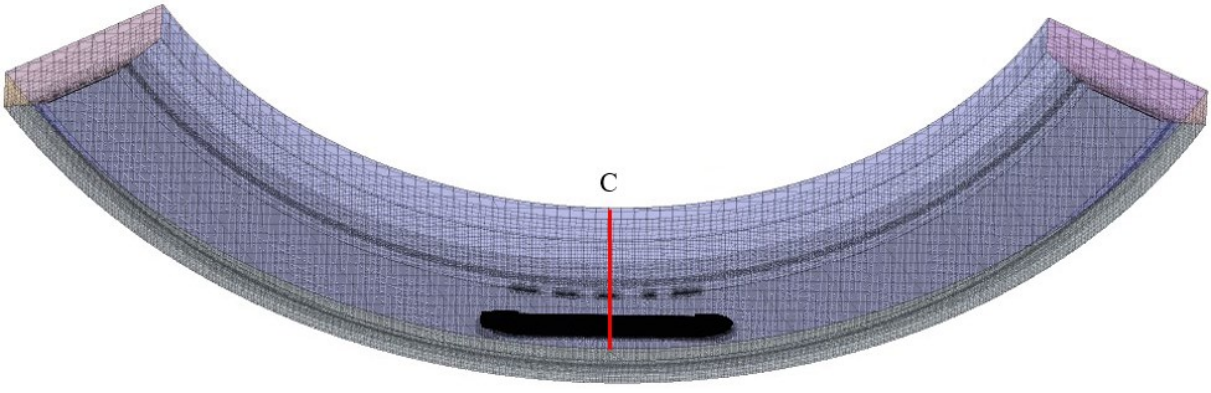

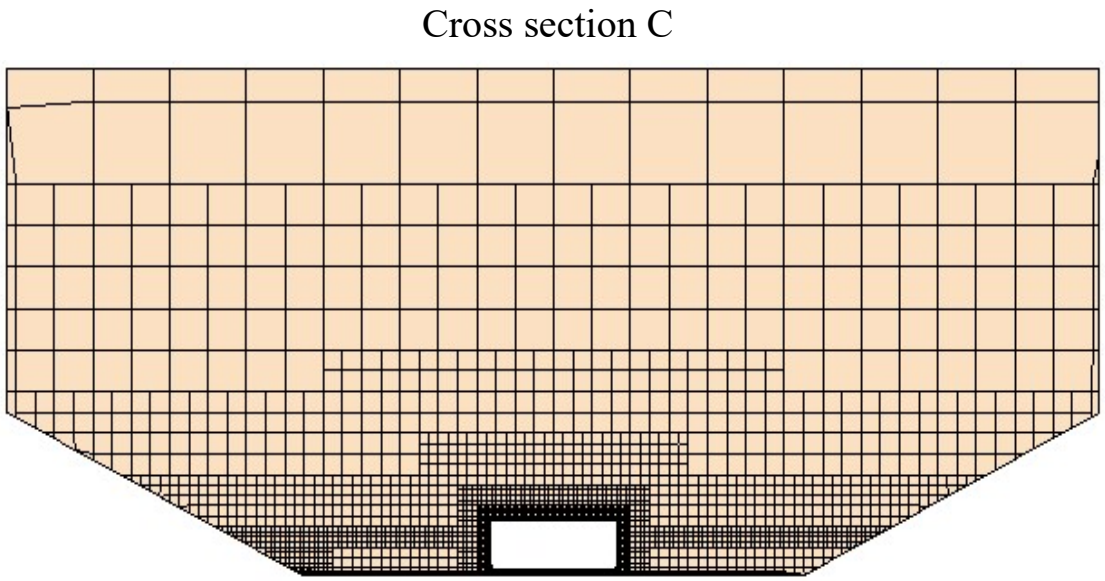

Fig 3. 10 Mesh scene for coarse, medium and fine grid settings

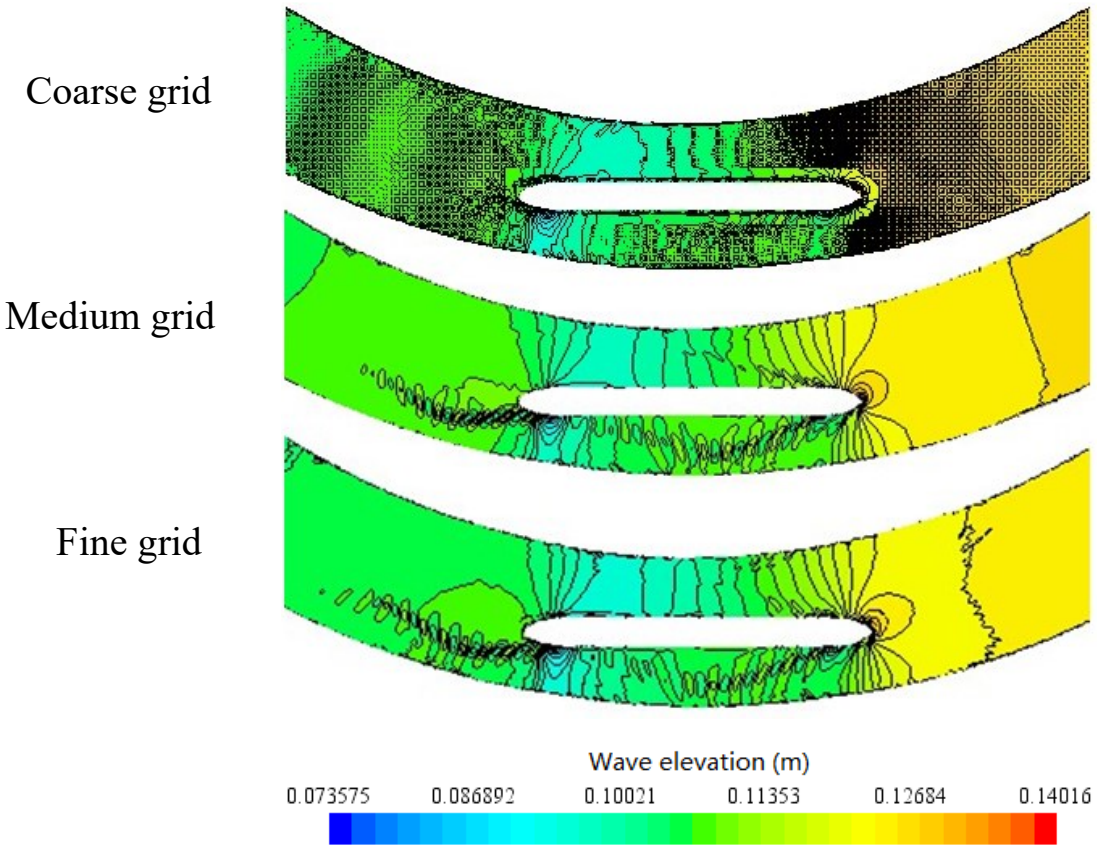

Fig 3. 11 Wave elevation for coarse, medium and fine grid settings

Table 3. 2 Mesh convergence results

Grid	Grid number	X'	Y'	N'
Coarse	513302	0.1183067	0.0323387	-0.0549988
Medium	1521722	0.1118393	0.0110841	-0.0598951
Fine	5449767	0.110775	0.0095047	-0.0598819
R_i	—	0.1645626	0.0743094	-0.002683
Convergence condition	—	Monotonic	Monotonic	Oscillatory
C_i	—	5.076712338	12.4572308	—
δ_i	—	0.000209641	0.000126787	—
P_i	—	5.206581997	7.500619321	—
U_i	—	0.001918929	0.003032049	0.002448143

（a）

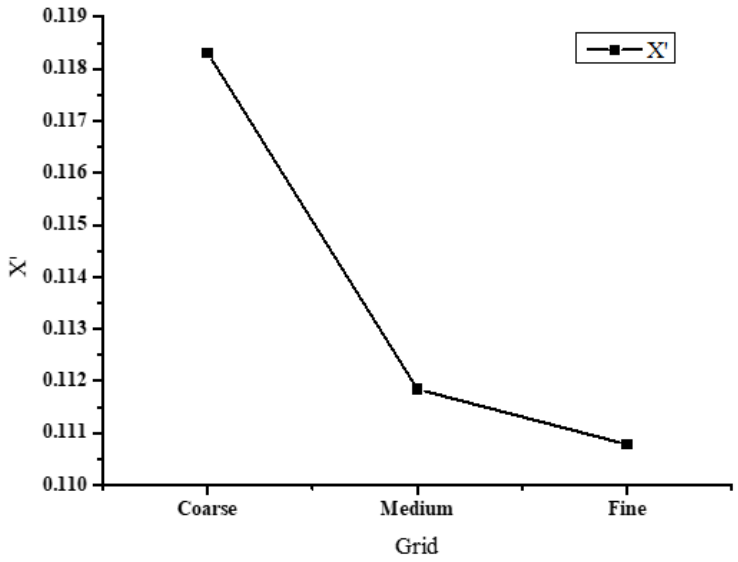

（b）

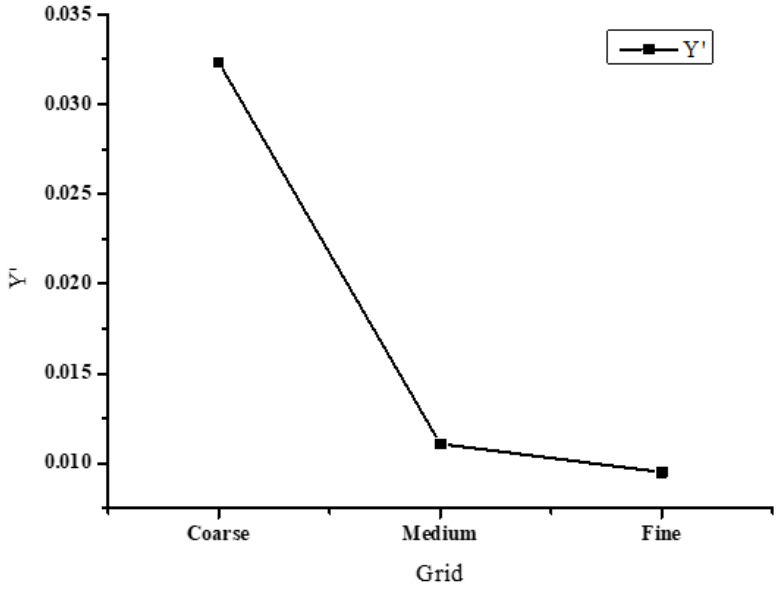

（c）

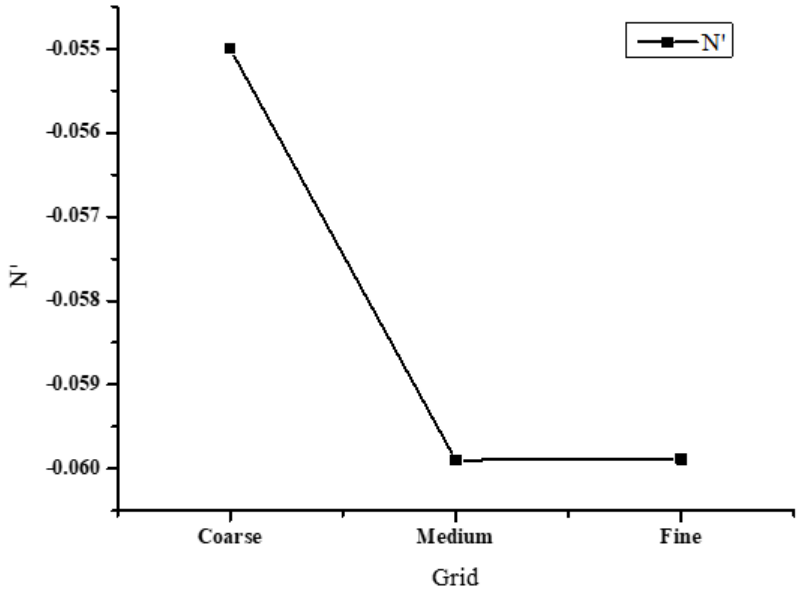

Fig 3. 12　Mesh convergence results for X', Y' and N'

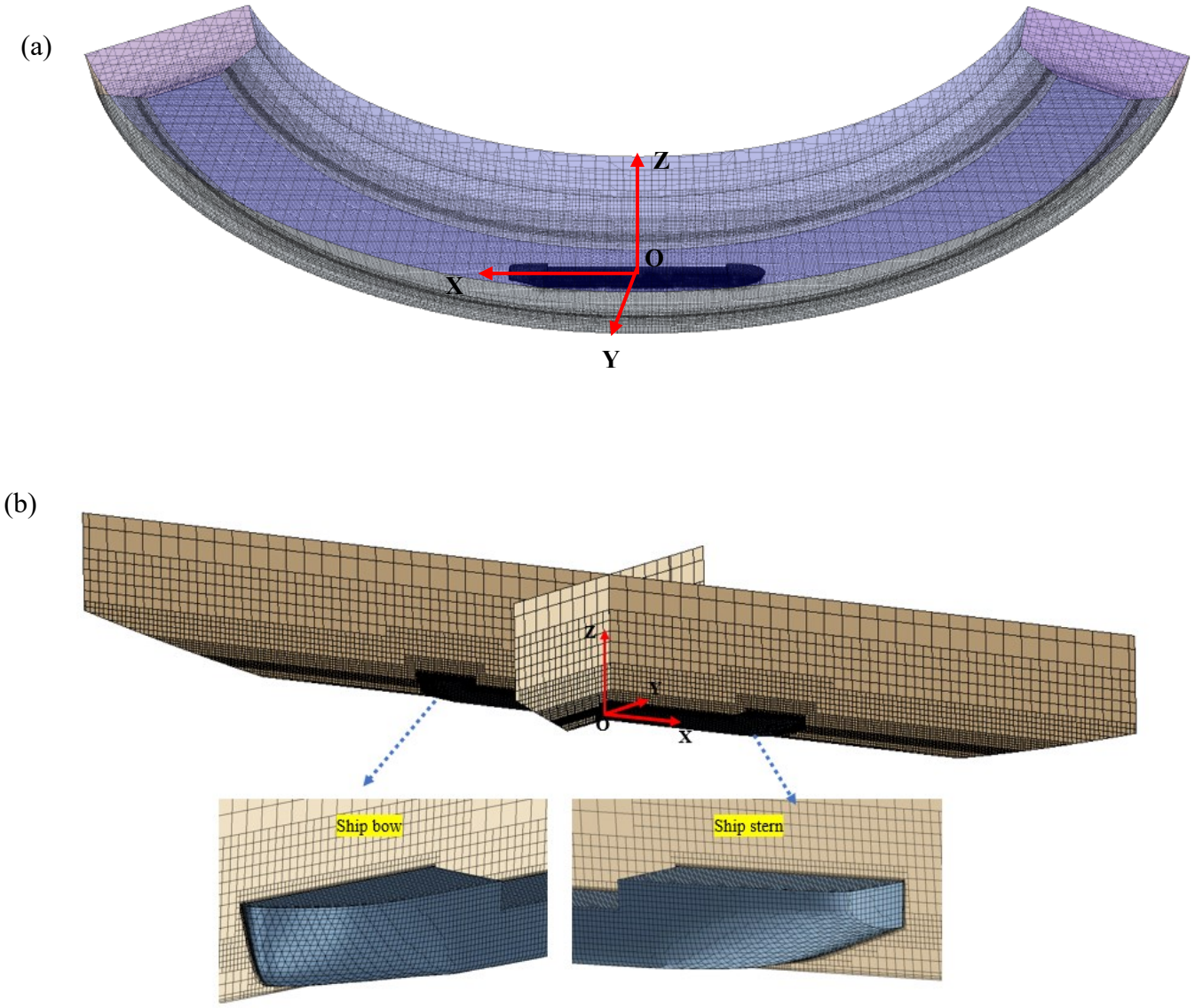

Fig 3. 13 Mesh scene of the computational domain

(a)Volume mesh scene of the entire computational domain (b)Volume mesh scene inside the computational domain

3.3.1.1 y^+ verification

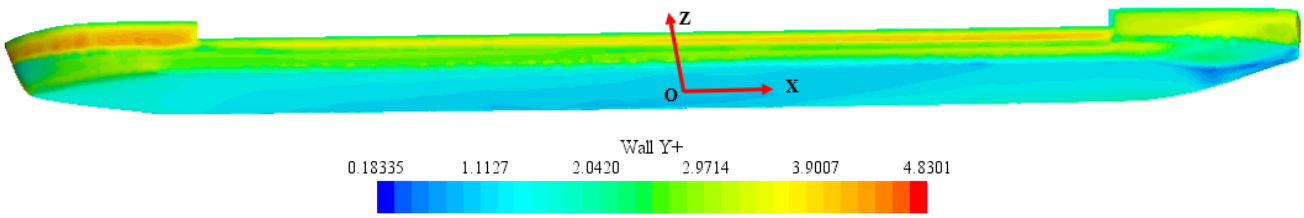

Fig 3. 14 y^+ verification for the simulation (α=120°, h/T=1.2, V_s=0.6173m/s, W=2.36m, and β=0°)

y^+ verification is conducted for all the simulations in this thesis, while the configuration with medium grid in Table 3. 2 (α=120°, h/T=1.2, V_s =0.6173m/s, W=2.36m, and β=0°) is taken as example. According to Fig 3. 14, simulations in this work belong to low-Reynold ones, since y^+ around the ship hull is below 5.

3.3.1.2 Mesh improvement with prism layers

A prism layer mesh model is utilized with a core volume mesh to generate orthogonal prismatic grids next the wall surfaces or boundaries. The layer of grids is essential to improve the accuracy of the flow solution.

When evaluating the forces and heat transfer on walls as well as flow properties like separation, prism layers enable the solver to properly resolve near wall flow. Separation then has an impact on integral outcomes like drag or pressure decrease. The resolution of the velocity and temperature gradients normal to the wall is necessary for accurate prediction of these flow characteristics. In contrast to what would be inferred by using gradients from a coarse mesh, these gradients in the viscous sublayer of a turbulent boundary layer are substantially steeper. A prism layer mesh makes it possible to resolve the viscous sublayer directly if the turbulence model supports it (low y^+ ~1). Alternatively, for coarser meshes it allows the code to fit a wall function more accurately (high $y^+ > 30$) [177, 178].

The thickness, number of layers, and distribution of the prism layer mesh are determined by the turbulence modelling strategy that is applied and the required fidelity of the physics. For proper resolution of the turbulence flow profiles in a turbulent shear layer, more than 10–20 cells are required in the cross-stream direction, depending on the Reynolds number. More cells are needed in order to treat the low y+ wall and dissolve the viscous sublayer [179, 180]. Coarser, high y+ wall-function type

meshes with just a few prism layers can produce good results if just the gross flow properties (such a first-order estimate of skin friction) are needed.

In addition to offering near wall mesh density, prism layers enable the use of high-aspect-ratio cells, improving cross-stream resolution without sacrificing too much stream-wise resolution. Near the wall, prism layers also lessen numerical diffusion. In a finite volume advection system, numerical diffusion is a discretization mistake that blurs discontinuities and steep gradients. When the flow is in line with the mesh, numerical diffusion is reduced [181-183]. As a result, precision is substantially improved by the employment of prism layers.

A subsurface is formed at the specified prism layer thickness values prior to the creation of the core volume mesh, thus "shrinking" (for internal flows) or "expanding" (for external flows) the beginning surface. This subsurface is used to construct the core mesh. The cell faces from the core mesh are then extruded back to the initial starting surface to create the prism layer mesh [184-186].

The prism mesher makes an effort to create a conformal mesh for the boundary pair whenever possible when used with a periodic interface. The boundary type indicated for the boundary pair in this case is superseded by the presence of a periodic interface. Instead, a prism mesh is generated depends on the interface level prism layer choice.

A prism layer is defined in terms of its thickness; the number of mesh layers within it; the size distribution of the layers; the function that is used to generate the distribution (geometric progression or hyperbolic tangent).

The prism layer thickness controls the total overall thickness of all the prism layers. The number of prism layers controls the number of mesh layers that are generated within the prism layer on a part surface or boundary, for example, there are 3 prism layers in Fig 3. 15.

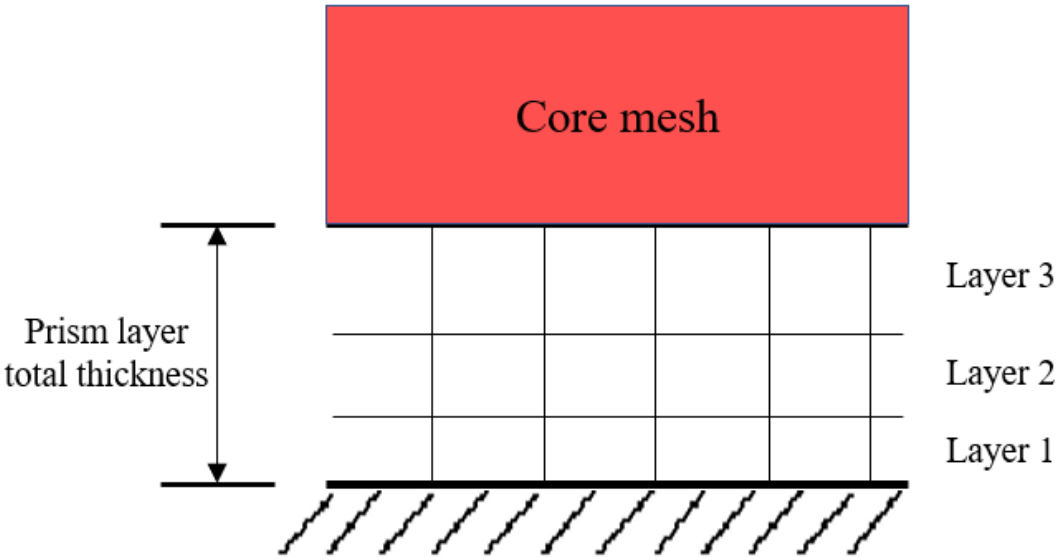

Fig 3. 15 Illustration for prism layers

While the distribution or stretching of the layers normally covers three items, that is, prism layer stretching, thickness of near wall prism layer, and prism layer thickness ratio.

- Stretch factor

The stretch factor is the ratio of the thickness of a mesh layer to the thickness of the preceding layer.

$$Stretch\ factor = \frac{n_2}{n_1}$$ (See Fig 3. 16)

The minimum allowed value is 1.0, which leads to uniformly spaced prism layers. Any value larger than 1.0 will give rise to non-uniformly spaced prism layers with a low prism layer height nearer to the wall that grows progressively in every prism layer away from the wall.

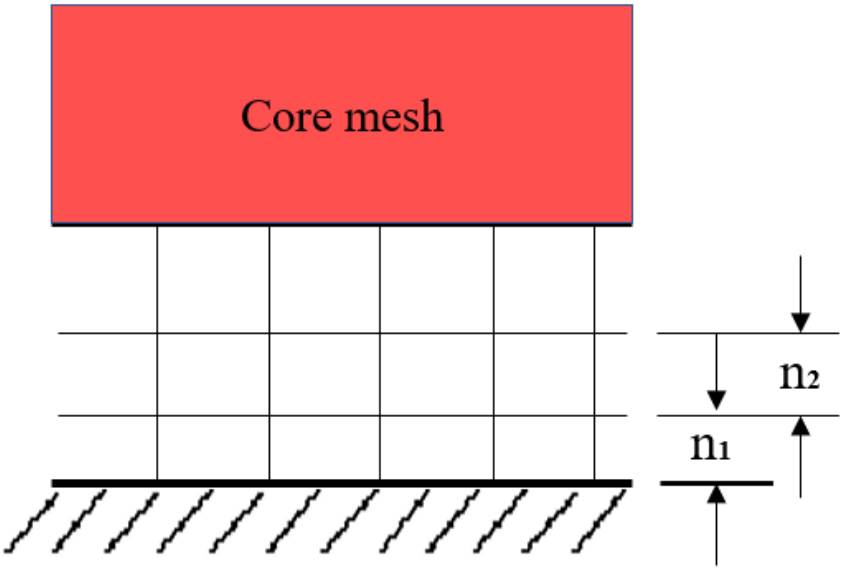

Fig 3. 16 Graphic for stretch factor

- Wall thickness

Wall thickness means the thickness of the layer that is immediately next to the wall boundary (called the near wall layer), which corresponds n_1 in Fig 3. 16. A stretch factor is automatically calculated and applied to the remaining prism layers to get the proper thickness distribution (between the near wall layer and the start of the core mesh). The entire thickness of the prism divided by the number of layers is the upper limit for the Wall Thickness value. A linear distribution is utilized if a larger value is given.

- Thickness ratio

The thickness ratio means the ratio of the thickness of the prism layer next to the core mesh to the thickness of the prism layer next to the wall. A stretch factor is automatically calculated for the intermediate layers, and the minimum allowed value is 1.0. The thickness ratio can be expressed as (see Fig 3. 17):

$$Thickness\ ratio = \frac{n_3}{n_1}$$

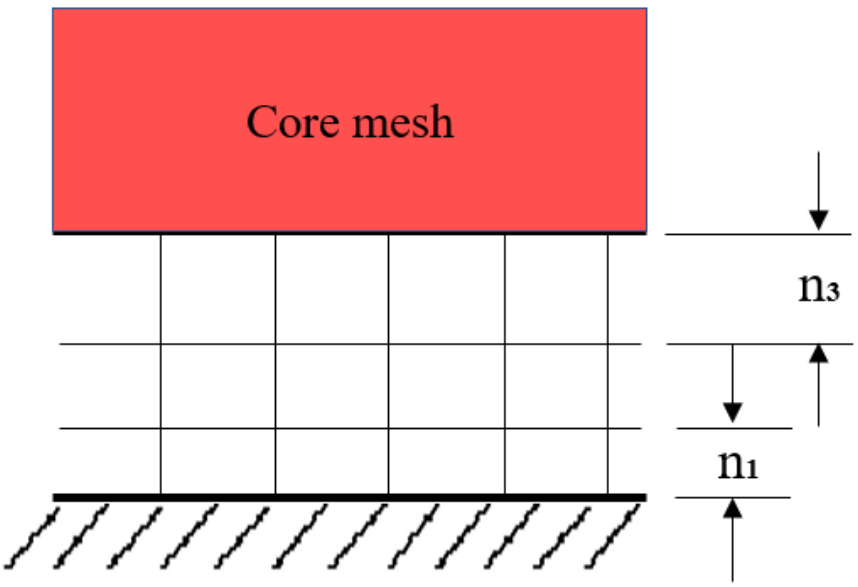

Fig 3. 17 Graphic for thickness ratio

There are two kinds of functions that are used to generate the distribution. One is the geometric progression, which uses a simple geometric relationship (stretching factor) distribute the mesh layers. The starching factor between adjacent mesh layers is always calculated as a constant value, and this has been introduced above.

The other is hyperbolic tangent. This method distributes the cell layers according to a one-parameter hyperbolic tangent stretching function expressed as:

$$s(n_i) = 1 + \frac{\tanh[F_s(n_i/N - 1)]}{\tanh(F_s)} \tag{3.8}$$

Where N is the total number of layers, n_i is the current node, F_s is the overall stretching factor, and $s(n_i)$ is the distribution value for node n_i $(0 \leq n_i \leq N)$.

The relationship between nodes and layers is shown in Fig 3. 18.

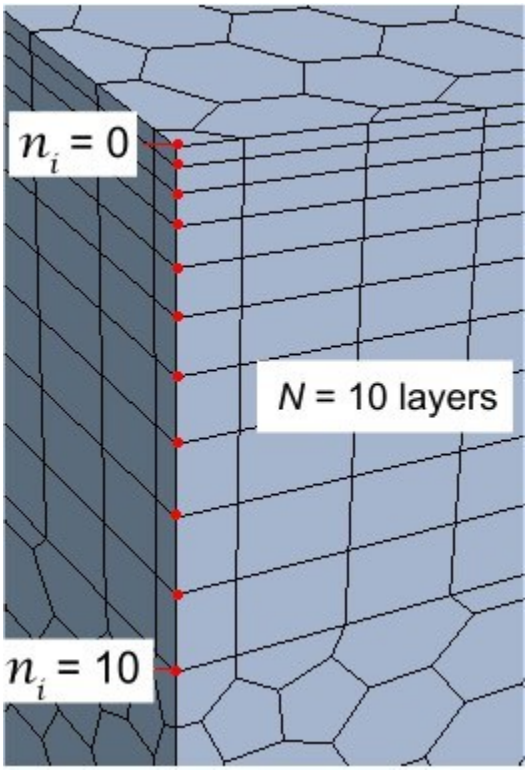

Fig 3. 18 Relation between nodes and layers (Source: Starccm+ users' guidelines)

3.3.2 Validation of the CFD model

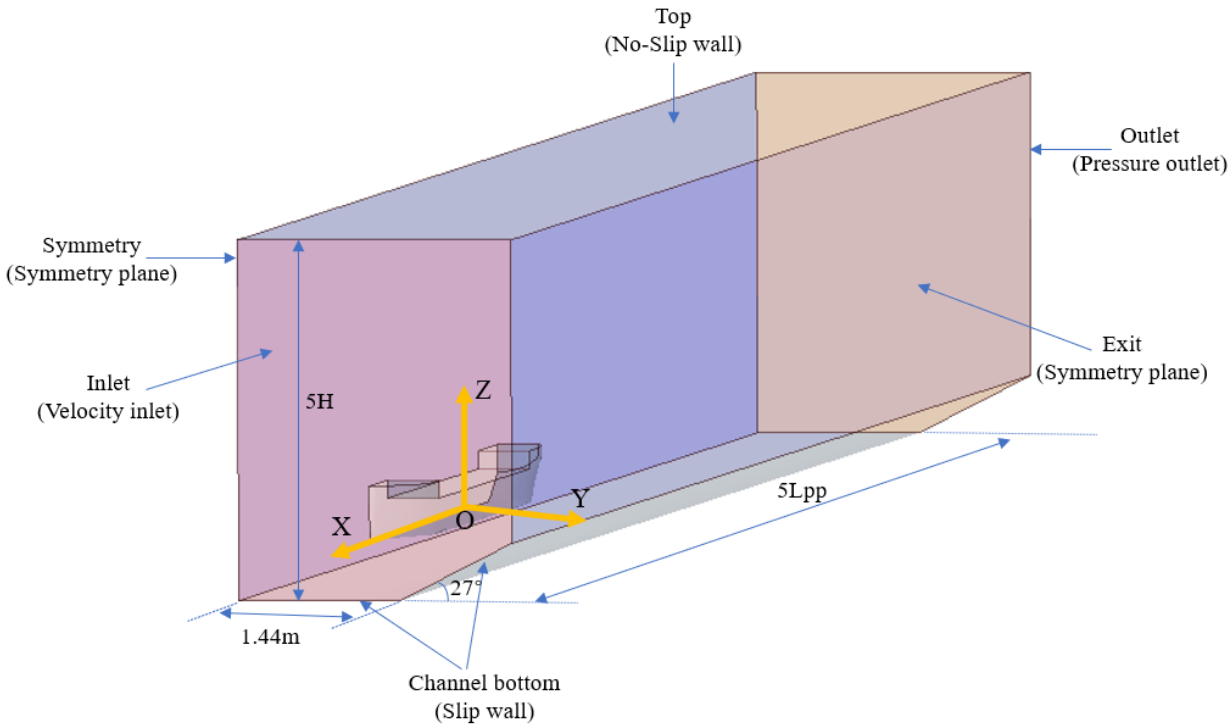

Fig 3. 19 Computational domain of the simulations for validation

The validation test was conducted with the same ship model in a rectangular channel, and the computational domain is illustrated in Fig 3. 19. In this study, the scaled model is simulated fixed in a confined channel which is the same as that in the experiment, due to the fact that there will be a large number of meshes generated and the geometry of the ship model and the fluid domain are strictly symmetric as well, only half the ship model is simulated in STARCCM+ for the sake of economizing time using the symmetry boundary condition. The channel configuration and ship model are all 1/25 times as large as the original size. The fluid domain extends up to $4\times L_{pp}$, where there is $1\times L_{pp}$ ahead of the ship, and $2\times L_{pp}$ behind the ship according to the ITTC recommendation guidelines. The channel bottom is 1.44m in half width, connected by a slope with an angle of 27 degrees. The settings are in agreement with the towing tank in Liege university where the experiments were conducted (see Fig 3. 20). The length of the towing tank is 100m, width is 6m and depth is 3.5m. The height of the simulated fluid domain is 5 times ship moulded depth. The *h/T* ratio is 1.8, and UKC (under keel clearance) is 0.08m. Inlet is assumed as velocity inlet; Outlet is pressure outlet; the plane Symmetry and Exit are set symmetry plane; Top is no-slip wall; Channel bottom is considered moving wall that is applied the same velocity as the ship.

(a)

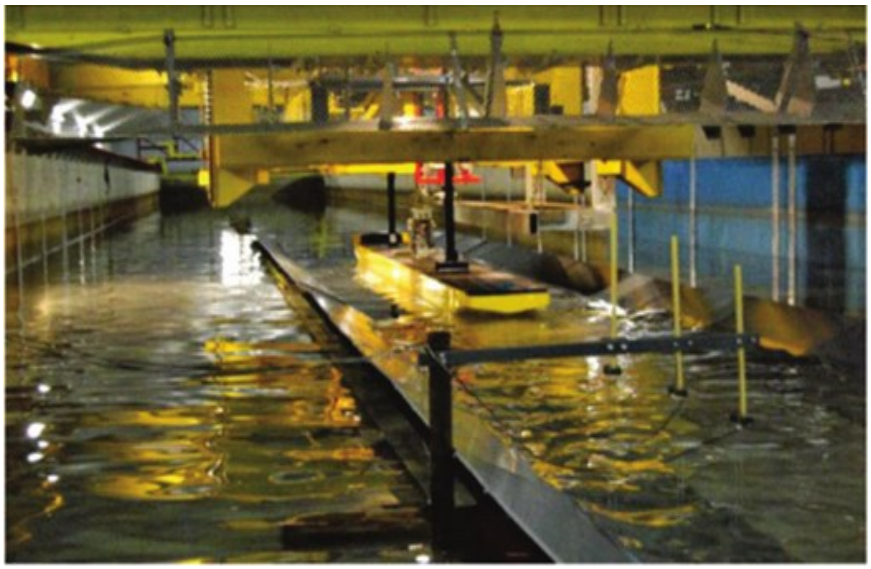

(b)

Fig 3. 20 Towing tank for shallow and restricted experiments in Liege university

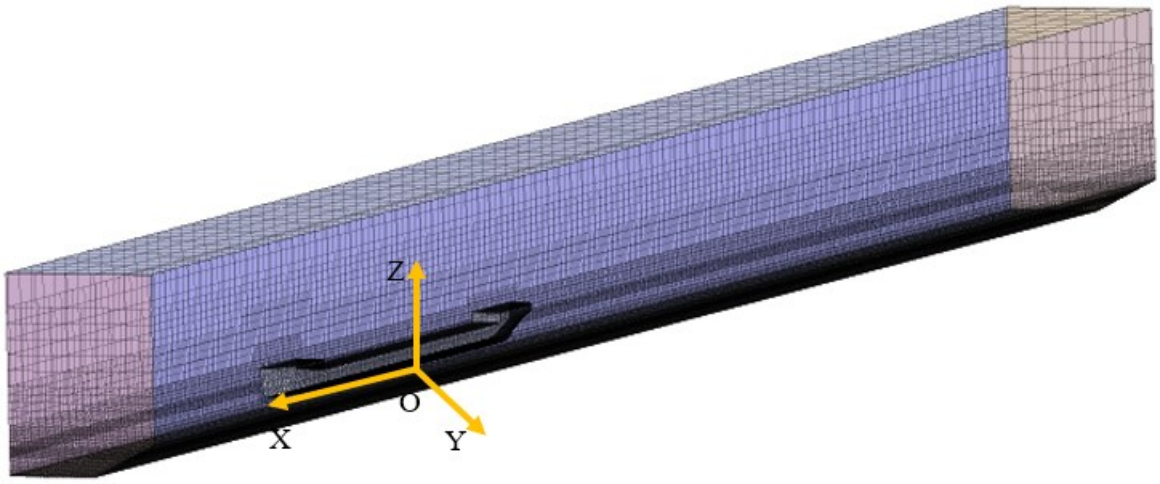

Fig 3. 21 Mesh scene of the simulations for validation

To simulate accurately, two custom controls are used to refine the meshes on the free surface and the underwater ship part respectively. Meanwhile, two surface controls are established. One surface control is applied to the ship surface to create meshes that are fine enough on the ship hull, and the other surface control is implemented on Top, Inlet, Outlet, and Ext so as to coarsen the meshes far from the ship hull. The mesh scene of the whole fluid domain can be seen in Fig 3. 21. Totally, more than 1 million cells are generated.

The ship speeds equal to those from experiments are rendered to the current and wind at the inlet, so the ship is equivalent to navigating at the same experimental speeds. The resistances calculated from simulations are compared with those from the experiments that were conducted in the towing tank. This aims at demonstrating the reliability of the CFD model in this work.

Three sets of ship speeds ranging from 0.335m/s to 0.575m/s (most often used in inland navigation) are selected in this numerical simulation and the resistances in x-direction are compared with those in experiments respectively. Stemming from the confinement of the channel and the very small UKC allowed for, it takes all of the three sets of simulations a long time-step to attain convergence. According to the resistance report output, the results of these simulations with those from experiments are compared (see Table 3. 3). The wave elevation contours are illustrated in Fig 3. 22, where Kelvin waves can be noticed. With V_s increasing, waves generated around the ship are becoming more serious, and wave elevation at bow is higher as well.

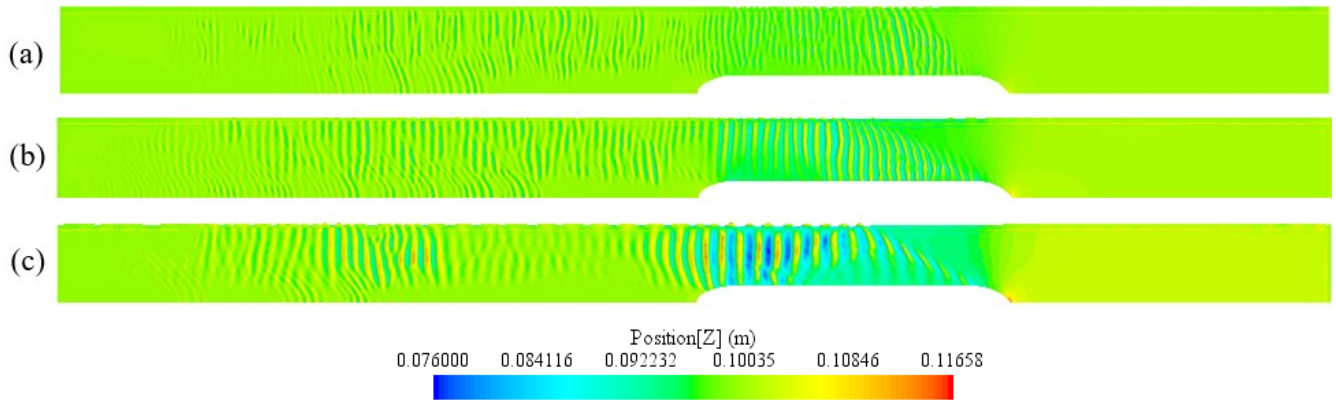

Fig 3. 22 Wave elevation contours for validation simulations

(a)*Vs*=0.335m/s, (b) *Vs*=0.4485m/s, (c) *Vs*=0.575m/s

Table 3. 3 Comparisons between simulations and experiments

Ship speed $V_s/m\ s^{-1}$	Resistance of numerical simulation X_n/N	Resistance of experiment (divided by 2) X_e/N	Errors E/%
0.335	0.690084	0.659	4.7%
0.4485	1.23664	1.194	3.5%
0.575	2.15804	2.124	1.6%

From Table 3. 3, only slight errors occur between the results from experiments and simulations, which are within 5% for all the three sets selected. Based on this, a good agreement between experiments and numerical simulations can be seen from the results. The CFD results tend to overrate the magnitude of the expected resistance, compared to the towing tank experiments. It should be noted that the standard deviations of the experimental resistance results should be within the range of 5%. Therefore, the validation against the experiments can be considered approved.

3.4 Initial conditions

To accelerate the solutions and cut down on the amount of CPU time needed, three initial conditions must be managed. The first one is the pressure, which is set as the hydrostatic pressure of flat wave field function, meaning that the initial pressure is applied by the wave's current, and STARCCM+ calculates and displays this value in the initial condition. In order to prevent the superposition of values, the velocity is set

as the velocity of flat Vof wave field function, which represents the wave current parameters. Setting up the volume fractions for each kind of the fluid is the next stage. The fractions are set as the composite since they will vary all the time. As a result, the volume fractions of the heavy and light fluids are set as volume fraction of heavy fluid and volume fraction of light fluid, respectively.

3.5 Solver settings

The time step by implicit unsteady was set to be 0.05 seconds after estimation, and the temporal discretization is selected as 2^{nd} order. On the other hand, the maximum inner iterations are set as 10 for all the simulations. The physical maximum time was determined in order that all the hydrodynamic forces became steady with only minimal changes.

3.6 Conclusion remarks

In this chapter, validation and verification studies were conducted to test the accuracy and validity of the CFD model. The mesh sensitivity analysis was executed according to ITTC guidelines. Trimmed meshes and prismatic meshes were utilized to produce meshes in the computational domain. By custom controls and volumetric controls, the meshes near the ship hull were refined while meshes far away from the ship were coarsened. The results of validation tests were then compared with those from experiments done in the towing tank of Liege university. A good agreement between experiments and numerical simulations can be observed.

Simulation setups were established and described. The relative frame motions were introduced to produce centrifugal force in the computational domain, and specific channel settings with appropriate boundary conditions were described.

The proper initial conditions for simulations and solver parameters were defined after estimation.

Chapter 4

4. Effect of navigational environment on ship hydrodynamics

This section concerns about the bending effect on ship hydrodynamics under variation of the environment of navigation (channel geometry). The maneuverability of inland ships is crucial according to the introduction of previous sections, including the ability of inland navigation on lakes, rivers, and artificial waterways, which have size restrictions due to the width and depth of the channel. So the effect of some key parameters, such as channel angle (α), channel bottom width (W) and channel slope angle (γ) are researched. These parameters are important factors in determining the conditions of the waterways and are not related to the ship itself. The sensitivity analysis of these parameters are conducted so that the influence exerted by them can be integrated into the ship simulator.

4.1 Simulation case settings

All the cases are deemed in restricted curved channels, and the details of four different configuration groups (Config. A to C) are illustrated in Table 4. 1. Config. A is employed to evaluate the effect of channel angle (α) on ship hydrodynamics, where a series of h/T ratio variations are the parameters to be researched, meanwhile different channel angles are considered to concern about the effect brought by h/T ratio under different channel curvatures. While the other conditions are kept both constant and severe. Similarly, the other configuration groups namely Config. B, Config. C, and Config. D are set in the same way.

The simulation results based on the configuration settings in Table 4. 1 are displayed and analyzed in detail. Resistance force (X), sway force (Y) and yaw moment (N) of the ship are transformed into non-dimensional forms based on equation

(eq3.2), which are expressed as X', Y' and N' respectively. Also, the positive directions for X and Y are assumed the same as the positive directions of x and y coordinate axes, and the positive direction for N is counter-clockwise on paper (See Fig 3. 6). Meanwhile, the hydrodynamic forces and moment are divided into pressure component and frictional component due to $X' = X'_p + X'_f$, $Y' = Y'_p + Y'_f$, $N' = N'_p + N'_f$, where prime 'p' and 'f' indicate pressure and friction respectively. The detailed expressions are shown as follows:

$$X = \oiint_{ship} (-p\vec{n} + \tau\vec{t})ds \bullet \vec{\imath} \tag{4.1}$$

$$Y = \oiint_{ship} (-p\vec{n} + \tau\vec{t})ds \bullet \vec{\jmath} \tag{4.2}$$

Where p is pressure, τ is shear stress, $\vec{\imath}$ and $\vec{\jmath}$ are vectors coinciding with x and y axes respectively.

The effect of various parameters are analyzed and discussed in the following sections.

Table 4. 1 Simulation configurations for effect of navigational environment

	Config. A	Config. B	Config. C
	Channel angle variation	Channel bottom width variation	Channel slope angle variation
Total simulation case quantity	7	8	4
Channel angle, α / °	0, 30, 60, 75, 90, 105, 120	30, 120	87.34
h/T	1.2	1.2	1.2
Ship speed, $V_s/m\ s^{-1}$	0.6173	0.6173	0.6173
Channel bottom width, *W*/m	2.36	1.888, 2.36, 2.832, 3.304, 3.776	2.36

drift angle, β / °	0	0	0
Bank slope, γ / °	27	27	13, 27, 50, 90

4.2 Effect of channel angle (α) on ship hydrodynamics

This section analyzes the impact of α on ship hydrodynamics, in which the results are based on the simulations of Config. A in Table 4. 1. Under the condition of the same channel length, a common consensus should be pointed out that the larger α is, the smaller the channel radius. Configurations for different channel angles are shown in Fig 4. 1. According to Fig 4. 2, compared with that in straight channels, a sharp increase in X' can be noticed in curved channels, and this is due principally to the increase of X'_p, which is related to the free surface increase at the ship bow caused by the flow angle of attack (the angle between the ship body's centerline and the oncoming flow). While in curved channels, we observe a slight increase of X' as α grows, and there is no abrupt change as it is from straight channel to curved one with α changing. By analyzing the same figure, we note that the increase in X' is characterized by the increase of the friction component (X'_f) while X'_p is decreasing, and meanwhile, X'_p is always nearly double as large as X'_f.

It can be noticed in Fig 4. 3 that waves generated around the convex bank are disappearing with α growing, and there are only waves around the concave bank under large α. This behavior is principally due to the rotational flow in the bending zone, which contributes to the increase of X'_p. Combined with the streamlines in Fig 4. 5, it can be seen that the curvature of the mainstream is becoming larger as α grows, and streams come nearer the concave bank when passing through the ship, which causes a difference in water depth between convex and concave banks. Then the flow velocity around the ship will increase, resulting in an increase in X'_f.

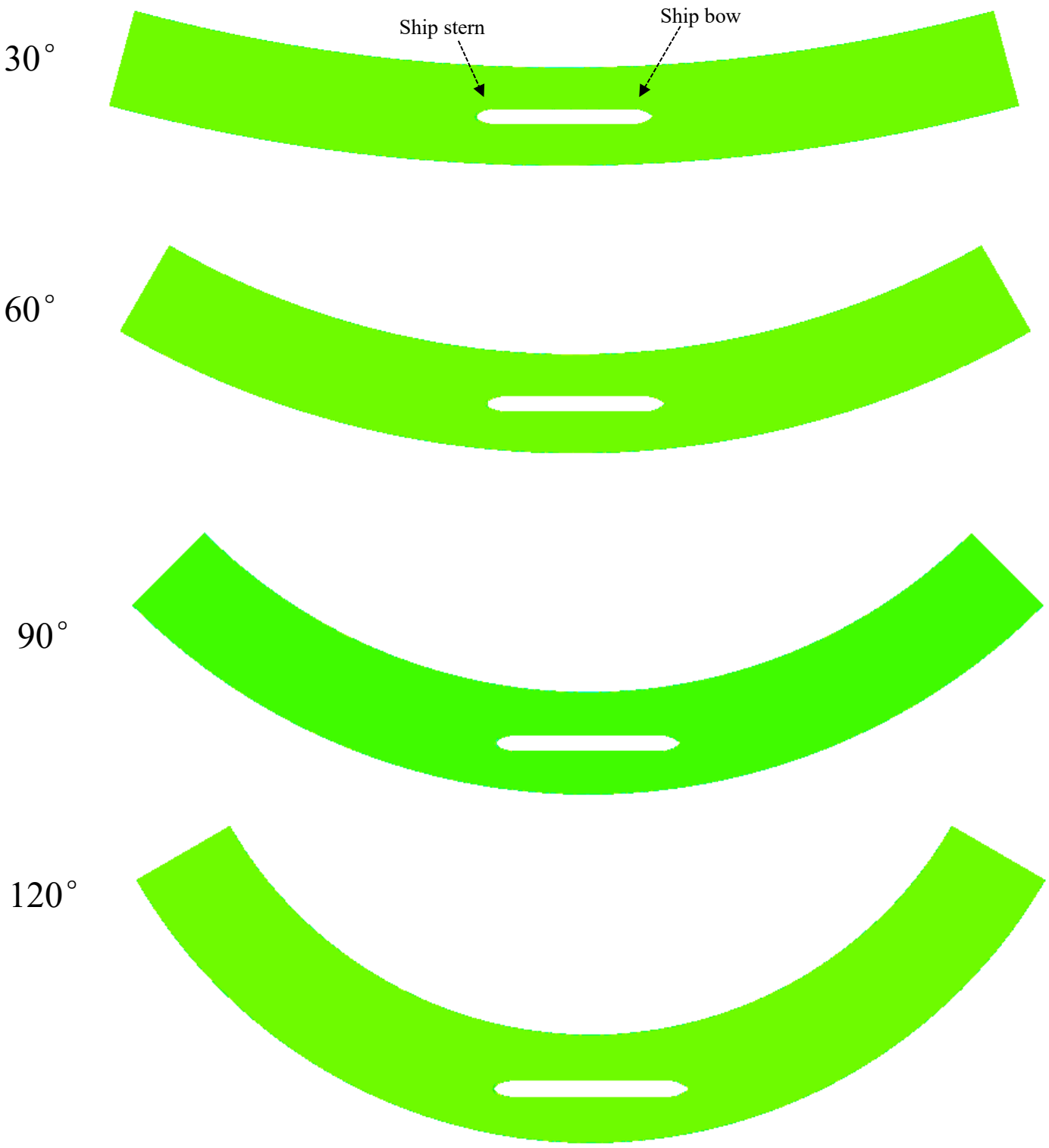

Fig 4. 1 Configurations of the computational domain for different channel angles

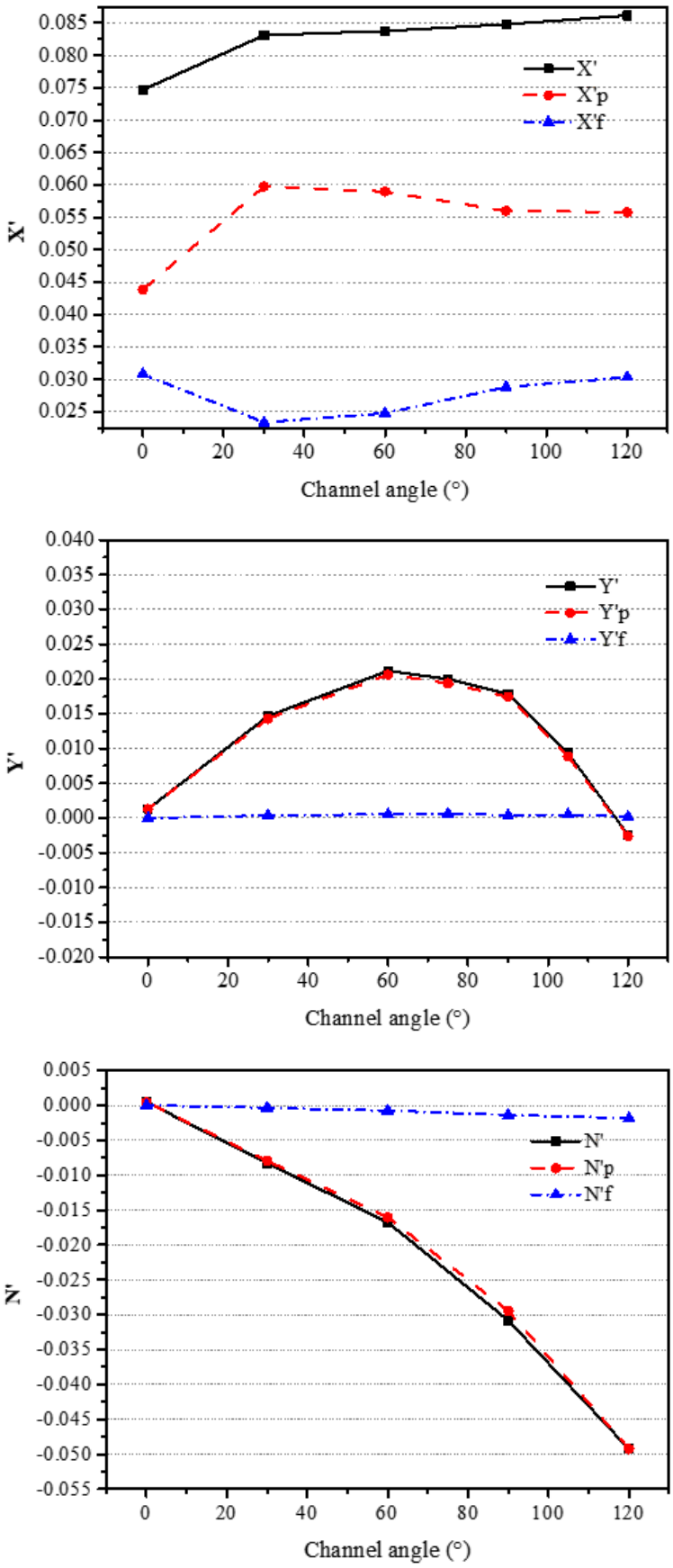

Fig 4. 2 Non-dimensional hydrodynamic forces and moment with pressure and frictional components under different α

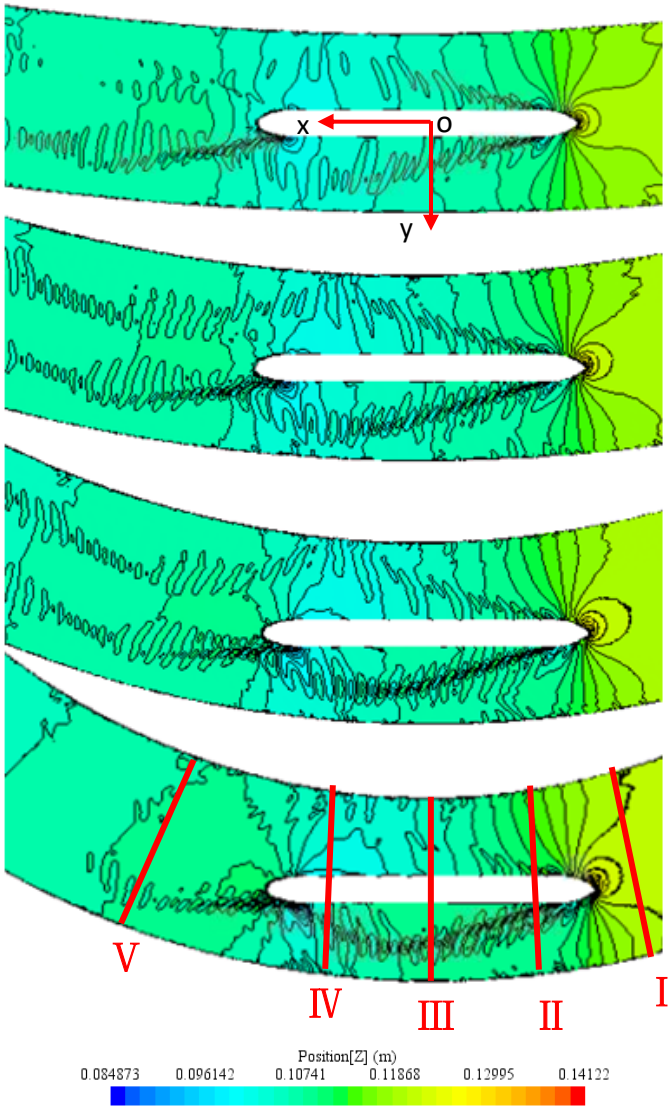

Fig 4. 3 Wave elevation contours in Config. A

(a) to (d): α=30°, 60°, 90°, 120°

(a)

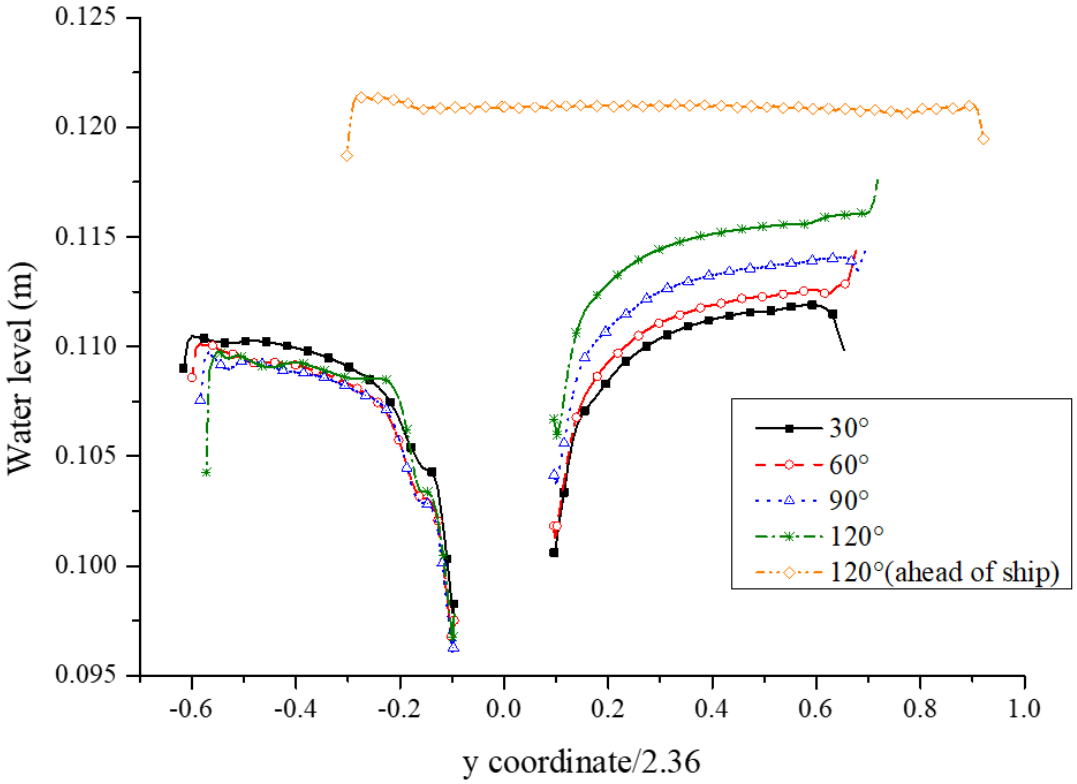
0.125
0.120
0.115
0.110
0.105
0.100
0.095
Water level (m)
-0.6
-0.4
-0.2
0.0
0.2
0.4
0.6
0.8
1.0
y coordinate/2.36
30°
60°
90°
120°
120°(ahead of ship)

(b)

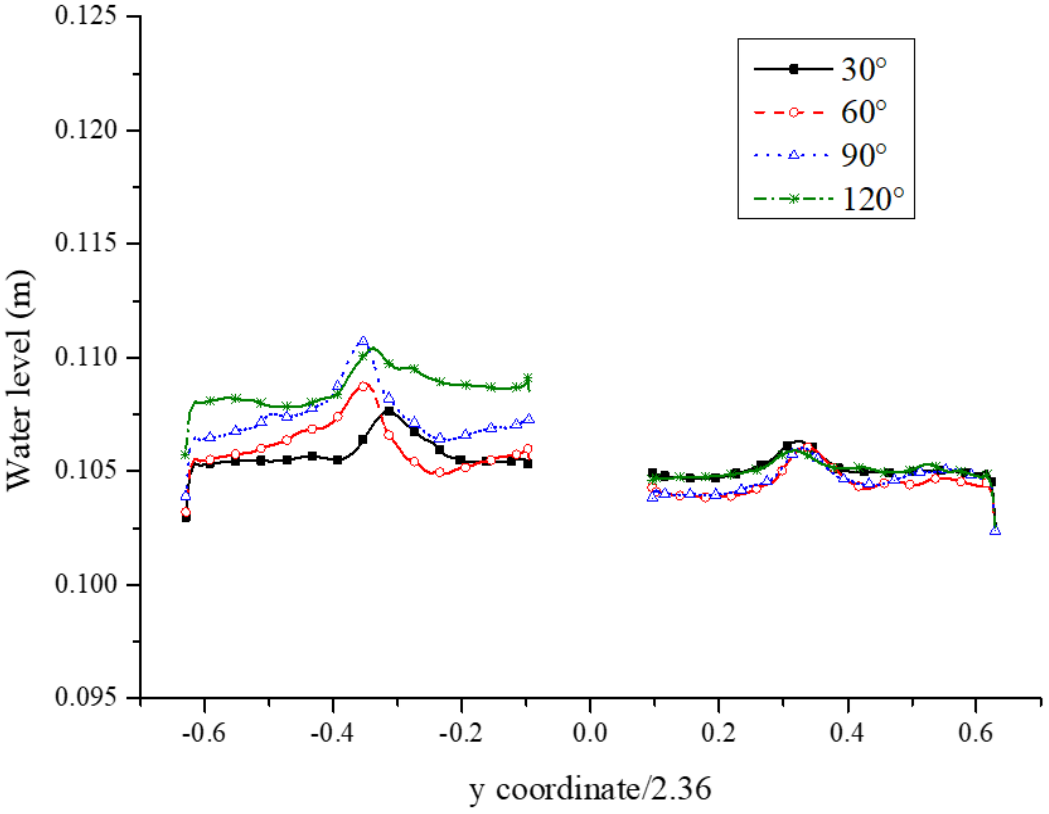
0.125
0.120
0.115
0.110
0.105
0.100
0.095
Water level (m)
-0.6
-0.4
-0.2
0.0
0.2
0.4
0.6
y coordinate/2.36
30°
60°
90°
120°

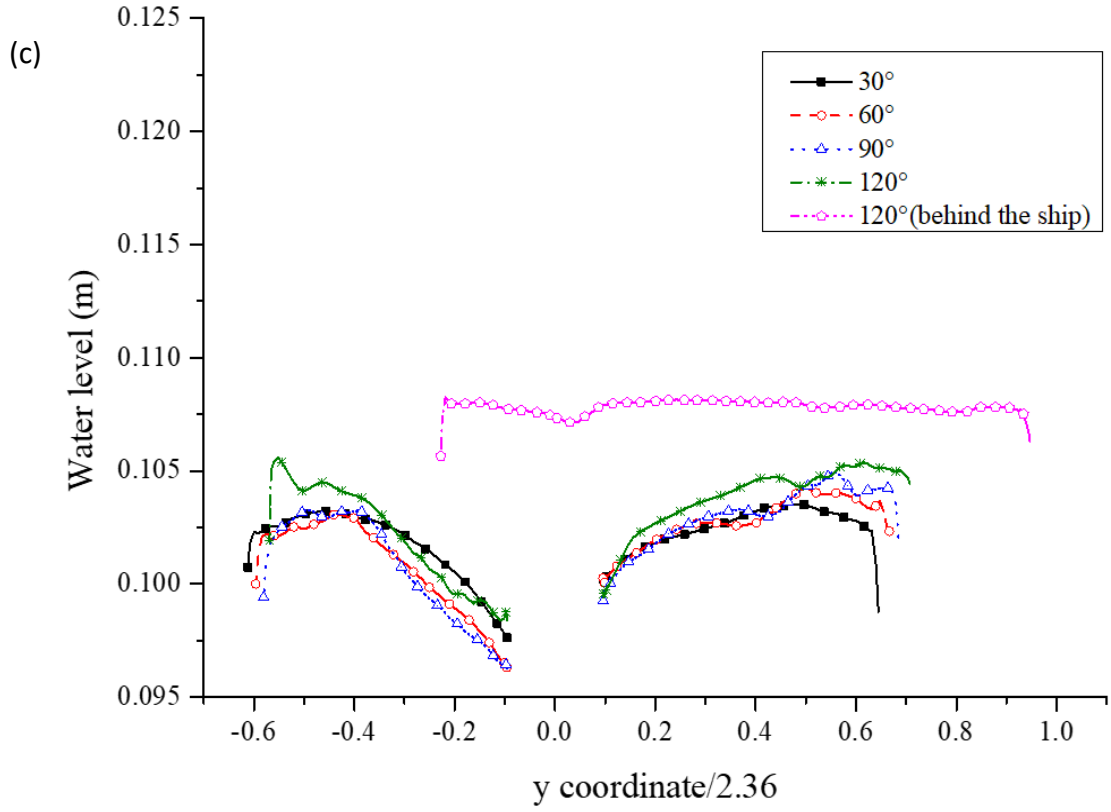

Fig 4. 4 Free surface elevation around the ship hull in Config. A

(a) cross section II (Bow section); (b) cross section III(Middle section); (c) cross section IV (Stern section)

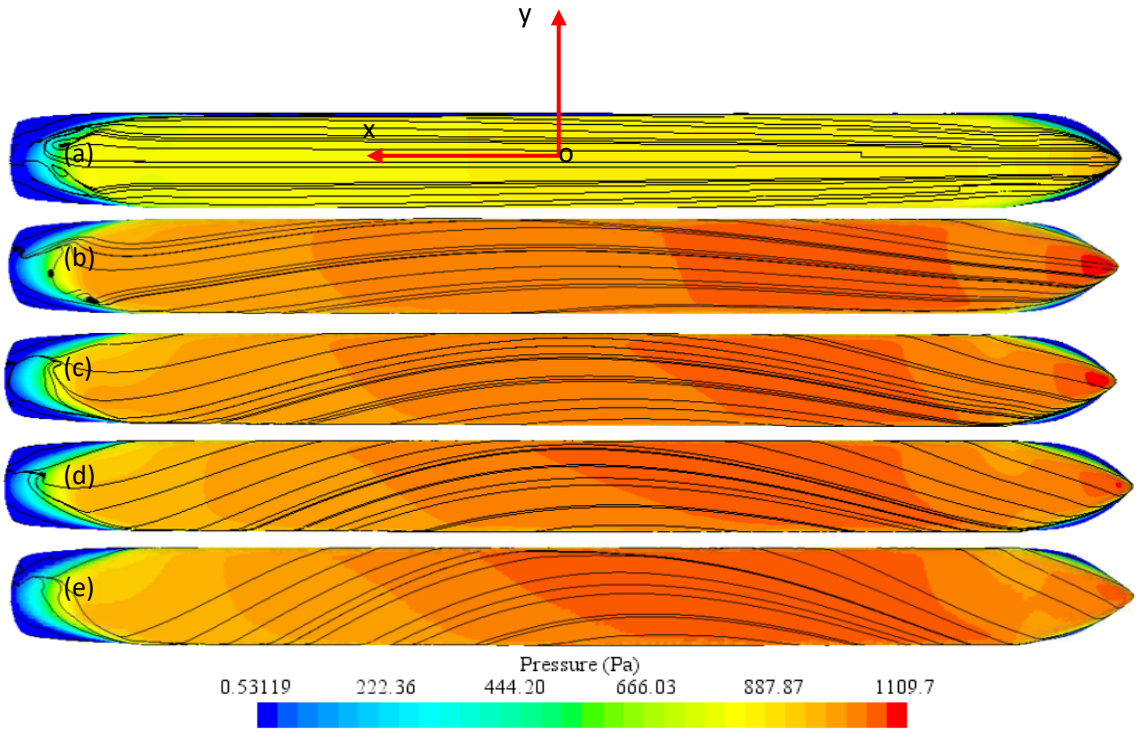

Fig 4. 5 Pressure distribution with streamlines along the ship hull in Config. A

(a) to (e): $\boldsymbol{\alpha}$=0°, 30°, 60°, 90°, 120°

Interesting results were observed for Y'. From Fig 4. 2, it can be noted that the Y' curve takes the form of Gaussian trend, where, an increase of Y' is noted for α less than a critical value of 60°. While Y' will decrease significantly for larger α. A sharp increase in Y' can also be observed in curved channels compared to that in straight channels. Y' increases by a relatively large margin as α grows for α<60° (increasing rate 44.39% for α from 30° to 60°). However, Y' starts diminishing after α exceeds the critical value 60°, and especially declines fast for α>90° (decreasing rate around 75.2%). It should be noted that Y' grows again changing from attractive force towards the concave bank to repulsive force for α>115°, which is under the influence of the large channel curvature. To verify this somewhat complex tendency of the curve, another two configurations (α=75° and α=105°) are added, and their results coincide with this trend. According to Fig 4. 3, wave reflections on convex bank sides are disappearing as α grows. By measurement, the Kelvin angle in curved channels is

about 19°, which is virtually indistinguishable from that in straight channels. From the discussion above, the mainstream will flow near the concave bank under large α. This not only intensifies the interaction between the ship and the concave bank in channels of large α, but also contributes to a higher water level around the concave bank (see Fig 4. 4). Consequently, Y' poses the trend of reversing its direction to the opposite to be attractive for the larger channel angle.

In the following contents, five cross sections are taken as illustrated in Fig 4. 3, and they are named in the following format: cross section I is ahead of ship, cross section II is the bow section, cross section III is the middle section, cross section IV is the stern section, and cross section V is behind the ship.

The water levels in cross sections I (ahead of ship) and V (behind the ship) are always nearly constant for all configurations, so only the two sections in the configuration of α=120° are displayed in Fig 4. 4 (a) and (c) as an example. For comparing easily, the same range is used for the vertical coordinates, while the horizontal coordinates are divided by the channel bottom width (2.36m, which corresponds to 59m width of real channel). As long as the ship navigates in bending zones, the water levels around the concave bank in the bow sections are lower than that around the convex bank, while the water levels around the concave bank in the middle section are higher. This shows the existence of circulation current in bending zones.

Besides, the water level around concave bank is ascending as α grows in the middle section, but the water level around convex bank slightly changes as function of α, which contributes to a difference in water level for larger α. Consequently, the decreasing trend in Y' at higher α will be produced in Fig 4. 2. Meanwhile, the water level around the convex bank in the bow section is also increasing as α grows, but it changes slightly around the concave bank and in the stern section. The higher water level around convex bank in the bow section, coupled with higher water level around

concave bank in the middle section will form an increasingly large torque that causes the fast increase in N'.

N' poses an increasingly rapid growing tendency as α grows. Also, the pressure components dominate in Y' and N' with appropriate frictional components around 0 due to the bow and stern forms effect. Thus, drift caused by N' can easily occur with α increasing. Based on the streamlines that correspond to the pattern associated to the wall shear stress in Fig 4. 5, the mainstream passing through the ship in bending zones behaves as a kind of spiral flow, which is the combination of loop flow and longitudinal flow. From the discussion above, a ship generally has to maneuver closer to the concave bank in order to avoid grounding. While according to the results in this section, the large yaw moment induced by the large curvature of main streamline (strong spiral flow) will make the ship drift further to the concave bank, which easily leads to collision with the bank. This will be more serious in large-curvature channels. This phenomenon is similar to the bank effect in straight channels when the ship is attracted to the bank.

Special attention should be paid when a ship is advancing in channels with large α, and frequent control of rudder angle can be taken to reduce yaw. According to equation (3.1), the larger the channel radius is, the smaller the channel angle is. Thus, the results here coincide with Ai and Gan (2013) that the larger is the curvature radius, the smaller is the chance of an accident, since N' will be very low for small channel angle (large channel radius) based on the results of this thesis.

4.3 Effect of channel bottom width (W) on ship hydrodynamics

The analysis of this section depends on the simulations from Config.B in Table 4. 1, which is committed to presenting the impact brought by W on ship hydrodynamics. Channel bottom width is illustrated in Fig 3. 7. Different channel bottom widths (W/B=4.195, 5.244, 6.293, 7.342, 8.391) that come from real channel data are

researched in this section.

According to Fig 4. 6, X' for α=30° and α=120° decreases almost identically as function of W, indicating little relevance of W variations on X' under different α. As W increases, waves around convex bank are becoming more significant, and X' for both α decreases at a relatively large rate (around 27.5%) for W below a critical value 2.36m (See Fig 4. 6). While X' reduces more slowly with the decreasing rate 18.7% for W>2.36m. The distances between the ship hull and banks are increasing with W enlarging, which reduces the restriction effect of both bank sides on the ship hull and thus lowers the ship resistance. Also, X'_p is more than double as large as X'_f for W below the critical value 2.36m, but maintains nearly twice larger than X'_f after W exceeds this value. Hence, broadening a channel to the critical value can come to a balance between the cost in channel construction and navigational safety. The wave elevation around the ship for both α=30° and α=120° is increasing as W grows(see Fig 4. 7), and consequently the pressure profile around the hull is increasing according to Fig 4. 8. However, the streamlines are affected little by the variations of W.

According to Fig 4. 6, Y' for α=30° decreases slowly pointing towards the concave bank as W grows, and at the same time, N' for α=30° decreases slightly and keeps at low values. However, Y' for α=120° is more sensitive to W. As W increases, Y' diminishes fast with a decreasing rate of 75.2% for W below a critical value (around 2.3m), the direction of which points towards the concave bank due to the very narrow channel. The wave generated by the hull is superimposed on the reflected wave from the bank wall. Water level on port side is higher than that on starboard side for small W according to Fig 4. 7 (f), which exerts a sway force pointing towards concave bank. Ships are prone to shore suction and shore cushion at this time. After that, the direction of Y' will reverse, and Y' continues increasing with W growing until a critical value (around 3.8m).

Meanwhile, N' for α=120° is always 6 to 4 times larger and decreases more

rapidly than that for α=30°. Besides, Y'_p and N'_p dominate all the time for both α. Based on the results discussed in the previous section, a ship sailing in a bending fairway will drift because of yaw moment. Thus, broadening channels is positive to eliminate ships' drift, especially for large-curvature channels, and the desired channel width should be far more than that in straight channels in order to minimize this effect. The results here coincide with the statistical results of accidents from Ai and Gan (2013), the wider is the channel, the safer is navigation in curved channels, since pilots can have more possibility to control their ships in wide channels, and consequently relative accident is lower with channel width increasing. Based on this work, except for a reversal of direction in Y' for large-curvature channels (α=120°), X', Y' and N' acting on the ship in wider curved channels will also stay around a relatively lower value compared with that in narrow channels under the same α.

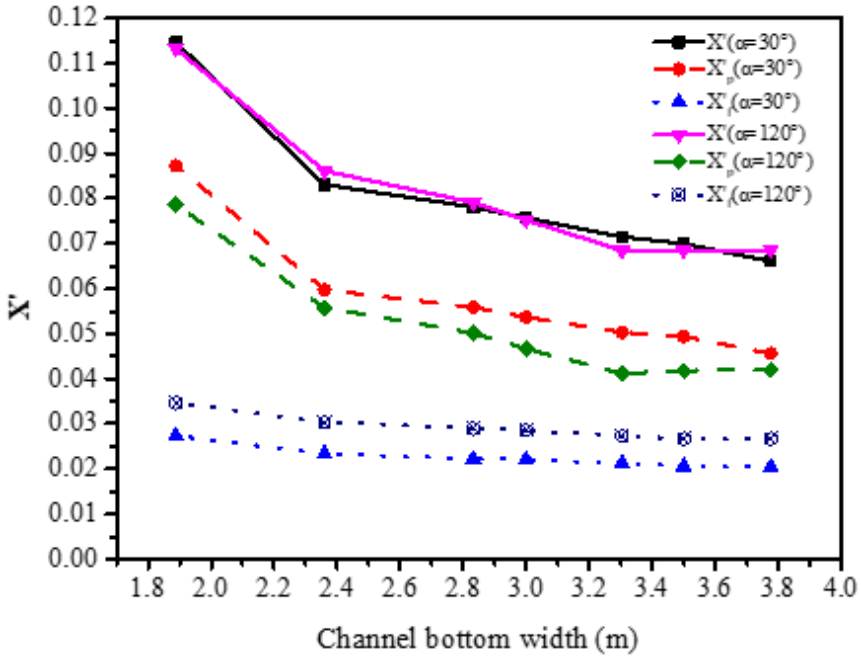

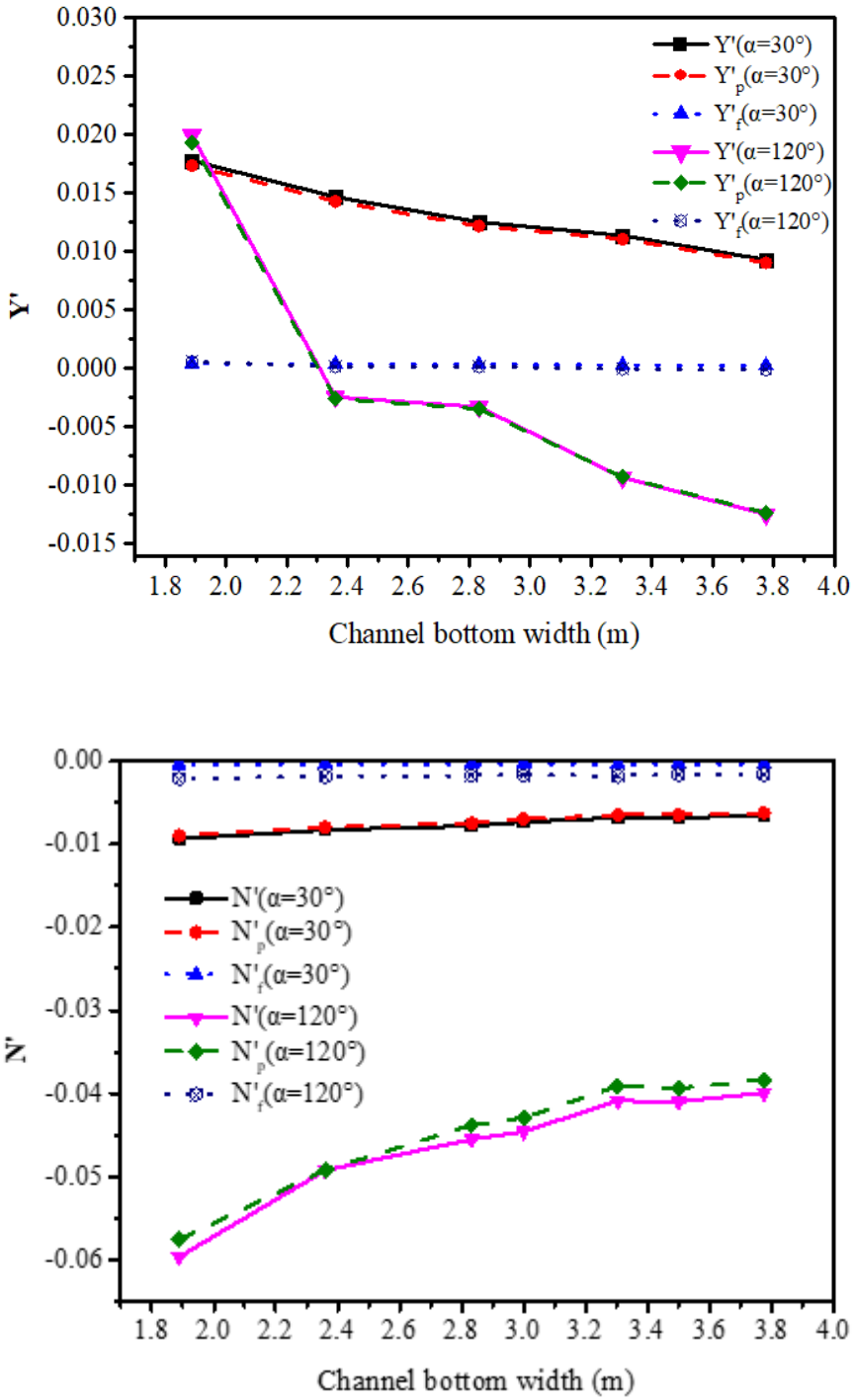

Fig 4. 6 Non-dimensional hydrodynamic forces and moment of the ship under different *W*

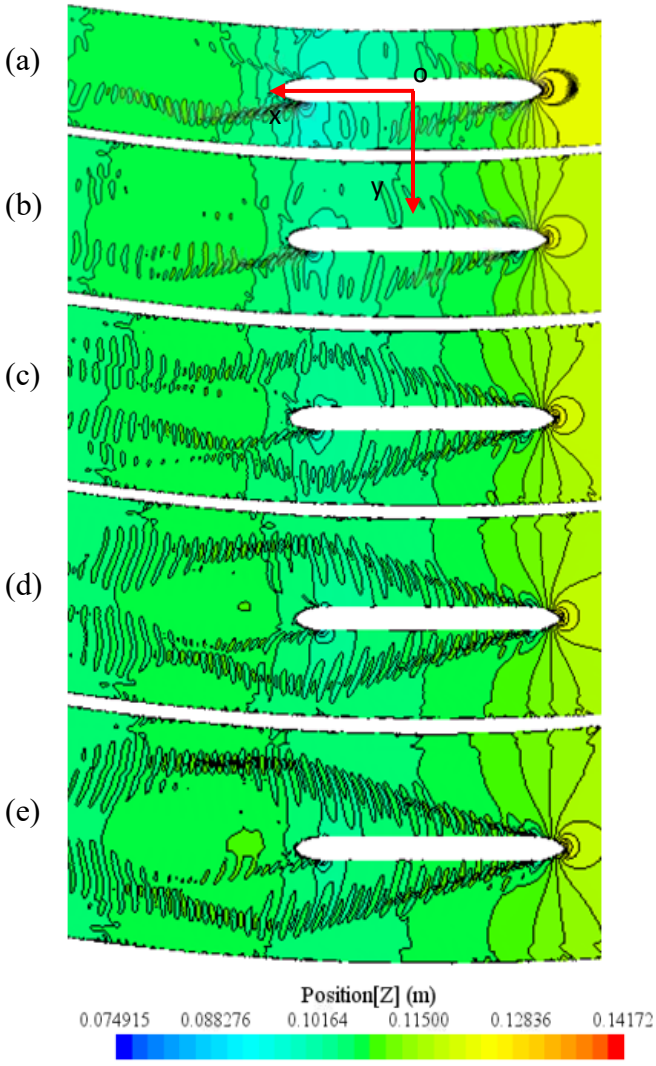
(a)
(b)
(c)
(d)
(e)
O
x
y
Position[Z] (m)
0.074915
0.088276
0.10164
0.11500
0.12836
0.14172

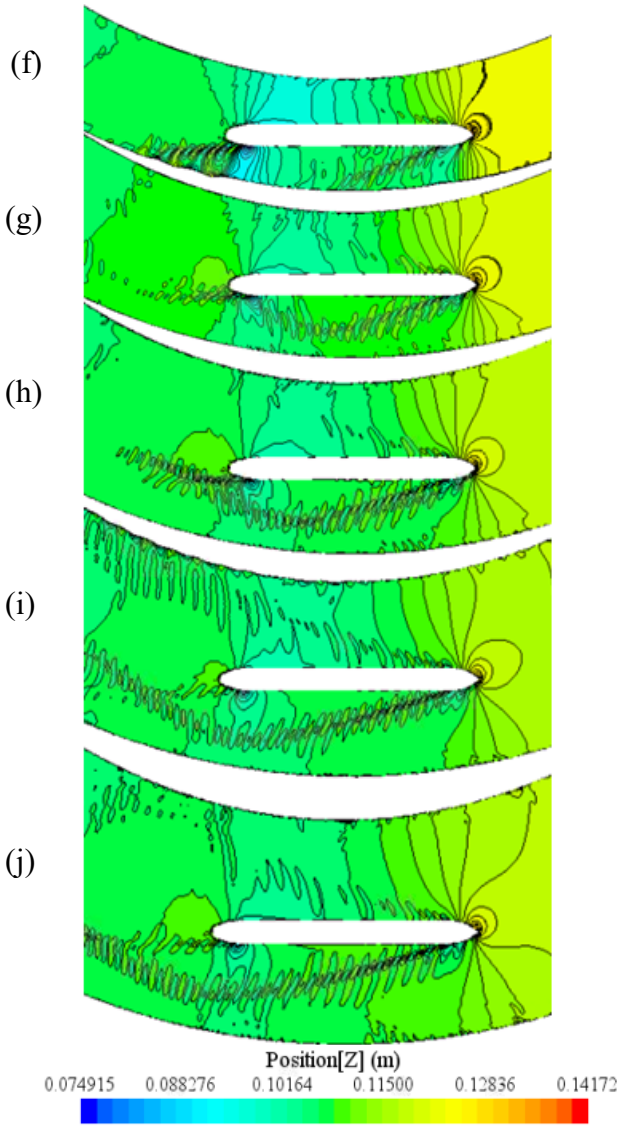

Fig 4. 7 Wave elevation contours of the configurations in Config. B

(a) to (e): W=1.888m, 2.36m, 2.832m, 3.304m, 3.776m for α=30°

(f) to (j): W=1.888m, 2.36m, 2.832m, 3.304m, 3.776m for α=120°

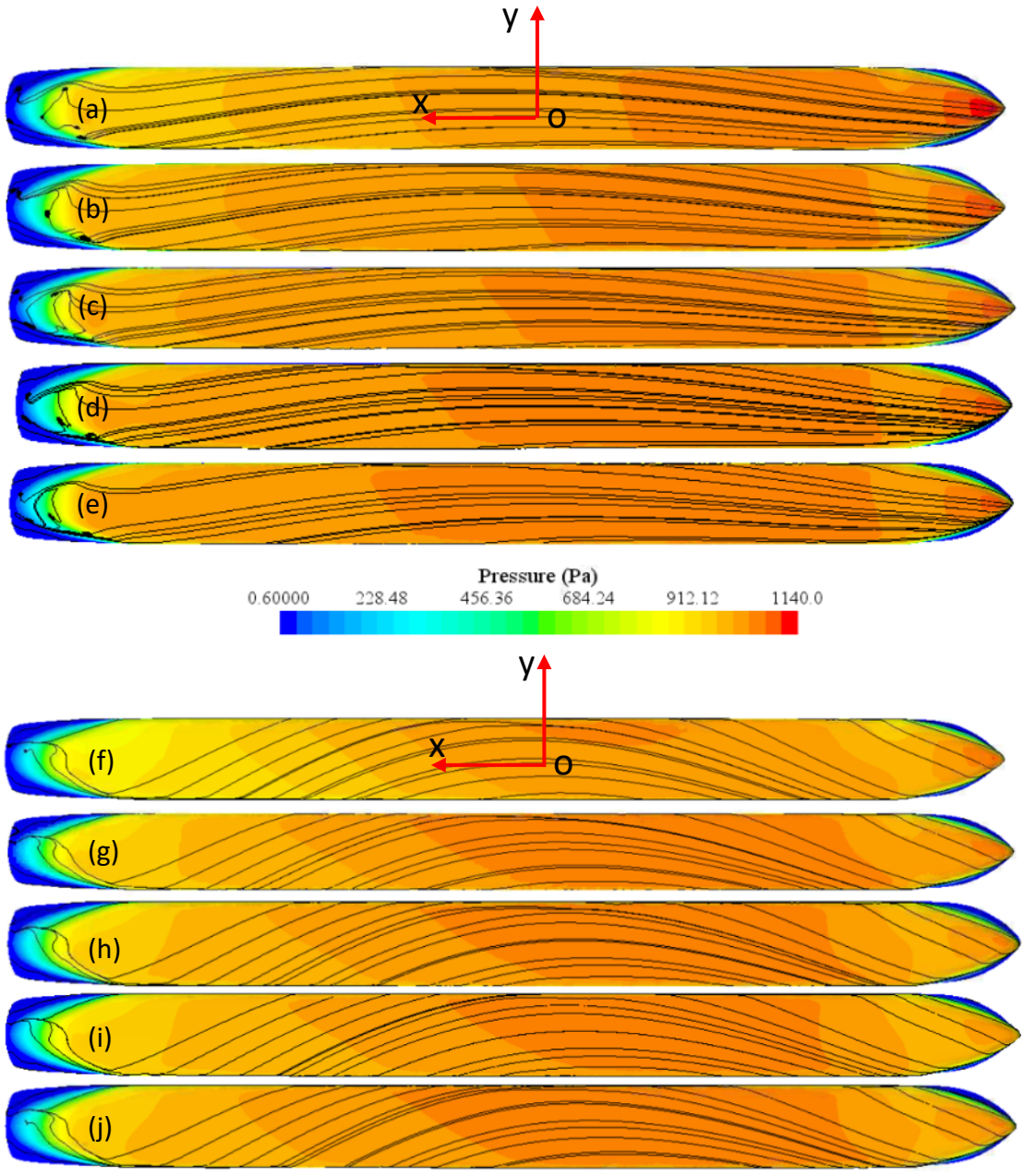

Fig 4. 8 Pressure distribution with streamlines around the ship hull in Config. B

(a) to (e): W= 1.888m, 2.36m, 2.832m, 3.304m, 3.776m for α=30°

(f) to (j): W= 1.888m, 2.36m, 2.832m, 3.304m, 3.776m for α=120°

4.4 Effect of channel slope angle (γ) on ship hydrodynamics

This section analyzes the effect brought by channel slope angle (γ) on ship hydrodynamics, which is based on the simulations from Config. C in Table 4. 1. The channel bottom width (W) is constant during this process. Channel slope angle γ is illustrated in Fig 3. 7.

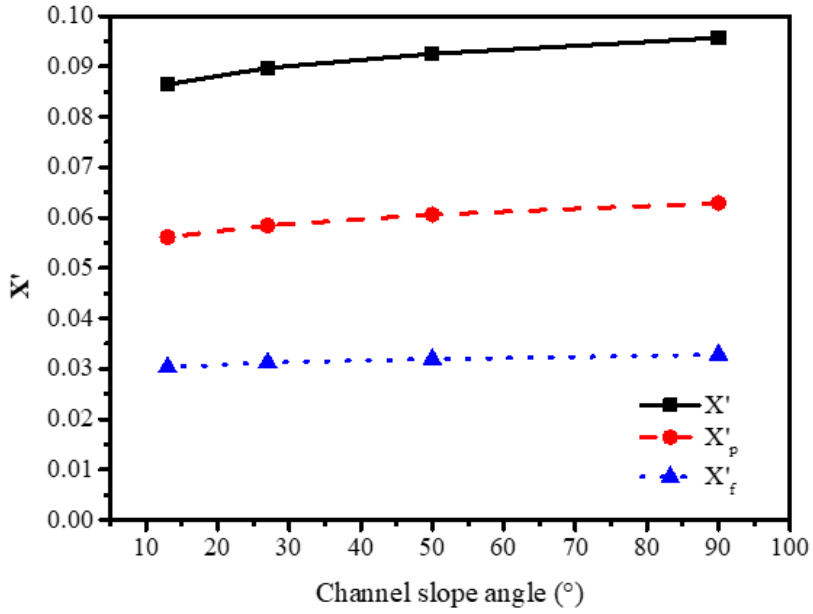

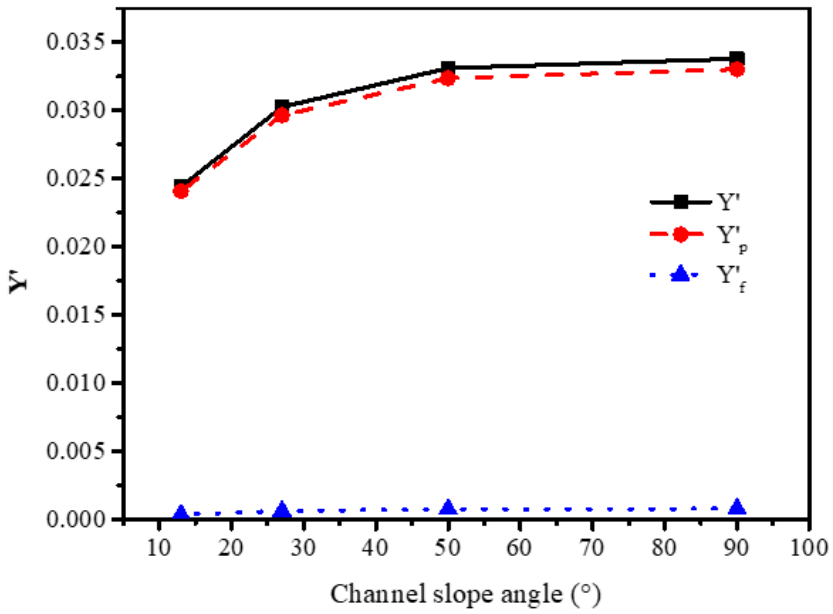

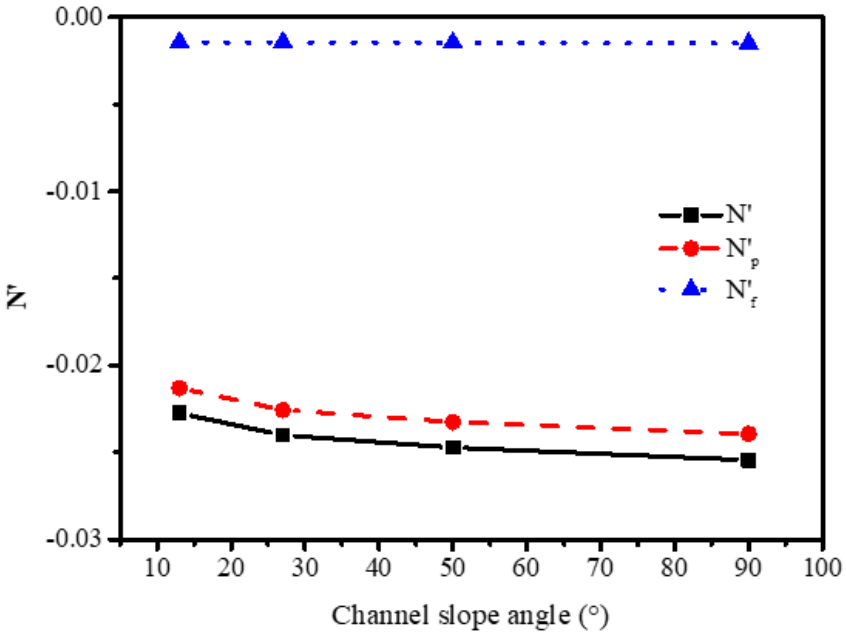

Fig 4. 9 Non-dimensional results of channel slope angle on ship hydrodynamics

According to Fig 4. 9, X' slightly increases as γ grows, and X'_p is around twice as large as X'_f. Ship waves are more generated as γ grows, the change of which is particularly noticeable for β<27º (see Fig 4. 10 (a) to (b)), which contributes to the increase in X'_p. Meanwhile, the wave elevation is decreasing during this procedure, and consequently the pressure around the ship is descending (see Fig 4. 11). Trim by stern will occur more easily for small slope angles. Also, we can observe that the pressure is more important on the starboard side, which conduces to the ship roll. However, the streamlines are hardly affected as function of γ.

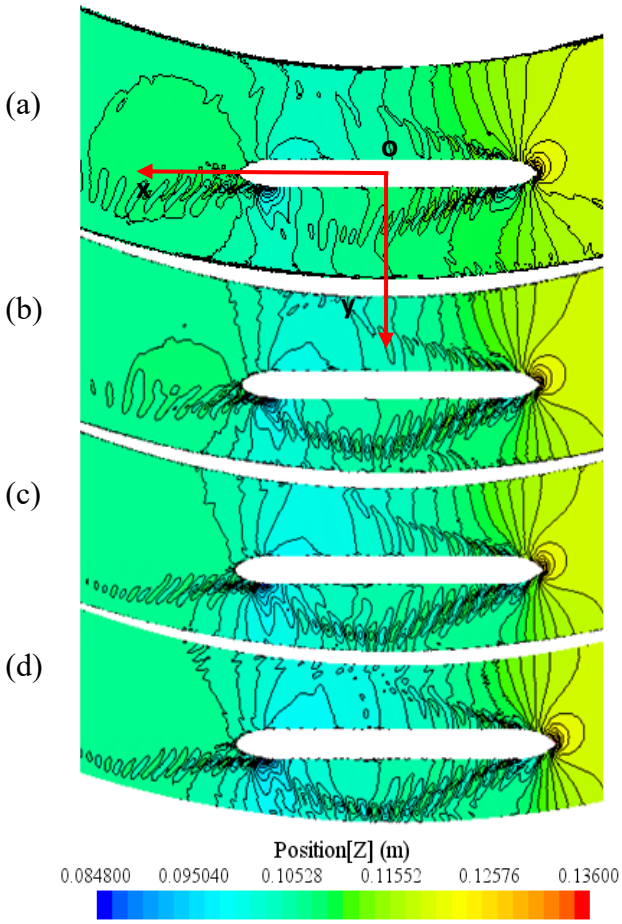

Fig 4. 10 Free surface elevation contours of slope angle variation

(a) to (d): slope angle is 13º, 27º, 50º, 90º respectively

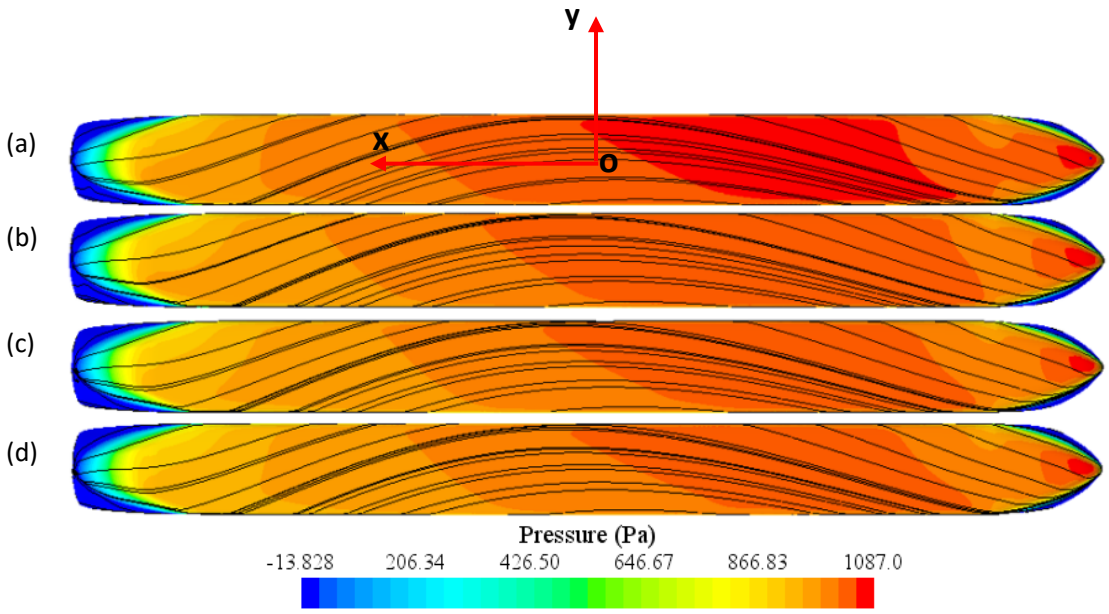

Fig 4. 11 Pressure contours with streamlines of slope angle variation

(a) to (d): slope angle is 13º, 27º, 50º, 90º respectively

There exists a critical value for the effect of γ (50º in this work) on Y' and N'. Y' increases by a comparatively large extent (increasing rate 23.95%) for γ<27º. Its direction points towards the concave bank, which can be noticed from the flowing direction of streamlines. While this growing rate slows down after γ exceeds 27º, especially negligible change can be observed in Y' for γ>50º (increasing rate 2.1%). For γ>27º, the wave profile becomes serious and nearly doesn't vary as function of γ. Bow waves around the concave bank will be backed up by the bank to act on the ship hull, applying a force towards the convex bank. This diminishes the force growth. On the other hand, the restraining effect of bank on ships is strengthening as γ grows, but this effect has gradually come to a limit after γ exceeds a critical value 50º. Y'_p dominates all the time with Y'_f around 0, which is caused by bow and stern effect. As γ grows, N' increases marginally with an increasing rate only 5.56% for γ<27º, but a similar phenomenon occurs with N' that the growing rate in N' is decreasing. Especially for γ>50º, N' hardly increases. N'_p dominates during this process.

4.5 Conclusion remarks

Concerning the very low values of frictional components in Y' and N', a new series of simulations were performed using a different methodology (overset mesh method) and very refined mesh (about 10million of elements). The goal is to confirm the component values for the two different approaches. One method (overset mesh method) is based on relative fluid flow due to moving domain capabilities; the other method is with a fixed ship in a moving domain. The results obtained from overset mesh method show that the frictional components in Y' and N' remain very small, and there are no differences in the results between the two methods except due to mesh considerations. In author's viewpoints, this behavior is due to the fact that, we suppose that the ship is navigating in calm water (no current is considered). However, the overset mesh method is not suitable for this case, because the ship approaches the inlet

boundary and compromises the minimum distance between both we have to keep. Hence, the frame motion technique is used to simulate the ship motion. This technique suppose that all meshes are moving with an opposite ship speed.

From the previous sensitivity analysis, we can make the following conclusions and recommendations:

(1) As α increases, X' of the ship grows very little. There exist a critical value of α for Y', and a fast downward trend of Y' can be observed after α exceeds this value. While N' grows at a rapid rate as α grows, which easily causes the ship to yaw.

The elevated pressure distributed around the hull can also be observed with α increasing due to the larger curvature of streamlines, especially for pressure at bow. Thus, the increasing tendency of trim by stern can be assumed in a channel of larger α. Besides, for larger α, the interaction between the ship and the concave bank is more serious, while it's much weaker with the convex bank.

(2) Channel bottom width has nearly the same effect on resistance force in curved channels with any channel angle. As W increases, X' reduces relatively fast below a critical W, while it reduces increasingly slowly beyond this critical width. Y' in small-curvature channels reduces slowly as W increases. While Y' is sensitive in large-curvature channels as function of W, since there exists a critical width, exceeding which sway force will increasingly rise rapidly in opposite side. This probably triggers controllability losing for a pilot. N' large-curvature channels decreases more obviously, and is always much higher than that in small-curvature channels.Besides, an upward trend can be found in the pressure distributed around the hull with channel bottom width increasing, but streamlines are slightly affected.

(3) Channel slope angle (γ) only affects ship hydrodynamics much at small angles, and X', Y', N' increase as the bank gets steeper. The changes in X', Y', N' all seem more obvious when γ is lower than a critical value (50 degrees). After that, the

restraining effect of γ comes to a limit so that ship hydrodynamics will hardly be influenced by the variance of it.

Chapter 5

5. Effect of ship behaviors and geometry on ship hydrodynamics

This section concerns about the bending effect on ship hydrodynamics under variation of ship geometry and behaviors, so some key parameters are researched, that is, h/T ratio, ship speed (V_s), drift angle (β) and ship type.

5.1 Simulation case settings

All the cases are deemed in restricted curved channels, and the details of four different configuration groups (Config. D to G) are illustrated in Table 5. 1. Config. D is employed to evaluate the effect of h/T ratio on ship hydrodynamics, where a series of h/T ratio variations are the parameters to be researched, meanwhile different channel angles (α) are considered to concern about the effect brought by h/T ratio under different channel curvatures. While the other conditions are kept both constant and severe. Similarly, the other configuration groups namely Config. E, Config. F, and Config. G are set in the same way.

Table 5. 1 Simulation configurations for effect of ship behavior and geometry

	Config. D	Config. E	Config. F	Config. G
	h/T variation	Ship speed variation	Drift angle variation	Ship type variation
Total simulation case quantity	9	20	4	6
Channel angle, α / °	0, 30, 120	30, 90, 120	30, 120	87.34
h/T	1.2, 1.5, 2.0, 3.0	1.2, 2.0	1.2	1.2

Ship speed, $V_s/m\ s^{-1}$	0.6173	0.205, 0.4115, 0.6173, 0.823	0.6173	0.6173
Channel bottom width, W/m	2.36	2.36	2.36	2.36
drift angle, β / °	0	0	0, 4, 9	0
Bank slope, γ / °	27	27	27	27
Ship length, L_{pp}/m	5.4	5.4	5.4	1.54, 2.68, 3.6, 4.4, 5.4, 7.2
Ship beam, B/m	0.45	0.45	0.45	0.202, 0.328, 0.38, 0.45, 0.45, 0.45

5.2 Effect of *h/T* ratio on ship hydrodynamics

Section 5.2 elaborates the effect of *h/T* ratio on ship hydrodynamics, whose consequences come from the simulations of Config. D in Table 5. 1. In this thesis, it's defined: *h/T*=1.2 very shallow waters, *h/T*=1.5 shallow waters, *h/T*=2.0 medium-deep waters, *h/T*=3.0 deep waters.

As is shown in Fig 5. 1, X' decreases rapidly for both α=30° and α=120° with *h/T* increasing, especially in shallow waters. Whereas for *h/T*>2 (medium-deep and deep waters), the decreasing trend slows down for channels of both α. At the same time, there is not much difference in X' between the two curves of large and small α as function of *h/T*, but X' in curved channels is always much larger than that in straight channels. Given that the two configurations (α=30° and α=120°) share a similar pattern of change in component variations, the component variation for α=30° is taken as example in Fig 5. 2, where X'_p and X'_f are also decreasing as *h/T* grows. When *h/T* is above 1.3 or so, X'_f gradually becomes dominated. According to Fig 5. 3, generated waves around the ship hull are less serious and the wave elevation is reduced as *h/T* increases.

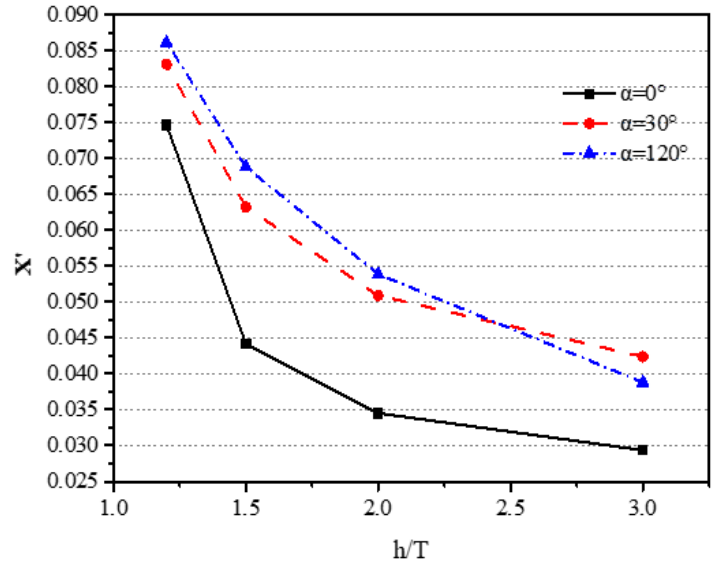

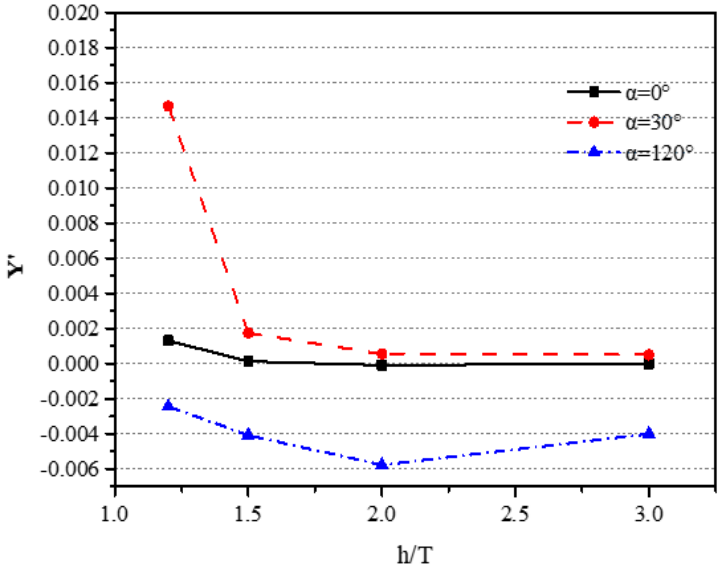

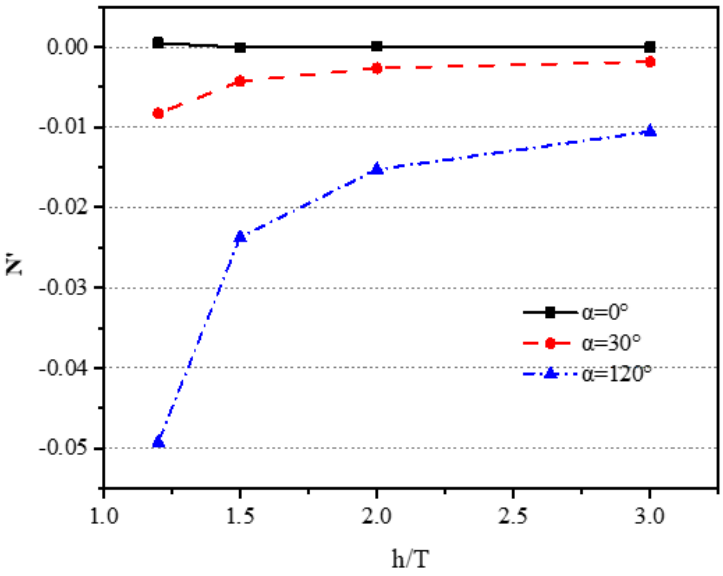

Fig 5. 1 Non-dimensional hydrodynamic forces and moment of the ship under different *h/T* ratios

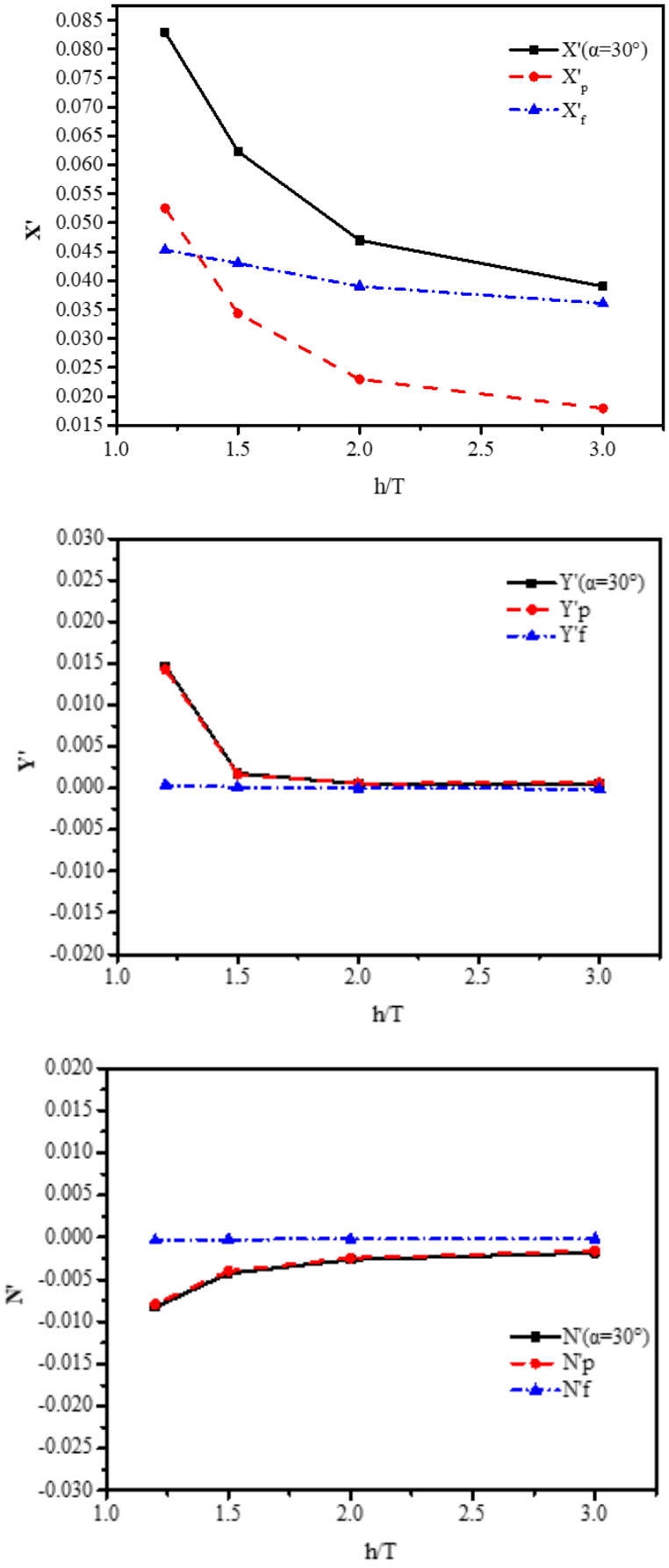

Fig 5. 2 Pressure and frictional components for α=30° in Config. D

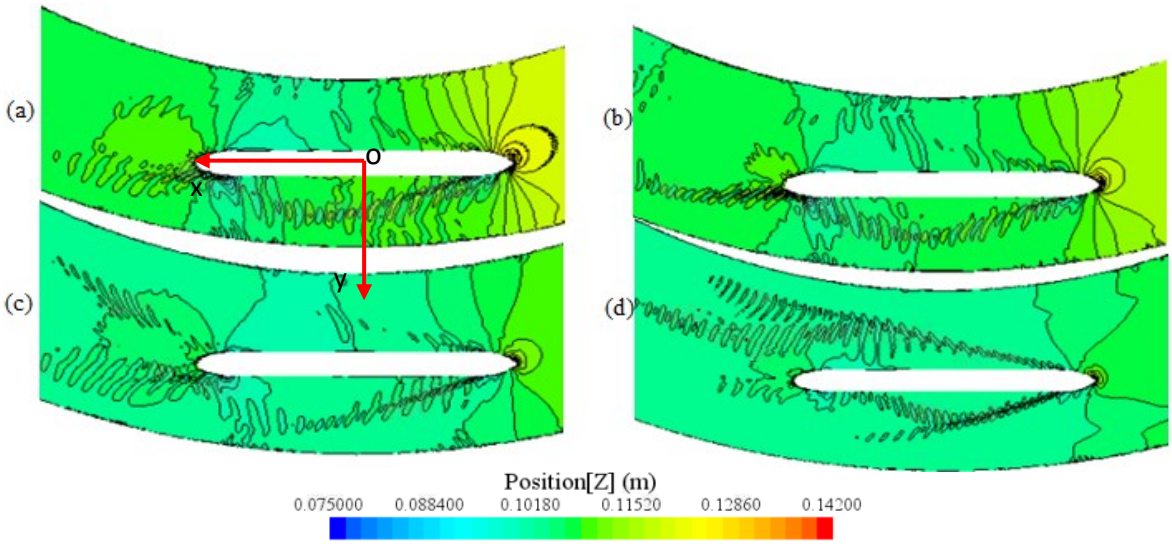

Fig 5. 3 Wave elevation contours of $\boldsymbol{\alpha}$=120° in Config. D

(a) to (d): *h/T*= 1.2, 1.5, 2.0, 3.0

A relatively large decline in Y' (decreasing rate 88.06%) in the channel of α=30° can be observed for *h/T* <1.5 (shallow waters), which declares the high sensitivity of Y' to *h/T* in shallow waters of the small-curvature channel. After *h/T* exceeds 1.5, Y' decreases slightly. While no large change can be noticed in the channel α=120°, which shows the influence of *h/T* is insensitive in the large-curvature channel. The direction of Y' is also opposite for channels with large (α=120°) and small (α=30°) α, and Y' for α=120° is normally slightly larger than that for α=30° apart from in the restricted waters (*h/T*<1.5).

For both α=120° and α=30°, N' decreases faster in shallow waters compared with that in deep waters as *h/T* increases. N' in the channel of α=120° diminishes fast, especially a reducing rate of 52.3% can be observed for *h/T*< 1.5 (shallow waters) as *h/T* grows. While N' in the channel of α=30° doesn't change much, except for the slightly noticeable variation for *h/T*< 1.5. However, Y' and N' change slightly as function of *h/T* ratio in straight channels. Also, Y'_p and N'_p dominate in Y' and N' with

their respective frictional components approaching 0, which is due to the bow and stern forms effect (see Fig 5. 2). According to the analysis above, the results here are broadly consistent with the statistical results from Ai and Gan (2013), that is, maritime accidents will increase apparently for *h/T* between 1.1 and 1.2, and this risk will diminish fast for *h/T* more than 1.3.

Similar results are observed as it is in the previous section. The smaller the *h/T* ratio, the higher the water level around the ship, which is obviously in bow and middle sections (see Fig 5. 4). This indicates that the ship will still squat in shallow waters, as it would in straight channels. However, the pressure around the hull is increasing during the process, so we can't confirm whether the ship will sink under such circumstances. Also, the water level difference between concave bank and convex bank is more pronounced with *h/T* reducing.

However, based on Fig 5. 5, pressure around the ship is increasing with *h/T* reducing in curved channels, no matter how large the channel angle is. Thus, the trend in pressure around the ship in restricted curved channels is different from our previous knowledge about the shallow water effect, that is, pressure drop can be observed in straight channels as *h/T* reduces (See Fig 5. 5 (i) to (l)). Also, the pressure distributed around the ship for α=120° is always higher than that for α=30°.

Under the same α (the same channel curvature), the curvature of streamline is stronger for lower *h/T* ratios, which signifies that stronger circulation current exists in the bending zone of such conditions, and this strengthens the pressure field around the hull. Under different α, the conclusion is the same as what's derived from Section 4.2, that is, pressure around the hull and curvature of streamlines are larger for greater α at the same *h/T* ratio. However, attention should be paid here that pressure and spiral flow are both stronger even in deep waters for large α. Hence, this brings more risk of trim by stern and yaw for the ship.

(a)

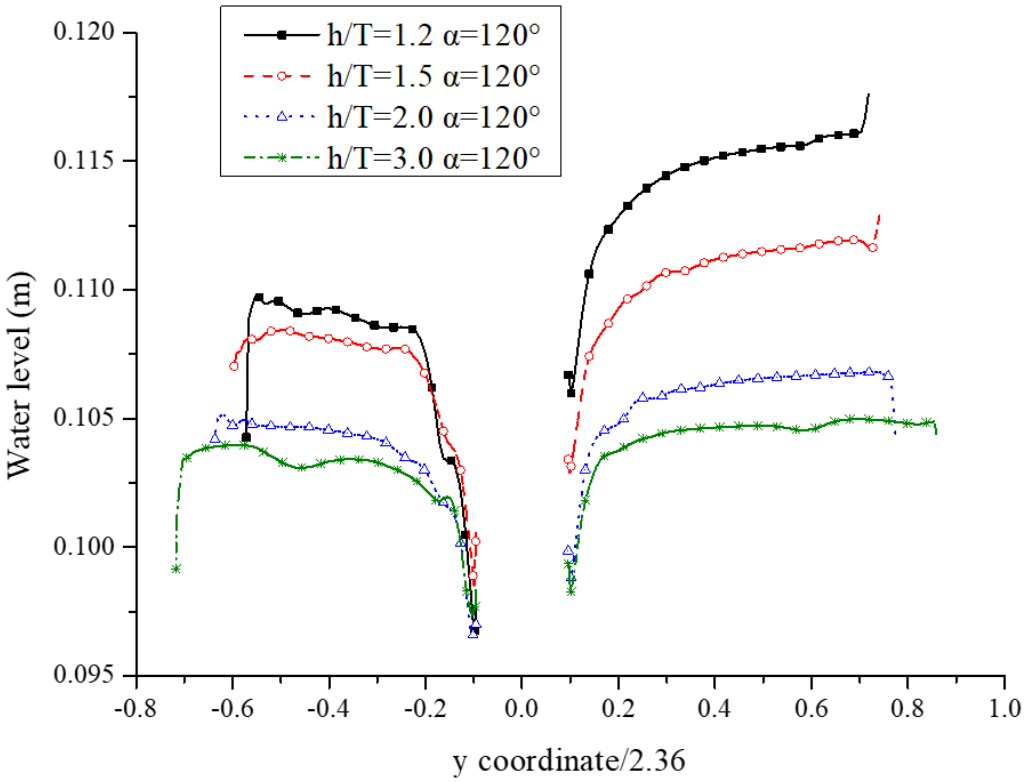
h/T=1.2 α=120°
h/T=1.5 α=120°
h/T=2.0 α=120°
h/T=3.0 α=120°
Water level (m)
0.120
0.115
0.110
0.105
0.100
0.095
-0.8
-0.6
-0.4
-0.2
0.0
0.2
0.4
0.6
0.8
1.0
y coordinate/2.36

(b)

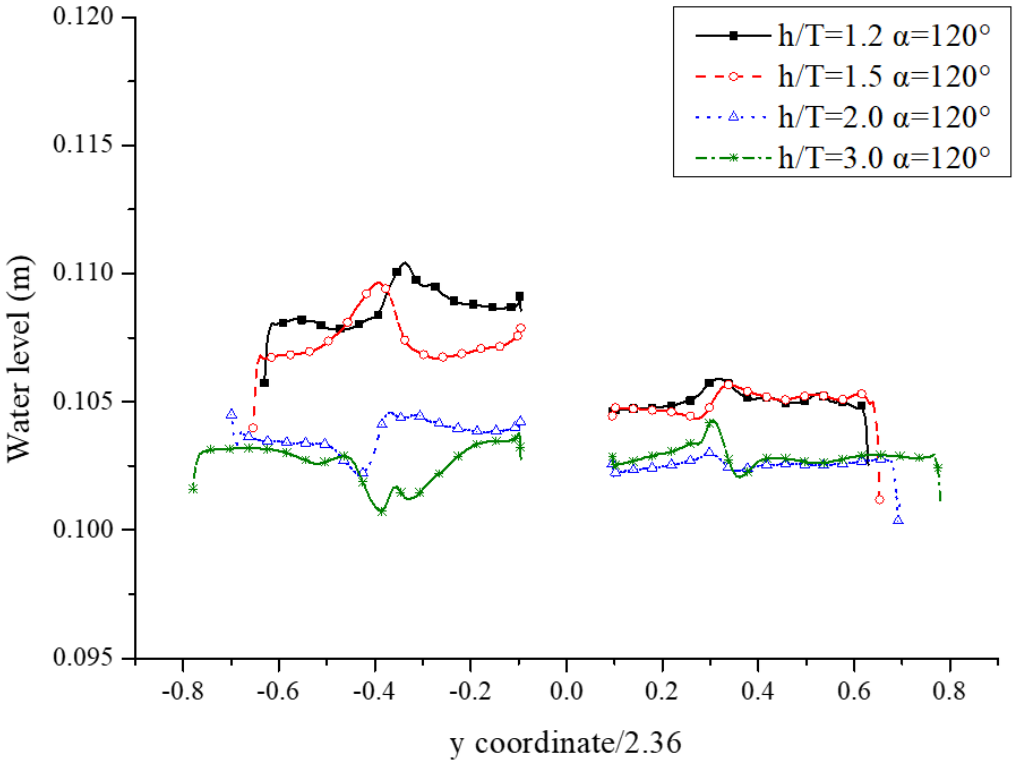
h/T=1.2 α=120°
h/T=1.5 α=120°
h/T=2.0 α=120°
h/T=3.0 α=120°
Water level (m)
0.120
0.115
0.110
0.105
0.100
0.095
-0.8
-0.6
-0.4
-0.2
0.0
0.2
0.4
0.6
0.8
y coordinate/2.36

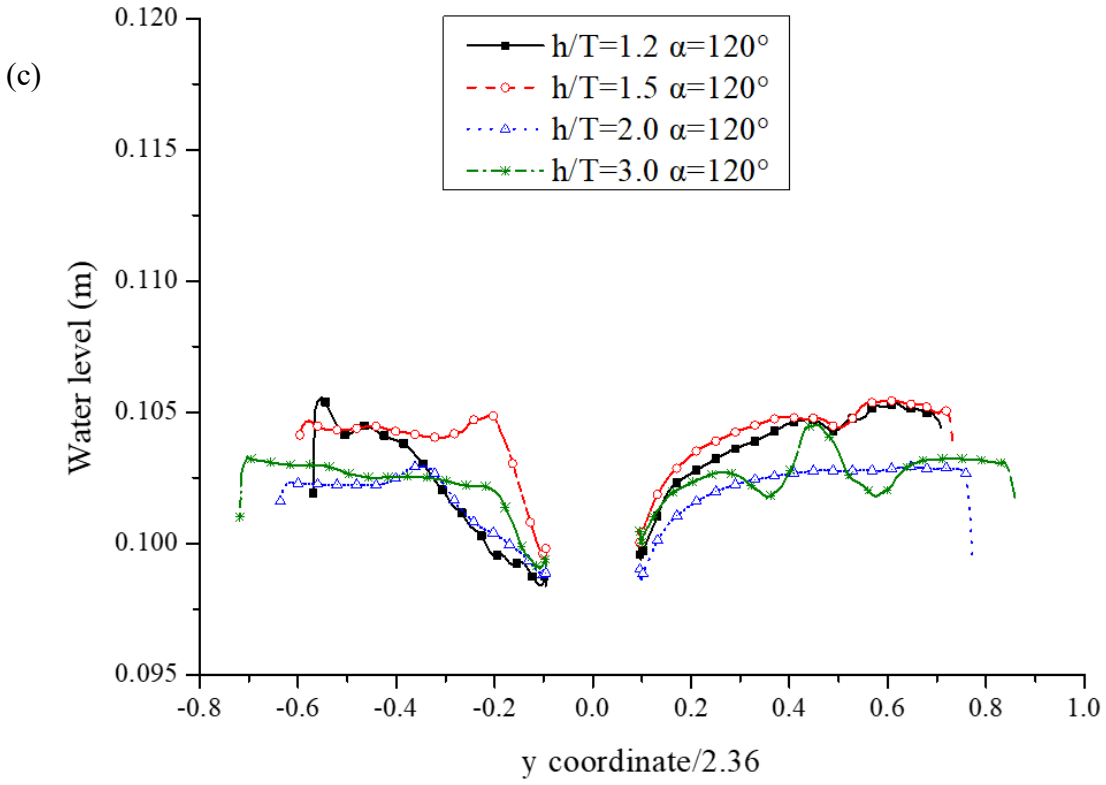

Fig 5. 4 Free surface elevation around the ship hull in Config. D

(a) cross section II (Bow section); (b) cross section III (Middle section); (c) cross section IV(Stern section)

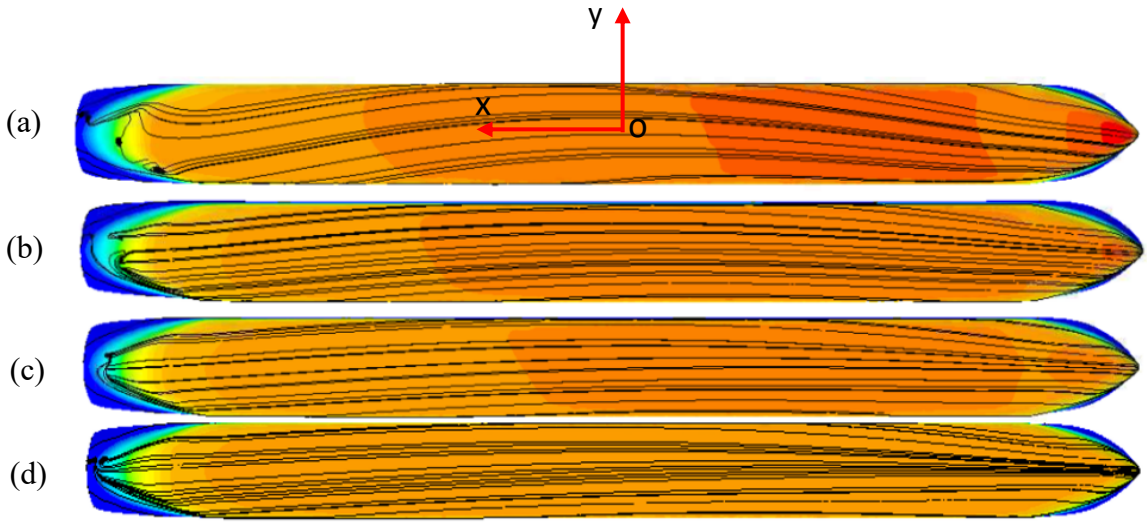

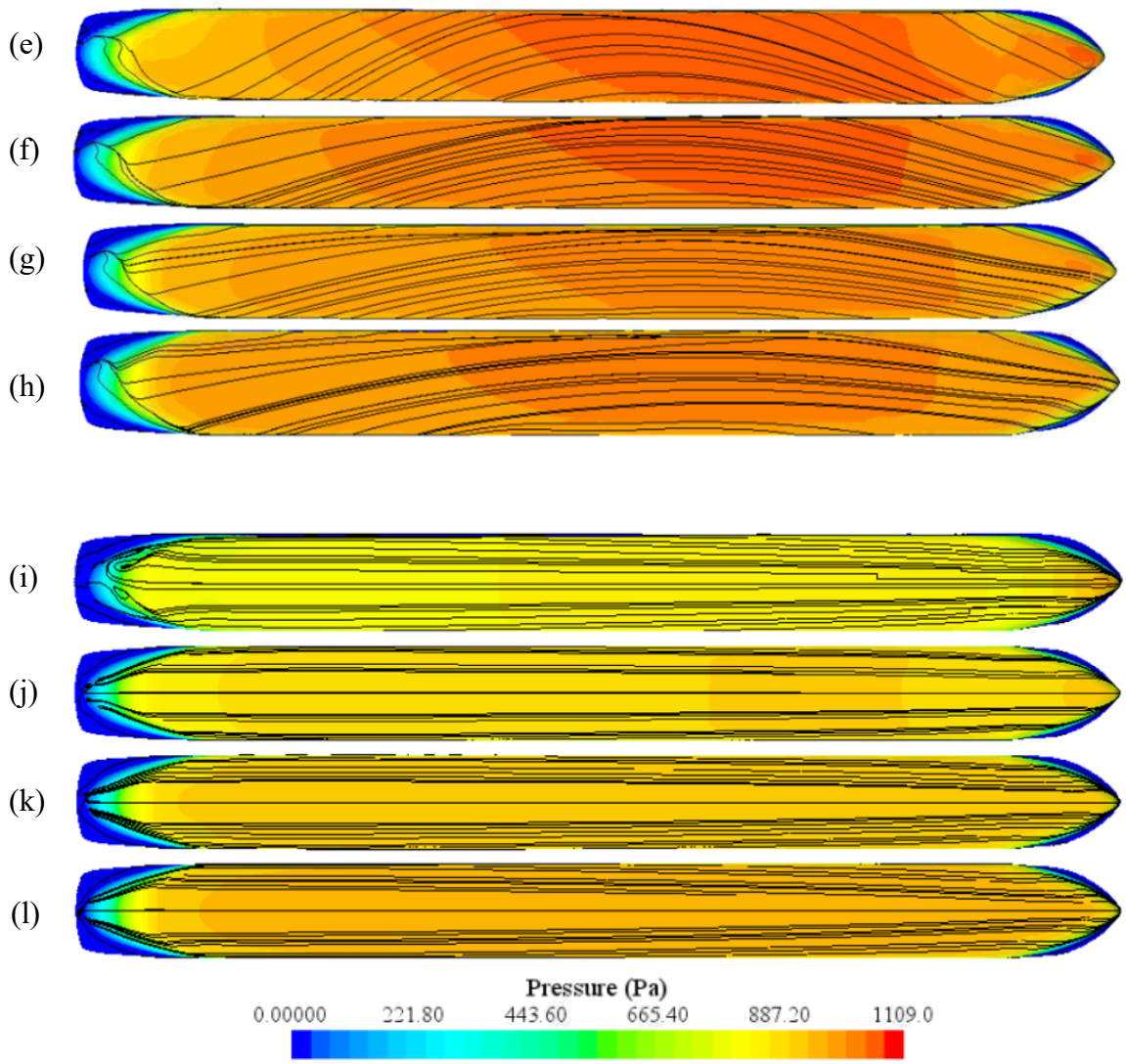

Fig 5. 5 Pressure distribution with streamlines along the ship hull in Config. D

(a) to (d): h/T= 1.2, 1.5, 2.0, 3.0 for α=30° (e) to (h): h/T= 1.2, 1.5, 2.0, 3.0 for α=120°

(i) to (l): h/T= 1.2, 1.5, 2.0, 3.0 for α=0°

Table 5. 2 shows the change of center of load of the ship hull with h/T increasing for the configuration $\boldsymbol{\alpha}$=120°, h/T=1.2. The center of load identifies a location where the resultant moment from the fluid flow acting on the ship hull is zero or as small as possible, or the fluid loads acting on the ship hull at the center of load represent as closely as possible a pure force acting through such a point. The G coordinate refer to x, y, and z coordinates of the center of load of the ship hull.

$\mathbf{G}$ is center of load, $\mathbf{F}$ is resultant force, $\mathbf{M_p}$ is resultant moment, $\mathbf{Q} = \mathbf{P} + a\mathbf{F}$ can be any other point along the line of action of the resultant force. Then the resultant moment of the loads on the part about $\mathbf{Q}$ can be expressed (Source: STARCCM+ user's guideline):

$$\begin{aligned} \mathbf{M_Q} &= \mathbf{M_p} + (\mathbf{G} - \mathbf{Q}) \times \mathbf{F} \\ &= \mathbf{M_p} - (a\mathbf{F}) \times \mathbf{F} \\ &= \mathbf{M_p} + 0 \\ &= \mathbf{M_p} \end{aligned} \tag{5.1}$$

Table 5. 2 Ship's center of load with *h/T* changing for configuration $\boldsymbol{\alpha}$=120°, *Vs*=0.6173m/s

h/T	1.2	1.5	2.0	3.0
G coordinate				
x	0.07444	0.0772	0.0495	0.0362
y	$-2.87*10^{-5}$	$-2.04*10^{-4}$	$-3.12*10^{-5}$	$-6.59*10^{-5}$
z	0	0	0	0

The change of *h/T* will exert a relatively large influence on the center of load of the ship hull. With *h/T* increasing, the center of load for the ship is moving backwards along *x* axis (opposite to the direction of *x* axis), while *y* coordinate differ slightly and *z* coordinate keeps constant. So the ship will have the trend of pitching during this process, while this can mitigate ship's sinkage by the stern. This is consistent with what's derived from Fig 5. 5.

5.3 Effect of ship speed (V_s) on ship hydrodynamics

Section 5.3 is dedicated to explaining the influence of V_s on ship hydrodynamics, where the results are based on Config. E in Table 5. 1.

According to Fig 5. 6, there is not much difference in X' at low V_s for all configurations. As V_s increases, X' is increasing faster and faster for all configurations. However, X' in very shallow waters (*h/T*=1.2) is always growing more rapidly than that in medium-deep waters (*h/T*=2.0), which means X' in shallow waters tends to be more sensitive to V_s than that in deep waters because of flow acceleration under the

ship keel. Based on the conclusion from Section 4.2, α poses little effect on X'. This is proved again here, and we can go further and conclude that V_s almost does not affect X' under different α. Whereas under different V_s, only h/T influences X' much. The configuration α=120° h/T=1.2 is taken as example in Fig 5. 7 to show the force and moment components. X'_p is gradually dominating in X' with V_s growing.

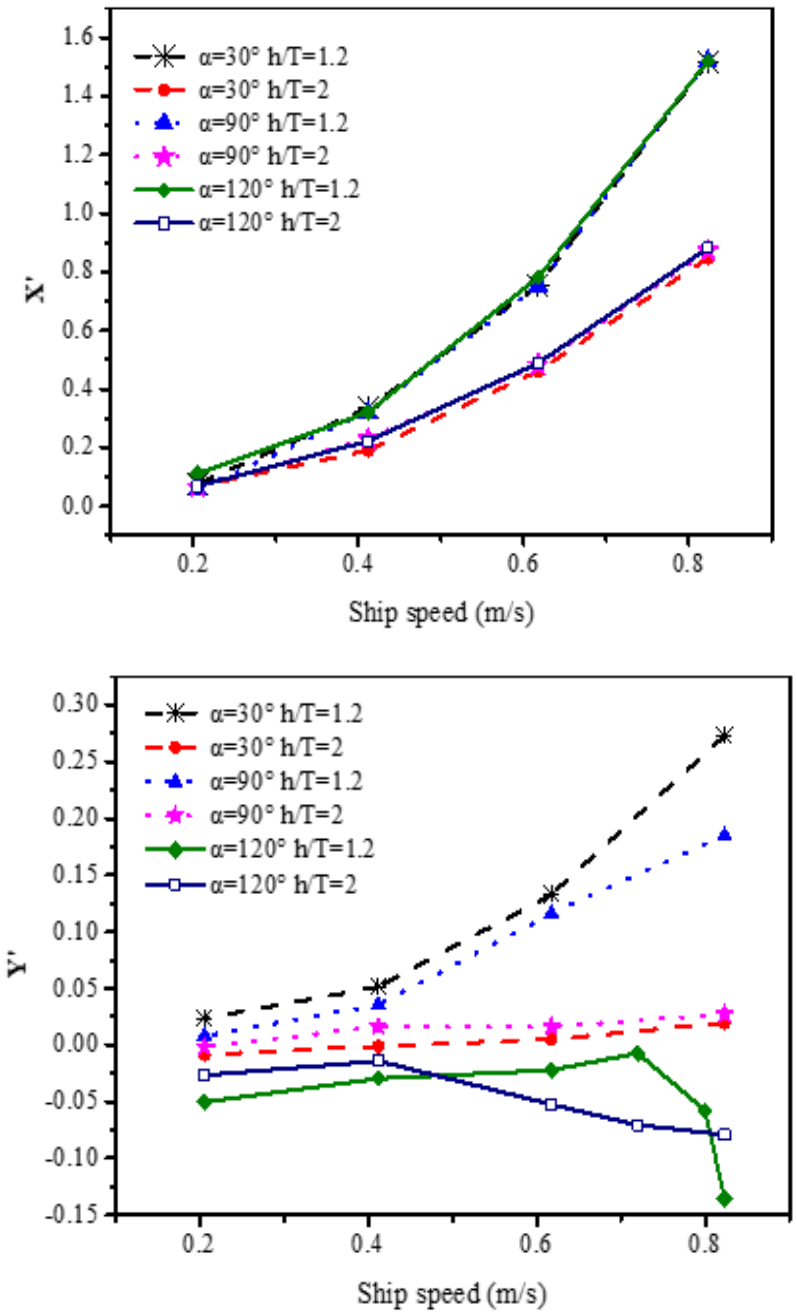

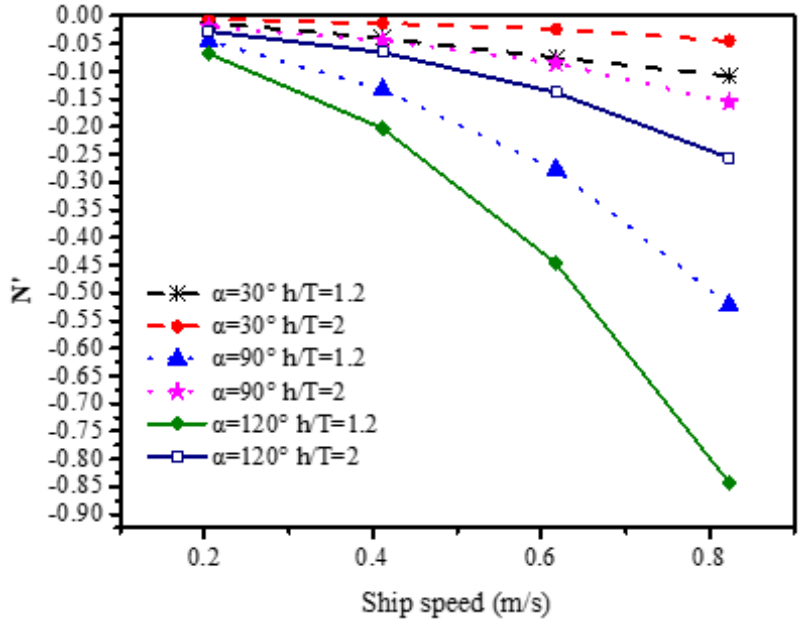

Fig 5. 6 Non-dimensional hydrodynamic forces and moment of the ship under different V_s

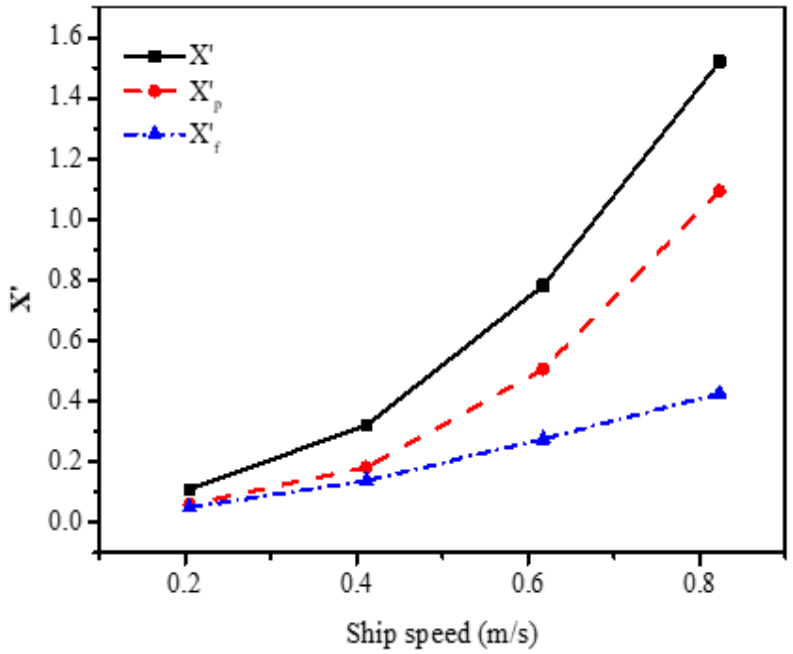

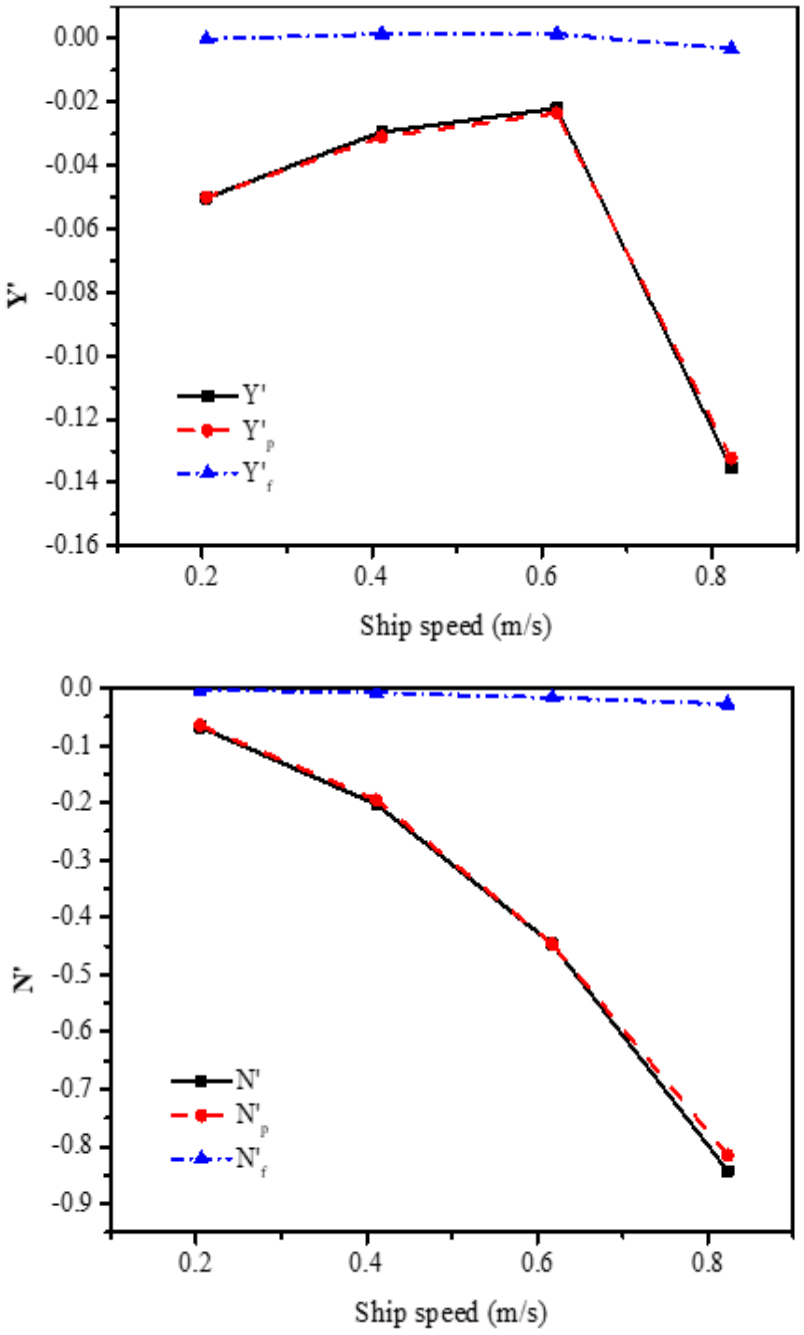

Fig 5. 7 Pressure and frictional components for $\boldsymbol{\alpha}$=120° h/T=1.2 in Config. E

As for Y', abnormal descending trends appear for the two configurations of α=120°. To verify the tendencies, two simulations of V_s=0.72m/s and V_s=0.8m/s are added to the configuration α=120°, h/T=1.2. Also, one simulation of V_s=0.72m/s is added to the configuration α=120°, h/T=2. Their results follow the trends of the two curves, which confirms the correctness of the curve tendencies. For α=30° and α=90°, Y' in very shallow waters (h/T=1.2) is increasing faster as V_s grows, while Y' in

medium-deep waters (h/T=2.0) nearly keeps constant. However, as for α=120°, Y' decreases very little for both deep and restricted waters when V_s is lower than a critical value. The critical value for shallow waters is around 0.72m/s, and is about 0.4115m/s for deep waters. The opposite direction of Y' in this configuration compared with the others has been proved in Section 4.2. When V_s exceeds the critical value, Y' starts increasing a lot as V_s grows, and the magnitude of increase in very shallow waters (h/T=1.2) is even more significant than that in medium-deep waters (h/T=2).

The wave elevation and pressure distribution around the ship for the configuration of α=120° and h/T=1.2 is taken as example to show the results of wave elevation and pressure distribution around the ship (see Fig 5. 8 and Fig 5. 10 respectively). For the ship in large-curvature channels (α=120°) at high V_s, the water level in middle section around the concave bank is higher than that around convex bank (see Fig 5. 9 b), which contributes to generating more waves and growth in hydrostatic pressure (see Fig 5. 8 and Fig 5. 10), and consequently, rapid growth in Y' in the opposite direction (attractive force towards the convex bank) for the configurations α=120° can be observed at high V_s. Also, the water level in middle section on the concave bank is higher than that in bow and stern sections, and this justifies the existence of circulation currents. However, as for the ship in large-curvature channel at low V_s (see Fig 5. 9 a), or in small-curvature channel at high V_s, there is not much difference in the water level between concave and convex banks around the ship. However, the curvature of spiral flow passing through the ship is slightly affected by V_s.

As V_s grows, N' is increasing for all the configurations here. However, it's obvious that N' enlarges fast in the channel with larger α and in shallower waters. Only in the channel with large α (α=90° and 120°), h/T ratio influences N' obviously at different V_s . The pressure components dominate in both Y' and N'(see Fig 5. 7).

Hence, it's necessary for a ship to advance at a low V_s in order to minimize or avoid the effect of spiral flow in curved channels on ship maneuverability.

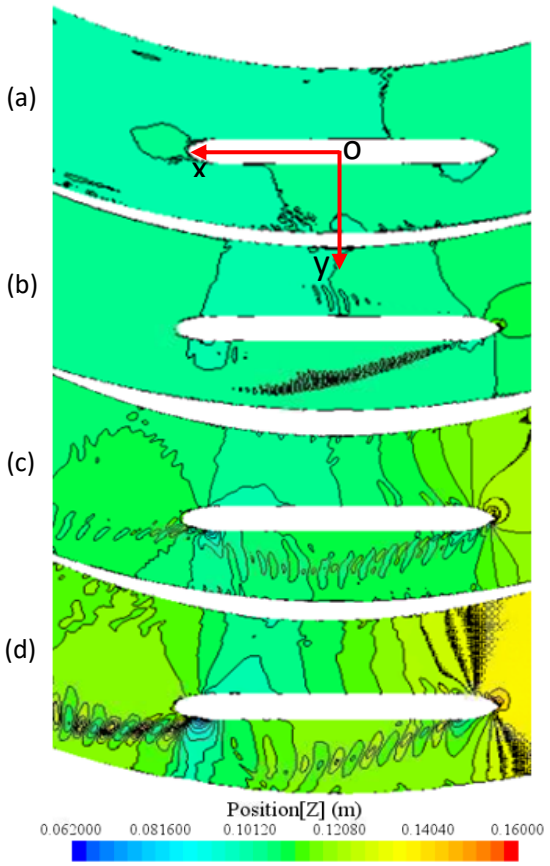

Fig 5. 8 Wave elevation contours for configuration of α=120°, h/T=1.2 in Config. E (a) to (d): V_s=0.205m/s, 0.4115m/s, 0.6173m/s, 0.823m/s

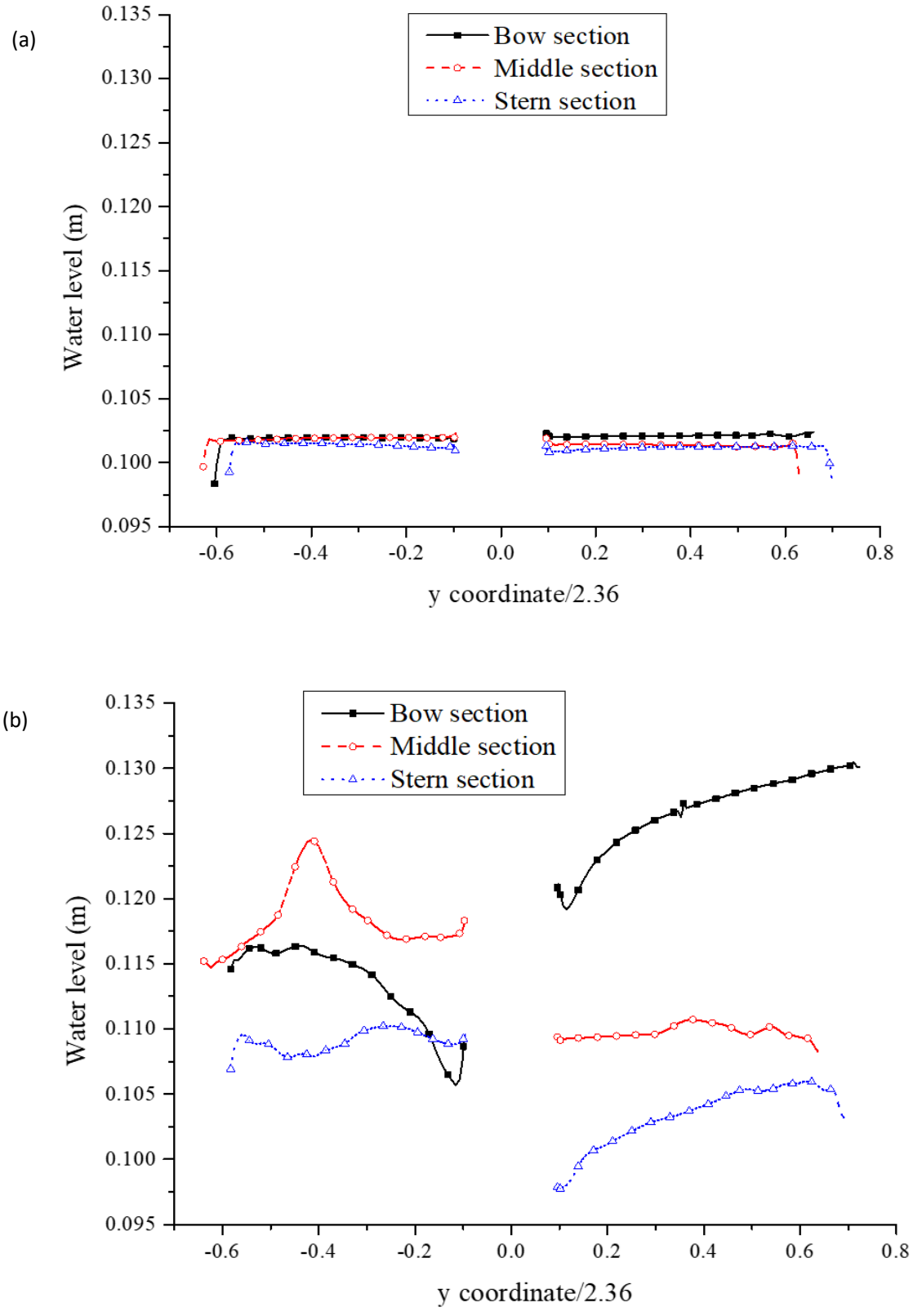

Fig 5. 9 Free surface elevation around the ship hull for configuration of α=120°, h/T=1.2 in Config. E

(a) V_s=0.205m/s (b) V_s=0.832m/s

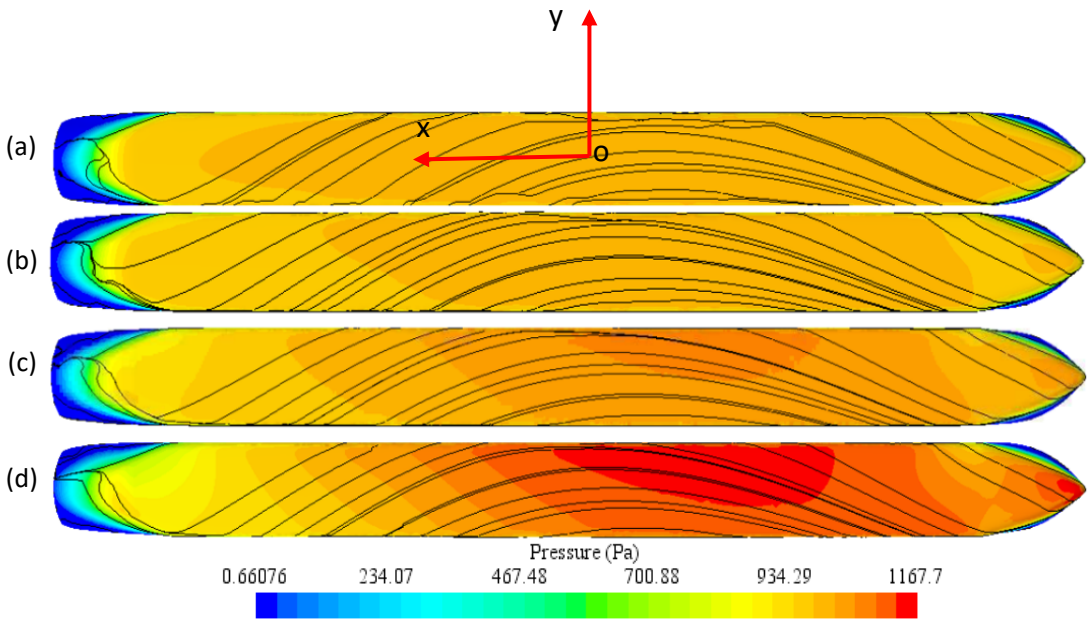

Fig 5. 10 Pressure distribution around the hull for configuration of $\boldsymbol{\alpha}$=120°, h/T=1.2 in Config.3

From (a) to (d): V_s=0.205m/s, 0.4115m/s, 0.6173m/s, 0.823m/s

Table 5. 3 shows the change of center of load of the ship hull with V_s increasing for the configuration $\boldsymbol{\alpha}$=120°, h/T=1.2. The G coordinate refer to x, y, and z coordinates of the center of load of the ship hull.

Table 5. 3 Ship's center of load with V_s changing for configuration $\boldsymbol{\alpha}$=120°, h/T=1.2

Vs G coordinate	0.205	0.4115	0.6173	0.823
x	0.0385	0.04634	0.07104	0.1204
y	$-2.92*10^{-5}$	$-2.76*10^{-5}$	$-1.198*10^{-5}$	$-7.39*10^{-5}$
z	0	0	0	0

The change of V_s will exert a large influence on the center of load of the ship hull. With V_s increasing, the center of load for the ship is moving ahead along x axis, while y coordinate differ slightly and z coordinate keeps constant. So the ship will have the trend of pitching during this process, which causes sinkage by the stern. This also corresponds to what's derived from Fig 5. 10.

5.4 Effect of drift angle (β) on ship hydrodynamics

Drift angle β is a significant controllability parameter for pilots. Section 5.4

illustrates and analyzes the results from Config. F in Table 5. 1, the aim of which is to profile the effect of β on ship hydrodynamics. Fig 5. 11 shows that β has a considerable effect on X', Y' and N'. Moreover, pressure components dominate with frictional ones around 0 for hydrodynamic forces and moment.

X', Y' both increase faster and faster as β grows, especially surges can be noticed starting from β>4°. However, X', Y' for α=120° are always growing more rapidly than those for α=30°, and the magnitudes of the former are always larger. This is caused by the stronger spiral flow which results in larger lateral velocities in channels with larger α. With the increase of β, N' decreases fast in the negative direction and then increases rapidly in the positive direction for both α=30° and α=120°, which declaring the high sensitivity of β on N'. Flow angle of attack by the current will decrease as β grows, and consequently the ship bow will be less affected by the incoming current, while ship stern will be influenced more (see Fig 5. 12).

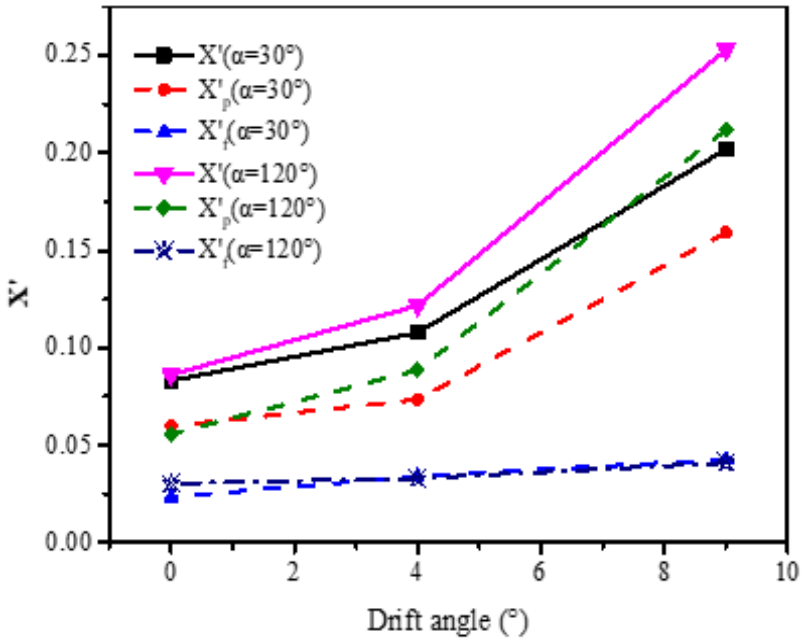

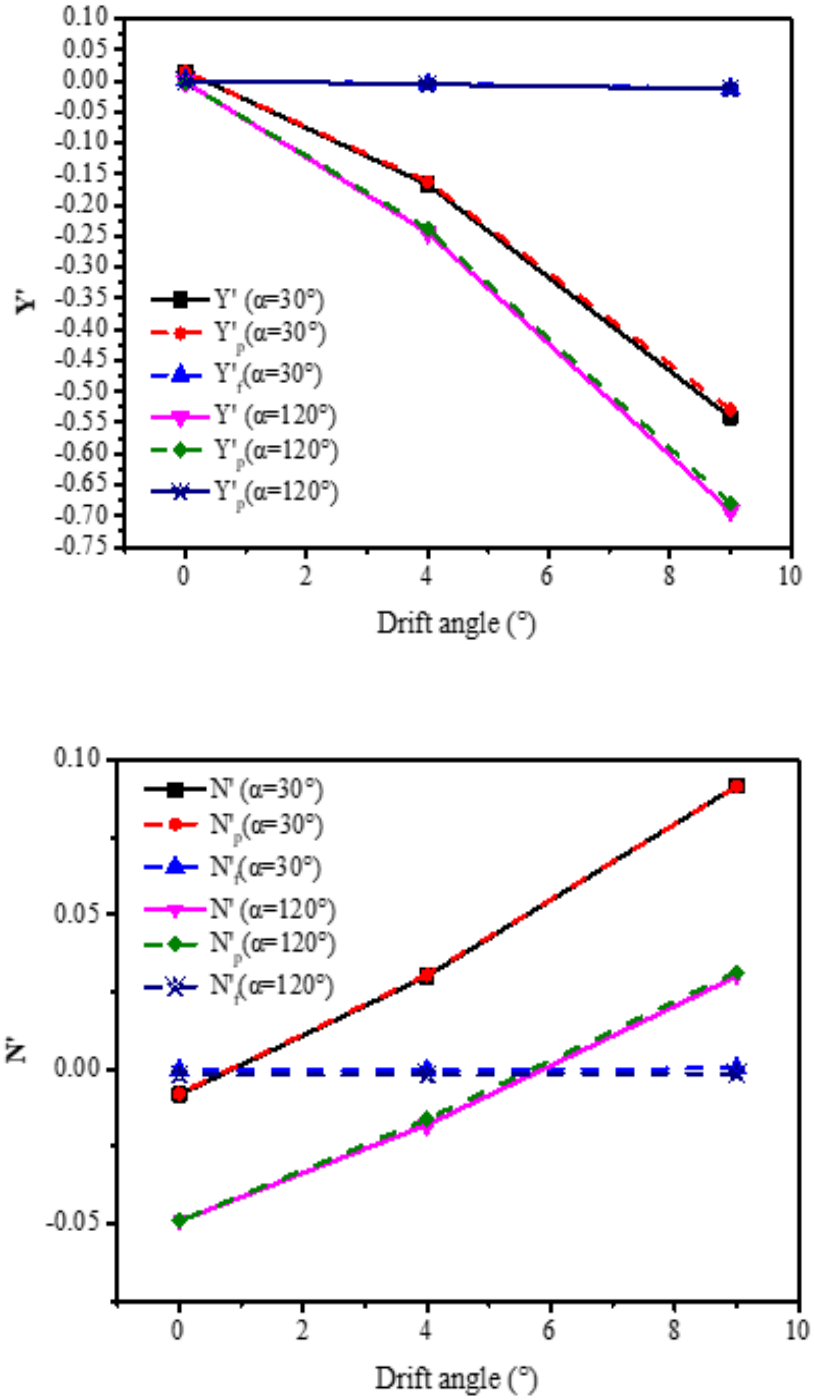

Fig 5. 11 Non-dimensional hydrodynamic forces and moment of the ship under different β

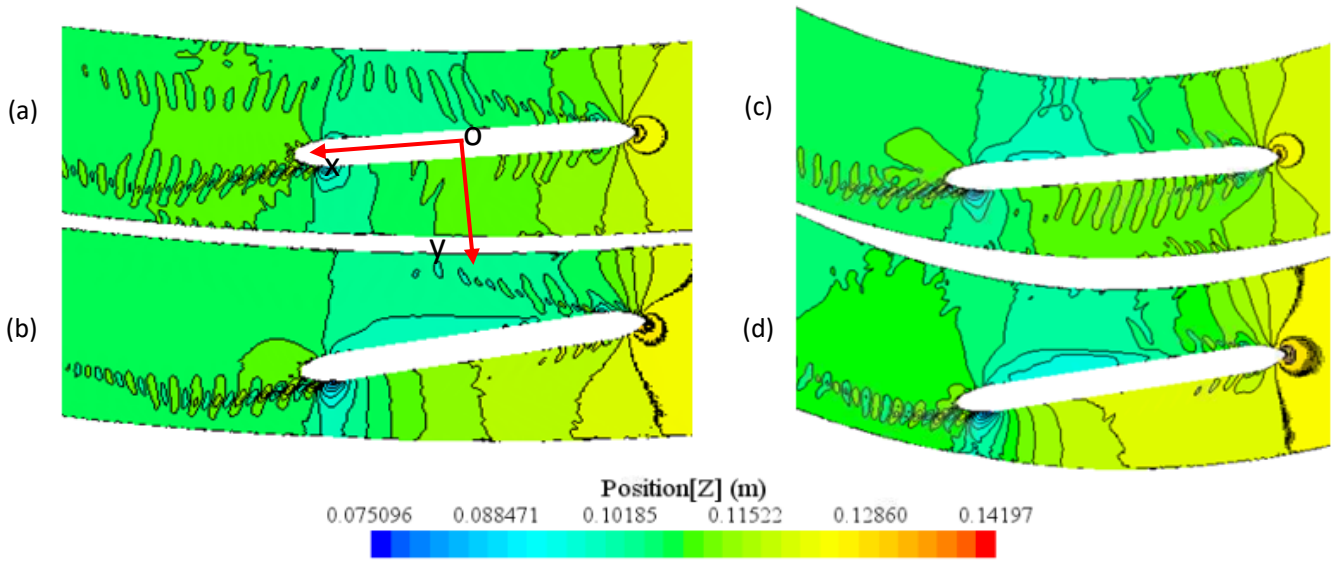

Fig 5. 12 Wave elevation contours in Config. F

(a)α=30°, β=4° (b) α=30°, β=9° (c) α=120°, β=4° (d) α=120°, β=9°

The critical β of direction reverse for α=30° is within the range of 0° to 1°, which is smaller than the range of 5° to 6° for α=120°. The reason is that the channel curvature for α=30° is much smaller, and consequently, the mainstream is passing near the centerline of the fairway. Also, the ship is navigating along the centerline in the middle section of the channel, so the mainstream will act on the ship stern and compensates the yaw moment once drift begins happening (see Fig 5. 14 a). This is beneficial for the ship to correct its course in time. While for α=120° where the channel curvature is very large, the mainstream flows near the concave bank in the middle section of the fairway due to a large centrifugal force. It is not that sensitive and useful to adjust course by way of the current anymore, since the ship needs a large β to encounter the streamlines. What's worse, X' and Y' will surge after β surpasses the critical value. Coupled with the large N', accidents are more prone to occurring for ships navigating in large-curvature fairways. At this time, pilots have to correct the yaw continually once the ship goes off course.

According to Fig 5. 13, the results here are different from the findings above. The

water level around concave bank in the bow and middle sections is higher than that around convex bank. Meanwhile, the larger the β, the higher the water level in the two sections, which will trigger a larger water level difference between concave bank and convex bank. This is verified by Fig 5. 12 that waves generated on starboard side at bow are less important than that on port side. The flow section between ship stern and concave bank is narrowing with β increasing, so the water level is becoming higher contributing to higher pressure distributed around the ship (see Fig 5. 14). On the other hand, the bow section of starboard side will also be in direct contact with the incoming current, which is particularly obvious for α=120° where the mainstream owns larger centrifugal force (see Fig 5. 12). Therefore, it is extremely disadvantageous for a ship passing a curved channel with an improper β, since drift contributes to yaw moment and therefore, the ship's deflection will become more and more serious. It's concluded that β must be controlled within the critical range to avoid accidents, based on which, the high maneuvering technology of a pilot is required when a ship passes a curved channel.

(a)

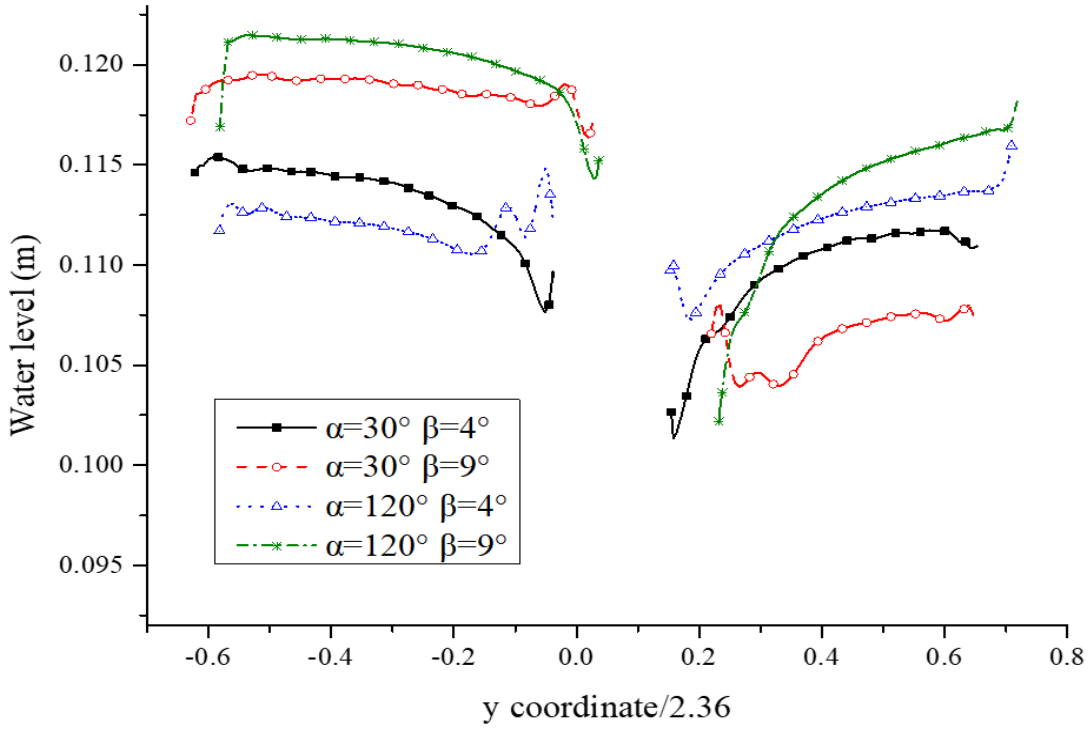

(b)

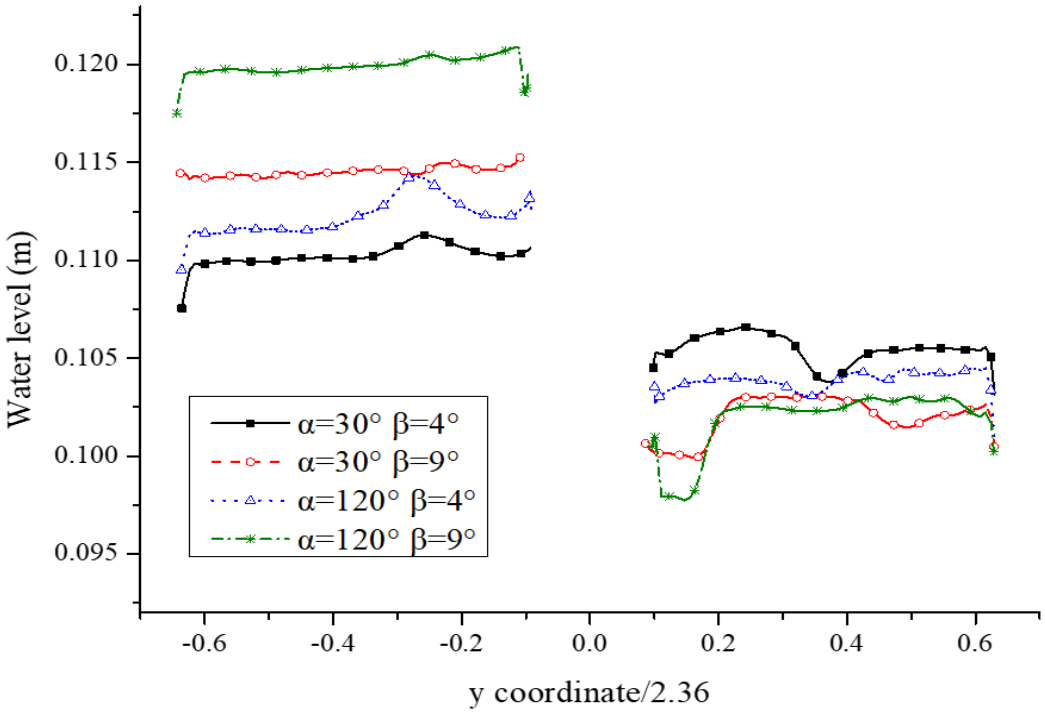

(c)

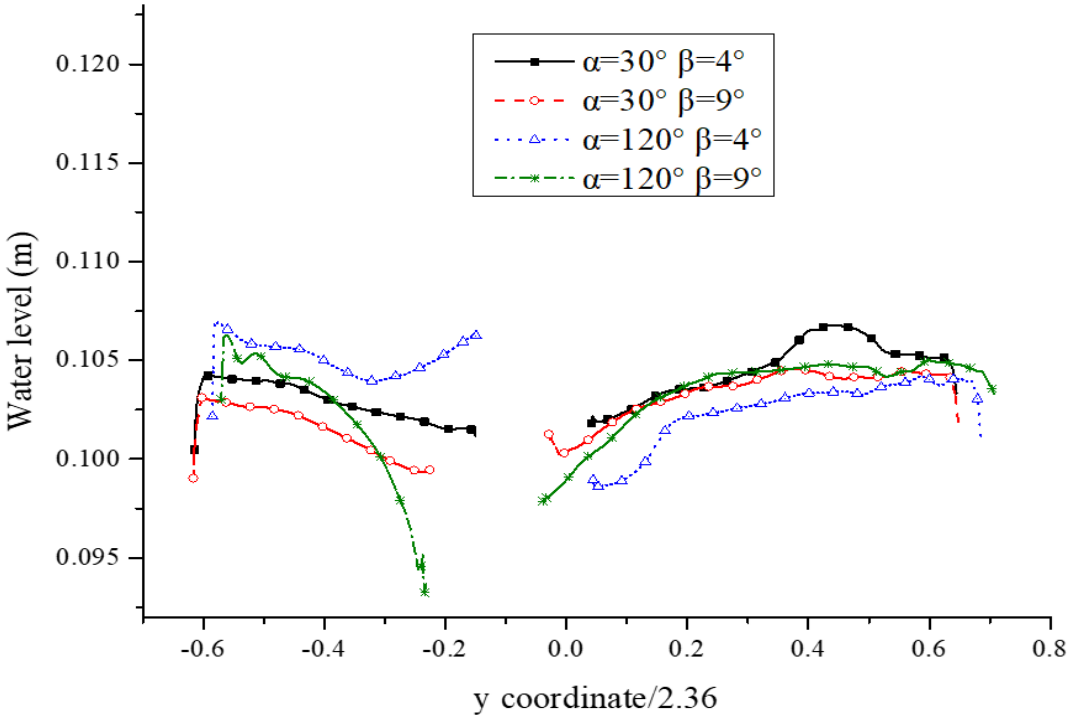

Fig 5. 13 Free surface elevation around the ship hull in Config. F

(a) cross section II (Bow section); (b) cross section III (Middle section); (c) cross section IV (Stern section)

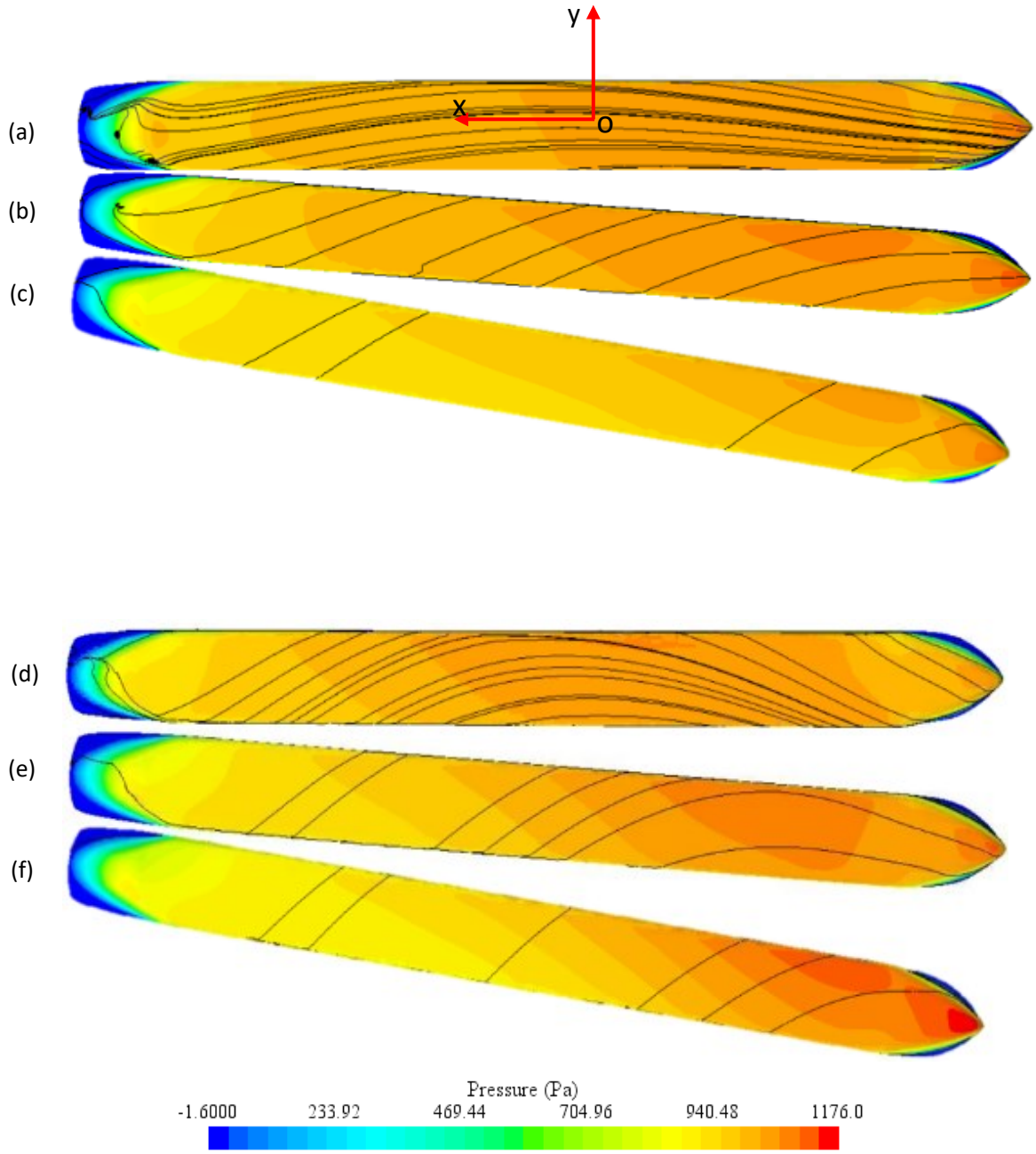

Fig 5. 14 Pressure distribution with streamlines along the ship hull in Config. F

(a)α=30°, β=0° (b)α=30°, β=4° (c) α=30°, β=9° (d) α=120°, β=0° (e) α=120°, β=4° (f) α=120°, β=9°

5.5 Effect of ship type on ship hydrodynamics

The curved channels will limit the size of ships that pass the curves. In this section, different inland ship types (different ship length and beam) are selected, such as Péniche Freycinet (classeI), Dortmund-EMS-Kanaal (DEK) (classe III), Rheine Herne

Kanaal(RHK) (classe IV), and so on. These real ships are scaled by a scale factor of 1/25 in the simulations. Among the different ship types, ship length is the most influential factor in narrow bending zones. Thus, this section analyzes the effect brought by ship type (chiefly ship length) on ship hydrodynamics, which is based on the simulations from Config. G in Table 5. 1.

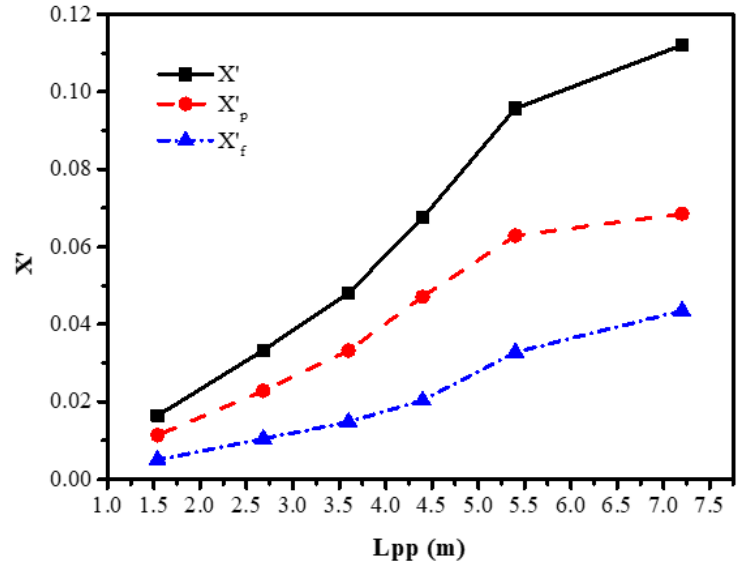

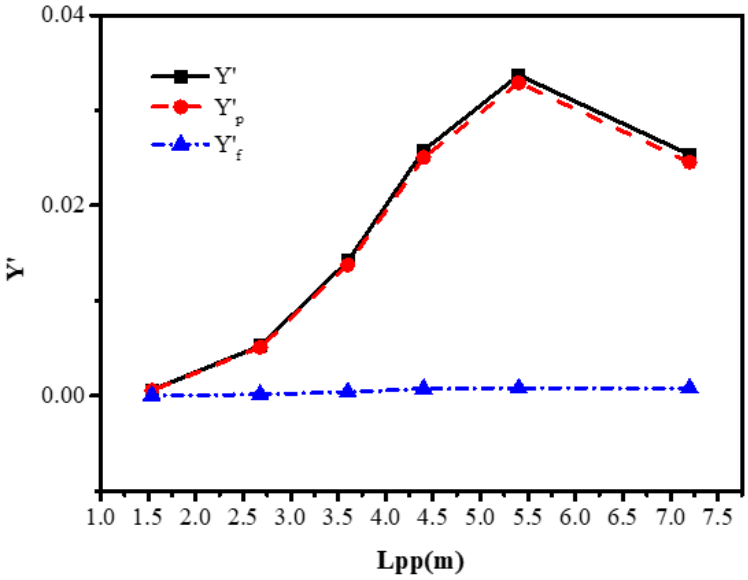

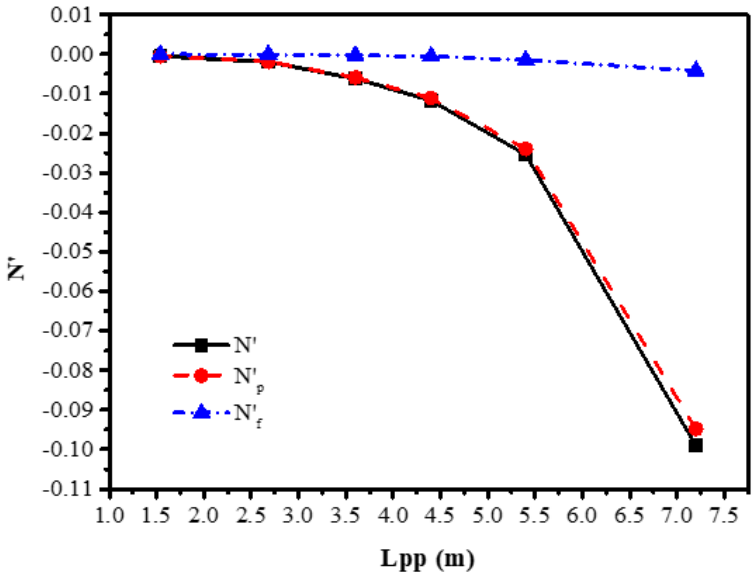

Fig 5. 15 Non-dimensional results of ship type on ship hydrodynamics

As L_{pp} grows, X' increases more and more rapdily for L_{pp} < 5.4m, which is due to the increase of both X'_p and X'_f (see Fig 5. 15). This is because of the larger contacting area between the ship hull and current during this process. Also, bow waves generated around the convex bank and stern waves are both becoming less serious.

According to free surface change at bow (see (a) to (f) in Fig 5. 18), free surface elevation around convex bank is becoming higher than that around concave bank, while the free levels around concave bank are proximately always the same. Moreover, the water level at stern nearly keeps constant during this process. Y' consequently increases faster for L_{pp} < 5.4m. However, the streamline curvature of flow can also be influenced a lot by the change of ship length, and will become extremely larger when the ship is long enough (from Fig 5. 17 (e) to (f)). Therefore, Y' can be noticed decreasing from L_{pp} =5.4m to L_{pp} =7.2m. Owing to the larger curvature of mainstream, there is relatively less part of mainstream flowing through the bottom of the hull, and X' also grows slowly from L_{pp} =5.4m to L_{pp} =7.2m as a result.

The free level change mentioned above, combined with the larger curvature of streamlines around the ship in the case of large L_{pp} (signifying that stronger spriral

flow exists) will cause N' to increase more and more rapidly as L_{pp} grows. Therefore, long ship is more prone to drifting in curved channels. Due to different ship beams of the models, pressure distributed on the ship bottom (see Fig 5. 17) and wave elevation (see Fig 5. 16) around the hull both show a trend of decreasing first and then increasing.

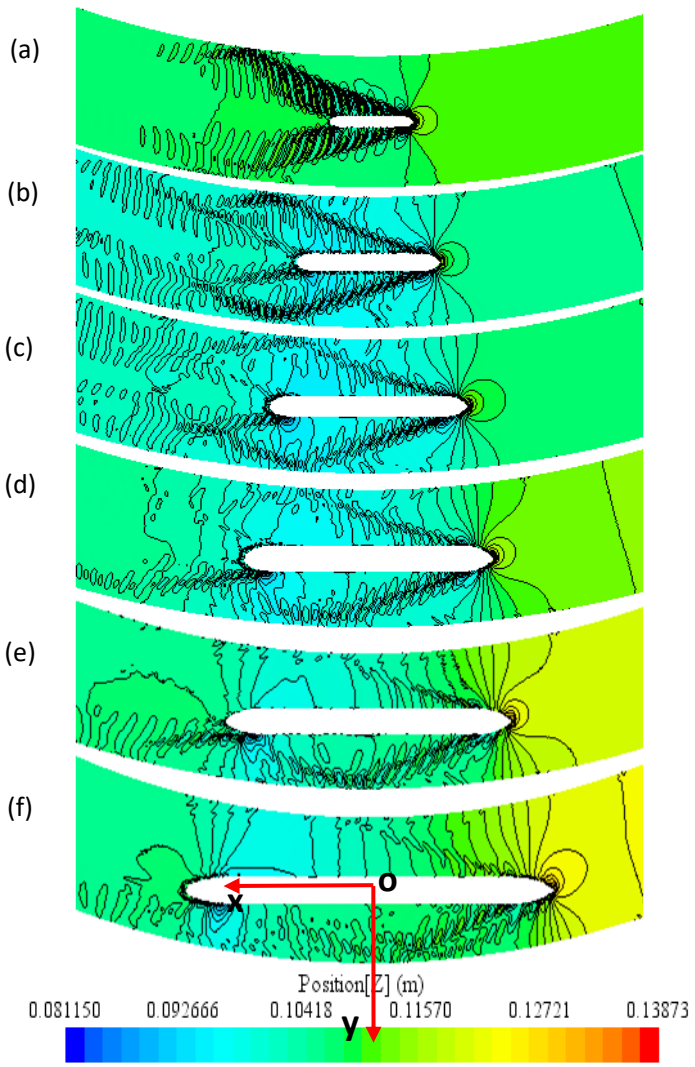

Fig 5. 16 Free surface elevation contours of ship type variation

(a) to (f): L_{pp} = 1.54m, 2.68m, 3.6m, 4.4m, 5.4m, 7.2m

corresponding beam = 0.202m, 0.328m, 0.38m, 0.45m, 0.45m, 0.45m

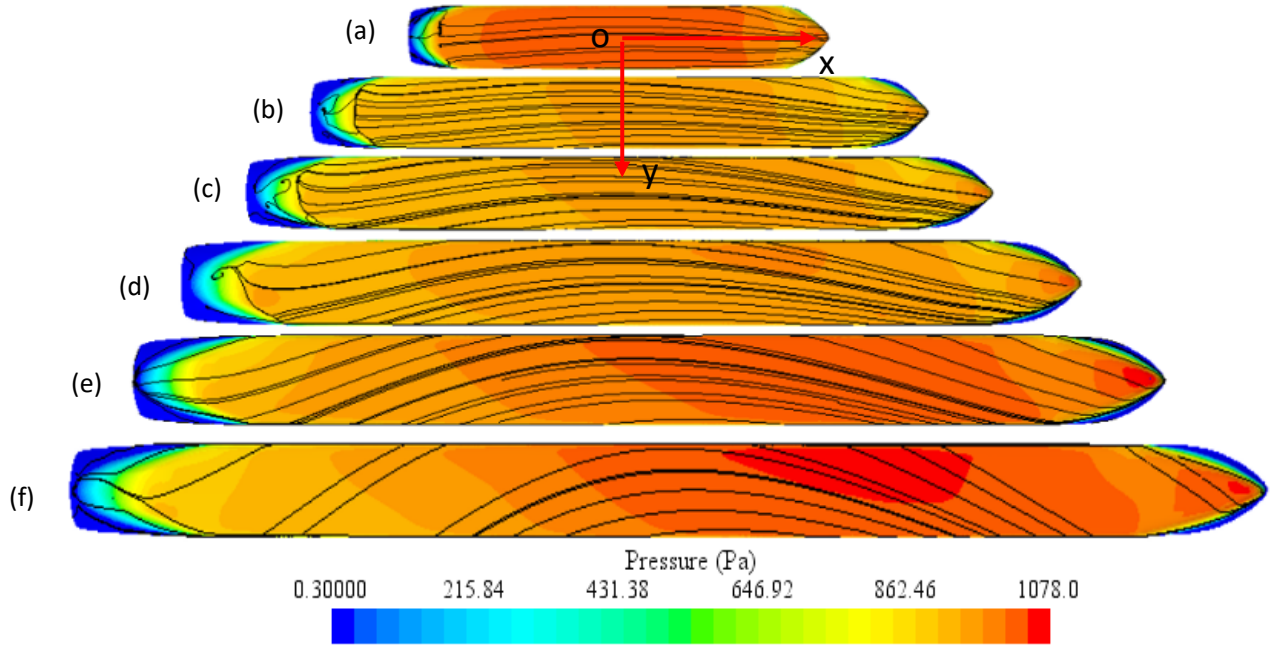

Fig 5. 17 Pressure contours with streamlines of ship type variation

(a) to (f): L_{pp} = 1.54m, 2.68m, 3.6m, 4.4m, 5.4m, 7.2m

corresponding beam = 0.202m, 0.328m, 0.38m, 0.45m, 0.45m, 0.45m

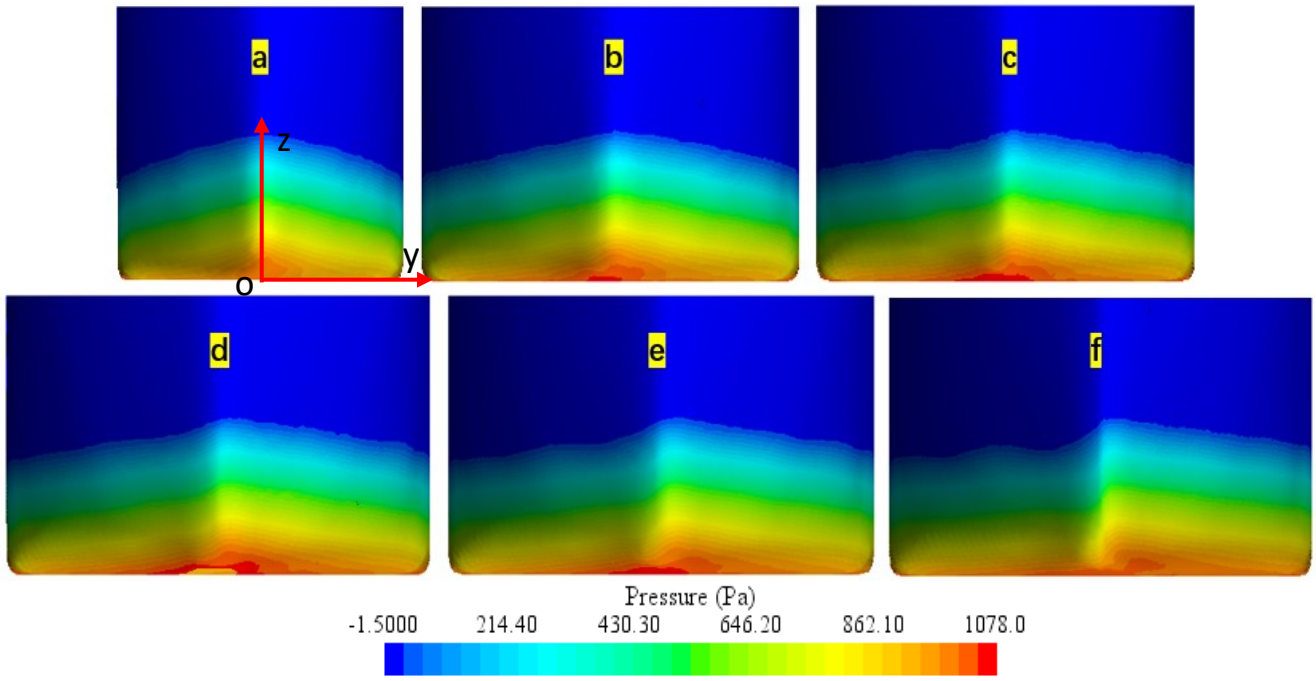

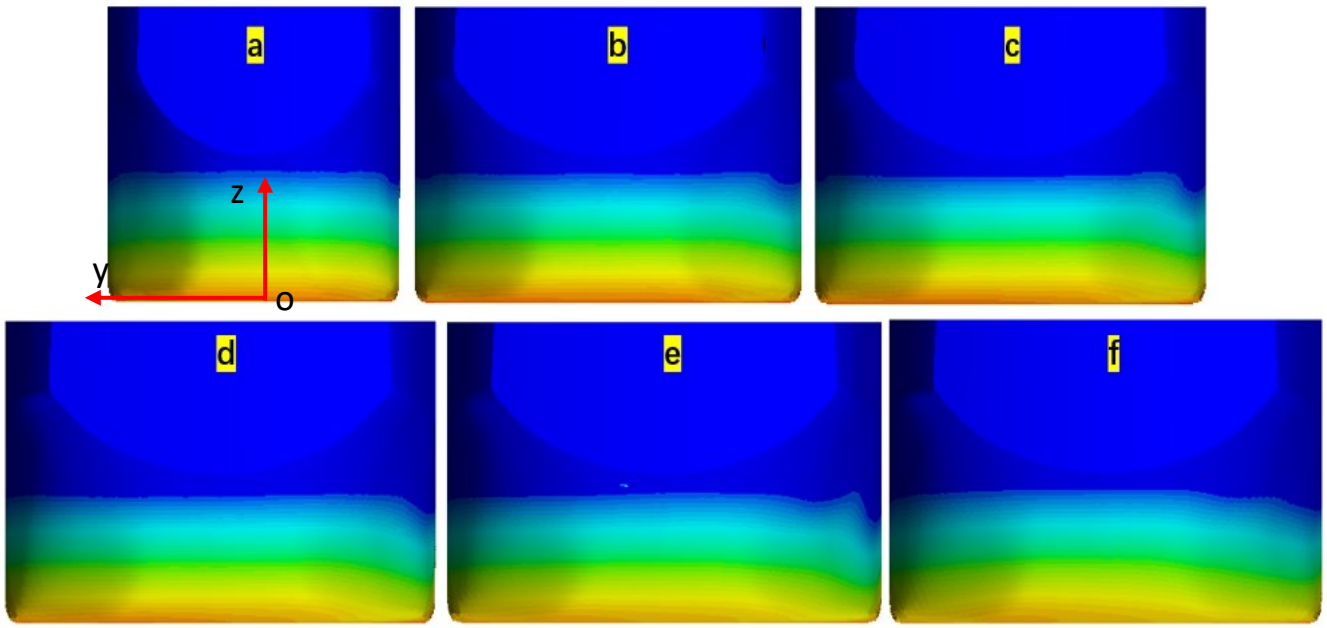

Fig 5. 18 Pressure distribution at bow and stern for ship type variation

(a) to (f): L_{pp} = 1.54m, 2.68m, 3.6m, 4.4m, 5.4m, 7.2m;

corresponding beam = 0.202m, 0.328m, 0.38m, 0.45m, 0.45m, 0.45m

5.6 Ship hydrodynamics considering propellers and rudders

Propeller and rudder are two essential components of a ship's propulsion system. Both of them play a critical role in controlling the movement and stability of ships. Propellers generate forward thrust, while rudders are used to steer ships. The propeller influences ship's moments by generating thrust and causing the ship to move forward. The thrust generated by the propeller creates a force that acts along the ship's longitudinal axis, causing the ship to pitch and yaw. While the amount of the thrust generated by the propeller is determined by various factors, such as the pitch of the blades, the speed of the ship, and the power of the engine [187, 188].

The rudder, on the other hand, is used to control the ship's yaw moment by changing the direction of the water flow around the ship's stern. By deflecting the water flow, the rudder creates a force that acts perpendicular to the longitudinal axis of the ship, causing it to yaw [189]. The effectiveness of the rudder depends on various

factors, such as its size, shape, and position on the ship, as well as the speed and direction of the water flow.

By working together, these two components allow the ship to move in the desired direction and maintain its stability in various sea conditions. While the interaction between propeller and rudders is an important consideration in ship design and operation. By carefully designing and optimizing these components, ship designers and operators can ensure optimal performance, stability, and safety [239].

Some researchers have ever attempted in this domain. Using large eddy modelling, the development of the propeller tip vortex and its impact on the rudder surface pressure fluctuation were studied by Hu et al.[190]. On a system made up of a marine propeller and a hydrofoil that acts as a rudder, large eddy simulations are reported by Posa and Broglia for four different directions of the latter, simulating maneuvering circumstances in marine propulsion [191]. Wang et al. [192] examined the features of the wake dynamics of a propeller moving ahead of a rudder in open water by a numerical technique based on the detached eddy simulation. With CFD technique, Villa et al.[193] concentrated on the forces generated by the rudder varying the propeller loading conditions and the mutual position between the two devices, which provides information that can be used to describe and enhance a widely-used semi-empirical technique based on the actuator disk theory. However, little research has focused on the propeller and rudder effect on ship hydrodynamics when a ship is passing a curve.

In this section, in order to study the balance of the moments applied on the ship's hull and generated by the rudders, two propellers and four rudders (two rudders behind each propeller) are added (see Fig 5. 19).

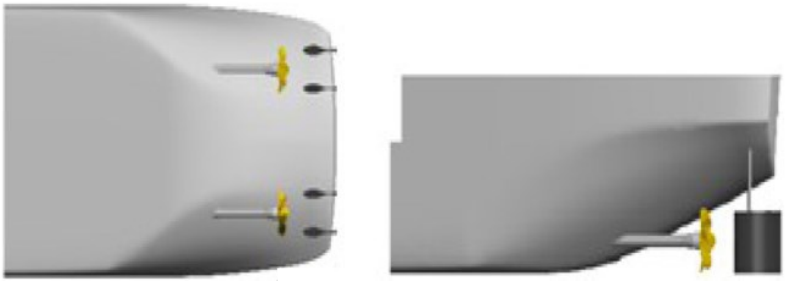

Fig 5. 19 Ship with propellers and rudders

The drift angle of the ship is varied by considering two propeller rates (256.25 *rpm* and 771.62 *rpm*). The main objectives of this study is to find the critical values of rudders angle and ship drift angle that ensure the controllability of the ship (rudders moment should be larger than the moment applied on the ship hull)

5.6.1 Propeller and rudder modelling

The ship model is simulated with 2 propellers and 4 rudders. The propellers in the simulation are modelled by virtual disk in STARCCM+.

The virtual disk model is founded on the idea that actuator disks can be used to simulate propellers, turbines, rotors, fans, and other moving parts. The actuator disk approach is useful when how the rotor/propeller behavior will affect the flow are more concerned than the specifics of how the flow will interact with the rotating device's blades.

A source term spread over the area filled by the virtual disk represents the effect of the actuator disk on the flow field in the momentum equations. Depending on the application area, various distributions with varying degrees of accuracy can be used to represent the actuator's action.

For the virtual disk model, there are currently four methods implemented in STARCCM+ (Source: STARCCM+ users' guidelines):

●Body Force Propeller Method

●Blade Element Method

●1D Momentum Method

●User Defined Method

In this thesis, body force propeller method is used to simulate the propellers behind the ship model. This method simulates the effect of a marine propeller. The method simulates the flow field interaction between a ship's body and the propeller. The flow around the ship hull affects the flow that the propeller induces. The ship flow is also affected by the propeller. With this method, the detailed flow field around the propeller is not required, while only the correct propulsion specification is needed. Normally, the following approaches are used by this method:

Definition of a virtual disk regarding position and direction in which thrust is pr oduced (Source: STARCCM+ users' guidelines):

●Specification of a propeller performance curve

●Specification of an operating point (for example, rotational speed)

●Specification of an inflow method.

Then the distribution of the axial and tangential forces of the modeled propeller and its effect on the flow can be calculated.

The body force propeller method is used to model the effects of a propeller such as thrust and torque and thereby creating propulsion without actually resolving the g eometry of the propeller. The method employs a uniform volume force f_b distribution over the cylindrical virtual disk. The volume force varies in radial direction.

The radial distribution of the force components follows the Goldstein optimum and is given by:

$$f_{bx} = A_x r^* \sqrt{1 - r^*} \tag{5.2}$$

$$f_{b\theta} = A_\theta \cdot \frac{r^*\sqrt{1-r^*}}{r^*(1-r_h') + r_h'} \tag{5.3}$$

$$r^* = \frac{r' - r'h}{1 - r'h} \tag{5.4}$$

$$r'_h = \frac{R_H}{R_P} \text{ and } r' = \frac{r}{R_P} \tag{5.5}$$

Where f_{bx} is the body force component in axial direction, $f_{b\theta}$ is the body force component in tangential direction, r is the radial coordinate, R_H is the hub radius and R_P is the propeller tip radius.

The constant A_x and A_θ are computed as:

$$\begin{aligned} A_x &= \frac{105}{8} \cdot \frac{T}{\pi\Delta(3R_H + 4R_P)(R_P - R_H)} \\ A_\theta &= \frac{105}{8} \cdot \frac{Q}{\pi\Delta R_P(3R_H + 4R_P)(R_P - R_H)} \end{aligned} \tag{5.6}$$

where T is the thrust, Q is the torque, and Δ is the virtual disk thickness.

Then a propeller performance curve needs to be specified, which gives the dime nsionless thrust coefficientK_T, the torque coefficient K_Q , and the propeller efficiency as functions of the advance coefficient J.

$$\begin{aligned} K_T &= \frac{T}{\rho n^2 D_p^4} \\ K_Q &= \frac{Q}{\rho n^2 D_p^5} \\ J &= \frac{V_A}{nD_P} \end{aligned} \tag{5.7}$$

Where V_A is the speed of advance of the propeller, n is the rotation rate with the unit revolution per second (*rps*), and D_P is the propeller diameter.

The propeller type and propeller performance curve are shown in Table 5. 4 and Fig 5. 20 respectively. The rudder dimensions can be seen in Fig 5. 21. The mesh scene and positions for propellers and rudders are shown in Fig 5. 22.

Table 5. 4 Propeller type

Propeller type	Value at fixed pitch
Number of propellers(np)	2
Number of blades(z)	5
Propeller diameter [D_P(m)]	0.08
Hub diameter ratio [d_h/D_P(m)]	0.03

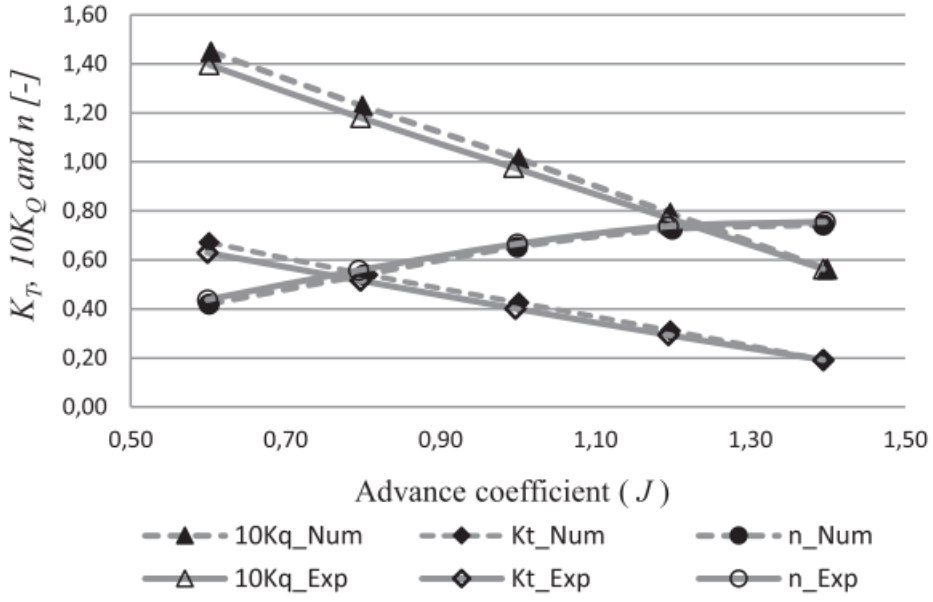

Fig 5. 20 Performance curve of propeller [78]

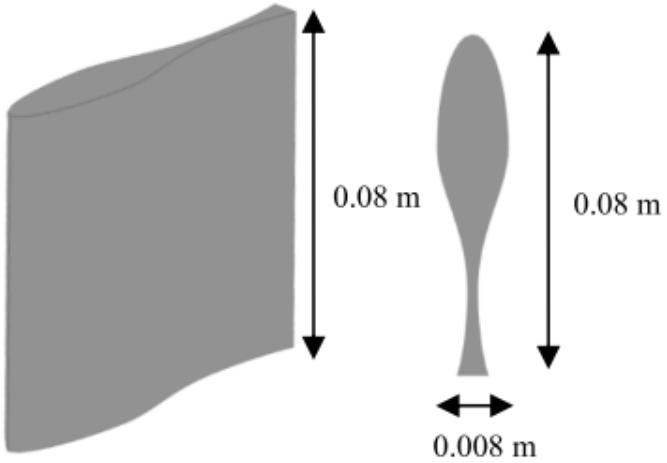

Fig 5. 21 Rudder dimensions: (a) standard view; and (b) top view [78]

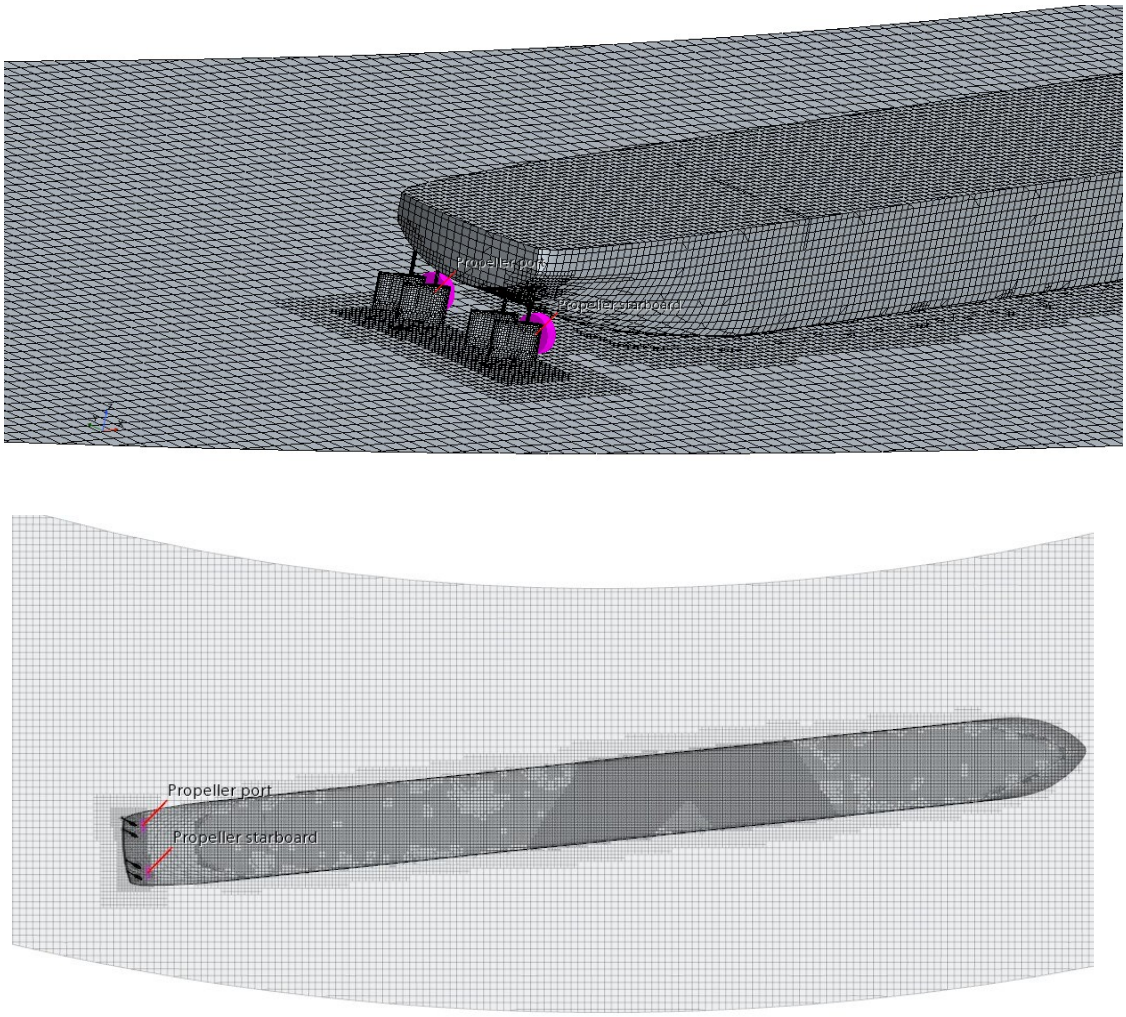

Fig 5. 22 Mesh scenes and locations for propellers and rudders in the simulations

The simulation configurations with appropriate results for propeller and rudder effect are listed in Table 6. 1. For all the configurations, the channel angle α = 120°, channel bottom width W=2.36m, h/T=1.2, channel slope angle γ is 27°, the rudder angles are all set 35°. Advance coefficient J =0.6 (See Fig 5. 20) is chosen due to the highest efficiency of propeller, hence according to equation (5.7), for V_s=0.205m/s , the propeller rate = 256.25 rpm; for V_s=0.6173m/s, the propeller rate =771.62 rpm. In addition, to obtain a good resolution of the flow field around the virtual disk, cylindrical volumetric refinement zones are added around both of the propellers in the simulations.

Table 6. 1 Simulation configurations for propeller and rudder effect

β (°)	0		3		6		9	
N' *rpm*	N_S'	N_R'	N_S'	N_R'	N_S'	N_R'	N_S'	N_R'
256.25	-0.072	-0.020	-0.024	0.031	0.007	0.030	0.057	0.028
771.62	-0.475	-0.147	-0.140	0.287	0.095	0.246	0.355	0.228

(N_S' : Moment of ship; N_R': Moment of rudder; β: Drift angle; *rpm*: propeller rate)

According to the results shown in Table 6. 1, when the ship is entering the bending channels with zero drift angle, the moment generated by rudders can never compensate the hydrodynamic moment applied to the ship. The critical drift for the ship model under the condition of rudder angle 35°(the maximum rudder angle) is between 0 and 3 degrees. So if a pilot maneuvers the ship at 0 drift entering the bend, the ship will definitely lose control.

5.7 Conclusion remarks

According to the sensitivity analysis above, the following conclusions and recommendations can be obtained:

(1) X' is very sensitive to *h/T* ratio regardless of α, and X' decreases fast with *h/T* increasing. While the effect of *h/T* on Y' is small, and an obvious downward tendency in Y' can be only observed for small-curvature channels in shallow waters. N' is sensitive to both *h/T* and α. For α=120°, N' diminishes fast in shallow waters as *h/T* increases, but its magnitude of change becomes small for *h/T* > 2. For α=30°, N' goes down slowly with *h/T* increasing in shallow waters, while it's almost unchanged after that. Besides, X'_p dominates in shallow waters, but X'_f starts coming to dominance after *h/T* surpasses a critical value. Yet Y'_p and N'_p dominate all the time. Hence, an increase in water depth is beneficial for eliminating the resistance and yaw of a ship.

However, pressure around the ship will increase with *h/T* ratio reducing. This is different from what we know about the shallow water effect.

(2) X' increases faster and faster with V_s growing, especially in shallow waters. For $\alpha \leq 90°$ in shallow waters(*h/T*=1.2), Y' is increasing more and more with V_s ascending; For $\alpha \leq 90°$ in deep waters(*h/T*=2), Y' increases little with V_s growing. While for α=120°, Y' starts rising a little as V_s grows. But when V_s exceeds a critical value, Y' commences reducing due to the strong interaction with the concave bank. Moreover, the critical V_s for shallow waters is larger than deep waters, and Y' declines more seriously in shallow waters after the critical V_s. N' is increasing for all the configurations as V_s rises, but N' boosts faster for larger α and shallower waters. Specifically, *h/T* affects N' more for large α, while α influences N' more for shallow waters. Also, X'_p and X'_f occupy nearly the same proportion in X', while pressure components dominate in Y' and N'.

(3) β is a significantly sensitive parameter that impacts X', Y' and N' much. Also, the pressure components dominate with respective frictional ones around 0 in hydrodynamic forces and moment.

As β grows, X' and Y' increase faster and faster, and the increases of both X' and Y' are larger for the ship in the channel of large α. Particularly, X' and Y' in large-curvature channels are always more considerable and ascending faster than those in small-curvature ones. A critical β can be observed for N', and the critical β for small α is much smaller than that for large α. When β of a ship is below the critical value, N' is decreasing with β growing, and at this time the current helps recover the ship's course. However, when β is over the critical value, N' will start increasing in an opposite direction which contributes to the ship's continued yaw. In conclusion, ship's β must be maintained around the critical value to ensure good maneuverability when a ship is passing through a curved fairway.

(4) As ship length (L_{pp}) grows, X' and Y' increase gradually faster for ship length (L_{pp}) lower than the critical value 5.4m. However, X' starts increasing more slowly, while Y' decreases when L_{pp} exceeds this value. N' grows increasingly faster during this process. At bow, the free surface level on convex bank is becoming increasingly higher, while it's almost unchanged on concave bank. At stern, the water level keeps nearly the same around both bank sides. Besides, the curvature of flow streamlines of long ships can be noticed extremely larger than that of short ships.

(5) A Ship should have a drift angle when entering bending zones, since the rudder moment can not offset the ship moment when ship drift is 0.

Chapter 6

6. The integration of the channel bending effect in ship simulator

Ship simulator is a kind of device which can partially imitate the real situation and is specially designed to meet some specific purposes, so that the trainees can practice and show their abilities through the operation of the equipment in a controllable safe environment. As of today, ship simulators have become the most suitable equipment for the study of ship motion, dynamics, control strategies and algorithms under laboratory conditions, which even play a pivotal role in ensuring the safety of inland waterway transport. Normally, they can be used for data collection for ship behavior studies; evaluation of changes in the navigational environment; research into ship traffic accidents (mainly collisions); study of ship berthing and unberthing maneuvers; ship maneuverability studies; maritime analysis; port channel design development and pilotage trials, etc [194-196].

The study of ship simulators dates back to the 1960s. As early as 1967, the Swedish SSPA, who was one of the first institutions to study ship simulators, successfully developed a ship simulator using computer virtual reality technology. The SSPA is now working on a new multifunctional ship simulator, based on its extensive research in mathematical modelling of ship movements [197, 198]. The national ship model laboratory Wageningen in Netherland designed and developed the world's first fully functional large ship simulator for operational training in 1970, based on which most ship simulators in the world are designed [199, 200].

After decades of development, the ship simulator has gone through a process from single-degree-of-freedom motion simulation to six-degree-of-freedom motion simulation.

National Biodynamics Laboratory in USA has developed ship motion simulator with 3 Dofs, which is able to conduct research on the working ability and technical level of offshore staff under various sea conditions. Besides, Lakehurst of USA managed to design ship motion simulator with 6 Dofs, and it can simulate the movement law of ships in Class 5 sea conditions [201, 202]. KONGSBERG MARINETIME in Norway produces ship control simulator series products, enabling basic ship maneuvering simulation function, as well as dynamic positioning, engine compartment simulation, simulations of liquid cargo operation, etc. The Polaris ship bridge simulator developed by KONGSBERG has 26 ship bridge equipments and 8 simulation stations, which can realize joint training of multiple ships [203, 204].

A large full-mission ship simulator was developed by Canadian Institute of Navigation, whose horizontal angle of view can reach 360 °, and vertical angle of view can reach 27 °. The ship motion simulation mechanism with six degrees of freedom can realistically simulate the effects of hull vibration and wave impact [205, 206].

International Maritime Research Center in Japan developed a ship simulator with a cylindrical projection screen, on which the view within the bridge can be projected. Besides, there are also screens equipped on the ground to show the mooring view. The vertical angle of view of the simulator can reach 40 °, and the horizontal angle of view can arrive at 240° [207, 208].

Maritime simulator developers introduced above have been dedicated to developing navigational simulators for ages, and have succeeded in a mature system. However, they focus on simulators used for the open sea, while are not involved in the development of inland ship simulators. Due to inland canal restrictions and unique ship layouts, inland ship maneuverability has more difficult characteristics than that of seagoing ships.

Cerema in France is the only institute that has been committed to the development of an inland river ship simulator in France. The simulator can conduct a navigational

safety assessment of vessels' crossing inland bridges, considering different types and numbers of ships at the same time. Also, it can simulate ships crossing to study ship crossing effects in the Seine river. Last but not the least, it's also used to check whether infrastructures are compatible with inland navigation. However, relies on the experience of pilots who often carry out this type of simulations on the simulator. It has been reported on several occasions that the behavior of the ships at bending zones differs from reality, this feeling has also been recorded on other simulators. As expressed above, this behavior is completely due to the flow nature in these zones. Note that, the effect of navigation environment on the ship can be taken into consideration by two ways. The first is to find analytical or semi-analytical formulas to describe the desired effect. While the second one consists in making numerical simulations of potential type (3D) in real time to calculate the hydrodynamic forces that act on the ship. The latter is used especially when the force and moment variations can't be represented by a generalized formula.

Hence, the main objective of this section is to analyze the results obtained previously in order to verify the possibility of finding an analytical or semi-analytical formulas to correct the behavior of ships at bending zones.

6.1 Ship maneuvering models

The multi-degree-of-freedom motion system, as a vehicle for the ship simulator, is one of the most important parts of the simulator. It simulates the various surge, sway, yaw, roll, and acceleration of the ship during navigation, making the ship simulation more closely resemble real navigation. The essence of motion simulation is the real-time control of a multi-degree-of-freedom motion platform by a digital computer based on data from the ship's surging, rolling, drifting, pitching, yawing, and heaving during navigation to accomplish the desired motion pattern [209-212].

To simulate the ship's trajectory and motion, a mathematical method should be used to obtain the final equation system. The study of ship maneuverability usually

uses mathematical models to describe ship movements [213, 214]. The most widely used mathematical models based on equations of motion are the Abkowitz model and the MMG model [215-217]. Abkowitz model is a non-linear mathematical model of ship maneuvering motion, which was first proposed by Abkowitz in 1964 [236, 237]. This model regards the ship body, propeller, and rudder system as an integral whole, and expresses the hydrodynamic forces and moment applied on the entire body as equations relevant to motion state variables. In principle, the Abkowitz model is essentially a Taylor series expansion of the hydrodynamic forces and moments acting on a ship relative to various factors [235, 238]. However, the model structure is complex, especially in multi-degree-of-freedom forms, where the hydrodynamic derivatives sum up to a large number [89]. Besides, the physical meaning of some of the hydrodynamic derivatives in the model is not clear enough to facilitate an in-depth analysis of the maneuverability of the object concerned [93].

MMG model was proposed by the Japanese Manipulative Mathematical Modelling Group in the late 1970s [85, 218-221]. The MMG model considers the hydrodynamic forces and moments acting on the boat, the oars and the rudders separately, and introduces interference coefficients to characterize the mutual interference between the components Interference coefficients are introduced to characterize the mutual interference between the various components. Therefore, with this model, the hydrodynamic performance of ships, the oars and the rudder can be described separately. Besides, the model structure is clearer and the number of hydrodynamic derivatives is smaller with clearer physical meanings [222-225].

6.1.1 Abkowitz model

Ship motions with 6-Dofs in Abkowitz model are described based on two Cartesian coordinate system, that are, an inertial coordinate system fixed on the earth's surface (O_0-$x_0y_0z_0$), and a body-fixed coordinate system on the ship (O-xyz), whose origin is located at the mass center of the ship(denoted by M_G)(see Fig 6. 1). As this

work focuses on inland waterway navigation, the mathematical model here focuses on sway, surge and yaw. The motion equations are expressed as equation (6.1)[226]:

$$\begin{aligned}(m+m_x)\dot{u}-(m+m_y)vr &= X\\ (m+m_y)\dot{v}+(m+m_x)ur &= Y\\ (I_{zz}+J_{zz})\dot{r} &= N\end{aligned} \tag{6.1}$$

Where X represents resistance force in this thesis, Y is the force applied on the ship hull in y-axis, and N is the yaw moment around z-axis. $\dot{u}$, $\dot{v}$, and $\dot{r}$ represent cinematic and angular accelerations respectively, r is angular velocity of yaw, I_{zz} is inertia moment around z-axis, m denotes mass of the ship. J_{zz}, m_x, m_y are produced owing to added inertia and mass.

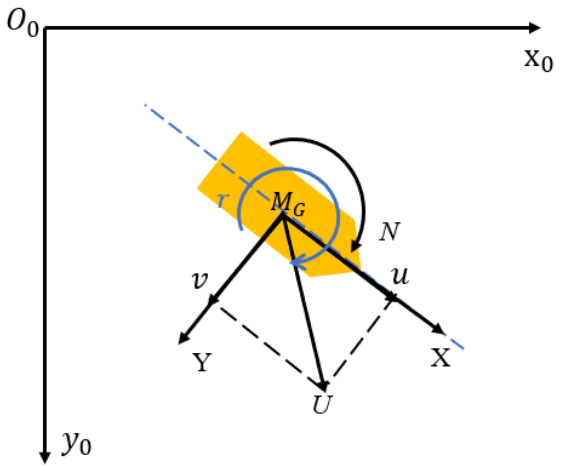

Fig 6. 1 Coordinate system for ship maneuvering motion in Abkowitz model

The hydrodynamic forces and moment in non-dimensional forms can be expressed in Taylor series expansion as equation (6.2):

$$
\begin{aligned}
X' = {} & X* + X_{\dot{u}}\dot{u}' + X_u\Delta u' + X_{uu}\Delta u'^2 + X_{uuu}\Delta u'^3 + X_{vv}v'^2 + X_{rr}r'^2 + X_{vvu}v'^2\Delta u' \\
& + X_{rru}r^2\Delta u' + X_{\delta\delta u}\delta^2\Delta u' + X_{vr}v'r' + X_{v\delta}v'\delta + X_{r\delta}r'\delta + X_{vru}v'r'\Delta u' \\
& + X_{v\delta u}v'\delta\Delta u' + X_{r\delta u}r'\delta\Delta u' + X_{\delta\delta}\delta\delta \\
Y' = {} & Y_u\Delta u' + Y_{uu}\Delta u'^2 + Y_{uuu}\Delta u'^3 + Y_{\dot{v}}\dot{v}' + Y_{\dot{r}}\dot{r}' + Y_v v' + Y_{vvv}v'^3 + Y_r r' + Y_{rrr}r'^3 \\
& + Y_{vrr}v'r'^2 + Y_{v\delta\delta}v'\delta\delta + Y_{vu}v'\Delta u' + Y_{vuu}v'\Delta u'^2 + Y_{r\delta\delta}r'\delta^2 + Y_{rvv}rv'^2 + Y_{ru}r'\Delta u' \\
& + Y_{ruu}r'\Delta u'^2 + Y_\delta\delta + Y_\delta\delta^3 + Y_{\delta vv}\delta v'^2 + Y_{\delta rr}\delta r'^2 + Y_{\delta u}\delta\Delta u' + Y_{\delta uu}\delta\Delta u'^2 \\
& + Y_{\delta\delta\delta u}\delta^3\Delta u' + Y_{vr\delta}v'r'\delta \\
N' = {} & N_u\Delta u' + N_{uu}\Delta u'^2 + N_{uuu}\Delta u'^3 + N_{\dot{v}}\dot{v}' + N_{\dot{r}}\dot{r}' + N_v v' + N_{vvv}v'^3 + N_{vrr}v'r'^2 \\
& + N_r r' + N_{rrr}r'^3 + N_{v\delta\delta}v'\delta\delta + N_{vu}v'\Delta u' + N_{vuu}v'\Delta u'^2 + N_{r\delta\delta}r'\delta^2 + N_{rvv}rv'^2 \\
& + N_{ru}r'\Delta u' + N_{ruu}r'\Delta u'^2 + N_\delta\delta + N_\delta\delta^3 + N_{\delta vv}\delta v'^2 + N_{\delta rr}\delta r'^2 + N_{\delta u}\delta\Delta u' \\
& + N_{\delta uu}\delta\Delta u'^2 + N_{\delta\delta\delta u}\delta^3\Delta u' + N_{vr\delta}v'r'\delta
\end{aligned}
\tag{6.2}
$$

Where hydrodynamic derivatives of the first order for X', Y' and Z' are decomposed into acceleration derivatives and velocity derivatives (depicted by $X_{\dot{u}}$, $Y_{\dot{v}}$, $Y_{\dot{r}}$, $N_{\dot{r}}$, $N_{\dot{v}}$ and X_u, Y_v, N_v, Y_r, N_r respectively). X_{uu}, X_{vv}, X_{rr} are uncoupled hydrodynamic coefficients and X_{vr} is hydrodynamic derivatives of cross-coupling for the second-order derivatives. X_{uuu}, Y_{vvv}, Y_{rrr}, N_{vvv}, N_{rrr} are uncoupled coefficients, and Y_{vrr}, Y_{rvv}, N_{vrr}, N_{rvv} are cross-coupled coefficients for the third-order derivatives. Dimensionless linear velocities along x and y axis are denoted by u' and v'. The fluctuation in surge velocity is Δu. The value of the reference steady state for X' is $X*$. δ is 0 as no rudders are considered in this work.

6.1.2 MMG model

In MMG model, Dofs of surge, sway and yaw are represented in the maneuvering motions of inland ships. According to Fig 6. 2, O_0-$x_0y_0z_0$, is the space-fixed coordinate system, inside which the plane x_0-y_0 corresponds to the water surface, and Z_0 point downward vertically. O-xyz is a moving coordinate system fixed on the ship, where the point O is the midship with the x, y, and z axes pointing, respectively, toward the bow, to the starboard, and downwards vertically.

Ψ is heading angle, δ is rudder angle, r is yaw rate. u and v_m are the velocity components in x and y directions.

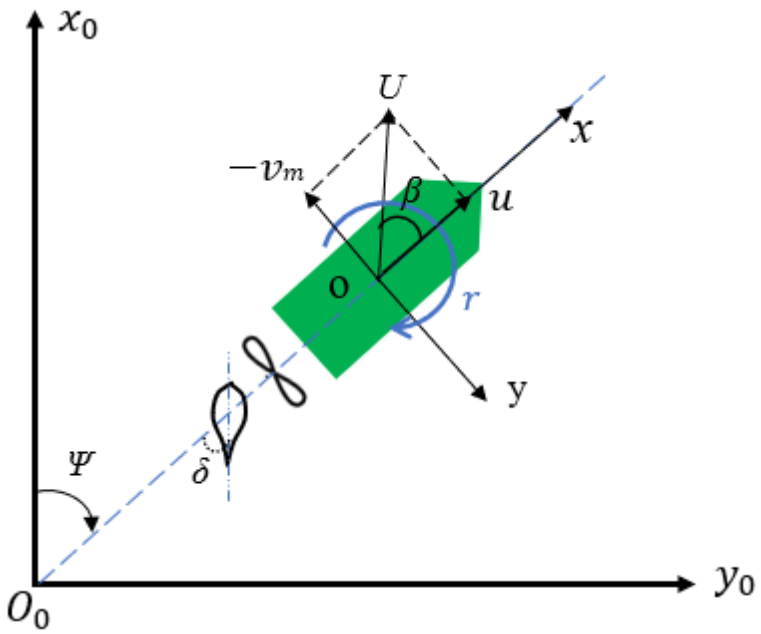

Fig 6. 2 Coordinate system for ship maneuvering motion in MMG model

The motion equations can be expressed as [225, 227, 228]:

$$\left.\begin{aligned} m(\dot{u} - vr) &= F_x \\ m(\dot{v} + ur) &= F_y \\ I_{zG}\dot{r} &= M_z \end{aligned}\right\} \tag{6.3}$$

Where u, v and r are unknown factors. F_x, F_y and M_z can be depicted as:

$$\left.\begin{aligned} F_x &= -m_x\dot{u} + m_y v_m r + X \\ F_y &= -m_y\dot{v}_m - m_x ur + Y \\ M_z &= -J_z\dot{r} + N_m - x_G F_y \end{aligned}\right\} \tag{6.4}$$

Here the added mass coupling terms are ignored.

The coordinate for center of gravity of ship is defined (x_G, 0, 0) in *O-xyz* system. So at the center of gravity, the lateral velocity component is denoted:

$$v = v_m + x_G r \tag{6.5}$$

After integrating equation (6.3) and (6.5) into equation (6.4), the resulting equations are as follows:

$$\left.\begin{aligned} (m + m_x)\dot{u} - (m + m_y)v_m r - x_G m r^2 &= X \\ (m + m_y)\dot{v}_m + (m + m_x)ur + x_G m\dot{r} &= Y \\ (I_{zG} + x_G^2 m + J_z)\dot{r} + x_G m(\dot{v}_m + ur) &= N_m \end{aligned}\right\} \tag{6.6}$$

Where, X, Y and N_m can be expressed:

$$\left.\begin{aligned} X &= X_{\mathrm{H}} + X_{\mathrm{R}} + X_{\mathrm{P}} \\ Y &= Y_{\mathrm{H}} + Y_{\mathrm{R}} \\ N_m &= N_{\mathrm{H}} + N_{\mathrm{R}} \end{aligned}\right\} \tag{6.7}$$

The subscripts H, R and P refer to ship hull, rudder and propeller respectively.

- Hydrodynamic forces applied on ship hull can be expressed [229, 230]:

$$\left.\begin{aligned} X_{\mathrm{H}} &= (1/2)\rho L_{pp} d U^2 X'_{\mathrm{H}}(v'_m, r') \\ Y_{\mathrm{H}} &= (1/2)\rho L_{pp} d U^2 Y'_{\mathrm{H}}(v'_m, r') \\ N_{\mathrm{H}} &= (1/2)\rho L_{pp}^2 d U^2 N'_{\mathrm{H}}(v'_m, r'), \end{aligned}\right\} \tag{6.8}$$

$$\left.\begin{aligned} X'_{\mathrm{H}}(v'_m, r') &= -R'_0 + X'_{vv} v'^2_m + X'_{vr} v'_m r' + X'_{rr} r'^2 + X'_{vvvv} v'^4_m \\ Y'_{\mathrm{H}}(v'_m, r') &= Y'_v v'_m + Y'_{\mathrm{R}} r' + Y'_{vvv} v'^3_m + Y'_{vvr} v'^2_m r' + Y'_{vrr} v'_m r'^2 + Y'_{rrr} r^3 \\ N'_{\mathrm{H}}(v'_m, r') &= N'_v v'_m + N'_{\mathrm{R}} r' + N'_{vvv} v'^3_m + N'_{vvr} v'^2_m r' + N'_{vrr} v'_m r'^2 + N'_{rrr} r'^3 \end{aligned}\right\} \tag{6.9}$$

Where v'_m is lateral velocity in non-dimensional form, r' is non-dimensional yaw rate. $X'_{vv}, X'_{vr}, X'_{rr}, X'_{vvvv}, Y'_v, Y'_{\mathrm{R}}, Y'_{vvv}, Y'_{vvr}, Y'_{vrr}, Y'_{rrr}, N'_v$, $N'_{\mathrm{R}}, N'_{vvv}, N'_{vvr}, N'_{vrr}$, and N'_{rrr} are all hydrodynamic derivatives on maneuvering. In this thesis, rudder and propeller are not considered, so the expressions for rudder and propeller are ignored here.

- Hydrodynamic force X_{P} by propeller can be calculated as:

$$X_{\mathrm{P}} = (1 - C_{\mathrm{P}})T \tag{6.10}$$

Where C_{P} is thrust deduction factor, T is propeller thrust, which can be expressed as follows:

$$\begin{aligned} T &= \rho n_{\mathrm{P}}^2 D_{\mathrm{P}}^4 K_T(J_{\mathrm{P}}) \\ K_T(J_{\mathrm{P}}) &= k_2 J_{\mathrm{P}}^2 + k_1 J_{\mathrm{P}} + k_0 \end{aligned} \tag{6.11}$$

k_2, k_1, k_0 are coefficients expressing K_T; J_{P} is propeller advanced ratio; K_T is propeller thrust open water characteristic; n_{P} is propeller revolution; D_{P} is propeller diameter.

J_{P} can be expressed:

$$J_{\mathrm{P}} = \frac{V_{px}(1-\xi_{\mathrm{P}})}{n_{\mathrm{P}} D_{\mathrm{P}}} \tag{6.12}$$

V_{px} is surge velocity at center of gravity; ξ_{P} is wake coefficient at propeller position in maneuvering motions, which will change with maneuvering motions.

$$\begin{aligned} &\xi_{\mathrm{P}}/\xi_{\mathrm{P0}} = \exp(-4\beta_{\mathrm{P}}^2) \\ &(1-\xi_{\mathrm{P}})/(1-\xi_{\mathrm{P0}}) = 1 + C_1(\beta_{\mathrm{P}} + C_2\beta_{\mathrm{P}}|\beta_{\mathrm{P}}|)^2 \\ &(1-\xi_{\mathrm{P}})/(1-\xi_{\mathrm{P0}}) = 1 + (1-\cos^2\beta_{\mathrm{P}})(1-|\beta_{\mathrm{P}}|) \end{aligned} \tag{6.13}$$

ξ_{P0} is wake coefficient at propeller position in straight moving; β_{P} is the geometrical inflow angle to the propeller in maneuvering motions.

●Hydrodynamic forces due to steering can be expressed [231, 232]:

$$\begin{aligned} X_{\mathrm{R}} &= -(1-C_{\mathrm{R}})F_N \sin\delta \\ Y_{\mathrm{R}} &= -(1+a_{\mathrm{H}})F_N \cos\delta \\ N_{\mathrm{R}} &= -(x_{\mathrm{R}} + a_{\mathrm{H}}x_{\mathrm{H}})F_N \cos\delta \end{aligned} \tag{6.14}$$

C_{R} is steering resistance deduction factor; F_N is rudder normal force; δ is rudder angle; a_{H} is rudder force increase factor; x_{H} is longitudinal coordinate of acting point of the additional lateral force component induced by steering; C_{R}, a_{H}, x_{H} primarily describe the hydrodynamic interaction between the ship's hull and rudder; δ is rudder angle; $F_N\sin\delta$ defines the longitudinal component of F_N; $F_N\cos\delta$ calculates the lateral component of F_N.

In view of the advantages of MMG model over the Abkowitz model, MMG maneuvering model is utilized in the inland ship simulator developed by CEREMA. The resistance force, sway force and yaw moment obtained in the previous sections are formulated as mathematical functions, and then integrated into the MMG model as hydrodynamic derivatives in the navigational simulator. Then the maneuvering model it can be improved by taking into account of the bending effect either by replacing the hydrodynamic forces and moment (X_{H}, Y_{H} and N_{H}) by forces calculated from potential 3D simulations, or by adding a correction term as follows:

$$\left.\begin{aligned} X &= X_{\mathrm{H}} + X_{\mathrm{R}} + X_{\mathrm{P}} + X_{\mathrm{BZ}} \\ Y &= Y_{\mathrm{H}} + Y_{\mathrm{R}} + Y_{\mathrm{BZ}} \\ N_m &= N_{\mathrm{H}} + N_{\mathrm{R}} + N_{\mathrm{BZ}} \end{aligned}\right\} \tag{6.15}$$

Where, X_{BZ}, Y_{BZ} and N_{BZ} are respectively the correction terms of the surge force, sway force and yaw moment. In the next section. Basing on the results given in the previous section, the corrections terms are a function of several parameters.

6.2 Fitting surfaces of the results for bending effect

In this part, the results of forces and moments presented in the previous sections will be fitted and mathematical formulation will be poposed by varying serveral parameters. The general idea of this investigation is to analyze the trend of the response surfaces of several parameters in order to propose a simplified mathematical formulas to represent the effect of the curves on the behavior of ships. After integrating these formulas into the existing inland navigational simulator developed by CEREMA (See Fig 6. 3), realistic trajectories can be predicted for a ship maneuvering in curved fairways. Prediction of hydrodynamics in bending zones will enable simulators to be used to determine optimum waterway conditions (for example, channel widths…) or to determine if ships can securely navigate within planned or existing channel geometries. Furthermore, secure operating ship speeds can be determined for particular operating conditions.

Similarly, some researchers have ever attempted incorporating the bank effect (ship-bank interaction) into navigational simulators [43, 233].

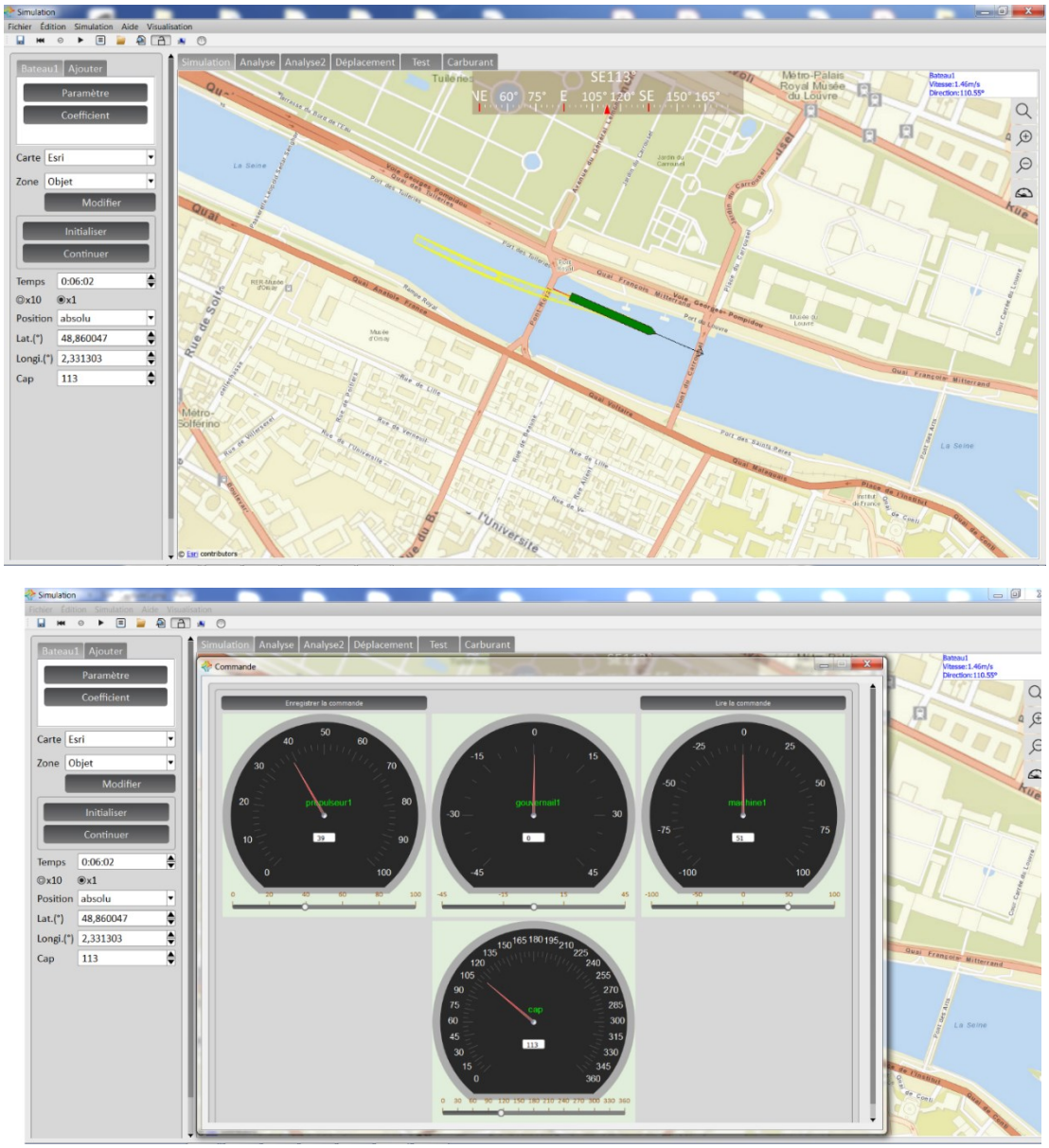

Fig 6. 3 Inland ship simulator of CEREMA

6.2.1 Fitting surfaces of X', Y', N' for h/T ratio effect

The results of X', Y' and N' obtained in Section 5.2 are fitted as smooth surfaces, which are illustrated in Fig 6. 4. The appropriate mathematical formulas for X', Y' and N' surfaces are displayed below each figure.

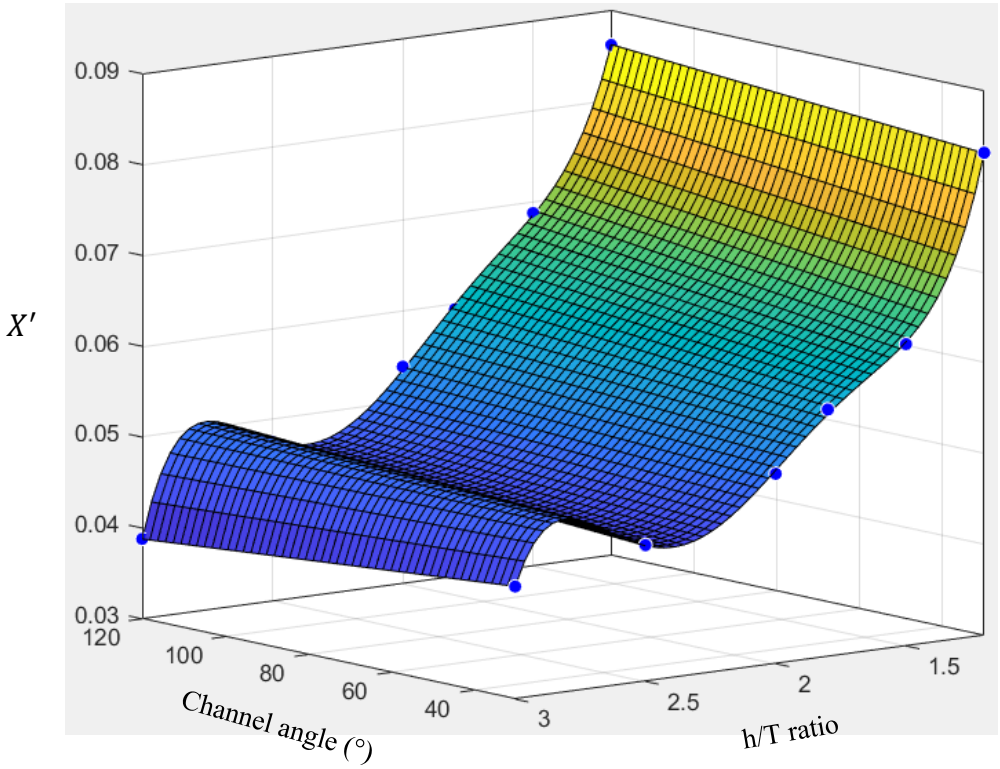

$$X' = 2.469 - 0.002788 * \alpha - 6.086 * (h/T) + 0.006075 * \alpha * (h/T) + 6.099 * (h/T)^2 - 0.004714 * \alpha * (h/T)^2 - 3.016 * (h/T)^3 + 0.001573 * \alpha * (h/T)^3 + 0.7323 * (h/T)^4 - 0.0001916 * \alpha * (h/T)^4 - 0.0697 * (h/T)^5$$

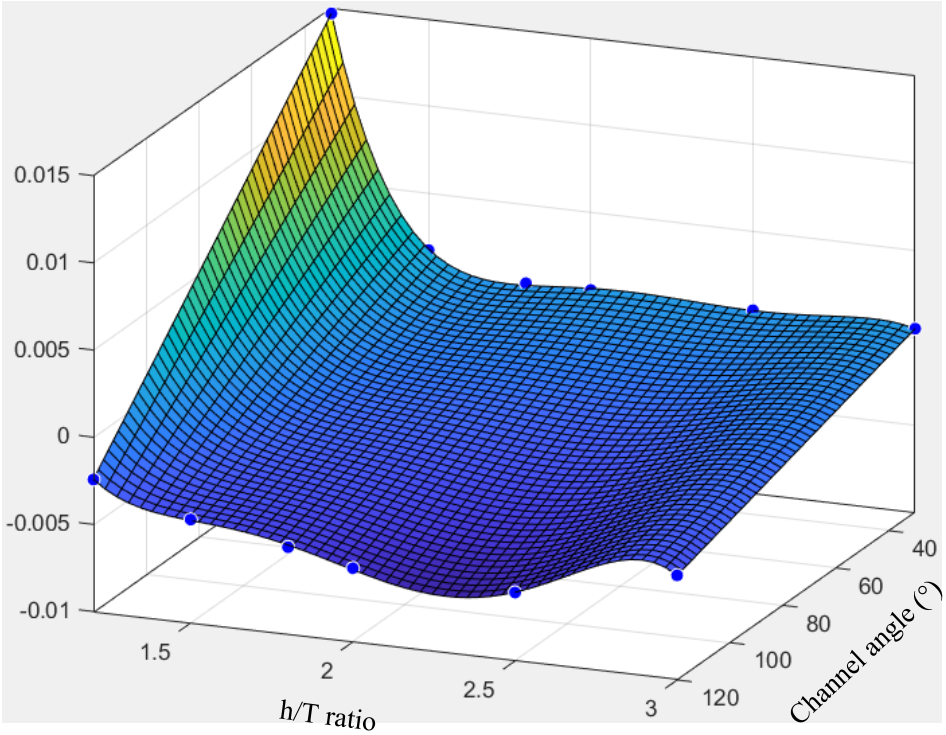

$Y' = 1.035 - 0.005139 * \alpha - 2.287*(h/T) + 0.009637* \alpha *(h/T) + 1.992 *(h/T)^2 - 0.006687 * \alpha *(h/T)^2 - 0.8539*(h/T)^3 + 0.002009* \alpha *(h/T)^3 + 0.1804*(h/T)^4 - 0.0002208* \alpha *(h/T)^4 - 0.01505 *(h/T)^5$

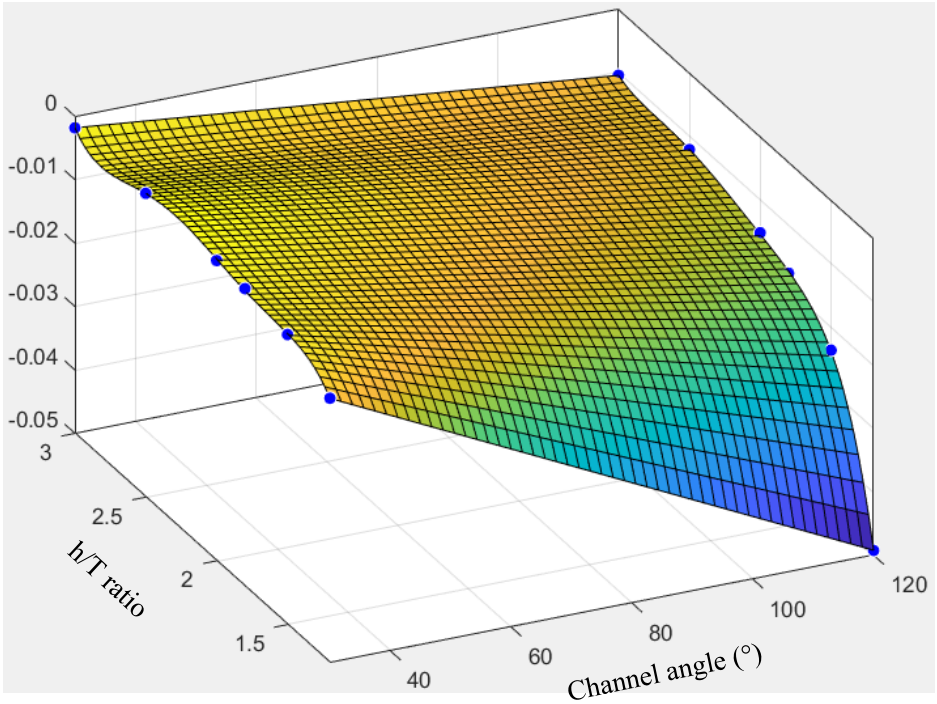

$N' =$ -0.5264 -0.007441 * α + 1.538*(h/T) + 0.01321* α *(h/T) -1.713*$(h/T)^2$ -0.008921 * α *$(h/T)^2$ + 0.9176*$(h/T)^3$ + 0.002654* α *$(h/T)^3$ -0.2374*$(h/T)^4$ -0.000292* α *$(h/T)^4$ + 0.02382 *$(h/T)^5$

Fig 6. 4 Fitting surfaces for results of *h/T* ratio effect

6.2.2 Fitting surfaces of X', Y', N' for ship speed (Vs) effect

To obtain a surface fitting, some other simulations are added to Section 5.3 for ship speed effect, so that the fitting surfaces superpose parameters channel angle and ship speed. X', Y', N' can be then fitted as surfaces as Fig 6. 5. The appropriate mathematical formulas are attached below the figures accordingly.

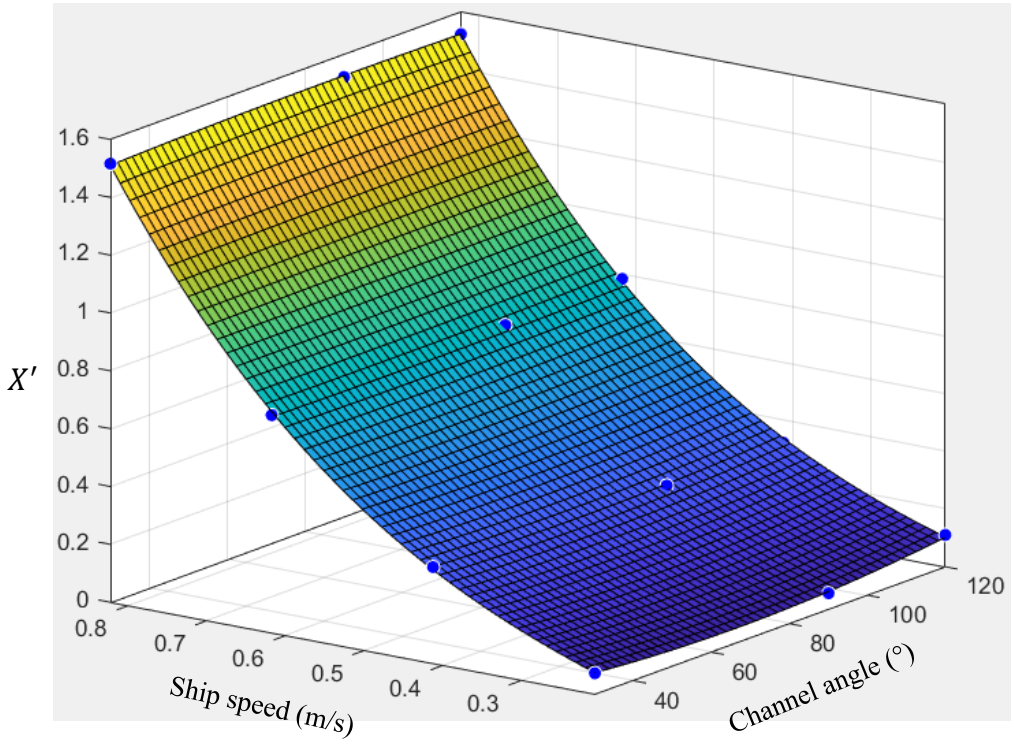

$X' =$ -0.01697 -0.003213 *α + 0.7257*V_s + 2.5e-05*α^2 + 0.003848* α *V_s -0.4259 *V_s^2 -3.564e^{-05} * α^2* V_s + 0.001191 * α *V_s^2 + 2.153 *V_s^3

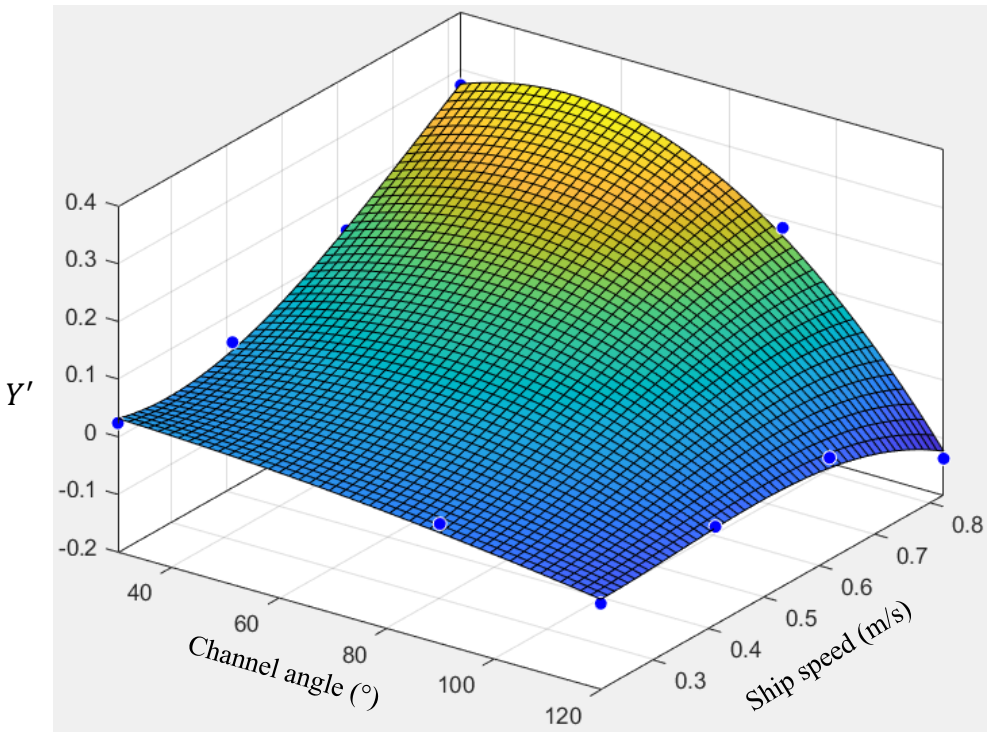

$Y' =$ 0.3184 -0.005386* α -1.929* V_s + 2.165e-05 *α^2 + 0.02963 * α * V_s + 2.89*V_s^2 -0.0001347*α^2* V_s -0.01483* α *V_s^2 -1.079 *V_s^3

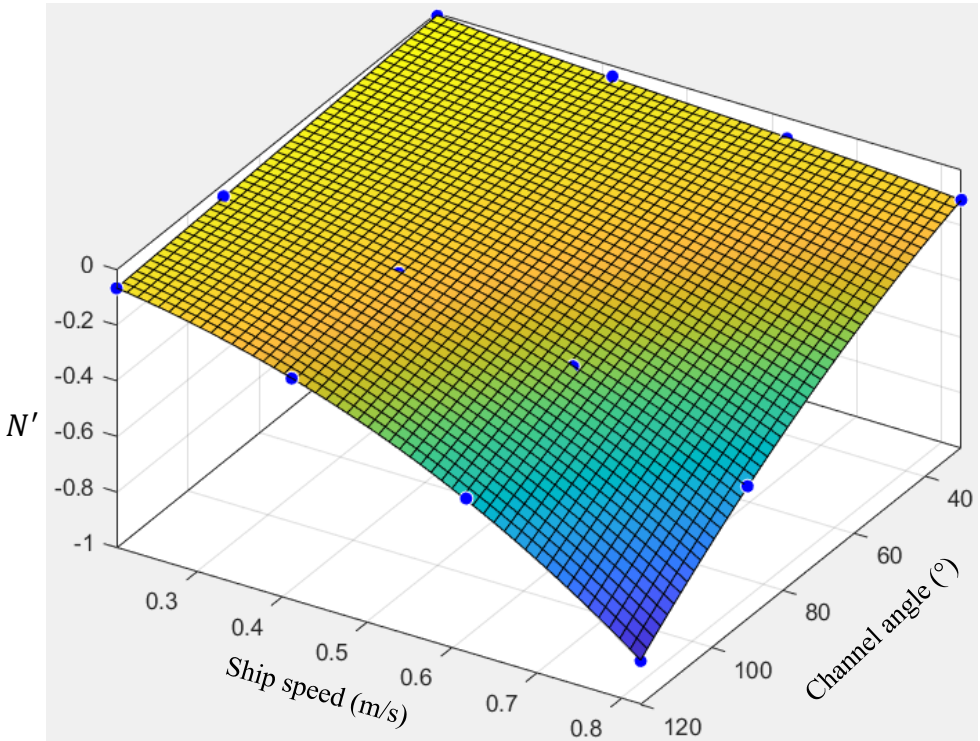

$N' = 0.1447 - 0.003087 * \alpha - 0.8714 * V_s + 1.426e^{-05} * \alpha^2 + 0.01471 * \alpha * V_s + 1.222 * V_s^2 - 6.531e^{-05} * \alpha^2 * V_s - 0.01656 * \alpha * V_s^2 - 0.4708 * V_s^3$

Fig 6. 5 Fitting surfaces for results of ship speed effect

6.2.3 Fitting surfaces of X', Y', N' for channel bottom width (W) effect

The results in Section 4.3 are fitted as surfaces, which are illustrated in Fig 6. 6. The appropriate mathematical formulas for X', Y' and N' surfaces are displayed below.

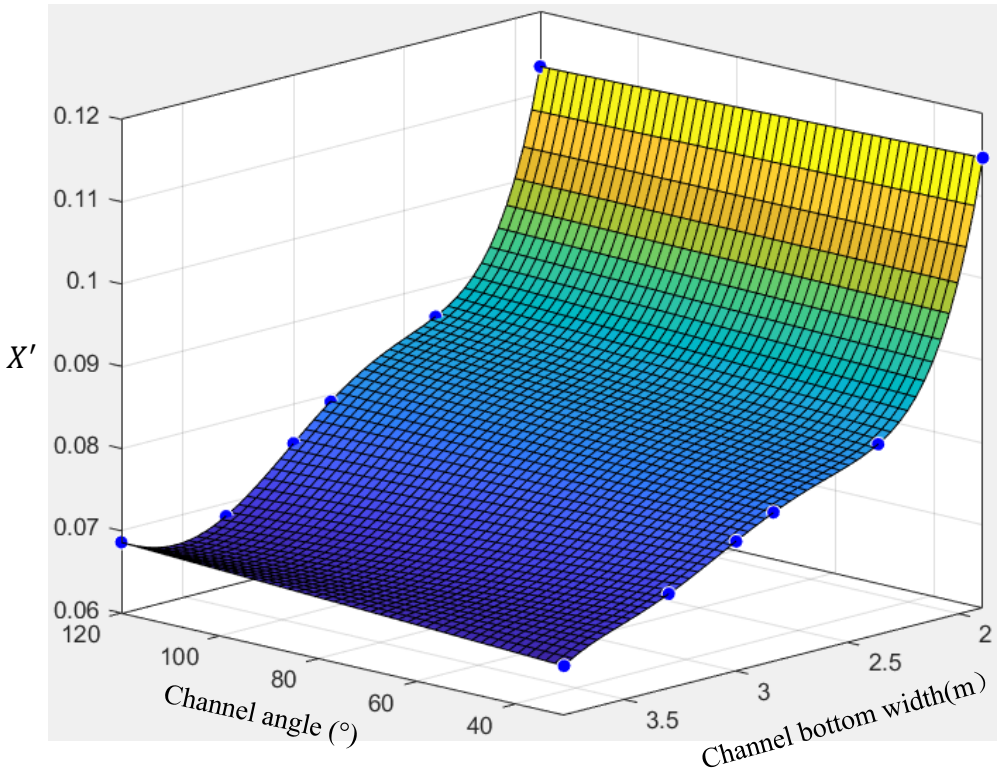

$X' = 5.723 + 0.001011 * \alpha - 9.472 * W - 0.002616 * \alpha * W + 6.334 * W^2 + 0.002064 * \alpha * W^2 - 2.107 * W^3 - 0.0006427 * \alpha * W^3 + 0.3485 * W^4 + 6.916e^{-05} * \alpha * W^4 - 0.02293 * W^5$

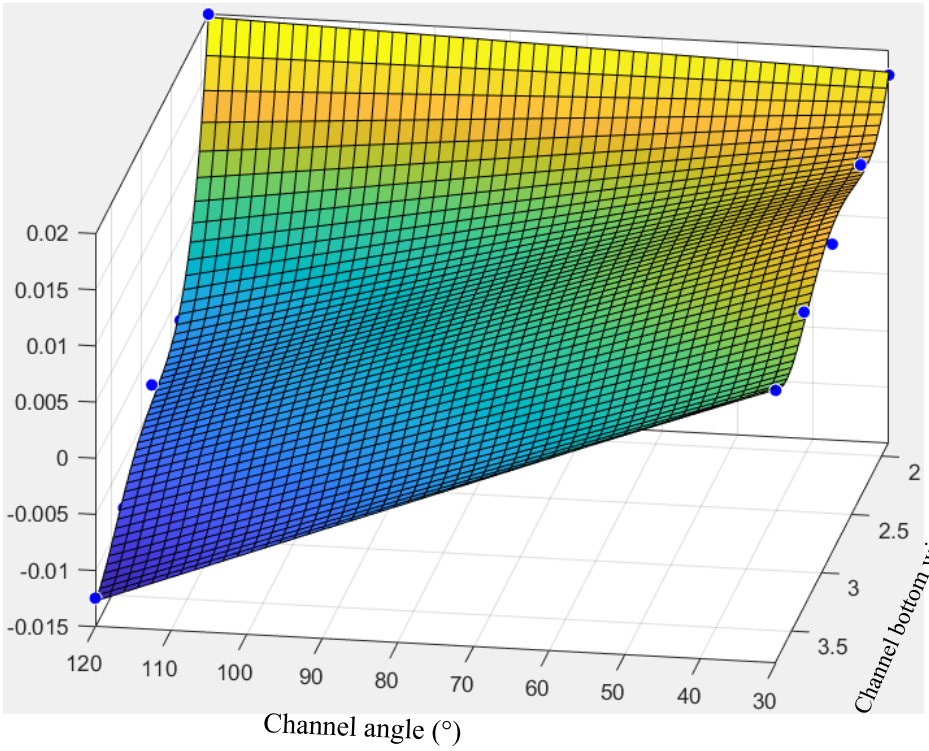

$$Y' = 0.722 + 0.004023 * \alpha - 1.096 * W - 0.004161 * \alpha * W + 0.6229 * W^2 + 0.001358 * \alpha * W^2 - 0.1533 * W^3 - 0.0001472 * \alpha * W^3 + 0.01379 * W^4$$

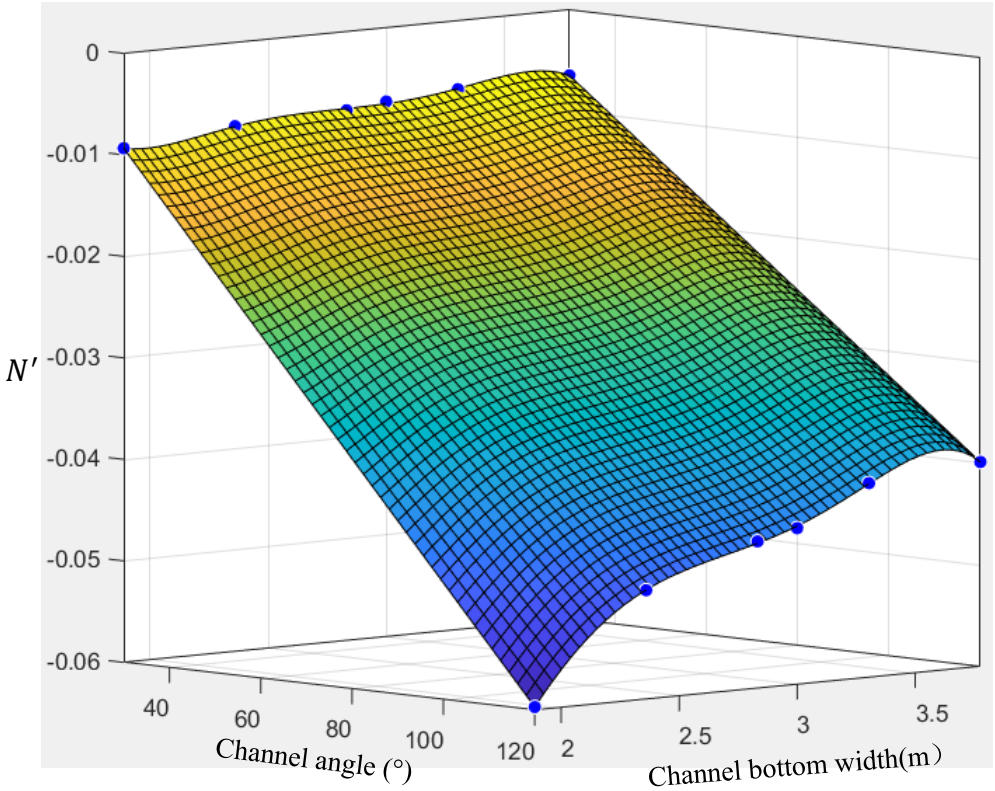

$N' = 1.368 - 0.007959 * \alpha - 2.477 * W + 0.01046 * \alpha * W + 1.779 * W^2 - 0.005473 * \alpha * W^2 - 0.6315 * W^3 + 0.001269 * \alpha * W^3 + 0.1107 * W^4 - 0.0001093 * \alpha * W^4 - 0.007673 * W^5$

Fig 6. 6 Fitting surfaces for results of channel bottom width effect

6.2.4 Fitting surfaces of X', Y', N' for drift angle (β) effect

The results in Section 5.4 are fitted as surfaces, which are illustrated in Fig 6. 7. Smooth surfaces with appropriate fitting formulas for X', Y' and N' are displayed below each figure.

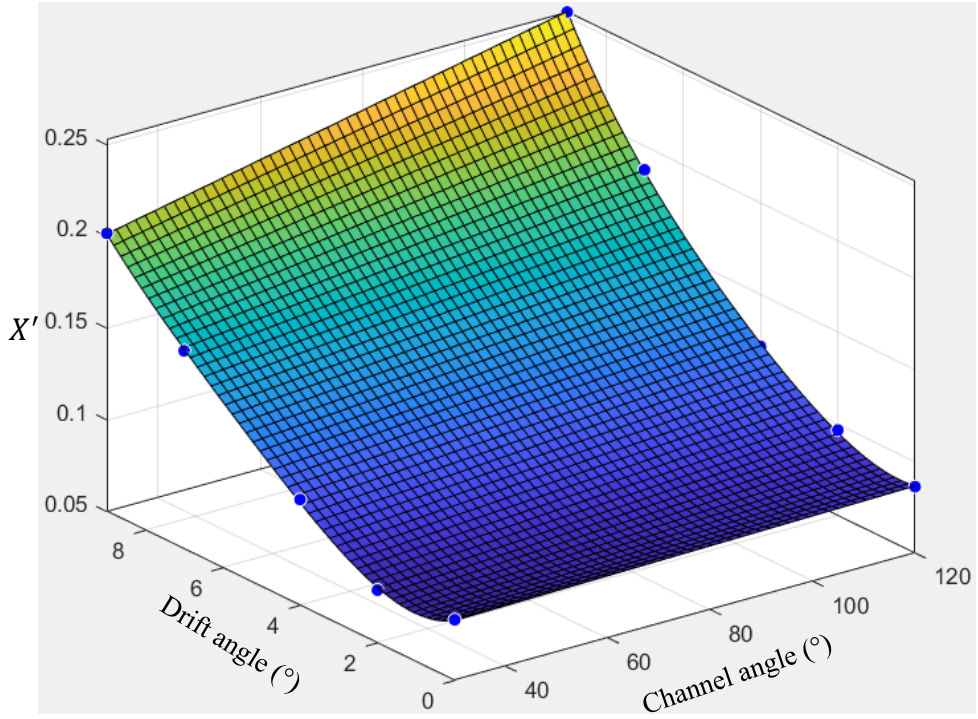

$X' = 0.08141 + 4.292e^{-05} * \alpha - 0.01615 * \beta + 0.0001014 * \alpha * \beta + 0.008229 * \beta^2 - 2.498e^{-05} * \alpha * \beta^2 - 0.0008967 * \beta^3 + 2.255e^{-06} * \alpha * \beta^3 + 3.587e^{-05} * \beta^4$

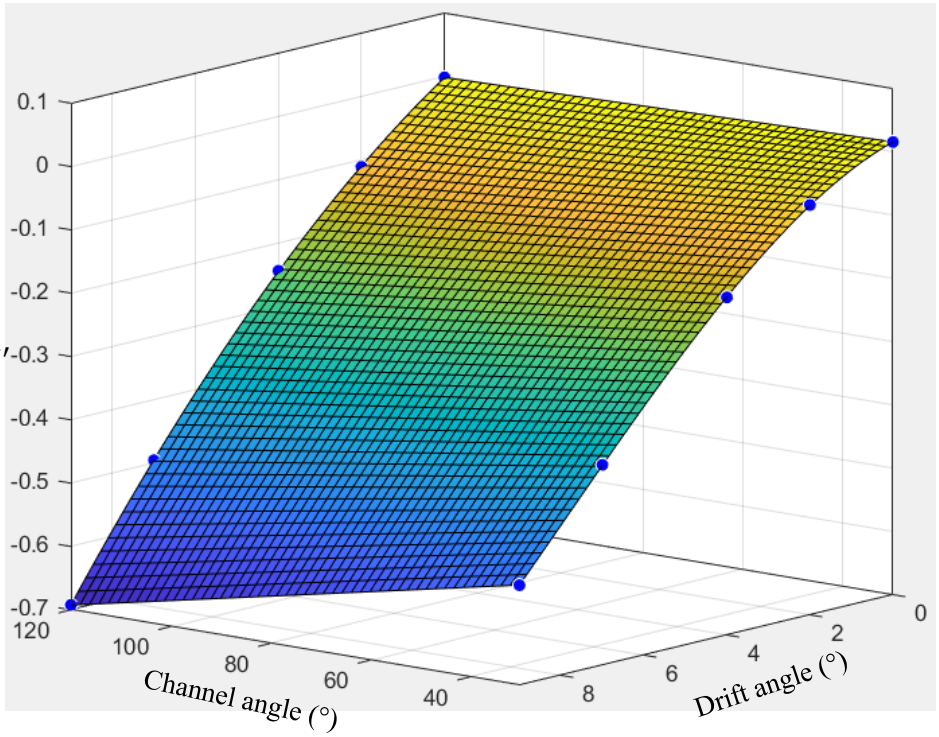

$$Y' = 0.0208 - 0.0001958 * \alpha - 0.01243 * \beta - 0.0002946 * \alpha * \beta - 0.008416 * \beta^2 + 4.365e^{-05} * \alpha * \beta^2 + 0.0003721 * \beta^3 - 3.245e^{-06} * \alpha * \beta^3 + 1.569e^{-06} * \beta^4$$

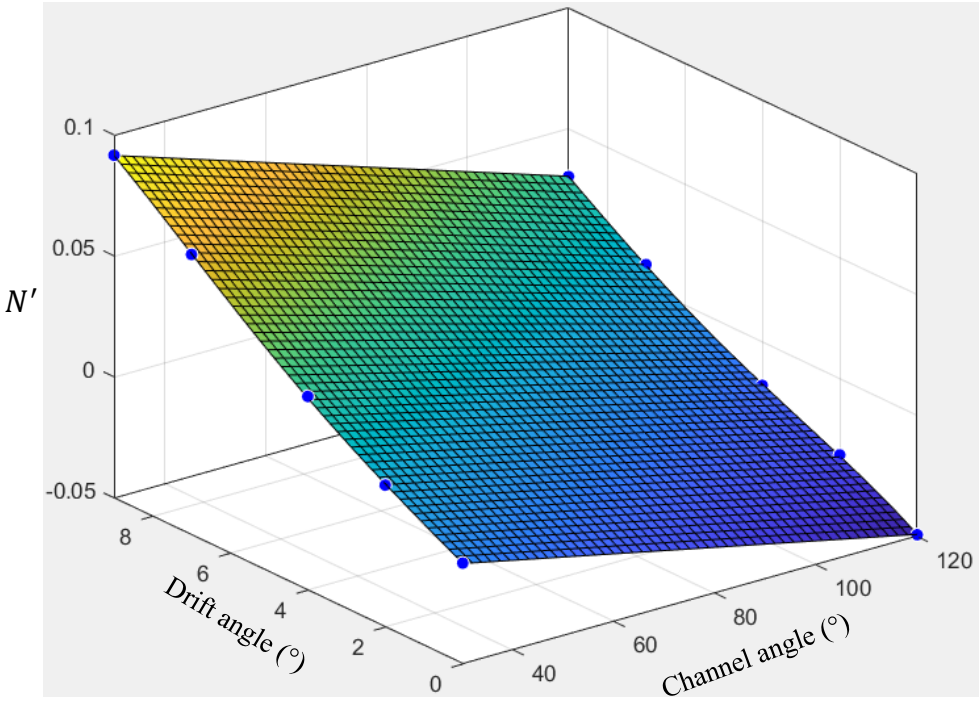

$$N' = 0.005146 - 0.0004521 * \alpha + 0.008214 * \beta + 1.689e^{-05} * \alpha * \beta + 0.0002149 * \beta^2 - 1.164e^{-05} * \alpha * \beta^2 + 8.629e^{-05} * \beta^3 + 7.705e^{-07} * \alpha * \beta^3 - 7.238e^{-06} * \beta^4$$

Fig 6. 7 Fitting surfaces for results of drift angle effect

By doing a first analysis, we observe that some forces and moment can be easily represented by a general formula, however, the hydrodynamic forces and moment (See Fig 4. 2, Fig 4. 6, Fig 5. 6...) in the bending zones are complex and hard to be represented by a simple mathematical formula. This is because of the physical phenomena (propulsive and attractive forces). Where the force can change direction by varying some parameters. This behavior is similar in part to the behaviors of bank effect, which requires an accurate and appropriate analysis for these fitting formulas.

6.1 Conclusion remarks

In this section, the development of navigational simulators are first introduced. Then the two well-known maneuvering models, Abkowitz model and MMG model are described in detail. The inland ship navigator by CEREMA adopts MMG model. Finally, the results obtained from previous sections are fitted as surfaces in 3D view, and appropriate mathematical formulas are displayed below each figure. Then these mathematical formulas can be transformed as hydrodynamic derivatives and integrated into the maneuvering model in the simulator of CEREMA. Due to a time limit, the integration of the results into the navigational simulation of CEREMA has been in progress and will be finished later.

Chapter 7

7. Conclusions and perspectives

7.1 Conclusions

In this thesis, a detailed numerical investigation was performed to study the hydrodynamic behavior of forces and moments in inland curved channels. For this purpose, a verified and validated CFD model based on unsteady RANS equations was used. This investigation has allowed us to better characterize the flow around ships navigating in inland curved areas and also to evaluate the impact of a series of vital parameters in bending zones (a series of navigational environmental parameters, including channel angle, channel bottom width, channel slope angle; a set of parameters related to ship behaviors and geometry, containing water depth to draft ratio, ship speed, drift angle and ship type (ship length)) on forces and moment acting on the ship. Interesting results have been obtained, among them the following:

(1) Contrary to what is known in naval hydrodynamics, when h/T ratio decreases or ship speed increases, the pressure at the bottom of the hull decreases, causing the sinkage. In the curved zones, the opposite is observed, the pressure will increase, especially at the bow zone. This increase is amplified when the channel angle increases.

(2) Compared to straight channels, the ship's resistance (X') is mostly impacted by the confinement (h/T) and the ship's speed (Vs). The increase of the channel angle amplifies significantly this behavior only for h/T variation, especially in very shallow, shallow and medium waters. This impact is principally due to the pressure component. Channel angle has no effect on the change in resistance due to changes in ship speed.

(3) The sway force is the most sensitive force to the changes in restricted channel configurations. Where, its evolution as a function of the channel angle takes the form of Gaussian trend. The sway force increases with the channel angle augmenting, but

the force starts reducing over a critical value of 60°, finally ends up changing direction. The similar phenomenon can be noticed in ship type variation, where sway force increases fast until ship length around 5.5m, but starts decreasing after this critical value. We can also observe that the sway force depends strongly on the ship's speed and the channel width, where this force changes its nature from an attractive force towards the concave bank to a repulsive force for a given value of ship's speed and channel width. This behavior is more visible for larger values of channel angle. The drift angle influence on sway force is characterized by a linear increase.

(4) The yaw moment acting on the ship decreases with increasing *h/T* ratio and channel bottom width. However, it increases with increasing the ship speed, the channel angle, the ship's drift angle and ship length. It is also noted that the ship's moment changes its sign when the ship's drift is larger than 6° in channel with larger channel angle 120°.

(5) The results obtained in the thesis have been fitted as surfaces with appropriate mathematical formulas, in order to be analyzed and used to propose simplified formulas for bending effect. Then what's been derived can be integrated into the inland navigational simulator developed by CEREMA.

7.2 Perspectives

Future efforts will be made to enhance the outcomes and remove the remaining obstacles.

- In this thesis, the ship was fixed in the computational domain, while 6 DOF motions and fluid structure interaction can be considered in the next work.
- The thesis aimed at investigating the effect brought by the change in every single parameter, rather than the effect due to a superposition of multiple parameters. So the drift angle effect was studied separately in Chapter 5.

Besides, if multiple parameters were superposed, there would be large quantities of simulations produced, which is beyond the initial expectation of this thesis. In later work, more simulations superposing drift angle with other parameters can be investigated, although this will be extremely time consuming.

Publications

A.1 Journal articles

[1] **Yang B.**, Kaidi S., Lefrançois E. (2022). Numerical investigation of the parameters that may seriously impact the ship controllability in restricted bending channels. Ocean Engineering, Volume 266, Part 1, 2022, 112735, ISSN 0029-8018. IF=4.372

DOI: https://doi.org/10.1016/j.oceaneng.2022.112735

[2] **Yang B.**, Kaidi S., Lefrançois E. (2022). CFD method to study hydrodynamics forces acting on ship navigating in confined curved channels with current. Journal of Marine Science and Engineering, 2022; 10(9):1263. IF=2.744

DOI: https://doi.org/10.3390/jmse10091263

[3] Lefrançois E., **Yang B.**, Kaidi S., Mohamad, N. (2022). Overcoming the added mass effect in FSI calculations relating to dynamic squat. Ocean Engineering. Volume 267, 2023, 113280, ISSN: 0029-8018. IF=4.372

DOI: https://doi.org/10.1016/j.oceaneng.2022.113280

A.2 Conference articles

[1] **Yang B.**, Kaidi S., Lefrançois E. Numerical investigation of curvature effect on ship hydrodynamics in confined curved channels. The 9th International Conference on Computational Methods in Marine Engineering (MARINE 2021), 2-4 June, 2021, Edinburgh, UK.

DOI: https://doi.org/10.2218/marine2021.6790

References

[1] V.M.Zoran Radmilović, "Role_of_Danube_Inland_Navigation_in_Europe, " International Journal for Traffic and Transport Engineering (IJTTE) 2011.

[2] K. Blanckaert and H. J. de Vriend, "Nonlinear modeling of mean flow redistribution in curved open channels," Water Resources Research, vol. 39, no. 12, 2003.

[3] K. Blanckaert and H. J. De Vriend, "Secondary flow in sharp open-channel bends," Journal of Fluid Mechanics, vol. 498, pp. 353-380, 2004.

[4] K. Blanckaert and H. J. De Vriend, "Turbulence structure in sharp open-channel bends," Journal of Fluid Mechanics, vol. 536, pp. 27-48, 2005.

[5] R. BOOIJ, "Modelling the Flow in Curved Tidal Channels and Rivers," International Conference on Estuaries and Coasts November 9-11, 2003, Hangzhou, China, conference 2003.

[6] S. Eskinazi and H. Yeh, "An Investigation on Fully Developed Turbulent Flows in a Curved Channel," Journal of the Aeronautical Sciences, vol. 23, no. 1, pp. 23-34, 1956.

[7] H. J. D. Vriend, "A Mathematical Model Of Steady Flow In Curved Shallow Channels," Journal of Hydraulic Research, vol. 15, no. 1, pp. 37-54, 1977.

[8] K. Blanckaert, "Flow separation at convex banks in open channels," Journal of Fluid Mechanics, vol. 779, pp. 432-467, 2015.

[9] J. P. T. K. H. J. D. Vriend, "Computation of the Flow in Shallow River Bends," Journal of Hydraulic Research, vol. 18, no. 4, pp. 327-342, 1980.

[10] O. Aseperi, "Dynamics of flow in river bends," Phd thesis, Colorado State University, DISSERTATION 2018.

[11] S.-l. Huang, Y.-f. Jia, H.-C. Chan, and S. S. Y. Wang, "Three-Dimensional Numerical Modeling of Secondary Flows in a Wide Curved Channel," Journal of Hydrodynamics, vol. 21, no. 6, pp. 758-766, 2009.

[12] F. S. Esfahani and A. Keshavarzi, "Effect of different meander curvatures on spatial variation of coherent turbulent flow structure inside ingoing multi-bend river meanders," Stochastic Environmental Research and Risk Assessment, vol. 25, no. 7, pp. 913-928, 2011.

[13] M. N. Uddin and M. M. Rahman, "Flow and erosion at a bend in the braided Jamuna River," International Journal of Sediment Research, vol. 27, no. 4, pp. 498-509, 2012.

[14] J. S. Bridge, "The interaction between channel geometry, water flow, sediment transport and deposition in braided rivers," Geological Society, London, Special Publications, vol. 75, no. 1, pp. 13-71, 1993.

[15] S. Pagliara, A. Radecki-Pawlik, M. Palermo, and K. Plesiński, "Block Ramps in Curved Rivers: Morphology Analysis and Prototype Data Supported Design Criteria for Mild Bed Slopes," River Research and Applications, vol. 33, no. 3, pp. 427-437, 2017.

[16] Z.-H. Chen, H.-G. Zhang, and W.-Z. Ai, Study of the curved inland effect to the ship's navigation and its countermeasures (Design, Manufacturing and Mechatronics). 2016, pp. 1429-1434.

[17] D. C. Lo, D.-T. Su, and J.-M. Chen, "Application of Computational Fluid Dynamics Simulations to the Analysis of Bank Effects in Restricted Waters," Journal of Navigation, vol. 62, no. 3, pp. 477-491, 2009.

[18] S.-j. Ma, M.-g. Zhou, and Z.-j. Zou, "Hydrodynamic interaction among hull, rudder and bank for a ship sailing along a bank in restricted waters," Journal of Hydrodynamics, vol. 25, no. 6, pp. 809-817, 2013.

[19] J. Xu et al., "Study on the squat of extra-large scale ship in the Three Gorges ship lock," Ocean Engineering, vol. 123, pp. 65-74, 2016.

[20] M. Terziev, T. Tezdogan, and A. Incecik, "A geosim analysis of ship resistance decomposition and scale effects with the aid of CFD," Applied Ocean Research, vol. 92, 2019.

[21] S. Duman and S. Bal, "A quick-responding technique for parameters of turning maneuver," Ocean Engineering, vol. 179, pp. 189-201, 2019.

[22] B. J. Dong, J. Lin, and Q. Chen, "Numerical Simulation of Ship Maneuvering on Bend Channel," Applied Mechanics and Materials, vol. 204-208, pp. 4578-4585, 2012.

[23] S. P. M. N. B. Chandra, "Numerical Estimation of Shallow Water Resistance of a River-Sea Ship using CFD," International Journal of Computer Applications 2013.

[24] K. Eloot, J. Verwilligen, and M. Vantorre, "A methodology for evaluating the controllability of a ship navigating in a restricted channel," Archives of Civil and Mechanical Engineering, vol. 7, no. 3, pp. 91-104, 2007.

[25] V. T. Nguyen and F. Nestmann†, "Applications of CFD in Hydraulics and River Engineering," International Journal of Computational Fluid Dynamics, vol. 18, no. 2, pp. 165-174, 2007.

[26] P. Z. Wanzheng Ai, "Navigation Ship’s Drift Angle Determination Method in Curved Channel," Journal of Coastal Research, 2020.

[27] H. Z. Wanzheng Ai , Pengfei Zhu and Hongfu Chi "A Study on Safe Ship Navigation in Curved Bridge Channel," Journal of Coastal Research, pp. 121–125, 2020.

[28] F.-c. J. a. W.-d. G. Yan-wei LI1, *, "Simulation Study on Ship Turning in the Continuous Curved Channel," 2017 International Conference on Electronic, Control, Automation and Mechanical Engineering (ECAME 2017), 2017.

[29] Yanmin Xu1, Junchao Zhao1,2 ,Hongbing Zou1,2, Chunming Zou1,2, Hongxu Guan1,2, "Simulation Study on Course Adaptive Control for Ship Navigating

in Continuous Curved Channel," Proceedings of the Twenty-seventh (2017) International Ocean and Polar Engineering Conference, 2017.

[30] W. W. a. W. A. Zhuohao Guo, "Thousand Ships and Thousands of Faces—Research on Navigation Evaluation Software of Curved Channel," 2018 3rd International Conference on Architectural Engineering and New Materials (ICAENM 2018), 2018.

[31] A. Arifjanov, L. Samiev, T. Apakhodjaeva, and S. Akmalov, "Distribution of river sediment in channels," IOP Conference Series: Earth and Environmental Science, vol. 403, 2019.

[32] O. Y. Maslikova, I. I. Gritsuk, and E. I. Debol'skaya, "The effect of flow velocity distribution on matter transport in a curved channel segment with the effect of moving ships taken into account," IOP Conference Series: Earth and Environmental Science, vol. 321, 2019.

[33] Srđan Vujičić, Robert Mohović, and I. Đ. Tomaš, "Methodology for Controlling the Ship's Path during the Turn in Confined Waterways," SCIENTIFIC JOURNAL OF MARITIME RESEARCH, 2018.

[34] W. Z. Ai, Gan, Xue Zhen, "Analysis on Navigation Reliability of Curved Channel," Applied Mechanics and Materials, vol. 275-277, pp. 2816-2820, 2013.

[35] H. Li, H. Dong, and P. Ji, "Curved water flow characteristics and its influence on navigation," Vibroengineering PROCEDIA, vol. 33, pp. 102-106, 2020.

[36] C.-K. Lee, "Assessment of Safe Navigation Including the Effect of Ship-Ship Interaction in Restricted Waterways," International Journal of Navigation and Port Research, vol. Vol.27, pp. 247-252, 2003.

[37] C.-K. Lee and S.-G. Lee, "Investigation of ship maneuvering with hydrodynamic effects between ship and bank," Journal of Mechanical Science and Technology, vol. 22, no. 6, pp. 1230-1236, 2008.

[38] C.-K. Lee, S.-B. Moon, and T.-G. Jeong, "The investigation of ship maneuvering with hydrodynamic effects between ships in curved narrow channel," International Journal of Naval Architecture and Ocean Engineering, vol. 8, no. 1, pp. 102-109, 2016.

[39] C. H. Wang and X. B. Cheng, "Research on Navigable Ship Model Test in Curved Waterway," Applied Mechanics and Materials, vol. 580-583, pp. 1918-1922, 2014.

[40] B. Yang, S. Kaidi, and E. Lefrançois, "Numerical investigation of the effect of confined curved waterways on ship hydrodynamics," MARINE 2021, p. 181, 2022.

[41] B. Yang, S. Kaidi, and E. Lefrançois, "Numerical investigation of the parameters that may seriously impact the ship control lability in restricted bending channels," Ocean Engineering, vol. 266, 2022.

[42] B. Yang, S. Kaidi, and E. Lefrançois, "CFD Method to Study Hydrodynamics Forces Acting on Ship Navigating in Confined Curved Channels with Current," Journal of Marine Science and Engineering, vol. 10, no. 9, 2022.

[43] L. Evert, "Experiment based mathematical modelling of ship-bank interaction," Phd thesis, vol. Faculteit Ingenieurswetenschappen en Architectuur, 2015.

[44] E. Lataire, M. Vantorre, and G. Delefortrie, "The influence of the ship's speed and distance to an arbitrarily shaped bank on bank effects," Proceedings of the ASME 2015 34th International Conference on Ocean, Offshore and Arctic Engineering, OMAE2015, May 31-June 5, 2015, St. John's, Newfoundland, Canada, 2015.

[45] M. V. Evert Lataire, Guillaume Delefortrie, "Longitudinally Directed Bank Effects," MARSIM2015, 8th – 11th September 2015, Newcastle University, 2015.

[46] A. M. M. Nakisa, Yasser M. Ahmed, F. Behrouzi, Jaswar Koto, A. Priyanto, A. Y. Sian, S. A. Ghazanfari, "Ship navigation effect on sedimentation in restricted waterways," Jurnal Teknologi (Sciences & Engineering) pp. 69:7 (2014), 143–147, 2014.

[47] L. Kobyliński, "Bank effect and operation of inland waterways vessels," Scientific Journals, vol. 37(109) ISSN 1733-8670, pp. pp. 50–55, 2014.

[48] H. Yasukawa, "Maneuvering hydrodynamic derivatives and course stability of a ship close to a bank," Ocean Engineering, vol. 188, 2019.

[49] H. Liu, N. Ma, and X. Gu, "Experimental study on ship-bank interaction of very large crude carrier in shallow water," Journal of Shanghai Jiaotong University (Science), vol. 23, no. 6, pp. 730-739, 2018.

[50] V. N. P. Petru Sergiu ȘERBAN, "Simulation of ship to shore interaction in shallow and narrow waters," Mircea cel Batran" Naval Academy Scientific Bulletin, vol. Volume XVIII 2015.

[51] M. Sano, H. Yasukawa, and H. Hata, "Directional stability of a ship in close proximity to channel wall," Journal of Marine Science and Technology, vol. 19, no. 4, pp. 376-393, 2014.

[52] A. Y. M. Sian, A.; Ahmed, Y.; Rahimuddin, "Simultaneous ship-to-ship interaction and bank effect on a vessel in restricted water," 2016.

[53] A. M. A. Y. Sian, A. Priyanto, Yasser M. Ahmed, "Assessment of ship-bank interactions on LNG tanker in shallow water," Jurnal Teknologi (Sciences & Engineering) 2014.

[54] E. Lataire, M. Vantorre, and G. Delefortrie, "The Influence of the ship's speed and distance to an arbitrarily shaped bank on bank effects," Journal of Offshore Mechanics and Arctic Engineering, vol. 140, no. 2, 2018.

[55] J. Jachowski, "Assessment of ship squat in shallow water using CFD," Archives of Civil and Mechanical Engineering, vol. 8, no. 1, pp. 27-36, 2008.

[56] A. Koop, "Using CFD to determine scale effects on current loads of offshore vessels in side-by-side configuration," Ocean Engineering, vol. 195, 2020.

[57] L. L. L Zou, G Delefortrie, E Lataire, "CFD PREDICTION AND VALIDATION OF SHIP-BANK INTERACTION IN A CANAL," 2nd International conference on ship manoeuvring in shallow and confined water, pp. p.413-422, 2011.

[58] S. Lee and C. Hong, "Study on the course stability of very large vessels in shallow water using CFD," Ocean Engineering, vol. 145, pp. 395-405, 2017.

[59] F. Stern et al., "Recent progress in CFD for naval architecture and ocean engineering," Journal of Hydrodynamics, vol. 27, no. 1, pp. 1-23, 2015.

[60] T. Tezdogan, A. Incecik, and O. Turan, "A numerical investigation of the squat and resistance of ships advancing through a canal using CFD," Journal of Marine Science and Technology, vol. 21, no. 1, pp. 86-101, 2015.

[61] T. Tezdogan, Y. K. Demirel, P. Kellett, M. Khorasanchi, A. Incecik, and O. Turan, "Full-scale unsteady RANS CFD simulations of ship behaviour and performance in head seas due to slow steaming," Ocean Engineering, vol. 97, pp. 186-206, 2015.

[62] T. Tezdogan, A. Incecik, and O. Turan, "Full-scale unsteady RANS simulations of vertical ship motions in shallow water," Ocean Engineering, vol. 123, pp. 131-145, 2016.

[63] Y. Liu, L. Zou, and Z.-J. Zou, "Computational fluid dynamics prediction of hydrodynamic forces on a manoeuvring ship including effects of dynamic sinkage and trim," Proceedings of the Institution of Mechanical Engineers, Part M: Journal of Engineering for the Maritime Environment, vol. 233, no. 1, pp. 251-266, 2017.

[64] M. V. Katrien Eloot "Ship behaviour in Shallow and Confined Water: an Overview of Hydrodynamic Effects through EFD," Assessment of stability and control prediction, 2011.

[65] J. A. Kramer, S. Steen, and L. Savio, "Experimental study of the effect of drift angle on a ship-like foil with varying aspect ratio and bottom edge shape," Ocean Engineering, vol. 121, pp. 530-545, 2016.

[66] P. Mucha, O. e. Moctar, T. Dettmann, and M. Tenzer, "An experimental study on the effect of confined water on resistance and propulsion of an inland waterway ship," Ocean Engineering, vol. 167, pp. 11-22, 2018.

[67] H. Liu, N. Ma, and X. Gu, "CFD prediction of ship-bank interaction for KCS under extreme conditions," Journal of Marine Science and Technology, 2021.

[68] Y. Liu, Z. Zou, L. Zou, and S. Fan, "CFD-based numerical simulation of pure sway tests in shallow water towing tank," Ocean Engineering, vol. 189, 2019.

[69] S. Song, Y. K. Demirel, M. Atlar, S. Dai, S. Day, and O. Turan, "Validation of the CFD approach for modelling roughness effect on ship resistance," Ocean Engineering, vol. 200, 2020.

[70] S. RoyChoudhury, A. K. Dash, V. Nagarajan, and O. P. Sha, "CFD simulations of steady drift and yaw motions in deep and shallow water," Ocean Engineering, vol. 142, pp. 161-184, 2017.

[71] N. K. Ivan Shevchuk, "STUDY OF UNSTEADY HYDRODYNAMIC EFFECTS IN THE STERN AREA OF RIVER CRUISERS IN SHALLOW WATER," VII International Conference on Computational Methods in Marine Engineering MARINE 2017, vol. 440-448, p. 8, 2017.

[72] L. Zou and L. Larsson, "Computational fluid dynamics (CFD) prediction of bank effects including verification and validation," Journal of Marine Science and Technology, vol. 18, no. 3, pp. 310-323, 2013.

[73] M. Terziev, T. Tezdogan, E. Oguz, T. Gourlay, Y. K. Demirel, and A. Incecik, "Numerical investigation of the behaviour and performance of ships advancing through restricted shallow waters," Journal of Fluids and Structures, vol. 76, pp. 185-215, 2018.

[74] P. Du, A. Ouahsine, P. Sergent, and H. Hu, "Resistance and wave characterizations of inland vessels in the fully-confined waterway," Ocean Engineering, vol. 210, 2020.

[75] P. Du, A. Ouahsine, K. T. Toan, and P. Sergent, "Simulation of ship maneuvering in a confined waterway using a nonlinear model based on optimization techniques," Ocean Engineering, vol. 142, pp. 194-203, 2017.

[76] S. Kaidi, H. Smaoui, and P. Sergent, "Numerical estimation of bank-propeller-hull interaction effect on ship manoeuvring using CFD method," Journal of Hydrodynamics, vol. 29, no. 1, pp. 154-167, 2017.

[77] H. S. Sami Kaidi, Philippe sergent, Fabrice Daly, "NUMERICAL INVESTIGATION OF THE IMPACT OF THE INLAND TRANSPORT ON BED EROSION AND TRANSPORT OF SUSPENDED SEDIMENT :," PIANC-World Congress Panama City, Panama 2018, 2018.

[78] S. Kaidi, H. Smaoui, and P. Sergent, "CFD Investigation of Mutual Interaction between Hull, Propellers, and Rudders for an Inland Container Ship in Deep, Very Deep, Shallow, and Very Shallow Waters," Journal of Waterway, Port, Coastal, and Ocean Engineering, vol. 144, no. 6, 2018.

[79] I. Razgallah, S. Kaidi, H. Smaoui, and P. Sergent, "The impact of free surface modelling on hydrodynamic forces for ship navigating in inland waterways: water depth, drift angle, and ship speed effect," Journal of Marine Science and Technology, vol. 24, no. 2, pp. 620-641, 2018.

[80] K. S. Razgallah I, Smaoui H and Sergent P, "Experimental Study of the Impact of Drift, Depth, and Lateral Restrictions on Inland Ship-Induced Waves under Small and Moderate Ship Speeds," Civil Engineering Research Journal, vol. 11, no. 4, 2021.

[81] S. Kaidi, E. Lefrançois, and H. Smaoui, "Numerical modelling of the muddy layer effect on Ship's resistance and squat," Ocean Engineering, vol. 199, 2020.

[82] J. Bechthold and M. Kastens, "Robustness and quality of squat predictions in extreme shallow water conditions based on RANS-calculations," Ocean Engineering, vol. 197, 2020.

[83] K. Elsherbiny, M. Terziev, T. Tezdogan, A. Incecik, and M. Kotb, "Numerical and experimental study on hydrodynamic performance of ships advancing through different canals," Ocean Engineering, vol. 195, 2020.

[84] K. Elsherbiny, T. Tezdogan, M. Kotb, A. Incecik, and S. Day, "Experimental analysis of the squat of ships advancing through the New Suez Canal," Ocean Engineering, vol. 178, pp. 331-344, 2019.

[85] M. Ueno and T. Nimura, "On Steady Drifting Motion of a Ship in Waves," IFAC Proceedings Volumes, vol. 33, no. 21, pp. 387-392, 2000.

[86] X.-g. Wang, Z.-j. Zou, X.-r. Hou, and F. Xu, "System identification modelling of ship manoeuvring motion based on ε-support vector regression," Journal of Hydrodynamics, vol. 27, no. 4, pp. 502-512, 2015.

[87] X.-g. Wang, Z.-j. Zou, L. Yu, and W. Cai, "System identification modeling of ship manoeuvring motion in 4 degrees of freedom based on support vector machines," China Ocean Engineering, vol. 29, no. 4, pp. 519-534, 2015.

[88] X. Yang, Y. Yin, and J. Lian, "A numerical study on flow field and maneuvering derivatives of KVLCC2 model at drift condition," Journal of Marine Engineering & Technology, vol. 20, no. 1, pp. 52-63, 2019.

[89] X.-g. Zhang and Z.-j. Zou, "Identification of Abkowitz Model for Ship Manoeuvring Motion Using ε -Support Vector Regression," Journal of Hydrodynamics, vol. 23, no. 3, pp. 353-360, 2011.

[90] D. B. Poojari, S. Janardhanan, and A. R. Kar, "Maneuverability Assessment of a Container Ship using Steady RANS Method," in The Twenty-fourth International Ocean and Polar Engineering Conference, 2014, vol. All Days, ISOPE-I-14-350.

[91] G. Taimuri, J. Matusiak, T. Mikkola, P. Kujala, and S. Hirdaris, "A 6-DoF maneuvering model for the rapid estimation of hydrodynamic actions in deep and shallow waters," Ocean Engineering, vol. 218, 2020.

[92] X. Tang, S. Tong, G. Huang, and G. Xu, "Numerical investigation of the maneuverability of ships advancing in the non-uniform flow and shallow water areas," Ocean Engineering, vol. 195, 2020.

[93] Y. Jian-Chuan, Z. Zao-Jian, and X. Feng, "Parametric Identification of Abkowitz Model for Ship Maneuvering Motion by Using Partial Least Squares Regression," Journal of Offshore Mechanics and Arctic Engineering, vol. 137, no. 3, 2015.

[94] P. Du, A. Ouahsine, K. T. Tran, and P. Sergent, "Simulation of the overtaking maneuver between two ships using the non-linear maneuvering model," Journal of Hydrodynamics, vol. 30, no. 5, pp. 791-802, 2018.

[95] S. M. Yeon, C. S. Kwon, Y. C. Kim, and K. S. Kim, "Study of the lift effect on wind load estimation for a semi-submersible rig using the maritime atmospheric boundary layer model," International Journal of Naval Architecture and Ocean Engineering, vol. 14, 2022.

[96] F. H. Sighard, "Fluid Dynamic Drag, Practical Information on Aerodynamic Drag and Hydrodynamic Resistance " 1965.

[97] J.-H. Lee and Y. Kim, "Study on steady flow approximation in turning simulation of ship in waves," Ocean Engineering, vol. 195, 2020.

[98] O. M. F. a. A. E. LOKEN, "Slow drift oscillations of a ship in irregular waves," Applied Ocean Research, 1979.

[99] W. Zhang, O. el Moctar, and T. E. Schellin, "Numerical study on wave-induced motions and steady wave drift forces for ships in oblique waves," Ocean Engineering, vol. 196, 2020.

[100] K. Mahesh, "Direct numerical and large–eddy simulation of complex turbulent flows," in Advanced Approaches in Turbulence, 2021, pp. 33-81.

[101] P. Du, H. Hu, F. Ren, and D. Song, "Bubble characterizations on hydrophobic surface using Lattice Boltzmann simulation with large density ratios," International Journal of Numerical Methods for Heat & Fluid Flow, vol. 27, no. 6, 2017.

[102] I. Shevchuk and N. Kornev, "A study of unsteady hydrodynamic effects in the stern area of river cruisers in shallow water," Ship Technology Research, vol. 64, no. 2, pp. 87-105, 2017.

[103] M. Kashiwagi, K. Endo, and H. Yamaguchi, "Wave drift forces and moments on two ships arranged side by side in waves," Ocean Engineering, vol. 32, no. 5-6, pp. 529-555, 2005.

[104] P. Du, J. Wen, Z. Zhang, D. Song, A. Ouahsine, and H. Hu, "Maintenance of air layer and drag reduction on superhydrophobic surface," Ocean Engineering, vol. 130, pp. 328-335, 2017.

[105] S. Roˇzman, "Wake pattern of a boat," UNIVERSITY OF LJUBLJANA, FACULTY OF MATHEMATICS AND PHYSICS DEPARTMENT OF PHYSICS, 2009.

[106] J. Klostermann, K. Schaake, and R. Schwarze, "Numerical simulation of a single rising bubble by VOF with surface compression," International Journal for Numerical Methods in Fluids, vol. 71, no. 8, pp. 960-982, 2013.

[107] M.-H. K. Jong-Chun Park, Hideaki Miyata, "Three-dimensional numerical wave tank simulations on fully nonlinear wave–current–body interactions," Journal of Marine Engineering & Technology, vol. 6, pp. 70–82, 2001.

[108] A. Kang and B. Zhu, "Wave–current interaction with a vertical square cylinder at different Reynolds numbers," Journal of Modern Transportation, vol. 21, no. 1, pp. 47-57, 2013.

[109] D. Lörstad and L. Fuchs, "High-order surface tension VOF-model for 3D bubble flows with high density ratio," Journal of Computational Physics, vol. 200, no. 1, pp. 153-176, 2004.

[110] I. López, B. Pereiras, F. Castro, and G. Iglesias, "Optimisation of turbine-induced damping for an OWC wave energy converter using a RANS–VOF numerical model," Applied Energy, vol. 127, pp. 105-114, 2014.

[111] S.-W. Park, S.-H. Kim, Y.-I. Kim, and I. Lee, "Hull Form Optimization Study Based on Multiple Parametric Modification Curves and Free Surface Reynolds-Averaged Navier–Stokes (RANS) Solver," Applied Sciences, vol. 12, no. 5, 2022.

[112] Z. Kok, J. Duffy, S. Chai, and Y. Jin, "Multiple Approaches to Numerical Modeling of Container Ship Squat in Confined Water," Journal of Waterway, Port, Coastal, and Ocean Engineering, vol. 146, no. 4, 2020.

[113] L. Oggiano, F. Pierella, T. A. Nygaard, J. De Vaal, and E. Arens, "Comparison of Experiments and CFD Simulations of a Braceless Concrete Semi-submersible Platform," Energy Procedia, vol. 94, pp. 278-289, 2016.

[114] L. Zou and L. Larsson, "Numerical predictions of ship-to-ship interaction in shallow water," Ocean Engineering, vol. 72, pp. 386-402, 2013.

[115] D. Kim, T. Tezdogan, and A. Incecik, "A high-fidelity CFD-based model for the prediction of ship manoeuvrability in currents," Ocean Engineering, vol. 256, 2022.

[116] D. Kim and T. Tezdogan, "CFD-based hydrodynamic analyses of ship course keeping control and turning performance in irregular waves," Ocean Engineering, vol. 248, 2022.

[117] P. M. Carrica, A. Mofidi, K. Eloot, and G. Delefortrie, "Direct simulation and experimental study of zigzag maneuver of KCS in shallow water," Ocean Engineering, vol. 112, pp. 117-133, 2016.

[118] C. Chen, G. Delefortrie, and E. Lataire, "Experimental investigation of practical autopilots for maritime autonomous surface ships in shallow water," Ocean Engineering, vol. 218, 2020.

[119] F. Linde., "3D modelling of ship resistance in restricted waterways and application to an inland eco-driving prototype," 2017.

[120] R. Maccormack and A. Paullay, "Computational efficiency achieved by time splitting of finite difference operators," presented at the 10th Aerospace Sciences Meeting, 1972.

[121] H. Jasak, "Error Analysis and Estimation for the Finite Volume Method with Applications to Fluid Flows," Phd thesis, Department of Mechanical Engineering Imperial College

of Science, Technology and Medicine, 1996.

[122] T. OHMORI, "Finite-volume simulation of flows about a ship in maneuvering motion," Journal of Marine Engineering & Technology, vol. 3, pp. 82-93, 1998.

[123] B. Blais, M. Lassaigne, C. Goniva, L. Fradette, and F. Bertrand, "A semi-implicit immersed boundary method and its application to viscous mixing," Computers & Chemical Engineering, vol. 85, pp. 136-146, 2016.

[124] R. V. Wilson, P. M. Carrica, and F. Stern, "Unsteady RANS method for ship motions with application to roll for a surface combatant," Computers & Fluids, vol. 35, no. 5, pp. 501-524, 2006.

[125] D. C. Wilcox, "Simulation of Transition with a Two-Equation Turbulence Model," AIAA Journal, vol. 32, no. 2, pp. 247-255, 1994.

[126] J. Wang, L. Zou, and D. Wan, "Numerical simulations of zigzag maneuver of free running ship in waves by RANS-Overset grid method," Ocean Engineering, vol. 162, pp. 55-79, 2018.

[127] Y. M. Shen, C. O. Ng, and Y. H. Zheng, "Simulation of wave propagation over a submerged bar using the VOF method with a two-equation k–ε turbulence modeling," Ocean Engineering, vol. 31, no. 1, pp. 87-95, 2004.

[128] P. K. Senecal, E. Pomraning, K. J. Richards, and S. Som, "An Investigation of Grid Convergence for Spray Simulations using an LES Turbulence Model," presented at the SAE Technical Paper Series, 2013.

[129] N. Sakamoto, P. M. Carrica, and F. Stern, "URANS simulations of static and dynamic maneuvering for surface combatant: part 1. Verification and validation for forces, moment, and hydrodynamic derivatives," Journal of Marine Science and Technology, vol. 17, no. 4, pp. 422-445, 2012.

[130] J. S. Zhang, Y. Zhang, D. S. Jeng, P. L. F. Liu, and C. Zhang, "Numerical simulation of wave–current interaction using a RANS solver," Ocean Engineering, vol. 75, pp. 157-164, 2014.

[131] E. Roohi, A. P. Zahiri, and M. Passandideh-Fard, "Numerical simulation of cavitation around a two-dimensional hydrofoil using VOF method and LES turbulence model," Applied Mathematical Modelling, vol. 37, no. 9, pp. 6469-6488, 2013.

[132] J. Yao, W. Jin, and Y. Song, "RANS simulation of the flow around a tanker in forced motion," Ocean Engineering, vol. 127, pp. 236-245, 2016.

[133] J. R. Edwards, C. J. Roy, F. G. Blottner, and H. A. Hassan, "Development of a One-Equation Transition/Turbulence Model," AIAA Journal, vol. 39, no. 9, pp. 1691-1698, 2001.

[134] J. C. Kok, "Resolving the Dependence on Freestream Values for the k-w Turbulence Model," AIAA Journal, vol. 38, no. 7, pp. 1292-1295, 2000.

[135] Y. A. H. A.A. Troshko, "A two-equation turbulence model of turbulent bubbly flows," International Journal of Multiphase Flow, vol. 27, pp. 1965-2000, 2001.

[136] S. T.-I. C. G. SPEZIALE "Analysis of an RNG based turbulence model for separated flows," International Journal of Engineering Science, vol. 20, pp. 1379-1388, 1992.

[137] P. R. Gunjal, V. V. Ranade, and R. V. Chaudhari, "Dynamics of drop impact on solid surface: Experiments and VOF simulations," AIChE Journal, vol. 51, no. 1, pp. 59-78, 2005.

[138] B. Mohammadi, "Analysis of the K-epsilon turbulence model," Editions MASSON; Paris (France);, 1993.

[139] W. N. Edeling, P. Cinnella, R. P. Dwight, and H. Bijl, "Bayesian estimates of parameter variability in the k–ε turbulence model," Journal of Computational Physics, vol. 258, pp. 73-94, 2014.

[140] W. W. L. T.-H. Shih, A. Shabbir, Z. Yang, and J. Zhu, "A New k-ε Eddy Viscosity Model for High Reynolds Number Turbulent Flows-Model Development and Validation," NASA Technical Memorandum 106721, 1994.

[141] W. W. L. Tsan-hsing Shin, Aamir Shabbir, Zhigang Yang, Jiang Zhu "A New k-ε Eddy Viscosity Model for High: Reynolds Number Turbulent Flows " Computers & Fluids, 1995.

[142] Z. Yang and T. H. Shih, "New time scale based k-epsilon model for near-wall turbulence," AIAA Journal, vol. 31, no. 7, pp. 1191-1198, 1993.

[143] M. K. F.R.Menter, R. Langtry, "Ten years of industrial experience with the SST turbulence model," Turbulence, Heat and Mass Transfer, 2003.

[144] A. Hellsten, "Some Improvements in Menter's k-w SST Turbulence Model," 29th AIAA Fluid Dynamics Conference June 15-18, 1998/Albuquerque, NM, 1998.

[145] G. E. A. Sokolichin, "Applicability of the standard k-ε turbulence model to the dynamic simulation of bubble columns: Part I. Detailed numerical simulations," Chemical Engineering Science vol. 54, pp. 2273-2284, 1999.

[146] R. P. H. P.J. RICHARDS, "Appropriate boundary conditions for computational wind engineering models using the k-ε turbulence model," Journal of Wind Engineering and Industrial Aerodynamics vol. 46 & 47, pp. 145-153, 1993.

[147] Q. W. Eric Dow, "Quantification of Structural Uncertainties in the k − ω Turbulence Model," 52nd AIAA/ASME/ASCE/AHS/ASC Structures, Structural Dynamics and Materials Conference, 4 - 7 April 2011, Denver, Colorado, 2011.

[148] F. R. Menter, "Influence of freestream values on k-omega turbulence model predictions," AIAA Journal, vol. 30, no. 6, pp. 1657-1659, 1992.

[149] R. Benzi, E. De Angelis, S. L'Vov V, and I. Procaccia, "Identification and calculation of the universal asymptote for drag reduction by polymers in wall bounded turbulence," Phys Rev Lett, vol. 95, no. 19, p. 194502, Nov 4 2005.

[150] E. L, P. F.S, and V. G, "Viscous flow simulations at high Reynolds numbers without wall functions: Is y+≃1 enough for the near-wall cells?," Computers & Fluids, vol. 170, pp. 157-175, 2018.

[151] N. Singh, A. K. Das, and B. K. Lodh, "Investigation of Turbulence for Wind Flow over a Surface Mounted Cube using Wall Y+ Approach," Indian Journal of Science and Technology, vol. 10, no. 8, pp. 1-11, 2017.

[152] V. K. Srivastav, A. R. Paul, and A. Jain, "Capturing the wall turbulence in CFD simulation of human respiratory tract," Mathematics and Computers in Simulation, vol. 160, pp. 23-38, 2019.

[153] J. Milton E. Vaughn, "Error versus y+ for Three Turbulence Models: Incompressible Flow Over a Unit Flat Plate," 18th AIAA Computational Fluid Dynamics Conference 25 - 28 June 2007, Miami, FL, 2007.

[154] S. M. S. a. S. C. C. Mohd ARIFF, "Wall Y+ approach for dealing with turbulent flow over a suuface mounted cube: part 1- low Reynolds number," Seventh International Conference on CFD in the Minerals and Process Industries CSIRO, Melbourne, Australia 9-11 December 2009, 2009.

[155] S. M. S. a. S. C. C. Mohd ARIFF, "Wall Y+ approach for dealing with turbulent flow over a surface mounted cube: part 2- high Reynolds number," Seventh International Conference on CFD in the Minerals and Process Industries CSIRO, Melbourne, Australia 9-11 December 2009, 2009.

[156] S. K. Rathore and M. K. Das, "Comparison of two low-Reynolds number turbulence models for fluid flow study of wall bounded jets," International Journal of Heat and Mass Transfer, vol. 61, pp. 365-380, 2013.

[157] a. S. C. C. Salim .M. Salim, "Wall y+ Strategy for Dealing with Wall-bounded Turbulent Flows," Proceedings of the International MultiConference of Engineers and Computer Scientists 2009 Vol II IMECS 2009, March 18 - 20, 2009, Hong Kong, 2009.

[158] C. W. H. A. B. D. NICHOLS, "Volume of Fluid (VOF) Method for the Dynamics of Free Boundaries," JOURNAL OF COMPUTATIONAL PHYSICS vol. 39, pp. 201-225 1981.

[159] N. D. Katopodes, "Volume of Fluid Method," in Free-Surface Flow, 2019, pp. 766-802.

[160] A. Albadawi, D. B. Donoghue, A. J. Robinson, D. B. Murray, and Y. M. C. Delauré, "Influence of surface tension implementation in Volume of Fluid and coupled Volume of Fluid with Level Set methods for bubble growth and detachment," International Journal of Multiphase Flow, vol. 53, pp. 11-28, 2013.

[161] I. Chakraborty, G. Biswas, and P. S. Ghoshdastidar, "A coupled level-set and volume-of-fluid method for the buoyant rise of gas bubbles in liquids," International Journal of Heat and Mass Transfer, vol. 58, no. 1-2, pp. 240-259, 2013.

[162] D. A. Hoang, V. van Steijn, L. M. Portela, M. T. Kreutzer, and C. R. Kleijn, "Benchmark numerical simulations of segmented two-phase flows in microchannels using the Volume of Fluid method," Computers & Fluids, vol. 86, pp. 28-36, 2013.

[163] I. Malgarinos, N. Nikolopoulos, M. Marengo, C. Antonini, and M. Gavaises, "VOF simulations of the contact angle dynamics during the drop spreading: standard models and a new wetting force model," Adv Colloid Interface Sci, vol. 212, pp. 1-20, Oct 2014.

[164] M. Owkes and O. Desjardins, "A computational framework for conservative, three-dimensional, unsplit, geometric transport with application to the volume-of-fluid (VOF) method," Journal of Computational Physics, vol. 270, pp. 587-612, 2014.

[165] D. Fuster et al., "Simulation of primary atomization with an octree adaptive mesh refinement and VOF method," International Journal of Multiphase Flow, vol. 35, no. 6, pp. 550-565, 2009.

[166] D. Gao, N. B. Morley, and V. Dhir, "Numerical simulation of wavy falling film flow using VOF method," Journal of Computational Physics, vol. 192, no. 2, pp. 624-642, 2003.

[167] S. Afkhami, Zaleski, S, Bussmann, M., "A mesh-dependent model for applying dynamic contact angles to VOF simulations," Journal of Computational Physics, vol. 228, no. 15, pp. 5370-5389, 2009.

[168] A. Ashish Saha and S. K. Mitra, "Effect of dynamic contact angle in a volume of fluid (VOF) model for a microfluidic capillary flow," J Colloid Interface Sci, vol. 339, no. 2, pp. 461-80, Nov 15 2009.

[169] J. Roenby, H. Bredmose, and H. Jasak, "A computational method for sharp interface advection," R Soc Open Sci, vol. 3, no. 11, p. 160405, Nov 2016.

[170] T. Ménard, S. Tanguy, and A. Berlemont, "Coupling level set/VOF/ghost fluid methods: Validation and application to 3D simulation of the primary break-up of a liquid jet," International Journal of Multiphase Flow, vol. 33, no. 5, pp. 510-524, 2007.

[171] P. M. Carrica, A. M. Castro, and F. Stern, "Self-propulsion computations using a speed controller and a discretized propeller with dynamic overset grids," Journal of Marine Science and Technology, vol. 15, no. 4, pp. 316-330, 2010.

[172] "Uncertainty Analysis in CFD Verification and Validation

Methodology and Procedures," ITTC – Recommended Procedures and Guidelines, vol. 7.5-03 -01-01 Page 1 of 13, 2017.

[173] "Procedure for Estimation and Reporting of Uncertainty Due to Discretization in CFD Applications," Journal of Fluids Engineering, vol. Vol. 130 / 078001-1, July 2008.

[174] Z.-r. Zhang, "Verification and validation for RANS simulation of KCS container ship without/with propeller," Journal of Hydrodynamics, vol. 22, no. S1, pp. 889-896, 2010.

[175] L. Zou, L. Larsson, and M. Orych, "Verification and validation of CFD predictions for a manoeuvring tanker," Journal of Hydrodynamics, vol. 22, no. S1, pp. 421-428, 2010.

[176] H. Jasak, V. Vukčević, I. Gatin, and I. Lalović, "CFD validation and grid sensitivity studies of full scale ship self propulsion," International Journal of Naval Architecture and Ocean Engineering, vol. 11, no. 1, pp. 33-43, 2019.

[177] P. Mannion, Y. Toparlar, B. Blocken, M. Hajdukiewicz, T. Andrianne, and E. Clifford, "Improving CFD prediction of drag on Paralympic tandem athletes: influence of grid resolution and turbulence model," Sports Engineering, vol. 21, no. 2, pp. 123-135, 2017.

[178] D. J. M. Mark A. Potsdam, "Unstructured Mesh CFD Aerodynamic Analysis of the NREL Phase VI Rotor," 47th AIAA Aerospace Sciences Meeting Including The New Horizons Forum and Aerospace Exposition 5 - 8 January 2009, Orlando, Florida, 2009.

[179] S. L. K. Jr., "Splitflow a 3D unstructured cartesian/ prismatic grid CFD code for complex geometries," 33rd Aerospace Sciences Meeting and Exhibit, January 9-12, 1995/ Reno, NV, 1995.

[180] M. C. Tobias Zitzmann, Peter Pfrommer, Simon Rees, Ljiljana Marjanovic, "Simulation of steady-state natural convection using CFD," Ninth International IBPSA Conference Montréal, Canada August 15-18, 2005, 2005.

[181] N. E. A. a. E. A.-S. c. a. A. Gaylard, "Mesh Optimization for Ground Vehicle Aerodynamics," CFD Letters, vol. 2(1) 2010.

[182] W. M. M. K. Guangyu Wu, Jang Whan Kim Hyunchul Jang, JimO'Sullivan, "Vortex Induced Motions of a Column Stabilized Floater, Part II: CFD Benchmark and Prediction," Deep Offshore Technology International Conference held in Aberdeen, Scotland, 14-16 October 2014., 2014.

[183] M. Tomac and D. Eller, "From geometry to CFD grids—An automated approach for conceptual design," Progress in Aerospace Sciences, vol. 47, no. 8, pp. 589-596, 2011.

[184] V. Dyedov, D. Einstein, X. Jiao, A. Kuprat, J. Carson, and F. D. Pin, "Variational Generation of Prismatic Boundary-Layer Meshes for Biomedical Computing," Int J Numer Methods Eng, vol. 79, no. 8, pp. 907-945, Aug 20 2009.

[185] R. V. Garimella and M. S. Shephard, "Boundary layer mesh generation for viscous flow simulations," International Journal for Numerical Methods in Engineering, vol. 49, no. 1-2, pp. 193-218, 2000.

[186] J. P. Steinbrenner, "Construction of Prism and Hex Layers from Anisotropic Tetrahedra," presented at the 22nd AIAA Computational Fluid Dynamics Conference, 2015.

[187] S. R. Turnock, "Prediction of ship rudder-propeller interaction using parallel computations and wind tunnel measurements," Phd thesis, Faculty of engineering and applied science, University of Southampton,, April 1993.

[188] C. D. Simonsen, "Rudder, propeller and hull interaction by RANS," Phd thesis, Department of naval architecture and offshore engineering, Technical university of Denmark, 2000.

[189] A. Posa, R. Broglia, and E. Balaras, "LES study of the wake features of a propeller in presence of an upstream rudder," Computers & Fluids, vol. 192, 2019.

[190] J. Hu, W. Zhang, S. Sun, and C. Guo, "Numerical simulation of Vortex–Rudder interactions behind the propeller," Ocean Engineering, vol. 190, 2019.

[191] A. Posa and R. Broglia, "Development of the wake shed by a system composed of a propeller and a rudder at incidence," International Journal of Heat and Fluid Flow, vol. 94, 2022.

[192] L. Wang, C. Guo, P. Xu, and Y. Su, "Analysis of the wake dynamics of a propeller operating before a rudder," Ocean Engineering, vol. 188, 2019.

[193] D. Villa, A. Franceschi, and M. Viviani, "Numerical Analysis of the Rudder–Propeller Interaction," Journal of Marine Science and Engineering, vol. 8, no. 12, 2020.

[194] A. B. P. Ameen M. Bassam, Stephen R. Turnock, and Philip A. Wilson, "Ship voyage energy efficiency assessment using ship simulators," VI International Conference on Computational Methods in Marine Engineering, 2015.

[195] N. K. Damitha Sandaruwan, Chamath Keppitiyagama and Rexy Rosa, "A six degrees of freedom ship simulation system for maritime education," The International Journal on Advances in ICT for Emerging Regions vol. 03 (02) :34 - 47, 2010.

[196] K. Murai, T. Okazaki, and Y. Hayashi, "A few comments on visual systems of a ship handling simulator for sea pilot training: Training for entering a port," Electronics and Communications in Japan, vol. 94, no. 9, pp. 10-17, 2011.

[197] Y. Shenhua, W. Xinghua, and C. Guoquan, "Design and Implement on Intelligent Ship Handling Simulator," presented at the 2010 International Conference on Digital Manufacturing & Automation, 2010.

[198] T. K. TADATSUGI OKAZAKI, YURIE HIRAI, JUN KAYANO, "Development of ship simulator system for designing auto-pilot," World Automation Congress, 2010.

[199] M. Hontvedt and H. C. Arnseth, "On the bridge to learn: Analysing the social organization of nautical instruction in a ship simulator," International Journal of Computer-Supported Collaborative Learning, vol. 8, no. 1, pp. 89-112, 2013.

[200] L. B.-j. Hu Qiong, Zheng Hao, "A 6-DOF Deep-ocean mining ship motion simulator," Information Technology Journal vol. 12(24): 8343-8348, 2013.

[201] M. Hontvedt, "Professional vision in simulated environments — Examining professional maritime pilots' performance of work tasks in a full-mission ship simulator," Learning, Culture and Social Interaction, vol. 7, pp. 71-84, 2015.

[202] F. Xiao, Y. Jin, Y. Yin, and Y. Li, "Design and Research of Marine Search and Rescue Simulation System," presented at the 2010 Second International Conference on Information Technology and Computer Science, 2010.

[203] E. van't Wout, M. B. van Gijzen, A. Ditzel, A. van der Ploeg, and C. Vuik, "The Deflated Relaxed Incomplete Cholesky CG method for use in a real-time ship simulator," Procedia Computer Science, vol. 1, no. 1, pp. 249-257, 2010.

[204] M. Wang, "Fuzzy-PID control of the 6-DOF deep-sea mining ship motion simulator," Int. J. Mechanisms and Robotic Systems, vol. Vol. 1, Nos. 2/3, 2013.

[205] I. Cohen, W.-P. Brinkman, and M. A. Neerincx, "Modelling environmental and cognitive factors to predict performance in a stressful training scenario on a naval ship simulator," Cognition, Technology & Work, vol. 17, no. 4, pp. 503-519, 2015.

[206] J. M. Varela and C. Guedes Soares, "Interactive 3D desktop ship simulator for testing and training offloading manoeuvres," Applied Ocean Research, vol. 51, pp. 367-380, 2015.

[207] M. Hontvedt, "A video study of the socio-technical organisation of ship simulator training," Department of Education, Faculty of Educational Sciences, University of Oslo, vol. Phd thesis, 2014.

[208] P. Zalewski, "Models of DP systems in full mission ship simulator," Scientific Journals, Maritime University of Szczecin, vol. 20(92) pp. 146–152, 2010.

[209] M.-C. Fang, K.-Y. Tsai, and C.-C. Fang, "A Simplified Simulation Model of Ship Navigation for Safety and Collision Avoidance in Heavy Traffic Areas," Journal of Navigation, vol. 71, no. 4, pp. 837-860, 2017.

[210] Y. Fukui, H. Yokota, H. Yano, M. Kondo, T. Nakano, and Y. Yoshimura, "4-DOF Mathematical Model for Manoeuvring Simulation including Roll Motion," Journal of the Japan Society of Naval Architects and Ocean Engineers, vol. 24, no. 0, pp. 167-179, 2016.

[211] Y. Y. Yo Fukui, Hiroyuki YANO, Masatoshi KONDO, "Investigation of effect of roll motion on maneuverability using 4-DOF mathematical model," MARSIM2015, 8th – 11th September 2015, Newcastle University, 2015.

[212] K. Wolsing, L. Roepert, J. Bauer, and K. Wehrle, "Anomaly Detection in Maritime AIS Tracks: A Review of Recent Approaches," Journal of Marine Science and Engineering, vol. 10, no. 1, 2022.

[213] R. B. Yong Liu, Xiaori Gao, "Ship trajectory tracking control system design based on sliding mode control algorithm " POLISH MARITIME RESEARCH, vol. 3 (99) 2018 Vol. 25; pp. 26-34, 2018.

[214] Y. K. Min-Guk Seo, "Effects of Ship Motion on Ship Maneuvering in Waves," 26th International Workshop on Water Waves and Floating Bodies, Athens, Greece, 2011.

[215] I. P. S. Asmara, E. Kobayashi, N. Wakabayashi, and K. B. Artana, "Probability of Ship on Collision Courses Based on the New PAW Using MMG Model and AIS Data," TransNav, the International Journal on Marine Navigation and Safety of Sea Transportation, vol. 9, no. 1, pp. 43-50, 2015.

[216] E. K. I Putu Sindhu Asmara, Trika Pitana, "Simulation of collision avoidance in lamong bay port by considering the PAW of target ship using MMG Model and AIS data," Marine Engineering Frontiers (MEF), vol. Volume 2, 2014.

[217] E. K. a. T. P. I. Putu Sindhu Asmara, "Simulation of collision avoidance by considering potential area of water for maneuvering based on MMG Model and AIS data," presented at the Proceedings of the 3rd International Conference on Simulation and Modeling Methodologies, Technologies and Applications, 2013.

[218] H.-p. Guo and Z.-j. Zou, "System-based investigation on 4-DOF ship maneuvering with hydrodynamic derivatives determined by RANS simulation of captive model tests," Applied Ocean Research, vol. 68, pp. 11-25, 2017.

[219] M. Ueno, Y. Yoshimura, Y. Tsukada, and H. Miyazaki, "Circular motion tests and uncertainty analysis for ship maneuverability," Journal of Marine Science and Technology, vol. 14, no. 4, pp. 469-484, 2009.

[220] Y. Xia, S. Zheng, Y. Yang, and Z. Qu, "Ship Maneuvering Performance Prediction Based on MMG Model," IOP Conference Series: Materials Science and Engineering, vol. 452, 2018.

[221] Z. Zhang, X. Zhang, and G. Zhang, "ANFIS-based course-keeping control for ships using nonlinear feedback technique," Journal of Marine Science and Technology, vol. 24, no. 4, pp. 1326-1333, 2018.

[222] X. N. Ning Wang, Yudong Liu, "Online self-constructing fuzzy neural identification for ship motion dynamics based on MMG model," Proceedings of the 10th world congress on intelligent control and automation, vol. July 6-8, Beijing, China, 2012.

[223] L. J. Yang and Y. H. Tao, "Calculation of the Coefficients of Ships Resistant Force in MMG Model Based on CFD," Advanced Materials Research, vol. 694-697, pp. 605-613, 2013.

[224] H. Yasukawa, T. Ishikawa, and Y. Yoshimura, "Investigation on the rudder force of a ship in large drifting conditions with the MMG model," Journal of Marine Science and Technology, vol. 26, no. 4, pp. 1078-1095, 2021.

[225] H. Yasukawa and Y. Yoshimura, "Introduction of MMG standard method for ship maneuvering predictions," Journal of Marine Science and Technology, vol. 20, no. 1, pp. 37-52, 2014.

[226] K. S. A. S. H. RAZGALLAH I., "Investigation of the confinement effect on hydrodynamic derivatives of a 135m inland containership," VII International Conference on Computational Methods in Marine Engineering (MARINE 2017), 2017.

[227] D. Kang and K. Hasegawa, "Prediction method of hydrodynamic forces acting on the hull of a blunt-body ship in the even keel condition," Journal of Marine Science and Technology, vol. 12, no. 1, pp. 1-14, 2007.

[228] Y. Yoshimura, "Mathematical model for manoeuvring ship motion (MMG Model)," Workshop on Mathematical Models for Operations involving Ship-Ship Interaction vol. August 2005 Tokyo, 2005

[229] Q. Zhang, X.-k. Zhang, and N.-k. Im, "Ship nonlinear-feedback course keeping algorithm based on MMG model driven by bipolar sigmoid function for berthing," International Journal of Naval Architecture and Ocean Engineering, vol. 9, no. 5, pp. 525-536, 2017.

[230] W. Zhang, Z.-J. Zou, and D.-H. Deng, "A study on prediction of ship maneuvering in regular waves," Ocean Engineering, vol. 137, pp. 367-381, 2017.

[231] J. V. Kramer and S. Steen, "Simplified test program for hydrodynamic CFD simulations of wind-powered cargo ships," Ocean Engineering, vol. 244, 2022.

[232] R. Sandeepkumar, S. Rajendran, R. Mohan, and A. Pascoal, "A unified ship manoeuvring model with a nonlinear model predictive controller for path following in regular waves," Ocean Engineering, vol. 243, 2022.

[233] J. Duffy, "Modelling of Ship-Bank Interaction and Ship Squat for Ship-Handling Simulation," Phd thesis, University of Tasmania, 2008.

[232] Maersk (Danmark). Update to vessel blockage in the Suez Canal. Retrieved from: <https://www.maersk.com/news/articles/2021/03/24/vessel-blockage-in-the-suez-canal> (accessed 08 April 2021)

[233] The conversation (UK). Stephen Turnock. Suez Canal blockage: what it takes to unwedge a megaship. Retrieved from:< https://theconversation.com/suez-canal-blockage-what-it-takes-to-unwedge-a-megaship-158006> (accessed 26 March 2021)

[234] The wall street journal (US). Amira El-Fekki. Ever given container ship that blocked Suez Canal sets sail after owner pays compensation. Retrieved from:< https://www.wsj.com/articles/ever-given-container-ship-that-blocked-suez-canal-is-set-to-sail-11625641021> (accessed 07 July 2021)

[235] Liu, B, Jin, Y, Magee, AR, Yiew, LJ, & Zhang, S. "System Identification of Abkowitz Model for Ship Maneuvering Motion Based on ε-Support Vector Regression." Proceedings of the ASME 2019 38th International Conference on Ocean, Offshore and Arctic Engineering. Volume 7A: Ocean Engineering. Glasgow, Scotland,

UK. June 9–14, 2019. V07AT06A067. ASME. https://doi.org/10.1115/OMAE2019-96699

[236] Abkowitz, Martin A., Lectures on Ship Hydrodynamics, Steering and Maneuverability, Hydro-og Aerodynamisk Laboratorium Report No. Hy-5, Lyngby, Denmark, May (1964).

[237] Strom-Tejsen, J., A Digital Computer Technique for the Prediction of Standard Maneuvers of Surface Ships,DTMB Report 2130, December (1965).

[238] Inoue, S, Hirano, M. and Kijima, K. Hydrodynamic Derivatives on Ship Manoeu-vring, International Shipbuilding Progress, Vol. 28, No.321, pp 112-125, (1981).

[239] Carlton, J., Radosavlijevic, D. & Whitworth, S. (2009). Rudder-Propeller-Hull Interaction: The Results of Some Recent Research, In-Service Problems and their Solutions. the First International Symposium on Marine Propulsors, June 2009, Trondheim, Norway.